

2011-01-01

# Effect of Process Parameter on Temperature Distribution, Microstructure, and Mechanical Properties of Self-Reacting Friction Stir Welded Aluminum Alloy 6061-T651

Monica Adriana Torres

University of Texas at El Paso, matorres9@miners.utep.edu

Follow this and additional works at: [https://digitalcommons.utep.edu/open\\_etd](https://digitalcommons.utep.edu/open_etd)



Part of the [Materials Science and Engineering Commons](#), and the [Mechanics of Materials Commons](#)

---

## Recommended Citation

Torres, Monica Adriana, "Effect of Process Parameter on Temperature Distribution, Microstructure, and Mechanical Properties of Self-Reacting Friction Stir Welded Aluminum Alloy 6061-T651" (2011). *Open Access Theses & Dissertations*. 2396.  
[https://digitalcommons.utep.edu/open\\_etd/2396](https://digitalcommons.utep.edu/open_etd/2396)

This is brought to you for free and open access by DigitalCommons@UTEP. It has been accepted for inclusion in Open Access Theses & Dissertations by an authorized administrator of DigitalCommons@UTEP. For more information, please contact [lweber@utep.edu](mailto:lweber@utep.edu).

EFFECT OF PROCESS PARAMETERS ON TEMPERATURE DISTRIBUTION,  
MICROSTRUCTURE, AND MECHANICAL PROPERTIES OF SELF-  
REACTING FRICTION STIR WELDED ALUMINUM ALLOY 6061-T651

MONICA ADRIANA TORRES OBREGON

Department of Metallurgical and Materials Engineering

APPROVED:

---

Luis Trueba, Ph.D., Chair

---

Stephen W. Stafford, Ph.D.

---

Heidi A. Taboada, Ph.D.

---

Benjamin Flores, Ph.D.  
Dean of the Graduate School

Copyright  
by  
Monica Torres  
2010

## **Dedication**

For my mom and dad, for their unconditional love, guidance, and infinite support.



EFFECT OF PROCESS PARAMETERS ON TEMPERATURE DISTRIBUTION,  
MICROSTRUCTURE, AND MECHANICAL PROPERTIES OF SELF-  
REACTING FRICTION STIR WELDED ALUMINUM ALLOY 6061-T651

by

MONICA ADRIANA TORRES OBREGON, B.S.

THESIS

Presented to the Faculty of the Graduate School of

The University of Texas at El Paso

in Partial Fulfillment

of the Requirements

for the Degree of

Master of Science

Department of Metallurgy and Materials Engineering, MME

THE UNIVERSITY OF TEXAS AT EL PASO

May 2011

## **Acknowledgements**

During my research experience, I had the opportunity to work with many talented individuals, who not only helped me with my project, but also gave the chance to learn from them; I specially want to thank my parents, my advisor Dr. Luis Trueba, Dr. Lucie Johannes, Dan Rybicki, Frank Orozco, the Materials and Processes Branch at the NASA Johnson Space Center and Jacobs ESCG. This thesis would not have been possible without their support, guidance, and invaluable assistance.

## **Abstract**

Self-reacting friction stir welding is the latest FSW tool configuration developed, it employs two shoulders—one on top and one on the bottom of the workpiece— this tool configuration offers many advantages over conventional welding techniques. However, the current lack of information and specifications limits its understanding and application. This investigation analyzed the effect of process parameters on temperature distribution, microstructure evolution, and final mechanical properties of 6061-T651 SR-FS welds. A factorial experiment was carried out, in which three-process parameters were analyzed—rotational speed, travel speed, and tool plunge force— three levels were analyzed for each parameter, except for a tool plunge force where four levels were investigated. A total of 36 welds were fabricated with one replicate for each set of parameters

The self-reacting friction stir welded joints revealed the same microstructural zones as conventional FSW; however, during SR-FSW a more symmetric microstructure between the crown and root of the weld was observed. The hardness of the weld was uniform through the thickness of the plate, apparently as a result of this microstructure symmetry. In contrast, during conventional FSW, the weld zone exhibits an inverted bell shape, with slightly higher hardness values on the root of the weld. During this investigation, the main microstructural defects encountered were the lazy S defect and voids. Tensile properties such as yield strength, tensile strength and elongation were evaluated. High rotational speed was found to have a significant effect on defect formation and final mechanical properties. During tensile tests, failure occurred in the region that corresponds to the heat-affected zone for defect-free samples. The samples that exhibited the lowest ductility and tensile strength, exhibited severe internal voids and fracture occurred in the nugget region. The optimum parameters to maximize the strength and ductility of SR-FS welded joints were found to be 450 rpm, 20 ipm, and 1350 lb<sub>f</sub>.

## Table of Contents

Acknowledgements.....	v
Abstract .....	vi
Table of Contents.....	vii
List of Tables.....	ix
List of Figures .....	x
Introduction .....	1
1.1 Friction Stir Welding Process .....	1
1.1.1 Friction Stir Welding Tool.....	5
1.1.2 Microstructural Evolution .....	10
1.1.3 Temperature Distribution during Friction Stir Welding .....	12
1.1.4 Friction Stir Welding Discontinuities .....	14
1.1.5 Hardness Profile .....	19
1.1.6 Mechanical Properties.....	20
1.2 Statement of the Problem.....	21
Experimental Procedure .....	22
2.1 Welding Equipment and Materials.....	22
2.1.1 Welding Procedure and Temperature Set-up .....	25
2.2 Overall Visual Appearance .....	28
2.3 Test Specimen Preparation .....	28
2.3.1 Microstructural Characterization.....	29
2.3.2 Microhardness Profile.....	30
2.3.3 Tensile Testing .....	31
Results.....	32
3.1 Temperature Analysis.....	32
3.2 Visual Inspection.....	48
3.3 Microstructure.....	60
3.4 Self-Reacting Friction Stir Welding Defects .....	94
3.4.1 Lazy S Defect .....	95
3.4.2 Voids .....	100

3.4.3 Other Metallurgical Observations .....	110
3.5 Microhardness Weld Profile .....	120
3.5.1 Summary of Microhardness Testing.....	127
3.6 Tensile Test.....	134
Discussion .....	142
4.1 Temperature .....	142
4.2 Visual Appearance .....	142
4.3 Microstructural Evolution.....	143
4.3.1 Weld Nugget Pattern.....	144
4.4 Microstructural Defects .....	147
4.4.1 Lazy S .....	147
4.4.2 Voids .....	147
4.5 Hardness .....	148
4.5 Tensile Properties.....	148
Conclusions .....	150
References .....	151
Curriculum Vita.....	160

## List of Tables

Table 1: Exemplar of Traditional FSW Welding Parameters .....	4
Table 2: Average Grain Size for a 6061-T6 Friction Stir Welded Joint [33] .....	11
Table 3: Traditional FSW Main Welding Zones Peak Temperatures [47].....	14
Table 5: Aluminum 6061-T651 Mechanical Properties per ASTM B209-07 .....	22
Table 6: Process Parameters and Levels .....	23
Table 7: Self-Reacting Friction Stir Welding Factorial Design .....	24
Table 8: Advancing and Retreating Side Temperatures at 0.75" from Tool Edge .....	46
Table 9: Welds with a Narrow Bead.....	57
Table 10: SR-FSW Joints Visual Quality .....	58
Table 11: Lazy S Defect Free Welds .....	99
Table 12: Subsurface Discontinuity.....	110
Table 13: Weld Nugget Size .....	129
Table 14: Self-Reacting Friction Stir Welding Tensile Test Results .....	136
Table 15: Tensile Strength for 1350 lb <sub>f</sub> Tool Plunge Force.....	138
Table 16: Tensile Strength for 1400 lb <sub>f</sub> Tool Plunge Force .....	138
Table 17: Tensile Strength for 1450 lb <sub>f</sub> Tool Plunge Force .....	139
Table 18: Tensile Strength for 1500 lb <sub>f</sub> Tool Plunge Force.....	139
Table 19: Self-Reacting Friction Stir Weld Joint Efficiency .....	140
Table 20: Samples with the Best Mechanical Properties .....	149
Table 21: Samples with the Lowest Mechanical Properties .....	149

## List of Figures

Figure 1: Schematic of the friction stir welding process. During the process, a rapidly rotating tool traverses the joining line forming a weld. The side of the weld where the direction of the tool rotation is the same as the direction of the tool travel is the advancing side. The opposite surface is the retreating side. The inset shows the friction stir tool shoulder and pin. ....	2
Figure 2: Material flow during friction stir welding [10]. ....	3
Figure 3: Friction stir welded joint. A semicircular pattern is observed in the crown of a conventional friction stir welded joint. ....	4
Figure 4: Friction stir welding tool configurations (a) fixed, (b) retractable, and (c) self-reacting. ....	6
Figure 5: Self-reacting friction stir welding tool. This tool configuration consists of one pin tool and two shoulders, one in the top and one in the bottom of the workpiece. ....	7
Figure 6: Start of the weld for a typical SR-FSW butt joint ....	8
Figure 7: End of the weld for a typical SR-FSW butt joint ....	8
Figure 8: SR-FSW semicircular pattern observed in crown (top) and root of the weld (bottom). ....	9
Figure 9: Friction stir weld microstructural zones. Four main regions have been identified in a friction stir weld, the base metal, (BM) the heat affected zone (HAZ), the thermo-mechanically affected zone (TMAZ) and the weld nugget. The base metal is not shown in the macrograph. The advancing side is presented on the right side of the macrograph. ....	10
Figure 10: Conventional frictions stir welded joint microstructure [16]. ....	12
Figure 11: Gallings defect in the crown of a friction stir welded joint. Excessive rotational speed, can lead to partial melting of the weld surface, causing galling or material smearing defect. The inset shows the tool rotational and traverse directions. ....	15
Figure 12: Flash and visible wormhole defects in the crown of a friction stir welded joint. Flashing defect (indicated by blue arrow) is the lip formed next to the weld due to excessive tool plunge force. Visible wormholes (indicated by red arrow) are internal cavities that extend to the surface. ....	16
Figure 13: Voids defect on a self-reacting friction stir welded joint. Voids are observed in nugget region on the advancing side of the weld. ....	17
Figure 14: Lazy S defect in the nugget region of a friction stir welded joint. This defect is associated with the lack of bonding due to the oxide layer on the surfaces of the plates to be joined. ....	18
Table 4: Aluminum 6061-T651 Chemical Composition per ASTM B209-07 ....	22
Figure 15: Self-reacting friction stir weld clamping system. ....	25
Figure 16: Thermal images taken during a self-reacting friction stir welding process. ....	27
Figure 17: Schematic of self-reacting friction stir welded plates. Welded plates were cross-section perpendicular to the welding direction to prepare tensile and metallographic test specimens. ....	28
Figure 18: Self-reacting friction stir weld microstructural characterization sample. ....	29
Figure 19: Microhardness profile. Hardness reading were taken as function of distance from the weld centerline every 3mm and at three depths (top, middle and bottom). White dots exhibit the microhardness indentations. The advancing side is shown on the right side and the crown of the weld on the bottom of the macrograph. ....	30
Figure 20: Self-reacting friction stir weld tensile test specimen dimensions. Tensile test specimens were prepared perpendicular to the weld direction. ....	31
Figure 21: Exemplar temperature profile as distance from tool shoulder edge during SR-FSW ....	32
Figure 22: Temperature profile for samples fabricated at 500rpm, 1500lb <sub>f</sub> and three different travel speeds. As the traverse speed decreased the temperature increased. ....	33
Figure 23: Temperature profile for sample fabricated at 500 rpm, 1450 lb <sub>f</sub> and three different travel speeds. The highest temperature was observed at a medium travel speed (Sample 7). ....	34

Figure 24: Temperature profile for sample fabricated at 500 rpm, 1400 lb <sub>f</sub> and three different travel speeds. The highest temperature was observed at a low travel speed (15 ipm) (Sample 8).	35
Figure 25: Temperature profile for sample fabricated at 500 rpm, 1350 lb <sub>f</sub> and three different travel speeds. A low travel speed (15 ipm) exhibited the highest temperatures.	36
Figure 26: Temperature profile for sample fabricated at 450 rpm, 1500 lb <sub>f</sub> and three different travel speeds. As the travel speed decreased the temperature increased.	37
Figure 27: Temperature profile for sample fabricated at 450 rpm, 1450 lb <sub>f</sub> and three different travel speeds. A higher travel speed (20 ipm) exhibited a higher temperature profile	38
Figure 28: Temperature profile for sample fabricated at 450 rpm, 1400 lb <sub>f</sub> and three different travel speeds. Temperature increased as the traverse speed decreased.	39
Figure 29: Temperature profile for sample fabricated at 450 rpm, 1350 lb <sub>f</sub> and three different travel speeds. Slightly higher temperatures were observed at a medium travel speed as compared to a high travel speed. Temperature data for Sample 22 is not included.	40
Figure 30: Temperature profiles for sample fabricated at 400 rpm, 1500 lb <sub>f</sub> and three different travel speeds. Higher temperatures were developed at a high travel speed (20 ipm).	41
Figure 31: Temperature profiles for sample fabricated at 450 rpm, 1350 lb <sub>f</sub> and three different travel speeds. Higher temperatures were observed at a medium travel speed as compared to a low travel speed. Temperature data for Sample 3 is not included.	42
Figure 32: Temperature profiles for sample fabricated at 450 rpm, 1350 lb <sub>f</sub> and three different travel speeds.	43
Figure 33: Temperature profiles for sample fabricated at 450 rpm, 1350 lb <sub>f</sub> and three different travel speeds.	44
Figure 34: Overall retreating side hottest and coldest welds temperature profiles. Sample 1 exhibited the higher temperatures, while Sample 30 showed the lowest temperatures. The red box indicates the time at which the analysis was carried-out.	47
Figure 35: SR-FSW semicircular pattern observed in (a) crown and (b) root of the weld.	48
Figure 36: Visible wormholes, Sample 17. Wormholes are internal voids that extend to the surface of the weld. This defect is highly detrimental to visual appearance of the weld.	49
Figure 37: Visible galling (rated 3) on the crown of Sample 4. Severe galling is characterized by a rough surface.	50
Figure 38: Light galling (rated 2) on the crown of Sample 36.	50
Figure 39: Small amount of continuous flash (rated as 2) observed on Sample 1.	51
Figure 40: Intermittent, decreasing flash (rated 1) observed on Sample 5.	51
Figure 41: Narrow weld beads (rated 1). Welds measuring less than the tool shoulder width were considered narrow.	52
Figure 42: Weld visual appearance as function of process parameters. The description of the visual appearance is shown below the image. The main visual appearance discontinuities observed were visible wormholes (blue arrow), galling (red arrow), and flashing (green arrow).	53
Figure 43: Weld visual appearance as function of process parameters. The description of the visual appearance is shown below the image. The main visual appearance discontinuities observed were visible wormholes (blue arrow), galling (red arrow), and flashing (green arrow).	54
Figure 44: Weld visual appearance as function of process parameters. The description of the visual appearance is shown below the image. The main visual appearance discontinuities observed were visible wormholes (blue arrow), galling (red arrow), and flashing (green arrow).	55
Figure 45: Welds visual appearance as function of process parameters. The description of the visual appearance is shown below the image. The main visual appearance discontinuities observed were visible wormholes (blue arrow), galling (red arrow), and flashing (green arrow).	56



Figure 46: Visual appearance main effects analysis. Rotational speed has a bigger effect in the weld visual appearance. The best visual appearance is achieved at low rotational speed, low travel speed, and high tool plunge force. ....	59
Figure 47: Self-reacting friction stir weld zones. The weld nugget, the thermo-mechanically affected zone (TMAZ), and the heat-affected zone are presented on the macrograph. The advancing side is shown on the right side of the macrograph. ....	60
Figure 48: SR-FSW weld zone bands macrograph from Sample 21. Bands (indicated by red arrows) running towards the center of the weld. White dots in the macrographs are microhardness indentations. ....	61
Figure 49: Weld nugget distinguishing “finger” pattern macrographs. A discernable concentric ring pattern is observed in the nugget region on (a) Sample 1, (b) Sample 5, and (c) Sample 9, and (d) Sample 6. ....	62
Figure 50: Weld nugget pattern macrographs. No distinct “finger like” pattern is observed in the weld nugget of Sample 34. ....	63
Figure 51: Representative microstructure from the center of the weld nugget, Sample 1. Dix-Keller’s reagent. ....	64
Figure 52: Representative microstructure from the center of the weld nugget, Sample 3. Dix-Keller’s reagent. ....	65
Figure 53: Representative nugget microstructure near the top shoulder. Dix-Keller’s reagent. ....	66
Figure 54: Representative nugget microstructure near the bottom shoulder. Dix-Keller’s reagent. ....	67
Figure 55: Representative advancing side nugget microstructure, Sample 5. Dix-Keller’s reagent. ....	68
Figure 56: Representative advancing side nugget microstructure, Sample 15. The microstructure is characterized by a fine grains. Dix-Keller’s reagent. ....	69
Figure 57: Advancing side nugget microstructure from sample 21. The microstructure is characterized by a fine grains. Dix-Keller’s reagent. ....	70
Figure 58: Advancing side nugget microstructure from Sample 13. What appear to be bands were observed in the nugget region in the advancing side. Dix-Keller etchant. ....	71
Figure 59: Advancing side nugget microstructure from Sample 2. What appear to be bands were observed in the nugget region in the advancing side. Dix-Keller’s reagent. ....	72
Figure 60: Retreating side nugget microstructure from Sample 9. A mixture of small and large grains is observed. Dix-Keller’s reagent. ....	73
Figure 61: Retreating side nugget microstructure from Sample 10. A mixture of small and large grains is observed. Dix-Keller’s reagent. ....	74
Figure 62: Nugget—TMAZ border. The transition zone between the nugget and the thermo-mechanically affected zone is more distinguishable on the advancing side (right side) compared to the retreating side (left side). Dix-Keller etchant. ....	75
Figure 63: Advancing side TMAZ microstructure from Sample 31. Dix-Keller etchant. ....	76
Figure 64: Advancing side TMAZ microstructure from Sample 31. Dix-Keller etchant. ....	77
Figure 65: Representative retreating side TMAZ microstructure Sample 10. Dix-Keller etchant. ....	78
Figure 66: Advancing side top shoulder thermo-mechanically affected zone microstructure, Sample 5. The microstructure in this region exhibits deformed grains bent toward the tool shoulder (red arrow). The advancing side is shown on the right side of the micrograph. Dix-Keller etchant. ....	79
Figure 67: Advancing side weld center thermo-mechanically affected zone microstructure, Sample 5. The microstructure in this region exhibits deformed grains. The advancing side is shown on the right side of the micrograph. Dix-Keller etchant. ....	80

Figure 68: Advancing bottom shoulder thermo-mechanically affected zone microstructure, Sample 5. The microstructure in this region exhibits deformed and bent grains, toward the tool shoulder (red arrow). The advancing side is shown on the right side of the micrograph. Dix-Keller etchant. ....	81
Figure 69: Comparison between the nugget and the thermo-mechanically affected zone microstructures near the top shoulder, Sample 5. The micrograph presents the TMAZ deformed and rotated grains (right) and the fine, recrystallized nugget microstructure (left). Dix-Keller etchant. ....	82
Figure 70: Nugget-TMAZ microstructure, near the bottom shoulder from Sample 10. The nugget microstructure (left bottom corner) exhibits fine, equiaxed grains, whereas, the TMAZ microstructure (right) is characterized by deformed grains. Dix-Keller etchant. ....	83
Figure 71: Representative advancing side heat-affected zone microstructure, Sample 14. Dix-Keller etchant. ....	84
Figure 72: Representative advancing side heat-affected zone microstructure, Sample 10. Dix-Keller etchant. ....	85
Figure 73: Representative advancing side heat-affected zone microstructure, Sample 9. Dix-Keller etchant. ....	86
Figure 74: Representative advancing side heat-affected zone microstructure, Sample 8. Dix-Keller etchant. ....	87
Figure 75: Representative retreating side heat-affected zone microstructure, Sample 14. Dix-Keller etchant. ....	88
Figure 76: Representative retreating side heat-affected zone microstructure, Sample 10. Dix-Keller etchant. ....	89
Figure 77: Representative retreating side heat-affected zone microstructure, Sample 9. Dix-Keller etchant. ....	90
Figure 78: Representative retreating side heat-affected zone microstructure, Sample 8. Dix-Keller etchant. ....	91
Figure 79: Parent metal microstructure. The base metal microstructure consists of elongated grains due to the rolling process. Dix-Keller etchant. ....	92
Figure 80: Parent metal microstructure. The base metal microstructure consists of elongated grains due to the rolling process. Dix-Keller etchant. ....	93
Figure 81: Lazy S defect and voids. The lazy S defect (indicated by arrows) and voids are observed in the nugget region of a self-reacting friction stir weld. The advancing side is shown on the right side of the micrograph. ....	94
Figure 82: Lazy S defects for the 1350 lb <sub>f</sub> plunge force. Welds that exhibited the lazy S defect are listed as function of process parameters. ....	95
Figure 83: Lazy S defects for the 1400 lb <sub>f</sub> plunge force. Welds that exhibited the lazy S defect are listed as function of process parameters. ....	96
Figure 84: Lazy S defects for the 1450 lb <sub>f</sub> plunge force. Welds that exhibited the lazy S defect are listed as function of process parameters. ....	97
Figure 85: Lazy S defects for the 1500 lb <sub>f</sub> plunge force. Welds that exhibited the lazy S defect are listed as function of process parameters. ....	98
Figure 86: Representative macrograph (Sample 7) from the typical location of voids, which are usually observed on the nugget region on the advancing side (circle) ....	100
Figure 87: Void concentration 0. No voids are observed (Sample 21). ....	101
Figure 88: Void concentration 1. Sample 34 represents a void concentration of 1, which is characterized by small voids in the same region. ....	102
Figure 89: Void concentration 2. Sample 11 represents a void concentration of 2, which is characterized by small voids distributed over larger areas. ....	103

Figure 90: Void concentration 3. Sample 7 represents a void concentration of 3, which is characterized by large voids distributed over larger areas. ....	104
Figure 91: Void concentration for a 1350 lb <sub>f</sub> plunge force. Micrographs exhibit the void concentration on the nugget region, as function of process parameters. Advancing side is on the right side for all micrographs. ....	105
Figure 92: Void concentration for a 1400 lb <sub>f</sub> plunge force. Micrographs exhibit the void concentration on the nugget region, as function of process parameters. Advancing side is on the right side for all micrographs. ....	106
Figure 93: Void concentration for a 1450 lb <sub>f</sub> plunge force. Micrographs exhibit the void concentration on the nugget region, as function of process parameters. Advancing side is on the right side for all micrographs. ....	107
Figure 94: Void concentration for a 1500 lb <sub>f</sub> plunge force. Micrographs exhibit the void concentration on the nugget region, as function of process parameters. Advancing side is on the right side for all micrographs. ....	108
Figure 95: Void concentration main effects plot. The steep line for rotational speed in the main effect plot is indicative of its higher effect on the void concentration, as compared to plunge force and travel speed. ....	109
Figure 96: Metallurgical discontinuity observed below the crown of the weld, in Sample 1 .....	111
Figure 97: Metallurgical discontinuity observed below the crown of the weld, in Sample 5. ....	112
Figure 98: Metallurgical discontinuity observed below the crown of the weld, in Sample 10. ....	113
Figure 99: Metallurgical discontinuity observed below the crown of the weld, in Sample 15. ....	114
Figure 100: Metallurgical discontinuity observed below the root of the weld (Sample 15). ....	115
Figure 101: Metallurgical discontinuity observed below the crown of the weld (Sample 26). ....	116
Figure 102: Metallurgical discontinuity observed below the crown of the weld (Sample 30). ....	117
Figure 103: Chemical analysis from the metallographic features observed on Sample 15 .....	118
Figure 104: SEM image from metallographic feature on Sample 15. ....	119
Figure 105: Self-reacting friction stir weld “w” shaped micro-hardness profile. Four main hardness zones have been identified: weld nugget, thermo-mechanically affected zone (TMAZ), heat affected zone (HAZ) and base metal (BM). ....	120
Figure 106: Hardness profile for samples fabricated at 500 rpm and 1500 lb <sub>f</sub> . ....	121
Figure 107: Hardness profile for samples fabricated at 450 rpm and 1500 lb <sub>f</sub> . ....	121
Figure 108: Hardness profile for samples fabricated at 400 rpm and 1500 lb <sub>f</sub> . ....	122
Figure 109: Hardness profile for samples fabricated at 500 rpm, and 1450 lb <sub>f</sub> . The sharp drop in hardness observed at a medium travel speed corresponds to a region in which voids exists. ....	122
Figure 110: Hardness profile for samples fabricated at 450 rpm and 1450 lb <sub>f</sub> . ....	123
Figure 111: Hardness profile for samples fabricated at 400 rpm, 1450 lb <sub>f</sub> . Sample 10 fabricated at a medium travel speed hardness data is not shown due to human error. ....	123
Figure 112: Hardness profile for samples fabricated at 500 rpm and 1400 lb <sub>f</sub> . The sharp drop in hardness observed at a medium travel speed corresponds to a region with voids. ....	124
Figure 113: Hardness profile for samples fabricated at 450 rpm and 1400 lb <sub>f</sub> . ....	124
Figure 114: Hardness profile for samples fabricated at 400 rpm and 1400 lb <sub>f</sub> . ....	125
Figure 115: Hardness profile for samples fabricated at 500 rpm and 1350 lb <sub>f</sub> . ....	125
Figure 116: Hardness profile for samples fabricated at 450 rpm and 1350 lb <sub>f</sub> . ....	126
Figure 117: Hardness profile for samples fabricated at 400 rpm and 1350 lb <sub>f</sub> . ....	126
Figure 118: More uniform weld nuggets. All tool plunge forces developed more uniform weld nugget at low rotational speed and high travel speed. ....	127
Figure 119: Microhardness comparison between a uniform nugget and a weld nugget with slightly higher values in the advancing side. ....	128

Figure 120: Comparison between a small (Sample 3) and a larger (Sample 11) weld nugget. ....	128
Figure 121: TMAZ-HAZ drop in hardness. Sample 28 exhibits a sharp drop in hardness in the retreating side, between TMAZ and HAZ, whereas, Sample 27 shows a minimum hardness difference. ....	130
Figure 122: Hardness depth profile for samples with low number of defects. The hardness at different depths did not exhibit significant differences. The advancing side is presented on the right side, and the crown of the weld on the bottom of the macrograph. ....	131
Figure 123: Hardness depth profile for samples with medium number of defects. The hardness at different depths did not exhibit significant differences. The advancing side is presented on the right side, and the crown of the weld on the bottom of the macrograph. ....	132
Figure 124: Hardness depth profile for samples with large number of defects. The hardness at different depths did not exhibit significant differences. The sharp drop in hardness on Sample 7 corresponds to the presence of voids. The advancing side is presented on the right side, and the crown of the weld on the bottom of the macrograph. ....	133
Figure 125: Tensile fracture in the nugget region. Samples that exhibited a low percent elongation exhibited tensile fracture in the nugget region (Sample 7). ....	134
Figure 126: Tensile fracture at the radius of the tool shoulder on the advancing side (Sample 32.) ....	135
Figure 127: Tensile fracture observed at the radius of the tool shoulder. Fracture generally occurred on the retreating side of samples that exhibited a high percent elongation (Sample 8). ....	135
Figure 128: Percent elongation main effects plot. All factors appear to have an influence on the percent elongation. ....	137
Figure 129: Tensile strength main effects plot. The rotational speed has a bigger effect on the tensile strength. ....	141
Figure 130: Friction stir welded joints microstructures. Conventional FSW [16] (top) and SR-FSW (bottom) microstructures. The advancing side is shown on the left side of the micrographs. ....	144
Figure 131: Dark field micrographs from a conventional friction stir weld nugget exhibiting the onion ring pattern [70]. ....	145
Figure 132: Exemplar of a SR-FSW nugget pattern (Sample 1). ....	146

## **Introduction**

The Welding Institute (TWI) developed a new welding technique in 1991 known as friction stir welding (FSW). Friction stir welding is a solid-state joining process in which no melting is involved; joining of materials is produced by frictional heat, pressure, and plastic deformation [1]. The advantages of this new technology over conventional welding techniques were quickly recognized, generating significant interest in understanding the process and its implications in order to further benefit from it [2]. Some of the advantages of the FSW process include: compatibility with all types of aluminum alloys, elimination of solidification defects associated with fusion welding, good joint mechanical properties, low distortion, no harmful fumes evolved during the process, and no need for filler material [2]. Although, friction stir welding is successfully being used in some aerospace and industrial applications such as rocket fuel tanks [3], the space shuttle external tank [2], and small passenger airplanes [3], proprietary considerations have prevented the dissemination of critical process information to the public, limiting its understanding, standardization, and further development [4].

### **1.1 FRICTION STIR WELDING PROCESS**

A schematic diagram of the conventional friction stir welding process is presented in Figure 1. During the friction stir welding process a rapidly rotating non-consumable tool consisting of a shoulder and a pin [2] is inserted into the workpieces [5]; subsequently, the tool traverses the joining line forming a weld [4]. The side of the workpiece where the direction of rotation is the same as the travel direction is the advancing side (ADV); the opposite surface is the retreating side (RE) [4] [6].

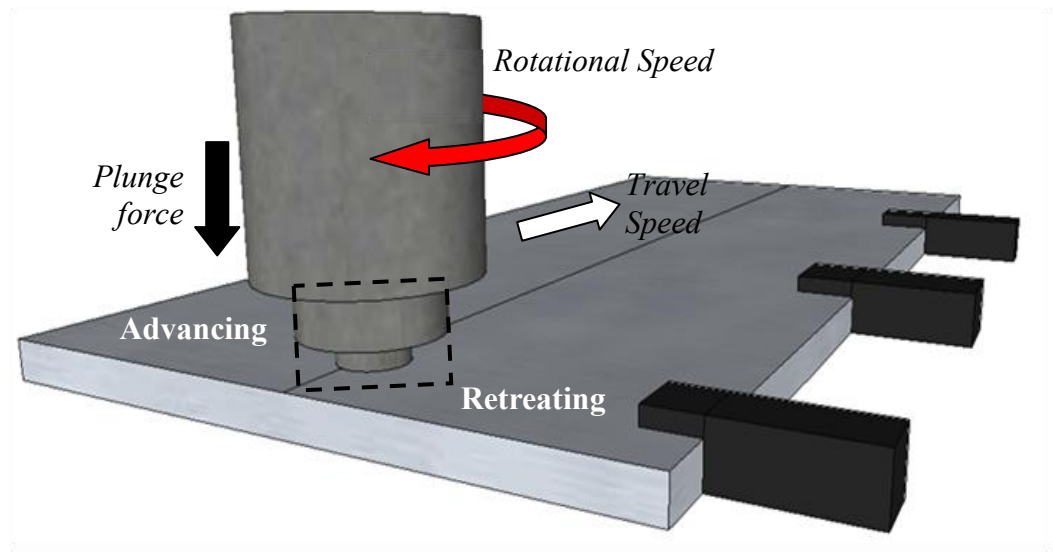
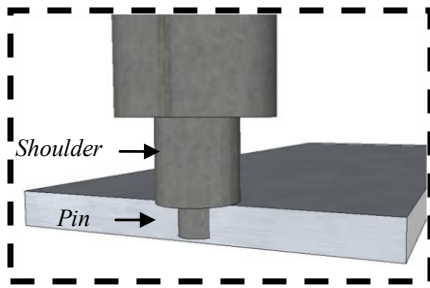


Figure 1: Schematic of the friction stir welding process. During the process, a rapidly rotating tool traverses the joining line forming a weld. The side of the weld where the direction of the tool rotation is the same as the direction of the tool travel is the advancing side. The opposite surface is the retreating side. The inset shows the friction stir tool shoulder and pin.

During the FSW process, the tool shoulder, which is in direct contact with the workpiece generates the frictional heat needed to soften the material without melting it and constrains the plastized material [4], whereas, the pin tool “stirs” the materials together, creating the joint [2]. Throughout the

friction stir welding process the material undergoes a quite complicated flow that involves rotational, longitudinal, and vertical movement of the plasticized material [7, 8]. Friction stir welding has been compared to an extrusion process where the softened material in front of the tool is pushed to the back of the tool and around to the retreating side [9]. According to Srivatsan et al. the FSW process comprises five metalworking zones (shown in Figure 2): pre-heat, initial deformation, extrusion, forging, and cool-down. During the FSW process, the frictional heat from the rotational movement of the tool raises the temperature in front of the pin (pre-heat), while the traverse tool movement causes an initial deformation region where the material is pushed upwards and downwards into the extrusion zone. In the extrusion zone, the material flows around the pin towards the rear. Subsequently, in the forging zone the material is forced by the shoulder into the cavity left behind by the traverse movement of the pin [10].

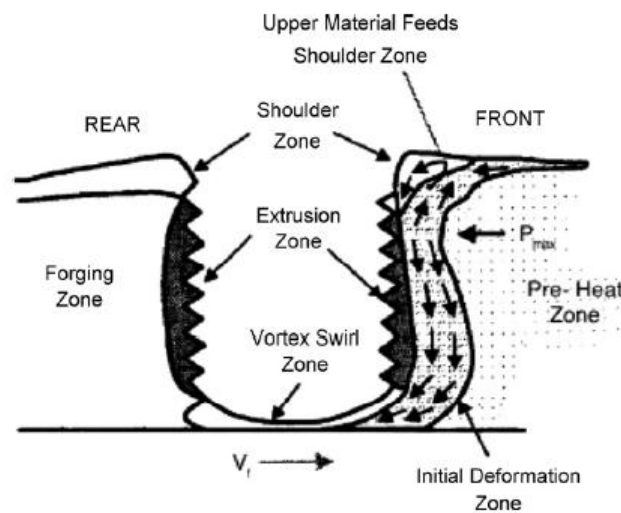


Figure 2: Material flow during friction stir welding [10].

The main process parameters involved in the FSW process are the rotational speed, the traverse speed, and the tool plunge force or plunge depth. Welds produced with a low rotational speed, high traverse speed, and low plunge force have been classified as cold welds, while welds produced at high rotational speed, low traverse speed and high plunge force are known as hot welds [2]. Table 1 is an exemplar of the welding parameters used under various conventional FSW investigations.

Table 1: Exemplar of Traditional FSW Welding Parameters

Research	Rotational Speed (rpm)	Traverse Speed (mm/s or mm/min)	Plunge Force or Plunge Depth
Elangovan et al. [11]	1200	1.25 mm/s (0.049 in/s)	7KN
Scialpi et al. [12]	1810	460 mm/min (18.11 ipm)	0.1mm (0.0039 in)
Kumar et al.[13]	1400	80 mm/min (3.14 ipm)	
Moreira et al.[14]	1120	224 mm/min (8.82 ipm)	
Sato et al.[15]	800-3600	6 mm/s (0.236in/s)	
Huijie et. al [16]	1500	800 mm/min (31.49 ipm)	
Viyajan et al.[17]	650	115 mm/min (4.52 ipm)	17KN

A friction stir welded joint exhibits a regularly spaced semi-circular pattern in the crown of the weld, as shown in Figure 3. This pattern is associated with the tool advance for each revolution [4] [18] [19].

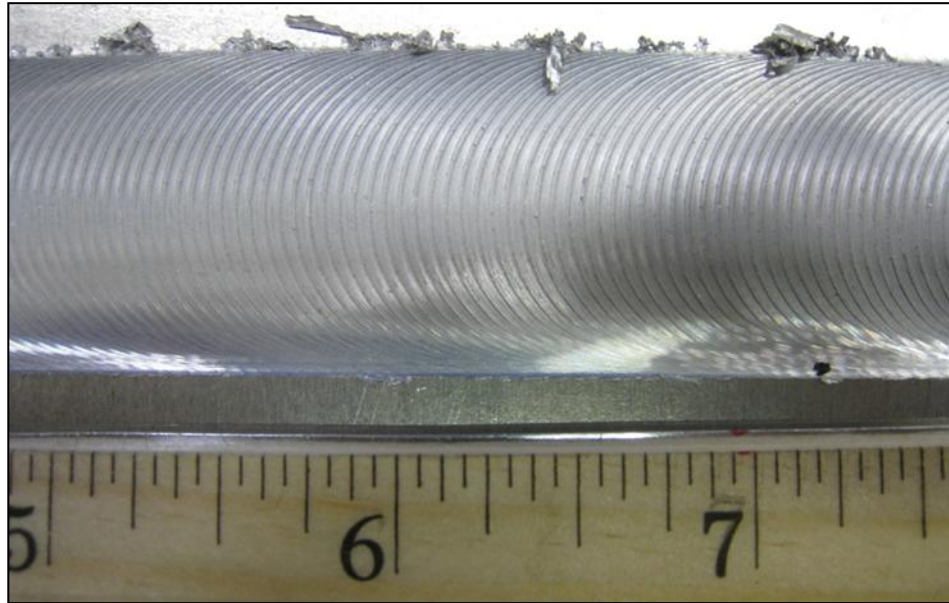


Figure 3: Friction stir welded joint. A semicircular pattern is observed in the crown of a conventional friction stir welded joint.



### **1.1.1 Friction Stir Welding Tool**

The friction stir welding tool plays an important role during the welding process—it produces the needed mechanical deformation and heat to soften the material and create a joint [2]; therefore, the tool features have a direct effect on the weld quality [3]. Some tool features such as the scroll shoulder pattern can reduce the shearing deformation damage in the microstructure adjacent to the weld surface, resulting in better fatigue resistance properties; however, aggressive shoulder features can lead to surface damage, such as excessive roughness, which can deteriorate the quality of the weld [20, 21].

Scialpi et al. studied the effect of three different shoulder geometries—scroll and fillet, cavity and fillet, and fillet only—on the mechanical properties of FS welded 6082 aluminum alloy joints. The fillet and cavity combination provided the best weld appearance and exhibited an increase in the longitudinal and transverse strength of the joint [12]. A similar study was carried-out by Fujii et al. They analyzed the effect of three different tool shapes on the welded joint strength of different aluminum alloys. For 6061-T6 joints, the tool shape did not exhibit a significant effect on mechanical properties, whereas the weldability of 5083-O was significantly influenced by rotational speed and tool shape [22]. The effect of the tool shoulder size on mechanical properties has been analyzed by various authors, who concluded that the tool shoulder size has a direct influence on the temperature distribution and thus on the dimension of the different welding zones and the final strength of the joint [23-24]. A higher frictional heat is generated by larger shoulder diameters due to a larger contact area, leading to a wider thermo-mechanically and heat-affected zones. Therefore, the tensile properties of the joints are deteriorated [24]. Smaller tool shoulder diameters lead to a narrower contact area, which result in less frictional heat generation, hence a lack of metal consolidation in the nugget region [24].

### **Friction Stir Welding Tool Configurations**

Since the invention of FSW, the process has advanced and evolved significantly, leading to the development of different tool designs. Today there are three main tool configurations available—fixed or conventional, retractable, and self-reacting (SR-FSW)—as shown in Figure 4. Each tool design has unique characteristics and capabilities, as discuss below.



Figure 4: Friction stir welding tool configurations (a) fixed, (b) retractable, and (c) self-reacting.

The conventional friction stir welding tool was the first tool developed and is currently the most studied. In this tool configuration, the shoulder and the pin are a single piece, which results in an exit keyhole in the workpiece when the tool is retracted. The length of the pin is approximately equal to the thickness of the materials to be welded [25], limiting its use to welds of constant material thickness [26]. During the welding process, a backing anvil is required to counteract the axial force exerted on the workpiece by the tool [25]. In contrast to the conventional tool configuration, the retractable tool is a two-piece tool where the shoulder and pin have independent movement [25]. This feature allows for variable thickness welding as the pin length can be automatically adjusted. The independent pin movement also allows for the incremental withdrawal of the tool from the workpiece at the end of the weld, eliminating the exit keyhole [27]. Like the conventional tool configuration, the retractable tool requires a backing anvil to provide the reaction force to the force exerted on the workpiece by the tool [28].

The self-reacting tool is the latest FSW tool configuration developed; it employs one pin and two shoulders—one on the top surface and one on the bottom surface of the workpiece—as shown in Figure 5. This tool configuration is referred to as self-reacting because the two shoulders each provide the reaction force, eliminating the need for a backing anvil and allowing for contoured welding [2]. During the SR welding process, the heat created by the two shoulders allows for faster welding speeds as compared to conventional FSW [2].

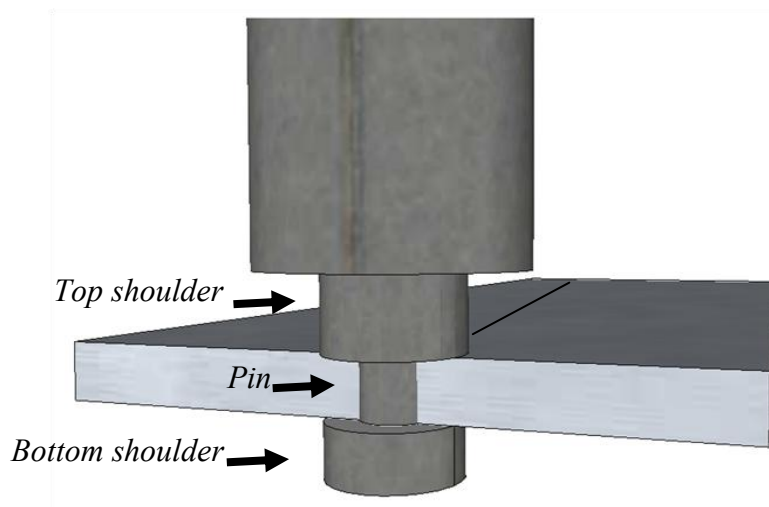


Figure 5: Self-reacting friction stir welding tool. This tool configuration consists of one pin tool and two shoulders, one in the top and one in the bottom of the workpiece.

In order to fabricate a butt joint configuration by SR-FSW, a hole is drilled through the workpiece; the pin is inserted through the hole, and the backing shoulder attached to the pin prior to welding. The start and the end of a typical SR-FSW are shown in Figure 6 and Figure 7, respectively.

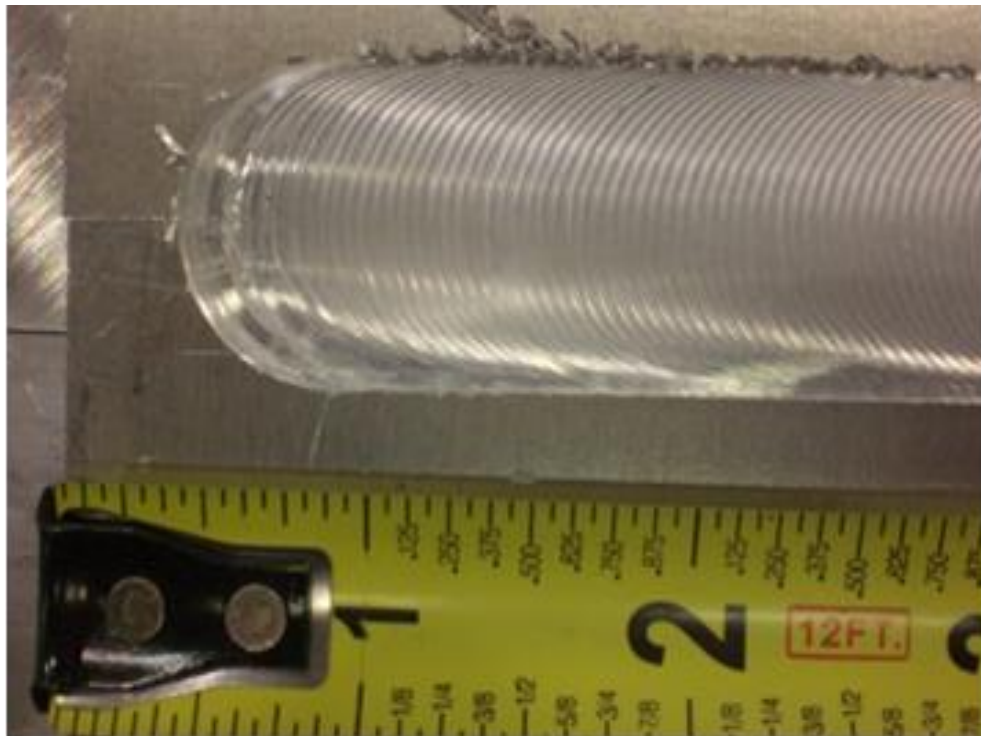


Figure 6: Start of the weld for a typical SR-FSW butt joint

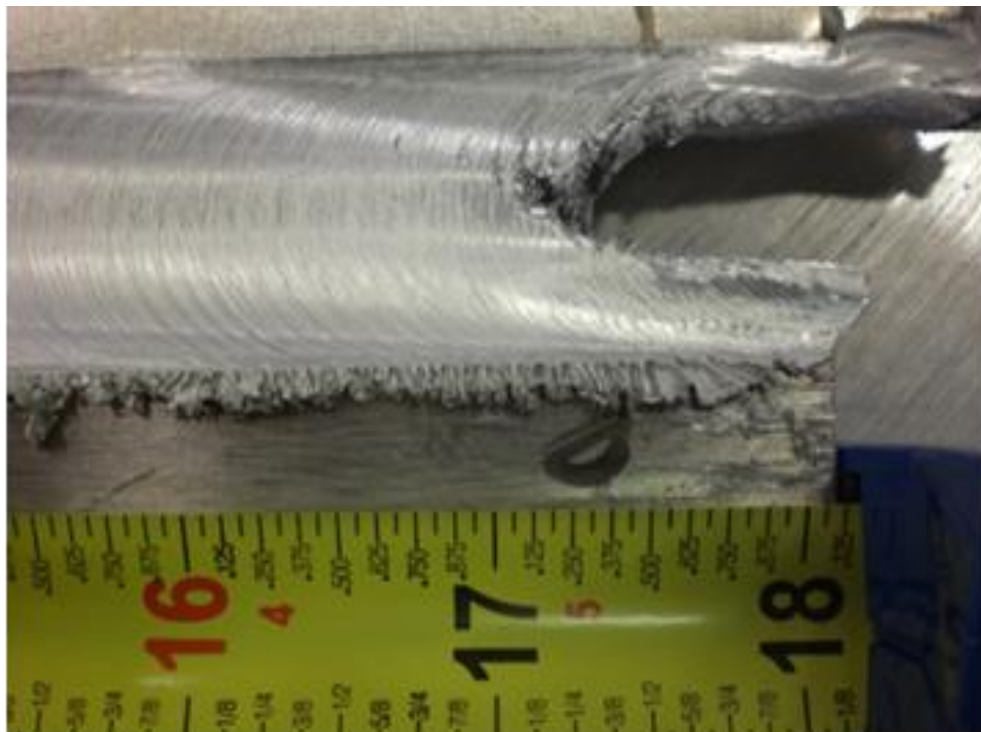


Figure 7: End of the weld for a typical SR-FSW butt joint

The contact of the workpiece with the top and bottom shoulders produces the semicircular pattern observed in the crown of a conventional FS weld. However, with the SR-FSW, the semicircular pattern appears in both the crown and the root of the weld, as shown in Figure 8.



Figure 8: SR-FSW semicircular pattern observed in crown (top) and root of the weld (bottom).



The SR-FSW tool configuration offers the advantage of eliminating the incomplete root penetration defect observed in conventional FS welded joints. Incomplete penetration takes place when an un-deformed region is formed in the root of the weld due to insufficient pin length or plunge force [1]. Failure has been observed in this unbound region [2]. Subsequent to welding, the self-reacting tool must be carefully cleaned, as extruded material can affect the welding capabilities of the tool [2]. The tool can be cleaned, mechanically or chemically; Matlack et al. developed a tool cleaning method where the friction stir welding tool having a surface with material residue from the welding process is heated until the residue is sufficiently plasticized, subsequently, the residue is removed with the aid of a cleaning tool [29].

### 1.1.2 Microstructural Evolution

A typical cross-section of a friction stir welded joint consists of four main microstructural zones, as shown in Figure 9 [6]. These are the unaffected metal, heat-affected zone (HAZ), thermo-mechanically affected zone (TMAZ), and stir zone or nugget [30] [13].

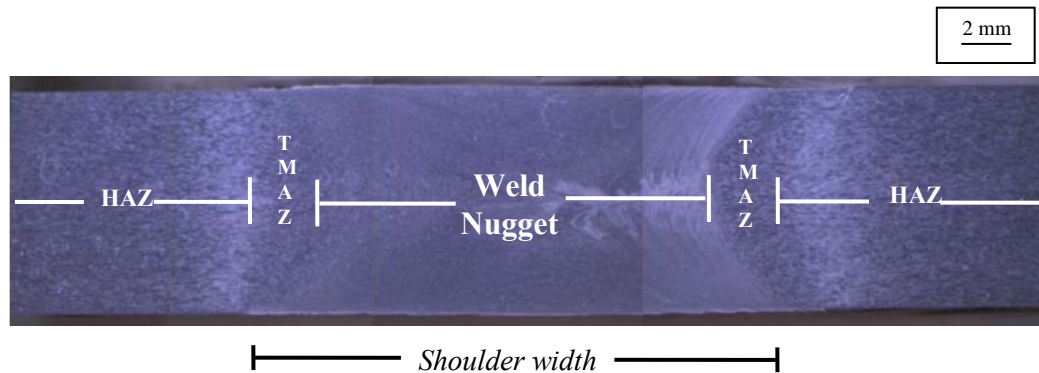


Figure 9: Friction stir weld microstructural zones. Four main regions have been identified in a friction stir weld, the base metal, (BM) the heat affected zone (HAZ), the thermo-mechanically affected zone (TMAZ) and the weld nugget. The base metal is not shown in the macrograph. The advancing side is presented on the right side of the macrograph.

The central portion of the weld is the nugget, which undergoes the highest temperatures and greatest amount of plastic deformation. The nugget exhibits a small, equiaxed, and dynamically recrystallized grain structure. The precipitates in this zone are normally dissolved because of the high temperatures and rapid cooling experienced [1][15]. In the weld nugget, a slight reduction of the parent metal hardness has been reported [31] [32]. Next to the nugget is the thermo-mechanically affected zone (TMAZ); this zone is characterized by rotated and deformed grains due to the effect of heat and plastic deformation produced by the stirring in the process. The hardness profile across the weld exhibits a sharp decrease in the TMAZ region [2]. Between the TMAZ and the base metal lies the heat-affected zone (HAZ). The original grain structure is retained in the HAZ, as it experiences lower temperatures [6]. However, heating in this region of the weld causes overaging of the precipitates. The hardness profile reaches a minimum in the HAZ, and then increases into the base metal [2]. Since no obvious differences exist between the microstructures in the HAZ and the parent metal, the HAZ is usually identified by this decrease in hardness [23]. Away from the weld line is the parent metal; its microstructure and mechanical properties are not affected by the welding process [2]. Table 2 presents the average grain diameter for the different welding zones from a 6061-T6 FS welded joint; fabricated at 1200 rpm and 200 mm/min (7.87 in/min), with a tool shoulder and pin diameter of 15mm (0.590 in.) and 6 mm (0.236 in.), respectively [33].

Table 2: Average Grain Size for a 6061-T6 Friction Stir Welded Joint [33]

<b>Weld Zone</b>	<b>Average Grain Size</b>
<b>Parent metal</b>	43 $\mu\text{m}$
<b>HAZ</b>	67 $\mu\text{m}$
<b>Nugget</b>	9 $\mu\text{m}$

The formation of the different microstructural zones during friction stir welding, strongly depends on the process parameters, the tool profile, and the material characteristics [17] [34] [35]. Rotational and traverse speeds have a significant influence on the microstructure [36]; it has been reported that a decrease in rotational speed and an increase in travel speed results in a finer microstructure due to the lower heat input produced [34]. The microstructure developed during conventional FSW exhibits an asymmetry between the top and bottom of the weld [37], which is characterized by an inverted bell-shaped weld nugget [38].

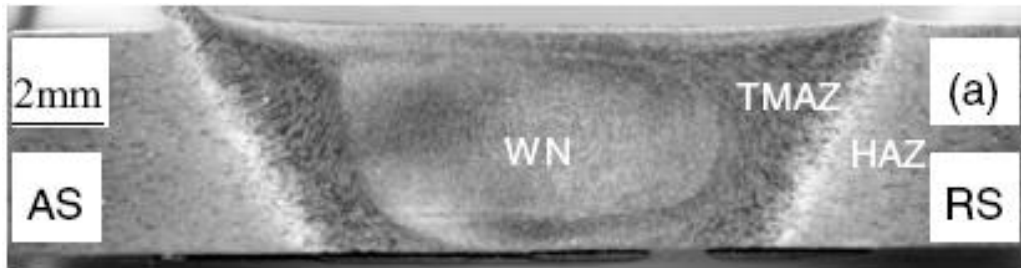


Figure 10: Conventional frictions stir welded joint microstructure [16].

### 1.1.3 Temperature Distribution during Friction Stir Welding

The thermal cycle experienced by the materials during the friction stir welding process is crucial to the final properties of the weld [39]. The amount of the heat that flows into the workpiece determines the quality of the weld, residual stresses, and distortion of the workpiece [40]. Numerous studies, including physical experimentation and analytical modeling have been done to understand the heat generation and to determine the thermal gradients evolved in the workpiece during the friction stir welding process. Chao et al. determined that 95% of the heat generated during a FSW process flows to the workpiece with the remaining 5% flowing to the tool [40].

Embedded thermocouples and infrared (IR) thermal imaging are among the methods used to map out the workpiece temperature field during FSW—the former being the most common method [2].



Thermocouples provide moderately accurate and consistent measurements [41]. Thermocouples are available in a variety of temperature ranges and can be used to quantify the surface and the interior temperature [42]; however, the temperature measurements are affected by thermocouple location and the workpiece thermal conductivity [2]. On the other hand, infrared cameras are a visualization technique able to measure the surface temperature of an object. IR cameras detect the radiation emitted by an object, which can be influenced by multiple factors such as, the emissivity of the object, ambient temperature, humidity, the radiation emitted by objects near the desired target, the distance between the object and the camera, among others [43]. The emissivity ( $\epsilon$ ) is the ratio of the actual radiation emitted from the surface of an object to that emitted from an idealized black body ( $\epsilon=1$ ) at the same temperature [43]. The influence of all these factors makes it difficult to obtain accurate readings, especially for highly reflective objects such as metals. However, some corrective actions such as coating the materials with a non-reflective paint can increase the emissivity of the plates; thus, improve the accuracy of the temperature readings. Currently some studies have used infrared cameras (IR) to measure the workpiece and tool temperature distribution during welding [44] [5] [45].

During FSW the heat field below the tool shoulder is asymmetric [46] with slightly higher temperatures on the retreating side [2]. Contrary to this, Adamowski **et al.** reported a higher temperature on the advancing side, with a temperature difference of 50 °C (122 °F), this difference is also attributed to the FSW process asymmetry [7]. During conventional friction stir welding the temperature reaches about 80 to 90% of the melting temperature of the material [40]. The peak temperatures for the different microstructural zones for a friction stir welded joint of 6061 aluminum alloy, are shown in Table 3 [47]. The maximum temperature during SR-FSW is 50°C (90°F) higher than with traditional FSW [2]; this can be attributed to the heat generated by the two shoulders and the lack of a backing anvil, which acts as a heat sink

Table 3: Traditional FSW Main Welding Zones Peak Temperatures [47]

<b>Weld Zone</b>	<b>Temperature (°C and °F)</b>
Nugget	480-550°C (896- 1022°F)
TMAZ	430-480°C (806-896°F)
HAZ	430°C (806°F)

#### 1.1.4 Friction Stir Welding Discontinuities

Friction stir welding offers many advantages over conventional welding procedures. Still, some imperfections have been encountered in friction stir welded joints. These imperfections, or defects, are directly related to the process variables [1]. Among these imperfections are galling or material smearing in the weld surface, excess weld flash, voids (or internal cavities), visible wormholes, joint line remnants (lazy-s), incomplete penetration [1] [2] and subsurface tearing [48]. Galling or material smearing has been observed in the crown of welds fabricated at high rotational speed. Figure 11 exhibits the galling defect in the crown of a friction stir welded joint. High rotational speed generates excessive heat input, leading to the partial melting of the material on the weld surface [1].

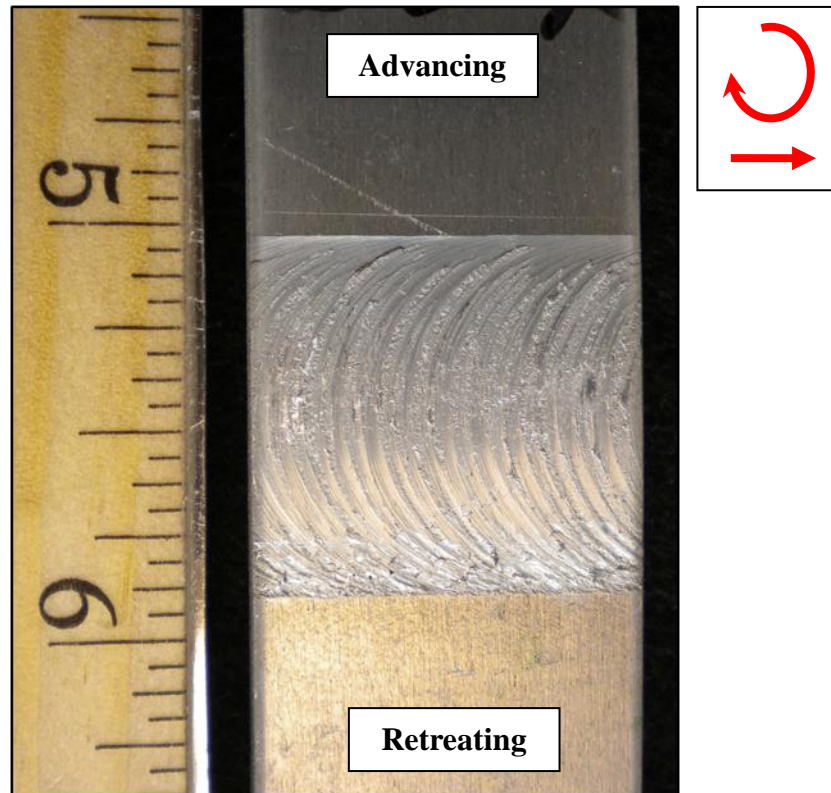


Figure 11: Galling defect in the crown of a friction stir welded joint. Excessive rotational speed, can lead to partial melting of the weld surface, causing galling or material smearing defect. The inset shows the tool rotational and traverse directions.

Another visual defect is the lip formation next to the weld; this feature is known as flashing. Flash is produced when material is extruded from the tool shoulder, due to an excessive tool plunge force [1]; this defect is usually observed on the retreating side of the weld, however it was occasionally observed in the advancing side as shown in Figure 12.

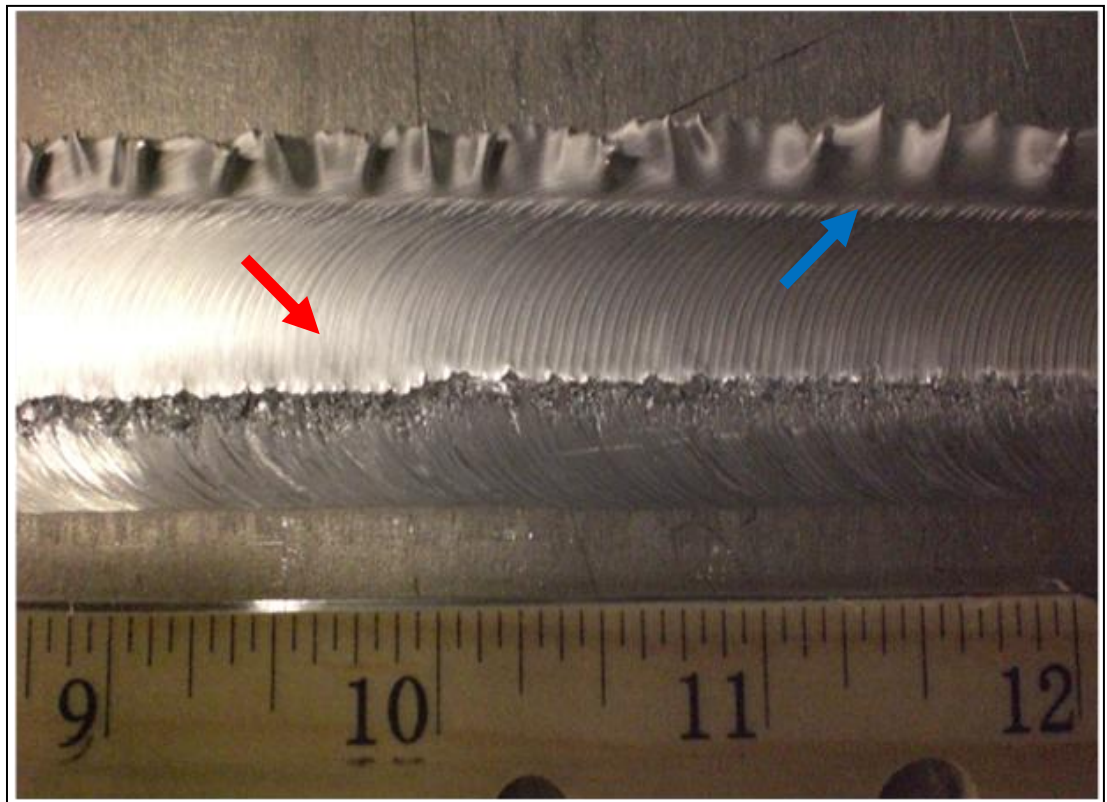


Figure 12: Flash and visible wormhole defects in the crown of a friction stir welded joint. Flashing defect (indicated by blue arrow) is the lip formed next to the weld due to excessive tool plunge force. Visible wormholes (indicated by red arrow) are internal cavities that extend to the surface.

Voids are generally found on the advancing side of the weld [2] close to the TMAZ [48]. A SR-FSW macrograph exhibiting voids on the nugget region in the advancing side is shown in Figure 13. The formation of voids has been attributed to different factors such as the low heat input produced by low rotational speed, which prevents the diffusion and bonding of the metal [49], too high rotational speed [50], or due to insufficient tool pressure, which causes incomplete bonding, leading to void formation [1]. Voids can extend to the surface of the weld (shown in Figure 12), when this occurs, voids are known as visible wormholes [1].



Figure 13: Voids defect on a self-reacting friction stir welded joint. Voids are observed in nugget region on the advancing side of the weld.

Incomplete root penetration is a metallurgical discontinuity that takes place when the deformation in the stir zone does not extend through the whole plate thickness, leaving an un-bonded region at the weld root [1]. This defect is eliminated by the self-reacting friction stir weld tool configuration [2]. Another defect that involves incomplete bonding is the joint line remnant [1], shown in Figure 14. This defect is also known as kissing bond, entrapped oxide [2], or lazy S discontinuity because of its shape [1].

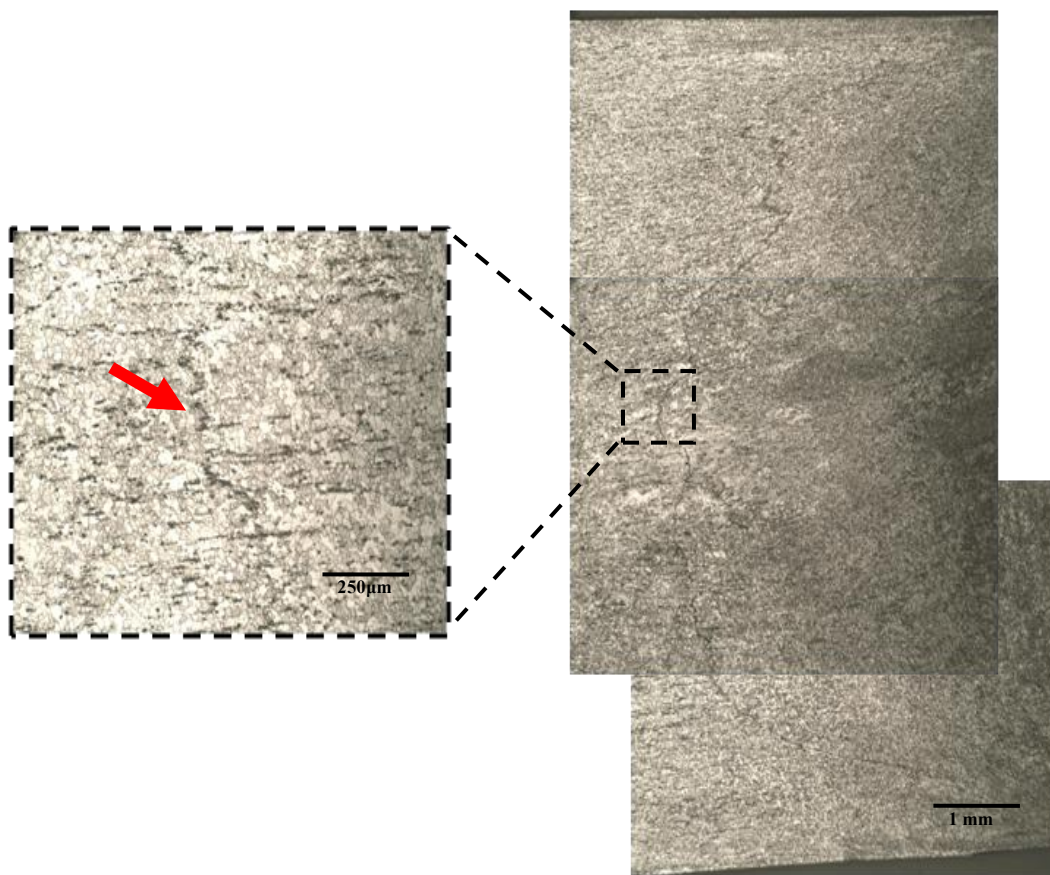


Figure 14: Lazy S defect in the nugget region of a friction stir welded joint. This defect is associated with the lack of bonding due to the oxide layer on the surfaces of the plates to be joined.

The joint line remnant defect is caused by the oxide layer on the faying surfaces of the plates to be joined [2]. During welding, this oxide layer is not completely dispersed, leaving a surface on which bonding is interrupted by oxide particles [1]. Insufficient cleaning of the workpieces prior to welding and a low heat input during welding [18] can prevent the oxide layer from diffusing, resulting in the lazy S defect [51]. Insufficient forge pressure, welding at a traverse speed that is too fast [2], or a rotational speed that is too low [51] can lead to insufficient heat input during welding. While the lazy S defect appears to have no influence on the final mechanical properties [52], it has been reported that it can induce crack initiation and significantly affect the fatigue life [51][53]. Subsurface tearing is a metallurgical discontinuity that has only been observed on SR-FS welded 2195 aluminum alloy joints, this defect can occur below the crown or root surface [48].

#### **1.1.5 Hardness Profile**

The weld zone hardness of aluminum 6061 FS welded joints is inferior to that of the base metal [11, 54]. Uematsu et al. reported softening in the weld zone of aluminum heat-treatable alloy, in contrast, slightly higher hardness on the weld center was reported for non-heat treatable alloys [37]. The hardness as function of distance from the weld center exhibits a “w” shape profile with four main hardness zones; nugget, TMAZ, HAZ, and base metal [2]. The middle section of the “w” shaped hardness profile corresponds to the weld nugget, where the hardness is nearly constant. The weld nugget exhibits an approximate hardness of 20-30% less than the base metal [2]. Elangovan et al. reported a hardness of 84 HV on the nugget region of an AA6061 FS welded joint [11]. Adjacent to the weld nugget the TMAZ experiences a sharp drop in hardness, reaching its minimum in the heat-affected zone, where it can reach about 40% less than the parent metal [2]. The HAZ has been reported to be the weakest part of the weld [31] [32][55] [56]. Higher hardness values have been observed on the advancing side of the weld [57].

A comparison between conventional and self-reacting friction stir welded 6056 aluminum joints fabricated under similar conditions revealed that both tool configurations exhibited the lowest hardness values on the retreating side. The lowest hardness point for conventional FSW was observed at an approximate distance of 4.5 mm (0.177 in.) from the weld center, while for SR-FSW the lowest hardness

occurred at 8 mm (0.315 in.). This region corresponds to the HAZ [58]. The hardness profile at three different depths from the top surface exhibited different characteristics for conventional FS welded joints [55] [56]. Lower hardness values were observed in the crown of the weld as compared to the root [54] as a result of the higher heat input produced by the contact of the tool shoulder with the workpiece [56]. SR-FSW hardness depth profile exhibited no significant differences [58].

Several authors have investigated the effect of process parameters on the hardness profile. It has been reported that the traverse speed has a bigger effect as compared to rotational speed [2]. Higher travel speeds exhibit a slightly higher hardness profile [59] and a narrower weld zone, due to a lower heat input [34][59][60]. No differences were observed in the hardness profile for aluminum 6063 FS welds fabricated at different rotational speeds, concluding that rotational speed has no significant effect on the hardness profile [15]. Welds fabricated at low traverse and rotational speeds exhibit a more uniform hardness in the nugget region [57] [60].

#### **1.1.6 Mechanical Properties**

Tensile properties of friction stir welded joints are lower than those of the base material. Elangovan et al. reported a 66% joint efficiency for a 6061-T6 FS welded joint; this is equivalent to a 40 to 45% reduction in strength as compared to the parent metal strength. The joint efficiency is the ratio of the tensile strength of the welded joint to the strength of the base metal [11]. Tensile fracture has been reported in the TMAZ-HAZ region, which corresponds to the lowest hardness point [58] [14]. Tensile fracture occurs either on the advancing [33][55, 61] or the retreating side [14] [16] [60] [62]. The base metal plays an important role in the fracture zone. Aluminum 6061 welded joints failed on the retreating side [63], whereas 2017-T351 joints failed on the advancing side [64]. The tensile properties of the welded joints are seriously deteriorated by internal defects, which lead to tensile fracture in the weld nugget in the region in which the defect exists [64].

Process parameters have a direct influence on welded joint mechanical properties. Viyajan et al. statistically determined that rotational speed plays a major role in the final tensile strength of friction stir welded joints, whereas the axial force does not have a significant impact [17]. Several authors have also reported that the tensile strength increases with increasing welding speed [7, 65] [57] [60] .



## **1.2 STATEMENT OF THE PROBLEM**

The self-reacting FSW tool configuration offers many advantages over prior FSW tool configurations. Still, it is a relatively new process and little information is available, limiting its understanding and applicability. The SR-FSW process involves complex interactions between, process parameters, alloy properties, and tool geometry that can influence the amount of heat and plastic deformation produced, which affect the final mechanical properties and quality of the weld. There is a need to conduct research to further understand the role of process parameters on defect free self-reacting friction stir welds, and advance the use of this technique. In particular, research needs to be conducted on the effects of process parameters on temperature distribution, microstructural development, defect formation, and thus mechanical properties and quality. The proper choice of process parameters will lead to the production of defect-free joints [4].

## Experimental Procedure

### 2.1 WELDING EQUIPMENT AND MATERIALS

The material used in this study was 6061-T651 per ASTM B209-07, with dimensions 14" x 18" x 0.3215" thick (355.59 x 457.2 x 8.16 mm). Plates were self-reacting friction stir welded along the rolling direction. Table 4 and Table 5 lists the chemical composition and mechanical properties of the aluminum plates used in this experiment, respectively.

Table 4: Aluminum 6061-T651 Chemical Composition per ASTM B209-07

Composition (wt%)									
Si	Fe	Cu	Mn	Mg	Cr	Zn	Ti	Other	Al
0.40-0.8	0.7	0.15-0.4	0.15	0.8-1.2	0.04-0.35	0.25	0.15	0.15	Remainder

Table 5: Aluminum 6061-T651 Mechanical Properties per ASTM B209-07

Tensile Strength	Yield Strength (0.2% offset)
42 ksi (290 MPa) (min)	35 ksi (241 MPa) (min)

The aluminum plates were self-reacting friction stir welded on an MTS iSTIR PDS friction stir welding machine. The friction stir welding machine has five degrees of movement: x, y, z, pitch, and roll that allow for different welding modes; such as, fixed, adjustable, and self-reacting. Tool depth during welding can be maintained by position or force-control. The latter was used in the present experiment.

The self-reacting friction stir welding non-consumable tool consisted of two tool shoulders and one pin tool. The two tool shoulders were 1 in. (25.4 mm) in diameter and were characterized by a scroll feature to promote material deformation and mixing. The tool shoulders were manufactured from H13 tool steel. For the pin, a “dust tool pin design” was used; this is a threaded pin with a major diameter of 0.500 in., and a minor diameter of 0.435 in. The pin tool was manufactured from MP159 alloy.

To evaluate the effects of process parameters on temperature distribution, weld visual appearance, defect formation, and final mechanical properties, a multivariate factorial experiment was designed. The process parameters evaluated in this study were tool rotational speed, traverse speed, and tool plunge force. The analyzed parameters and their respective levels, listed in Table 6, were selected from an established range of acceptable welding parameters in order to determine the best parameter combination. A total of 36 butt joints were fabricated for this investigation, with one replicate for each set of welding parameters. The run order was randomized to eliminate systematic error. The welding parameters and fabrication order are listed in Table 7.

Table 6: Process Parameters and Levels

Parameter/Level	1	2	3	4
Rotational Speed (rpm)	400	450	500	
Traverse Speed (ipm)	15	17.5	20	
Plunge Force (lbf)	-1350	-1400	-1450	-1500

Table 7: Self-Reacting Friction Stir Welding Factorial Design

<b>Weld #</b>	<b>Rotational Speed (rpm)</b>	<b>Travel Speed (ipm)</b>	<b>Plunge Force (lbf)</b>
<b>1</b>	450	17.5	1500
<b>2</b>	500	20	1400
<b>3</b>	400	20	1450
<b>4</b>	450	20	1450
<b>5</b>	400	17.5	1350
<b>6</b>	450	15	1500
<b>7</b>	500	17.5	1450
<b>8</b>	500	15	1400
<b>9</b>	400	20	1500
<b>10</b>	400	17.5	1450
<b>11</b>	500	15	1500
<b>12</b>	450	15	1400
<b>13</b>	400	15	1400
<b>14</b>	500	20	1350
<b>15</b>	400	20	1350
<b>16</b>	450	17.5	1400
<b>17</b>	500	20	1500
<b>18</b>	500	17.5	1400
<b>19</b>	400	15	1350
<b>20</b>	500	15	1350
<b>21</b>	400	15	1500
<b>22</b>	450	15	1350
<b>23</b>	500	20	1450
<b>24</b>	400	20	1400
<b>25</b>	450	20	1400
<b>26</b>	400	17.5	1500
<b>27</b>	500	17.5	1500
<b>28</b>	450	17.5	1350
<b>29</b>	450	17.5	1450
<b>30</b>	450	20	1500
<b>31</b>	400	15	1450
<b>32</b>	450	15	1450
<b>33</b>	500	15	1450
<b>34</b>	450	20	1350
<b>35</b>	400	17.5	1400
<b>36</b>	500	17.5	1350

### 2.1.1 Welding Procedure and Temperature Set-up

In order to fabricate a butt joint configuration by SR-FSW, a 17/32" (13.4938 mm) hole was drilled at 3/4" (19.05mm) from one side of the plates using a drill press. Surfaces to be welded were cleaned with methanol prior to welding to remove oils and any other sources of contamination that might compromise the weld quality. Plates were positioned on a base, as shown in Figure 15, and the SR-FSW pin tool was inserted through the previously drilled hole; the backing shoulder was attached to the pin prior welding. Plates were secured in a butt joint configuration by mechanical clamps, to prevent them from moving during welding. Weld parameters were adjusted to meet the factorial design requirements. An approximate dwell time of 10 seconds was allowed before welding. The welded samples were air-cooled and the SR-FSW tool was mechanically cleaned with a file after each welding process to remove any extruded material.

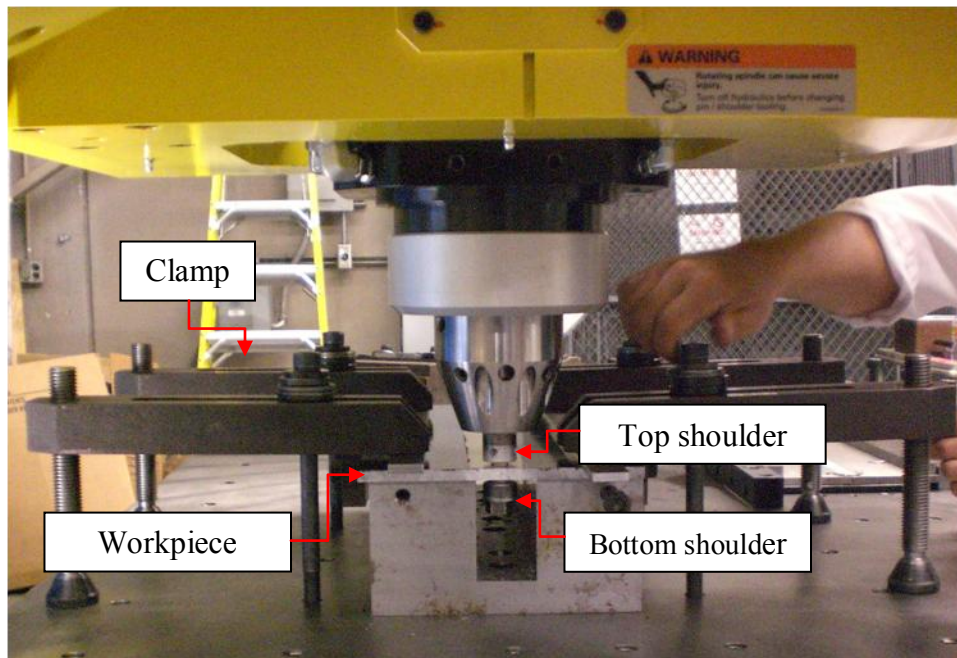


Figure 15: Self-reacting friction stir weld clamping system.

During the SR-FSW process, thermal images from the surface of the plates were recorded with a FLIR ThermaCAM S65 HS infrared camera (IR). The camera has a spatial resolution of 320 x 240 pixels and 4 temperature ranges, from -40°C to 1500°C, with a stated accuracy of  $\pm 2^{\circ}\text{C}$  or  $\pm 2\%$ . To measure the temperature accurately it is necessary to supply the following parameters to the IR camera: reflected apparent temperature, emissivity of the object, distance between the object and the camera, relative humidity and ambient temperature. To determine the emissivity, plates were partially painted with a dull black paint of known emissivity. Plates were heated in a furnace to ensure uniform heating to a temperature of 115°F for 15 minutes. Images were taken and imported into the ThermaCAM QuickReport software. Emissivity was set to that of the paint. The temperature was measured using the spot tool in the QuickReport software, and then the non-painted sample surface was analyzed. The emissivity of the non-painted plate was determined to be 0.04. No measures were taken to control the emissivity of the plates during the welding process.

During the welding process, the IR Camera was placed so as to maintain a constant distance of 1.9 ft between the plates and the camera. Images were recorded every 10 seconds. Relative humidity and ambient temperature were measured for each weld and supplied to the camera. The thermal images were analyzed with FLIR QuickReport1.2 software. Figure 16, exhibits exemplar thermal images from one of the welds. The temperatures on both the advancing and the retreating sides were measured at various locations away from the tool using a grid of known mesh size. The grid was placed over the recorded picture and the temperature at the desired location was measured with the spot tool. The obtained temperatures were plotted with a graphing software in order to create a temperature profile. These temperatures were used to determine the relationship between temperature and process parameters.

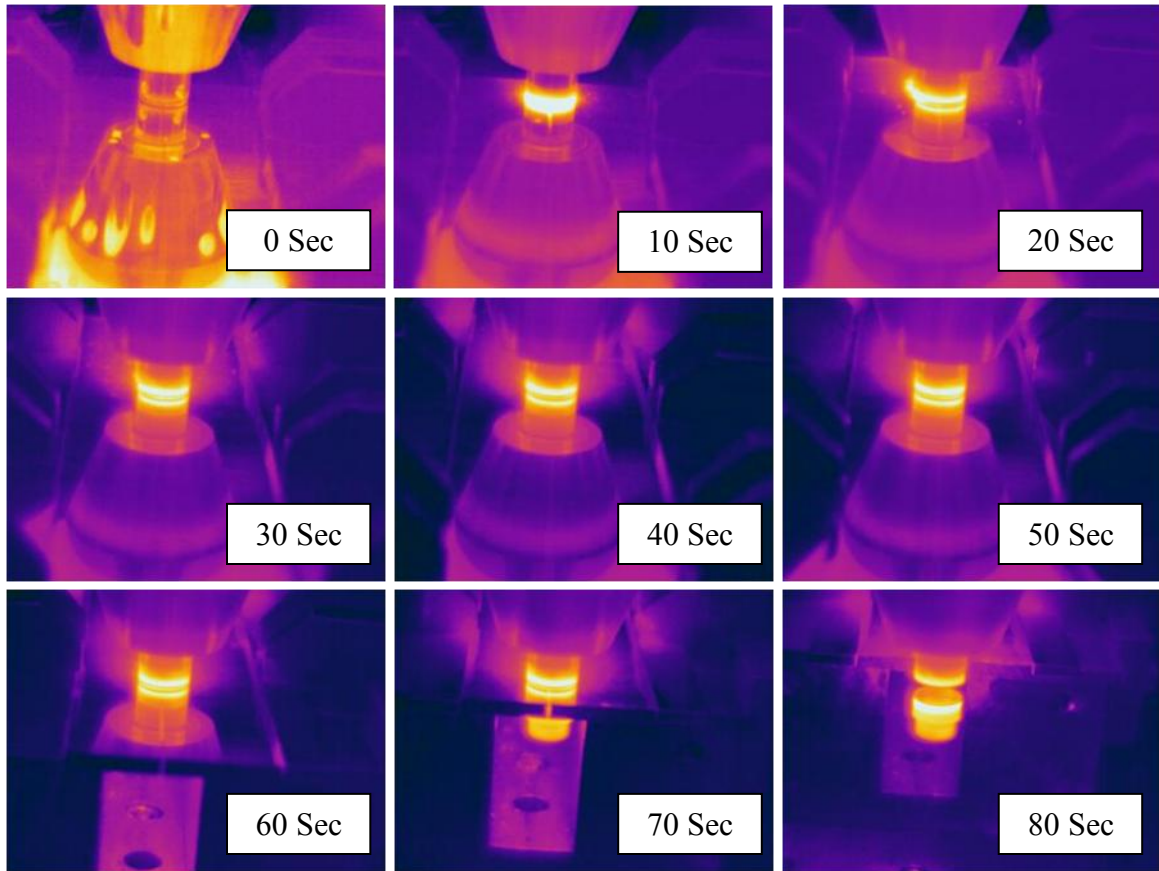


Figure 16: Thermal images taken during a self-reacting friction stir welding process.

## 2.2 OVERALL VISUAL APPEARANCE

Upon completion of the welds a visual inspection of the joints was performed. The crown of the welds was analyzed to determine its main characteristics and the presence of macroscopic defects such as visible wormholes, excessive flashing, and galling. Visual inspection of the welds was carried out in the middle section of the welded plates to eliminate transient effects; the start and the end of the weld were not analyzed

## 2.3 TEST SPECIMEN PREPARATION

After visual inspection, the middle section of the welded plates was cross-sectioned perpendicular to the welding direction using a water jet cutter in order to prepare mechanical test specimens as shown in Figure 17. The middle section was selected because it was believed to be representative of steady-state conditions. Mechanical and hardness testing were carried-out in the as-welded condition 12 months after the welds were fabricated.

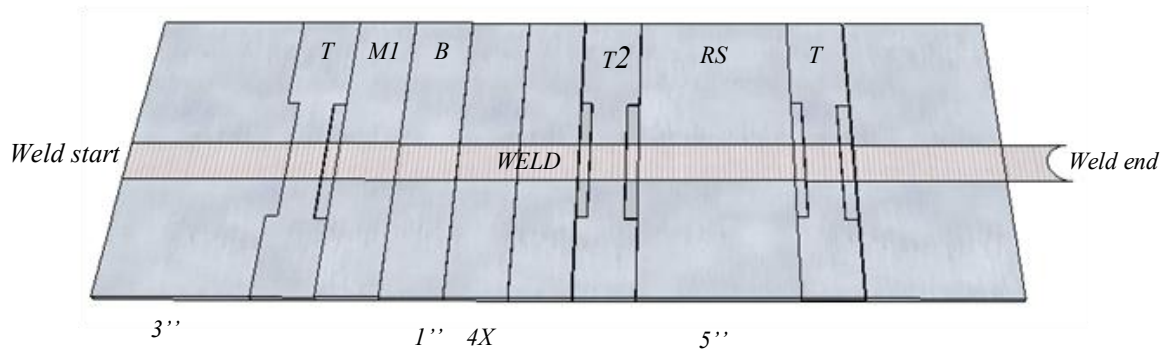


Figure 17: Schematic of self-reacting friction stir welded plates. Welded plates were cross-section perpendicular to the welding direction to prepare tensile and metallographic test specimens.



### 2.3.1 Microstructural Characterization

The microstructural characterization was performed on test sample M1 (shown in Figure 17) from each weld. Samples were prepared in a cross-section perpendicular to the welding direction, as shown in Figure 18.

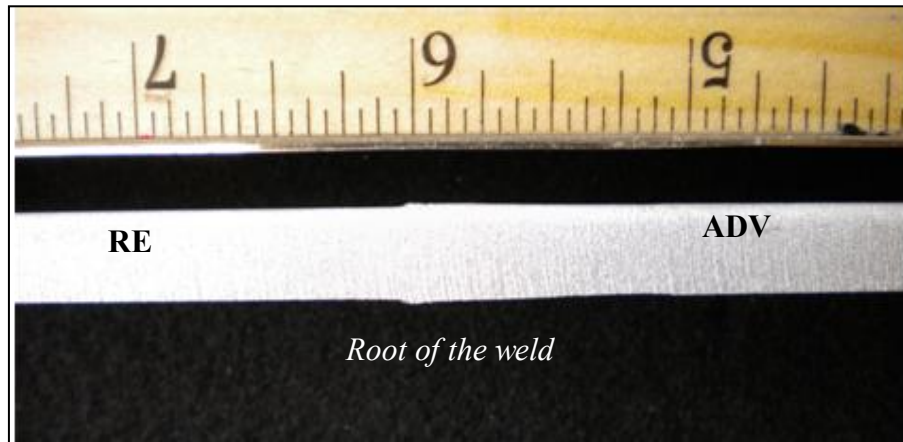


Figure 18: Self-reacting friction stir weld microstructural characterization sample.

The material was sectioned in the appropriate direction with water-cooled abrasive cut-off saw. Samples were then mounted, and polished following standard metallographic techniques. For optical microscopy after polishing, samples were etched with Dix-Keller's reagent (190 ml distilled water, 5 ml nitric acid, 3 ml hydrochloric acid and 2 ml hydrofluoric acid). Specimens were observed with a light microscope to determine the presence of defects and the main microstructural characteristics of the principal FSW regions: nugget, thermo-mechanically heat affected zone, heat-affected zone, and parent metal.

### 2.3.2 Microhardness Profile

Vickers microhardness testing was carried out at room temperature, in the as-welded condition. Testing was conducted using a 500 g load in a cross section perpendicular to the welding direction. The hardness profile was analyzed as a function of distance from the weld centerline and at three depths: top, middle, and bottom. Hardness readings were taken every 3 mm (0.118 in.). The surface was polished and etched, prior to hardness testing. Figure 19 presents the location in which where hardness readings were taken (white dots). The advancing side is shown on the right side with the retreating side on the left. The crown of the samples is shown on the bottom of the macrograph.

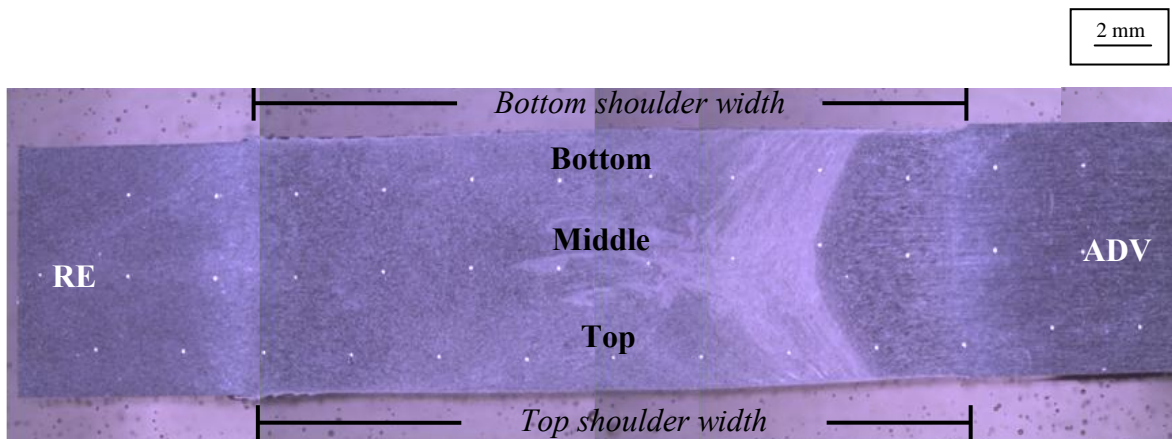


Figure 19: Microhardness profile. Hardness reading were taken as function of distance from the weld centerline every 3mm and at three depths (top, middle and bottom). White dots exhibit the microhardness indentations. The advancing side is shown on the right side and the crown of the weld on the bottom of the macrograph.

### 2.3.3 Tensile Testing

To evaluate the mechanical properties, tensile test specimens in location T2 (shown in Figure 17) were used for this investigation. Tensile tests were performed at room temperature, in the as-welded condition. The rectangular-shaped test specimens with gage a length of 50.8 mm (2 in.), 15.8 mm (0.622 in.) width, and 8.3 mm (0.327 in.) final thickness; were tested at a maximum strain rate of 0.001 mm/mm. A 2-in. (50.8 mm) extensometer was used to measure the elongation. The extensometer was placed at the middle section of the sample in the weld area. Tensile test specimen dimensions are shown in Figure 20; no efforts were made to ensure planarity of the specimens between the advancing and retreating sides.

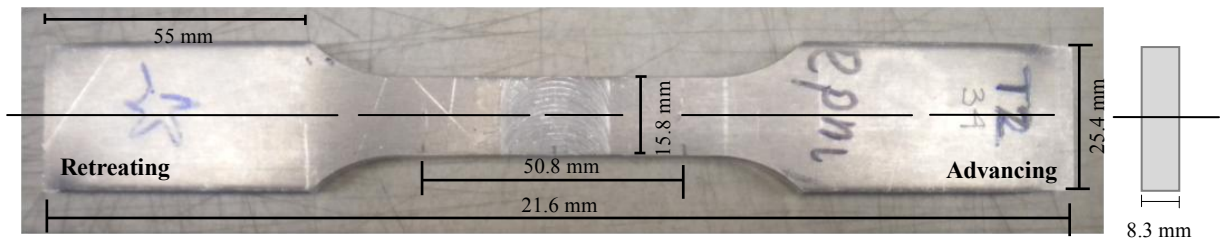


Figure 20: Self-reacting friction stir weld tensile test specimen dimensions. Tensile test specimens were prepared perpendicular to the weld direction.

## Results

### 3.1 TEMPERATURE ANALYSIS

As previously discussed, temperature measurements were made during the welding of the test pieces in this study in order to create a temperature profile in the vicinity of the weld for each sample. Figure 21 presents an exemplar temperature profile as a function of distance from the tool edge. Temperature data for Samples 3 and 22 are not included due to human error.

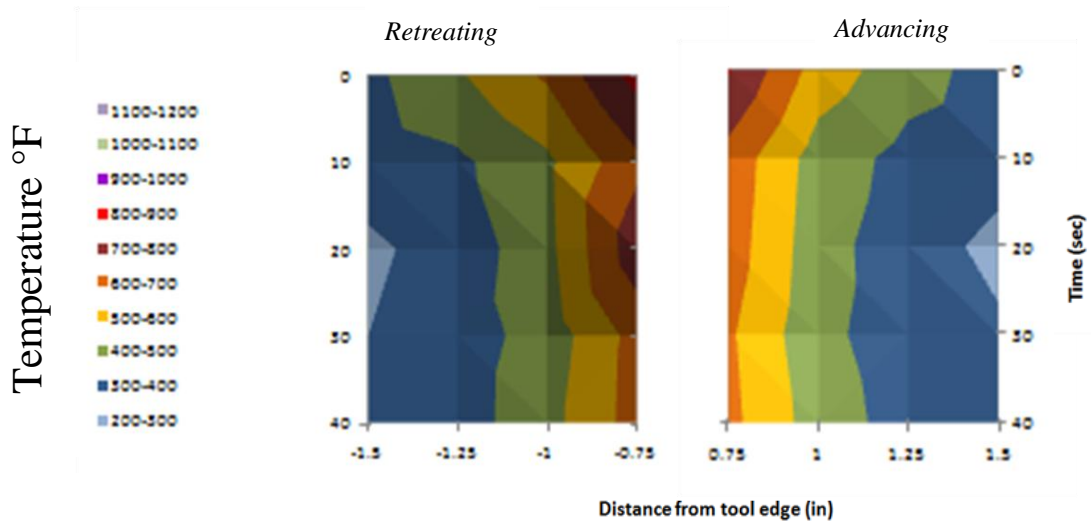


Figure 21: Exemplar temperature profile as distance from tool shoulder edge during SR-FSW

The temperature profiles obtained for each sample revealed a wide range of temperatures, with a minimum of 212°F and maximum of 1027°F. The highest temperature, which occurred in the vicinity of the weld is close to the alloys solidus temperature 1080°F. Slightly higher temperature were also observed at the start and end of each weld. These regions correspond to the dwell time and exit of the tool from the workpiece. The middle section of the weld exhibited a nearly constant temperature profile for all the analyzed samples, with an overall trend of higher temperatures on the retreating side, as opposed to the advancing side.

The temperature data collected during the experiment is presented in Figure 22 to Figure 33. Each figure presents the temperature profile for three levels of travel speed; rotational speed and tool plunge force are constant in each figure. The first graph from each figure corresponds to a high traverse speed (20 ipm), the middle to a medium traverse speed (17.5), and the last graph to a low traverse speed (15 ipm). Figure 22 presents the temperature profile for samples fabricated at high rotational speed (500 rpm) and high tool plunge force (1500 lb<sub>f</sub>). For this configuration, higher temperatures were achieved as the traverse speed decreased. The retreating side exhibited slightly higher values for the different traverse speeds.

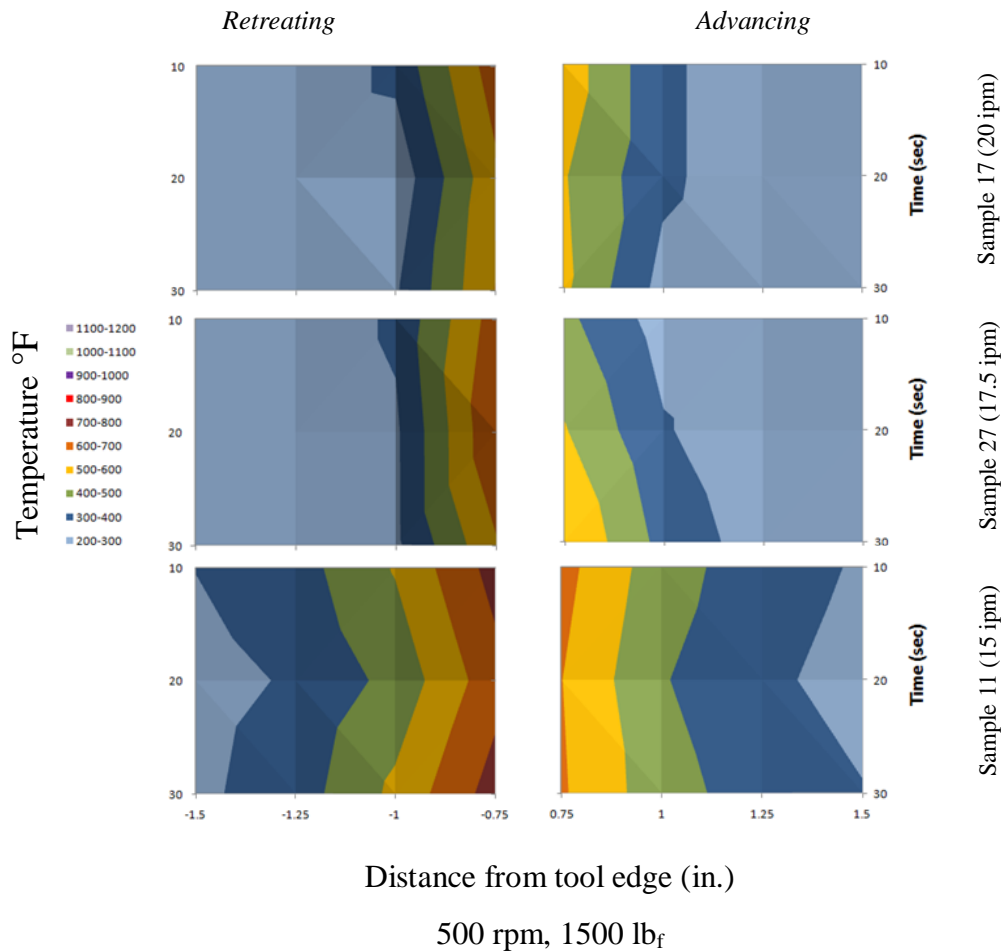


Figure 22: Temperature profile for samples fabricated at 500rpm, 1500lb<sub>f</sub> and three different travel speeds. As the traverse speed decreased the temperature increased.

Samples fabricated at medium-high tool plunge force (1450 lb<sub>f</sub>) and high rotational speed (500 rpm) reached higher temperatures at the medium travel speed, as shown in Figure 23 . At a high traverse speed no significant differences were observed between the advancing and the retreating sides, whereas, at medium and low travel speeds the retreating side exhibited higher temperatures.

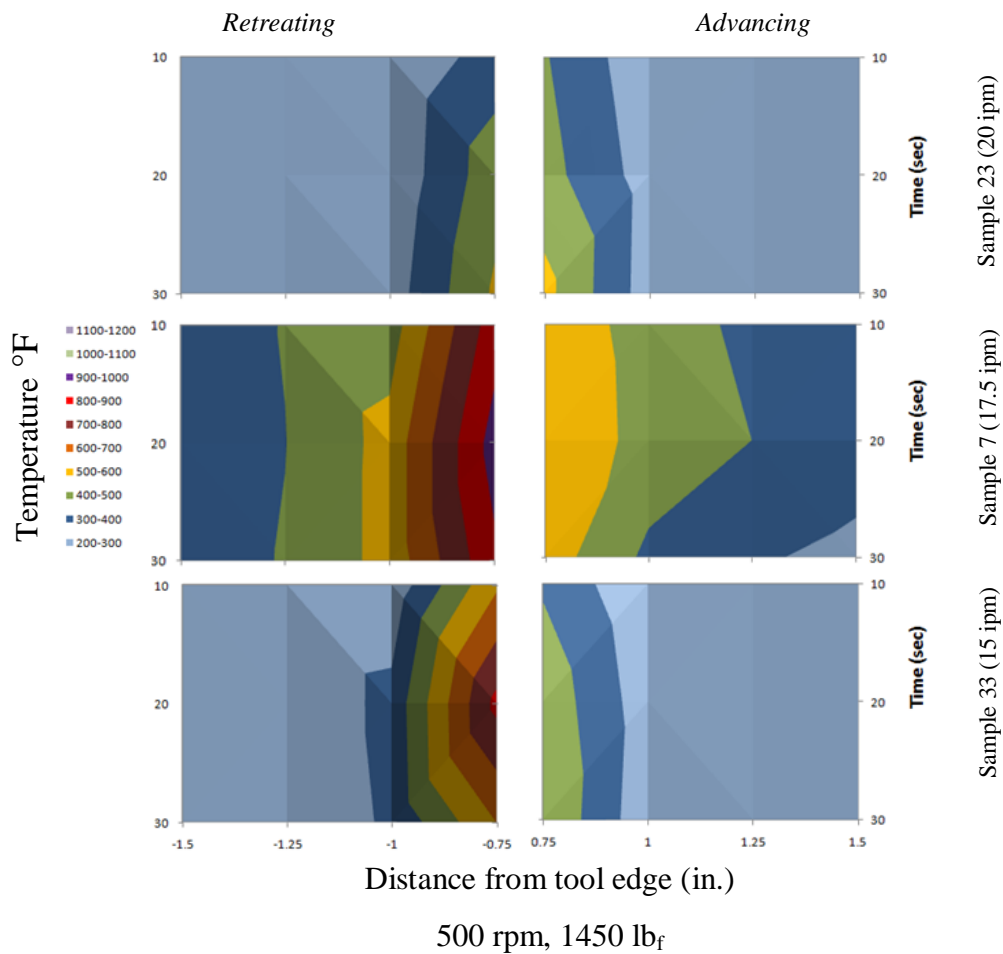


Figure 23: Temperature profile for sample fabricated at 500 rpm, 1450 lb<sub>f</sub> and three different travel speeds. The highest temperature was observed at a medium travel speed (Sample 7).

A combination of high rotational speed (500 rpm) and medium tool plunge force (1400 lb<sub>f</sub>), exhibited higher temperatures at a low travel speed, as shown in Figure 24. The retreating side exhibited higher temperatures, for the different traverse speeds.

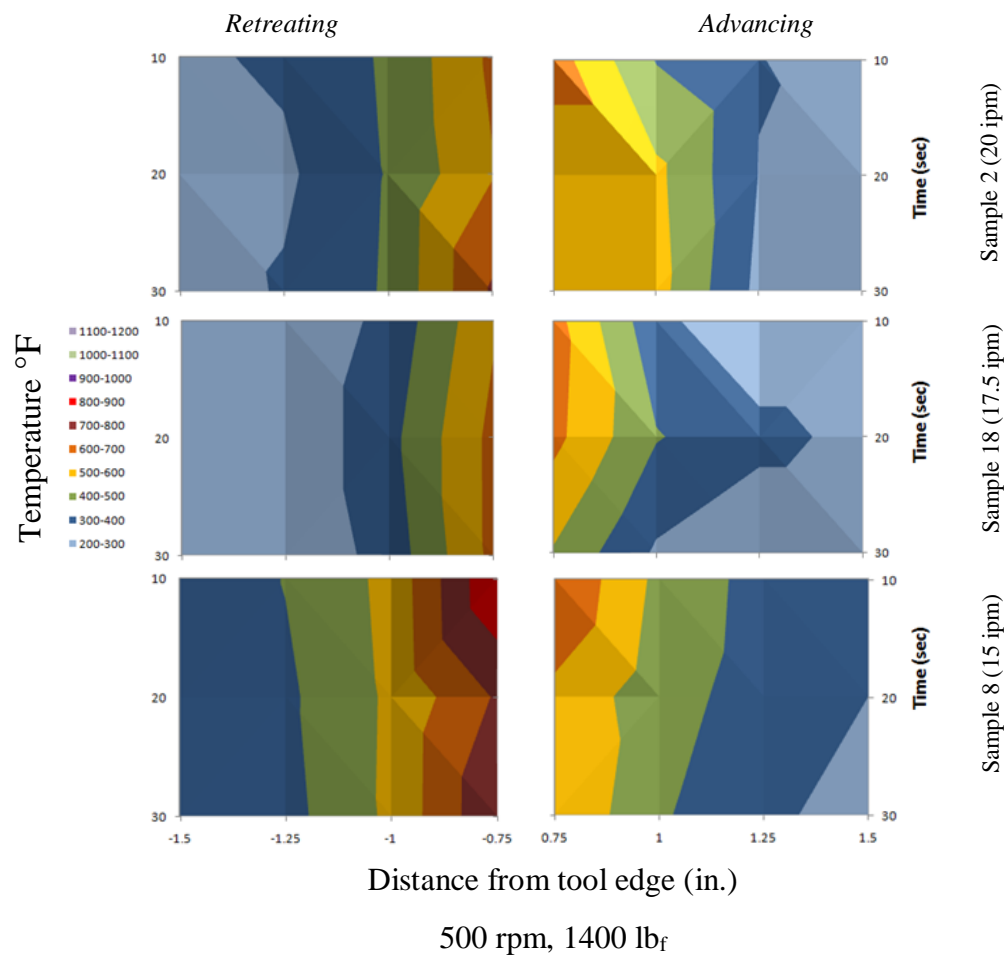


Figure 24: Temperature profile for sample fabricated at 500 rpm, 1400 lb<sub>f</sub> and three different travel speeds. The highest temperature was observed at a low travel speed (15 ipm) (Sample 8).

Samples fabricated at a high rotational speed (500 rpm) and low tool plunge force (1350 lb<sub>f</sub>) (shown in Figure 25) exhibited higher temperatures at a low traverse speed. The lowest temperatures were observed at a medium traverse speed (Sample 36).

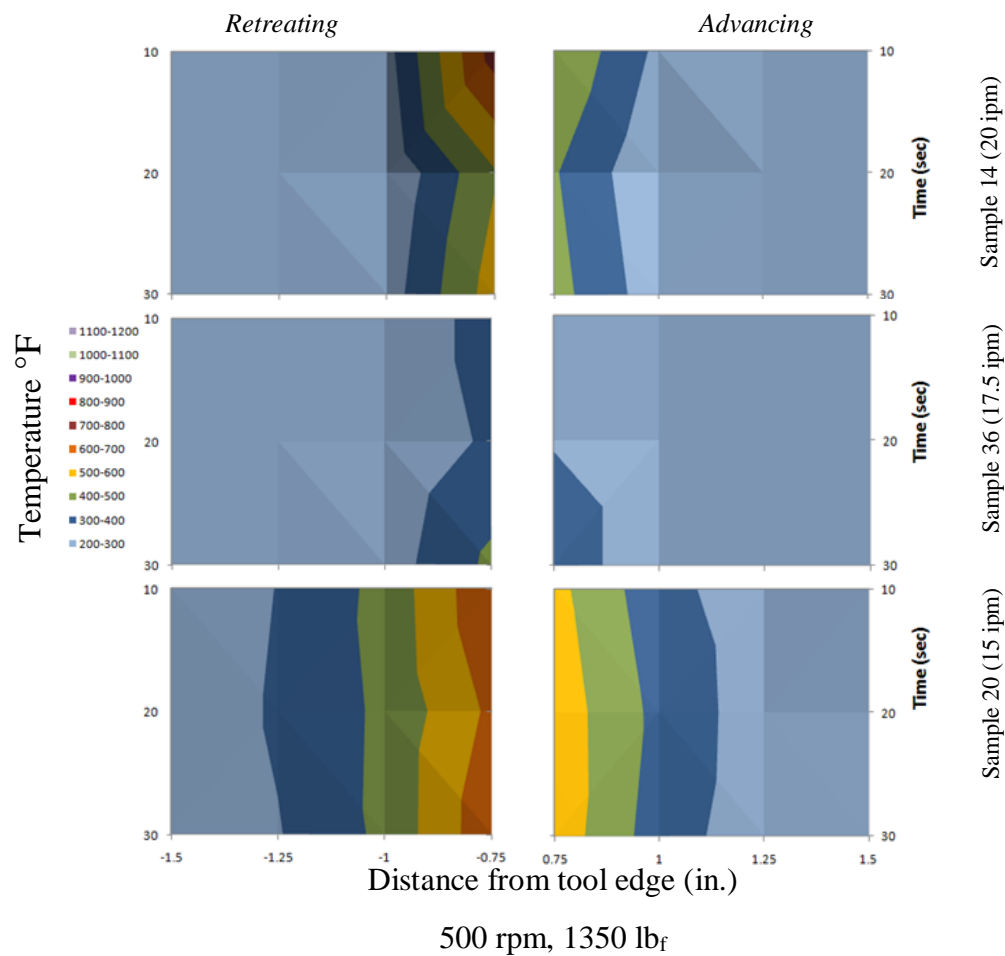


Figure 25: Temperature profile for sample fabricated at 500 rpm, 1350 lb<sub>f</sub> and three different travel speeds. A low travel speed (15 ipm) exhibited the highest temperatures.



Figure 26 presents the temperature plots for samples fabricated at a medium rotational speed (450 rpm), high tool plunge force (1500 lb<sub>f</sub>), and different traverse speeds. Higher temperature profiles were observed at a medium and low traverse speeds. The retreating side exhibited higher values for the different travel speeds, as compared to the advancing side.

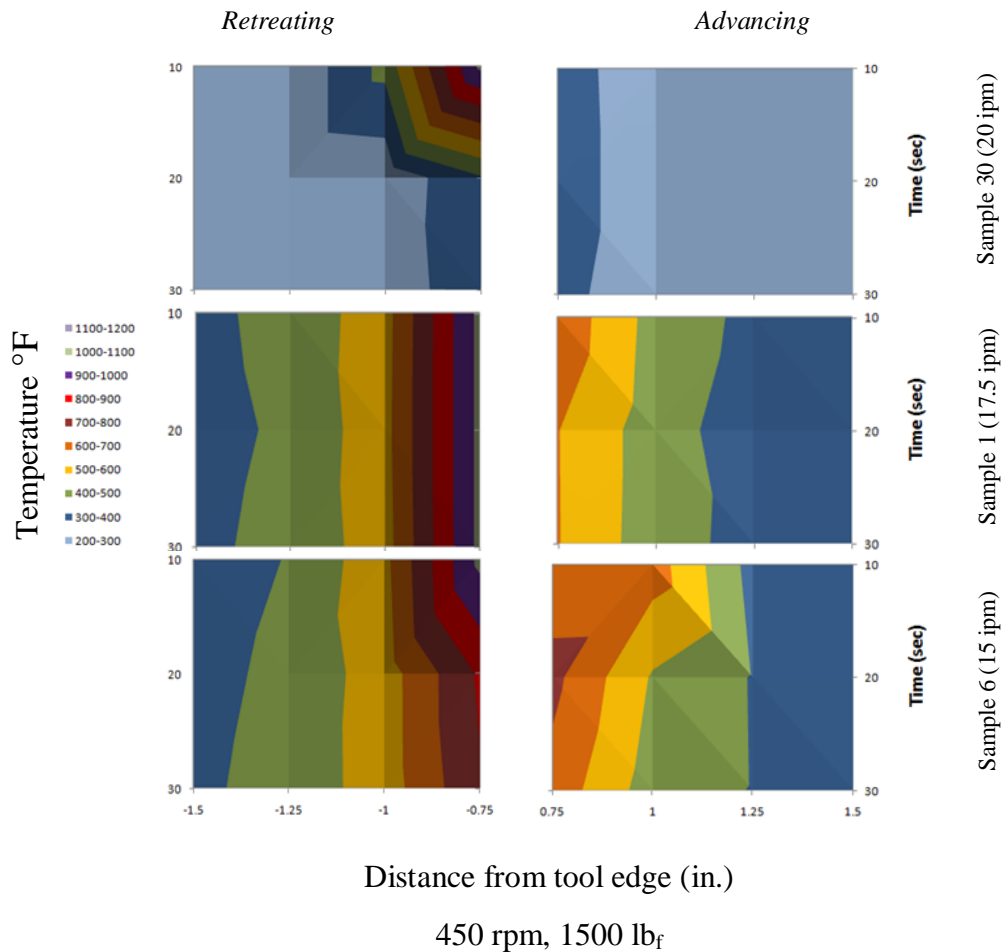


Figure 26: Temperature profile for sample fabricated at 450 rpm, 1500 lb<sub>f</sub> and three different travel speeds. As the travel speed decreased the temperature increased.

A process parameter combination of medium rotational speed (450 rpm) and medium-high tool plunge force (1450 lb<sub>f</sub>) exhibited higher temperatures at a high travel speed, as shown in Figure 27. The retreating side exhibited higher temperatures for all travel speeds.

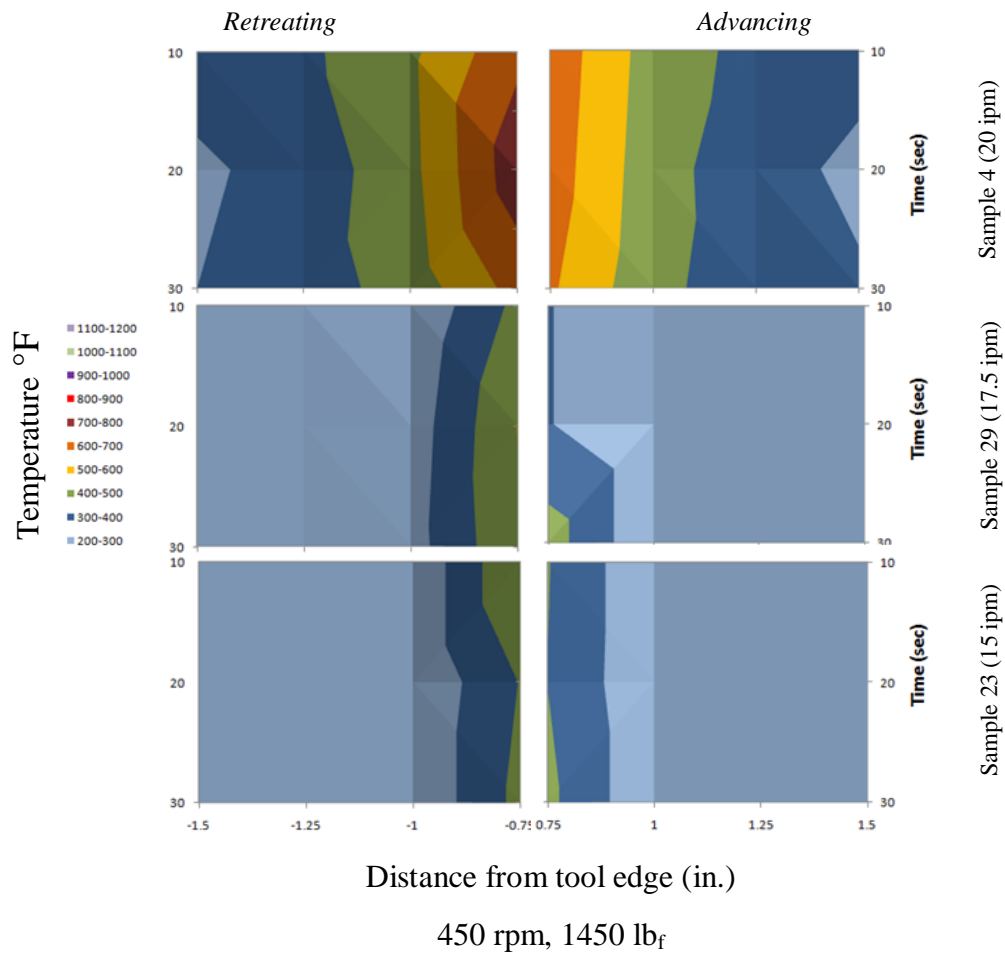


Figure 27: Temperature profile for sample fabricated at 450 rpm, 1450 lb<sub>f</sub> and three different travel speeds. A higher travel speed (20 ipm) exhibited a higher temperature profile

The temperature plots for samples fabricated at a medium rotational speed (450 rpm) and medium tool plunge force (1400 lb<sub>f</sub>) are presented in Figure 28. At this combination of parameters, the heat was observed to be distributed over a wider area as the travel speed decreased. A medium travel speed exhibited higher temperature in the retreating side, closer to the tool edge. The retreating side exhibited higher temperatures near the tool edge, as compare to the advancing side at each travel speed level.

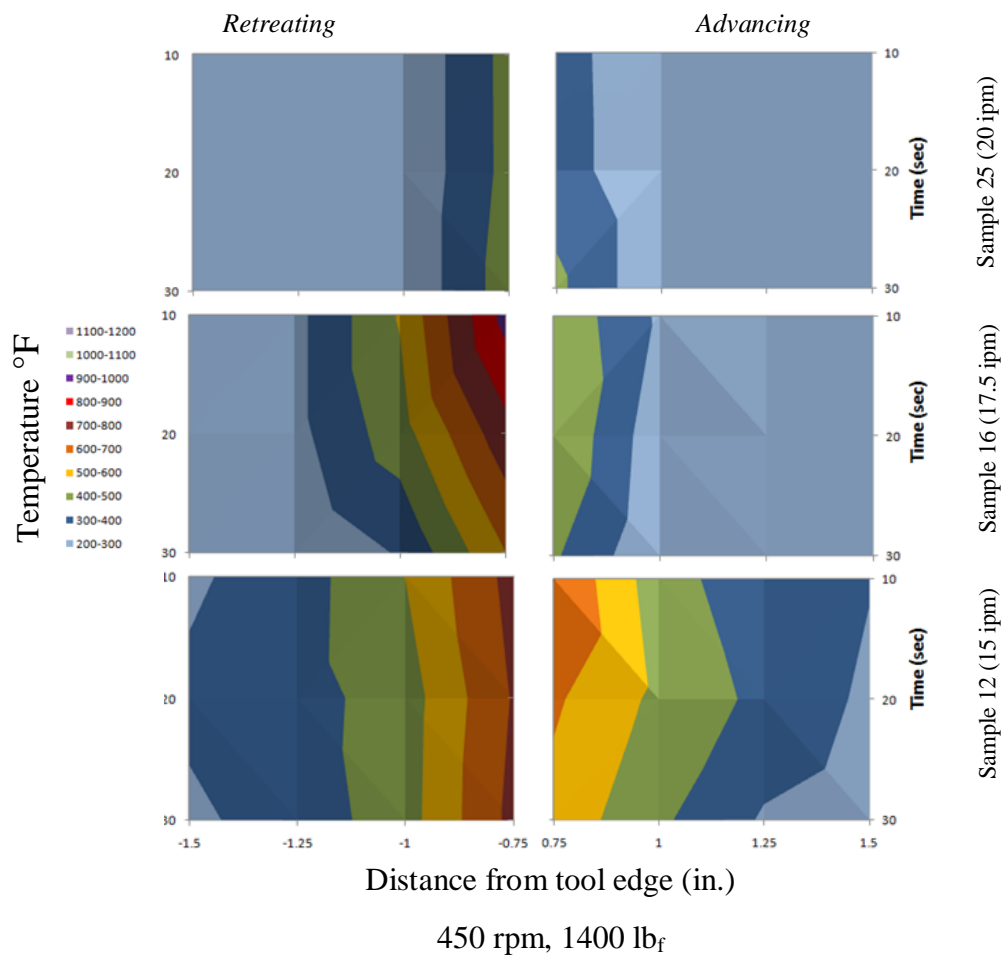


Figure 28: Temperature profile for sample fabricated at 450 rpm, 1400 lb<sub>f</sub> and three different travel speeds. Temperature increased as the traverse speed decreased.

A medium travel speed (17.5 ipm) exhibited higher temperatures compared to a high travel speed when a medium rotational speed (450 rpm) and a low tool plunge force (1350 lb<sub>f</sub>) were used, as shown in Figure 29. Temperature data for the low traverse speed is not available due to human error. In both cases, the retreating side exhibited higher temperatures than the advancing side.

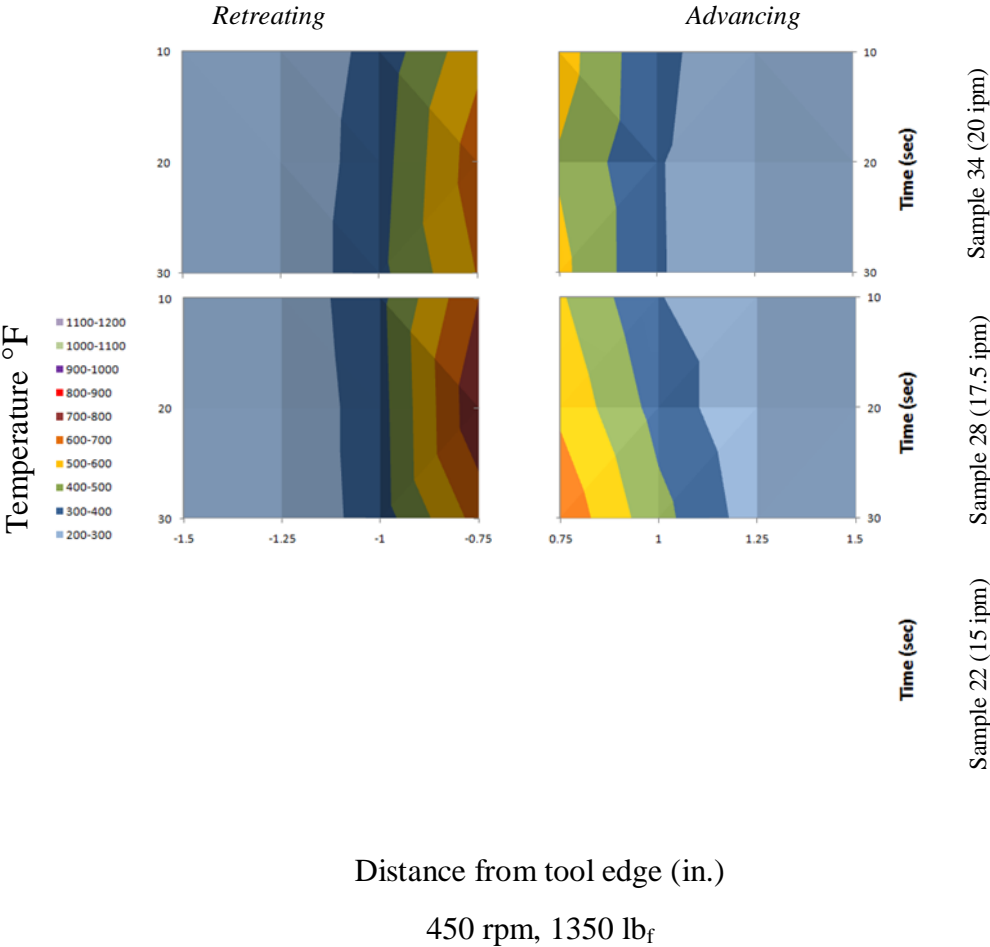


Figure 29: Temperature profile for sample fabricated at 450 rpm, 1350 lb<sub>f</sub> and three different travel speeds. Slightly higher temperatures were observed at a medium travel speed as compared to a high travel speed. Temperature data for Sample 22 is not included.

Temperature profiles for samples produced at the low rotational speed (400 rpm) and high tool plunge force (1500 lb<sub>f</sub>) are presented in Figure 30. At these levels of rotational speed and plunge force, higher temperatures were present at high traverse speeds as compared to lower traverse speeds. Samples 9 and 21 exhibited slightly higher temperature values on the advancing side.

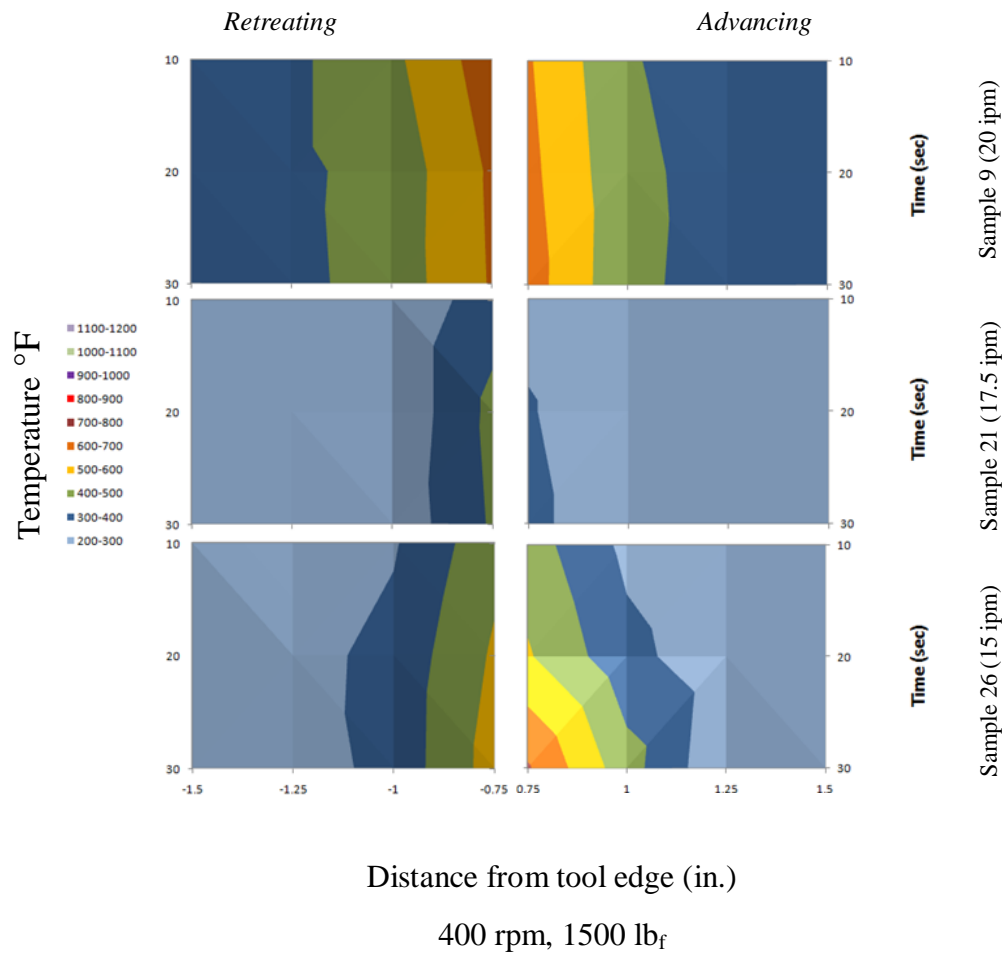


Figure 30: Temperature profiles for sample fabricated at 400 rpm, 1500 lb<sub>f</sub> and three different travel speeds. Higher temperatures were developed at a high travel speed (20 ipm).

The temperature data for low rotational speed (400 rpm) and medium-high tool plunge force (1450 lb<sub>f</sub>) as function of travel speed, is shown in Figure 31. Temperature data for a high travel speed, is not shown. Sample 10, fabricated at medium rotational speed exhibited higher temperatures over larger distances from the tool, as compare to low travel speed. The average temperature at 0.75” from the tool for sample 10 was 652°F for the advancing side and 720°F for the retreating side, whereas, for Sample 31, the average temperatures were 385°F and 440°F on the advancing and retreating sides, respectively.

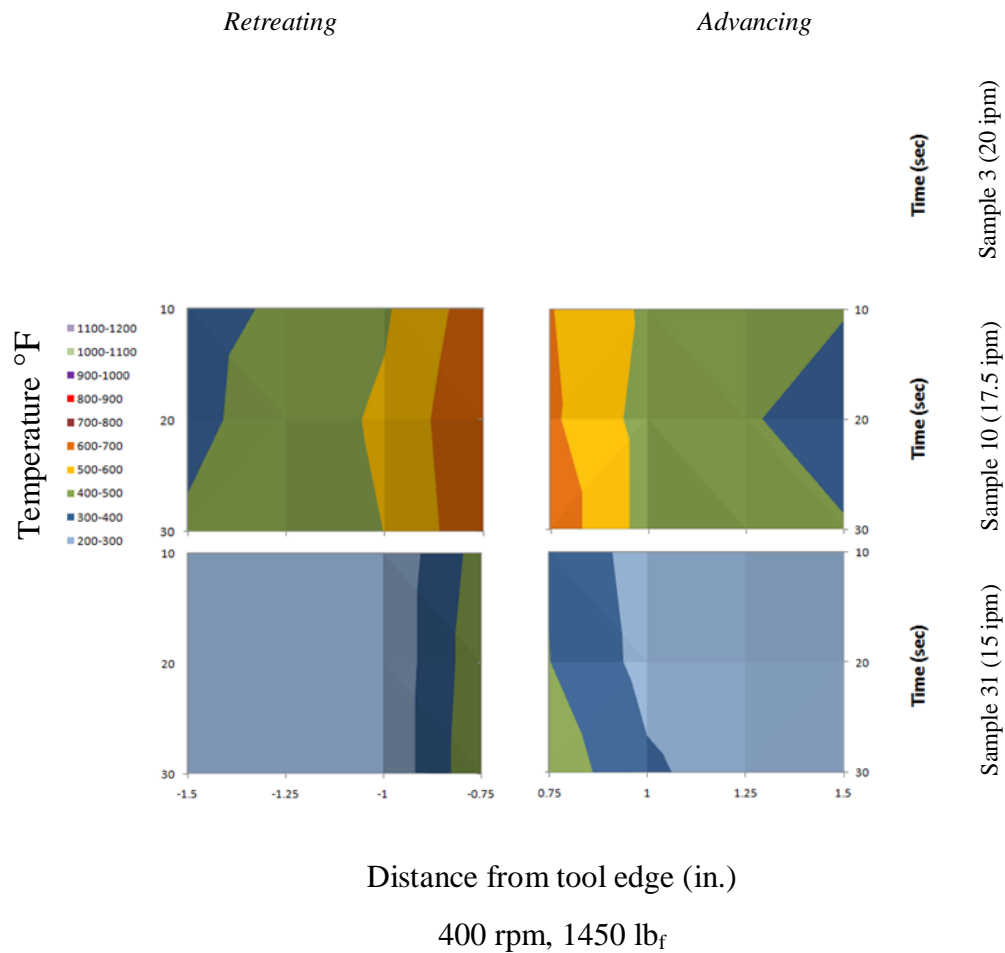


Figure 31: Temperature profiles for sample fabricated at 450 rpm, 1350 lb<sub>f</sub> and three different travel speeds. Higher temperatures were observed at a medium travel speed as compared to a low travel speed. Temperature data for Sample 3 is not included.

Figure 32 presents the temperature profiles for samples fabricated at low rotational speed (400 rpm) and medium tool plunge force (1400 lb<sub>f</sub>). Under these conditions, Sample 24, fabricated at high travel speed, exhibited high temperatures closer to the tool, whereas, at a low travel speed (Sample 13) the heat was spread over larger distances. A medium travel speed produced the lowest temperatures under these conditions.

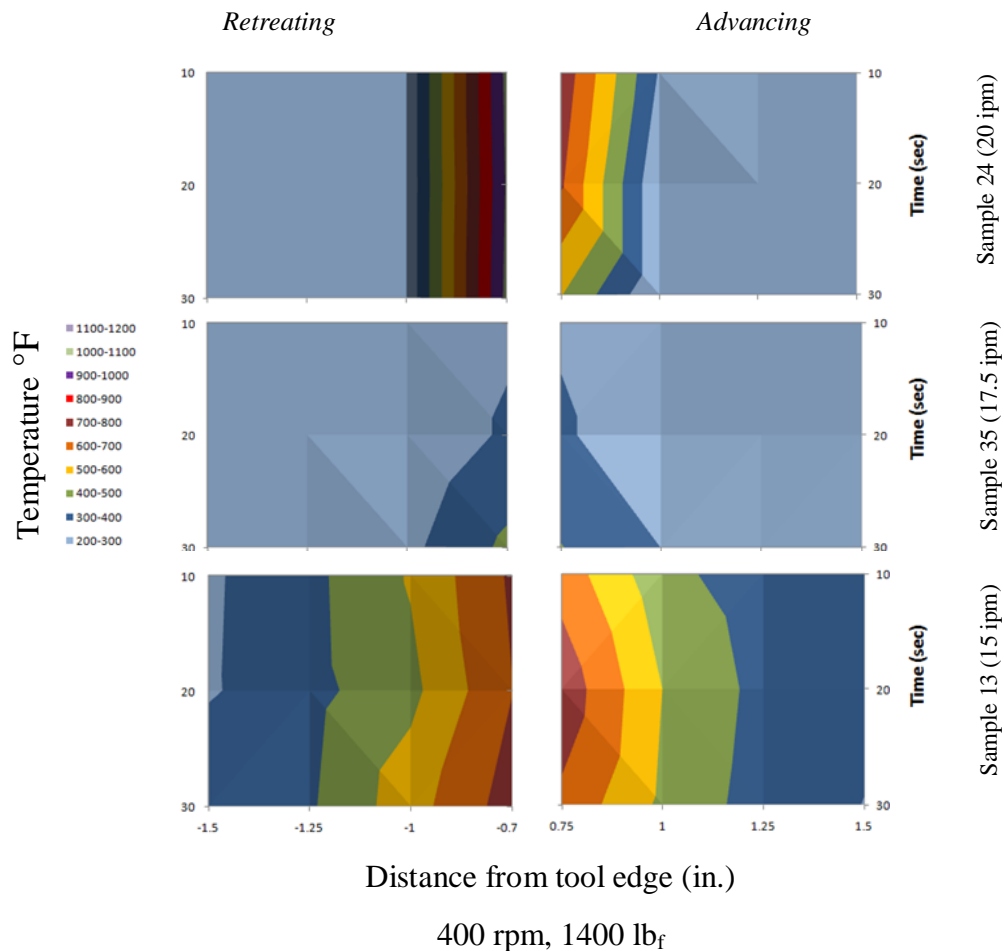


Figure 32: Temperature profiles for sample fabricated at 450 rpm, 1350 lb<sub>f</sub> and three different travel speeds.

Figure 33 exhibits the temperature plots for samples fabricated at low rotational speed (400 rpm) and low tool plunge force (1350 lb<sub>f</sub>). Higher temperatures and a wider heat distribution were observed at a medium travel speed (Sample 5). All travel speeds, exhibited higher temperatures on the retreating side.

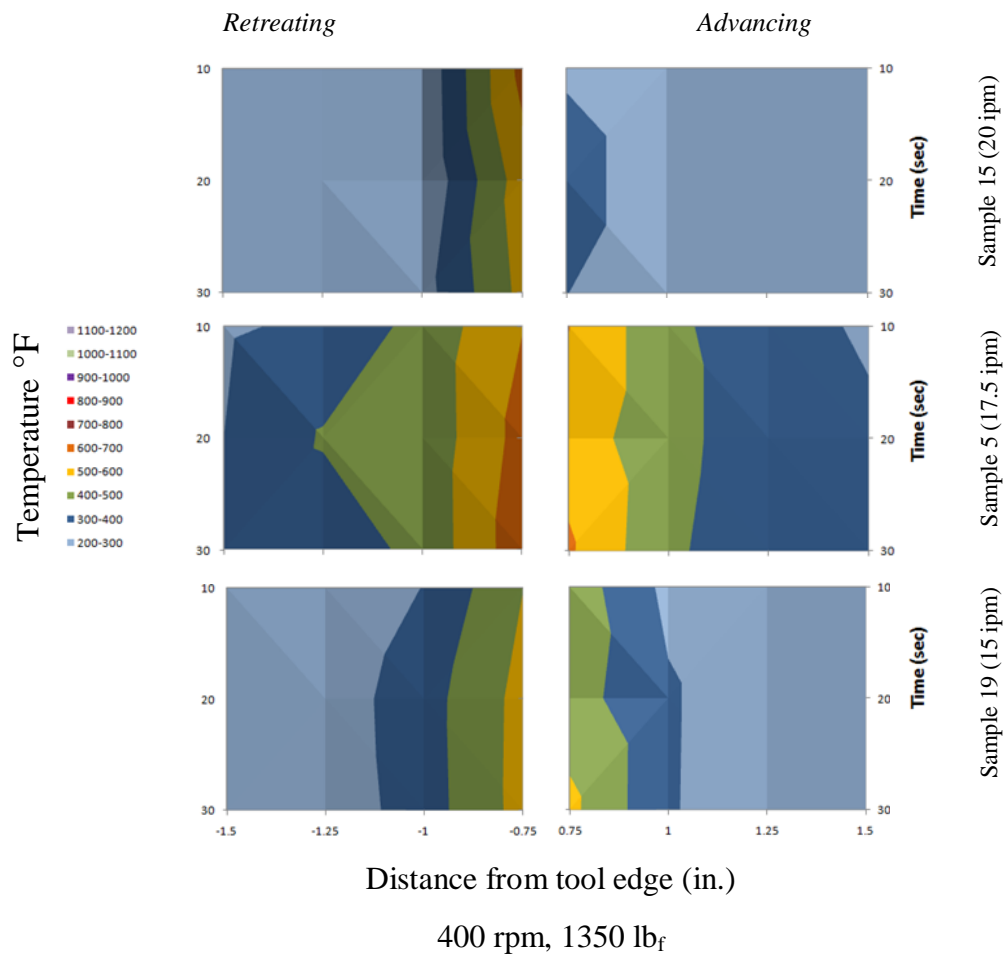


Figure 33: Temperature profiles for sample fabricated at 450 rpm, 1350 lb<sub>f</sub> and three different travel speeds.



The temperatures at 30 seconds into the welding process at a distance of 0.75" from the tool edge were analyzed on the retreating and the advancing sides of each weld to determine the hottest and coldest temperatures developed on each side of the weld. Table 8 presents the temperature at 30 seconds into the welding process, at a distance of .75" from the tool edge. Samples are listed from the highest to lowest temperatures observed on the retreating side, as higher temperatures were generally observed on the retreating side. The analysis was carried-out at 30 seconds into the weld because it is believed to be representative of steady-state conditions.

Table 8: Advancing and Retreating Side Temperatures at 0.75" from Tool Edge

Weld Number	Rotational Speed (rpm)	Travel Speed (ipm)	Tool Plunge Force (lbf)	Temperature Retreating side (°F)	Temperature Advancing side (°F)	Highest Temperature Side
1	450	17.5	1500	1027	606	Retreating
24	400	20	1400	1027	506	Retreating
7	500	17.5	1450	879	552	Retreating
8	500	15	1400	791	598	Retreating
6	450	15	1500	790	664	Retreating
13	400	15	1400	746	679	Retreating
11	500	15	1500	744	613	Retreating
12	450	15	1400	730	567	Retreating
2	500	20	1400	712	536	Retreating
10	400	17.5	1450	679	669	Retreating
20	500	15	1350	671	563	Retreating
5	400	17.5	1350	662	614	Retreating
28	450	17.5	1350	640	677	Advancing
4	450	20	1450	636	616	Retreating
18	500	17.5	1400	626	492	Retreating
9	400	20	1500	608	648	Advancing
34	450	20	1350	604	529	Retreating
17	500	20	1500	602	521	Retreating
33	500	15	1450	601	498	Retreating
16	450	17.5	1400	599	415	Retreating
27	500	17.5	1500	590	603	Advancing
14	500	20	1350	549	438	Retreating
21	400	15	1500	544	712	Advancing
19	400	15	1350	535	525	Retreating
15	400	20	1350	528	302	Retreating
23	500	20	1450	514	533	Advancing
29	450	17.5	1450	488	446	Retreating
31	400	15	1450	482	468	Retreating
25	450	20	1400	454	422	Retreating
32	450	15	1450	428	423	Retreating
36	500	17.5	1350	421	377	Retreating
35	400	17.5	1400	420	404	Retreating
26	400	17.5	1500	412	331	Retreating
30	450	20	1500	400	342	Retreating
3	400	20	1450	N/A	N/A	N/A
22	450	15	1350	N/A	N/A	N/A

The overall trend observed is for the retreating side to exhibit higher temperatures as compared to the advancing side of the weld. The highest temperature on the retreating side of the weld was 1027°F (Samples 1 and 24). This temperature is close to the solidus temperature of the alloy, which is 1080°F. In contrast, the highest temperature on the advancing side was 712°F (Sample 21). The lowest temperatures for the advancing and the retreating sides were 400°F (Sample 30) and 302°F (Sample 15), respectively. The overall retreating side hottest and coldest weld temperature profiles are presented in Figure 34. The hottest weld (Sample 1) was fabricated at a medium rotational speed, medium travel speed, and a high tool plunge force; whereas, the overall coldest weld (Sample 30) was fabricated at medium rotational speed, high travel speed, and high tool plunge force.

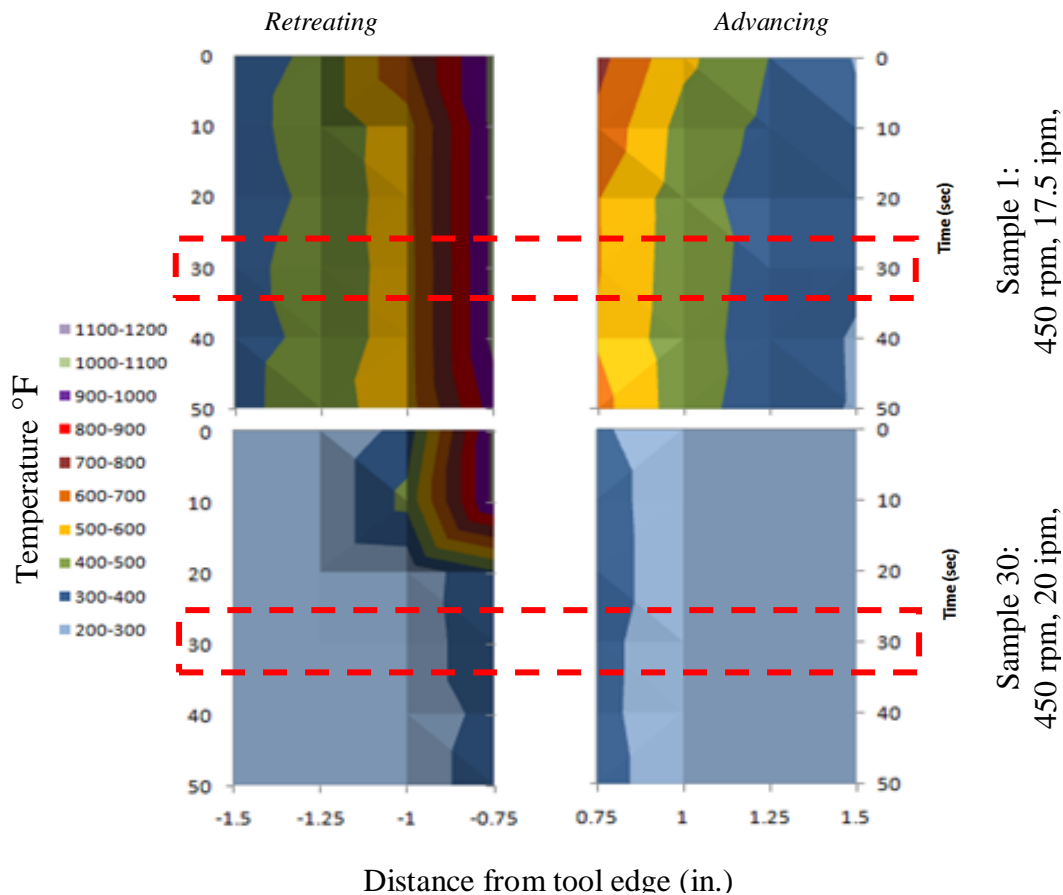


Figure 34: Overall retreating side hottest and coldest welds temperature profiles. Sample 1 exhibited the higher temperatures, while Sample 30 showed the lowest temperatures. The red box indicates the time at which the analysis was carried-out.

### 3.2 VISUAL INSPECTION

All the samples fabricated for this investigation exhibited the typical FSW semi-circular pattern on both the crown and root of the weld; an exemplar of this pattern is shown in Figure 35.

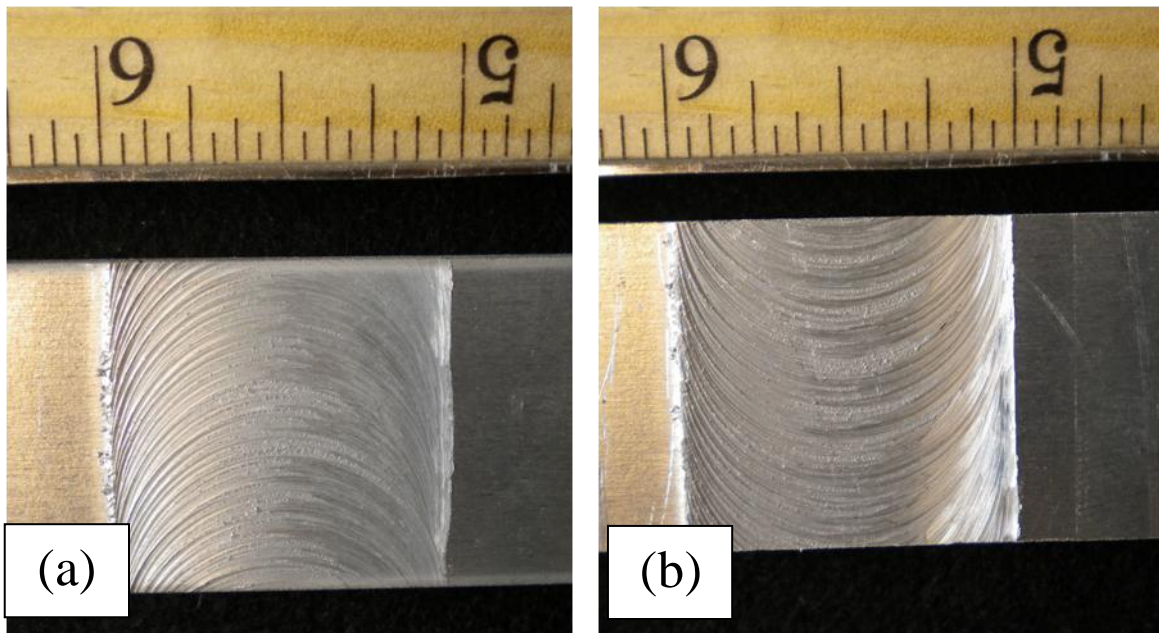


Figure 35: SR-FSW semicircular pattern observed in (a) crown and (b) root of the weld.

A visual appearance analysis of the crown of the weld was carried out to determine the presence of macroscopic defects. The main visual defects encountered were visible wormholes, galling, narrow bead, and a small amount of flash; these defects were rated from 1-4 according to their severity and impact on the visual appearance. The defects that have the largest negative influence on the weld visual appearance were rated as 4. A description of each defect and its effect on the welds visual appearance is discussed next.

Figure 36 present visible wormholes, which are internal voids that extend to the surface of the weld. Visible wormhole were detected on the advancing side of the weld, this defect was rated as 4, because it is highly detrimental to the weld visual quality.

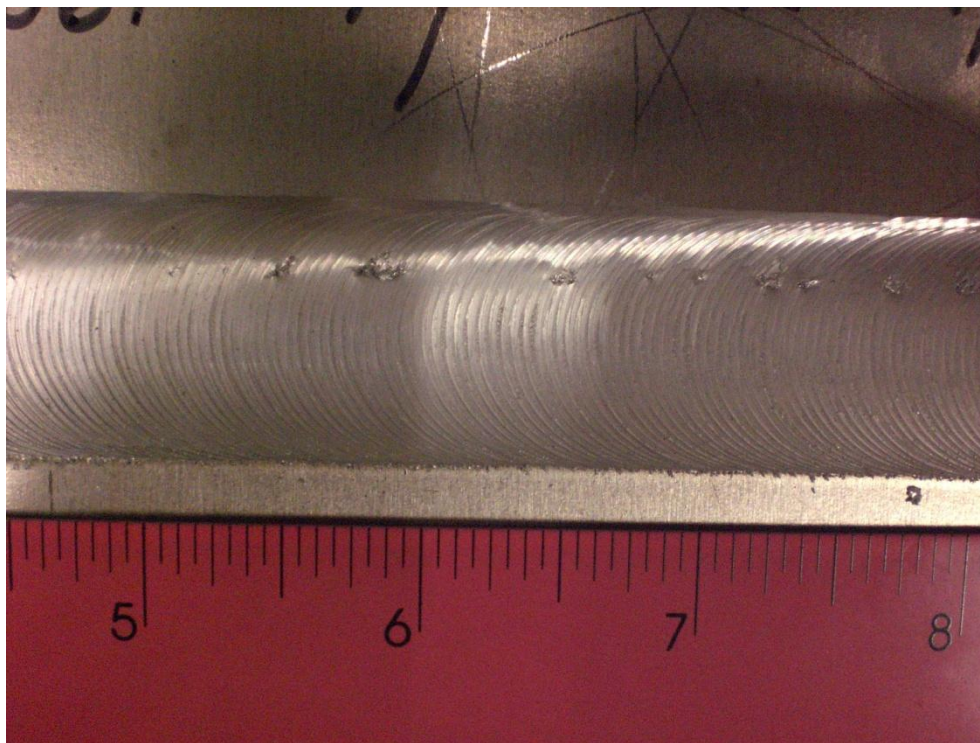


Figure 36: Visible wormholes, Sample 17. Wormholes are internal voids that extend to the surface of the weld. This defect is highly detrimental to visual appearance of the weld.



Galling is characterized by a rough and irregular surface appearance. The more severe the defect, the rougher the surface. Figure 37 exhibits severe galling and Figure 38 light galling. Severe galling was rated as 3, whereas, light galling was rated as 2.

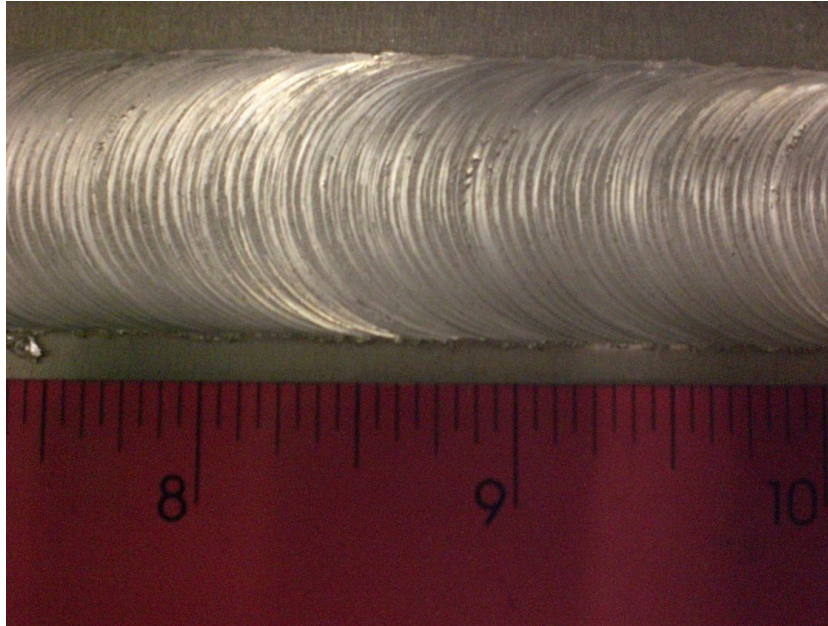


Figure 37: Visible galling (rated 3) on the crown of Sample 4.  
Severe galling is characterized by a rough surface.

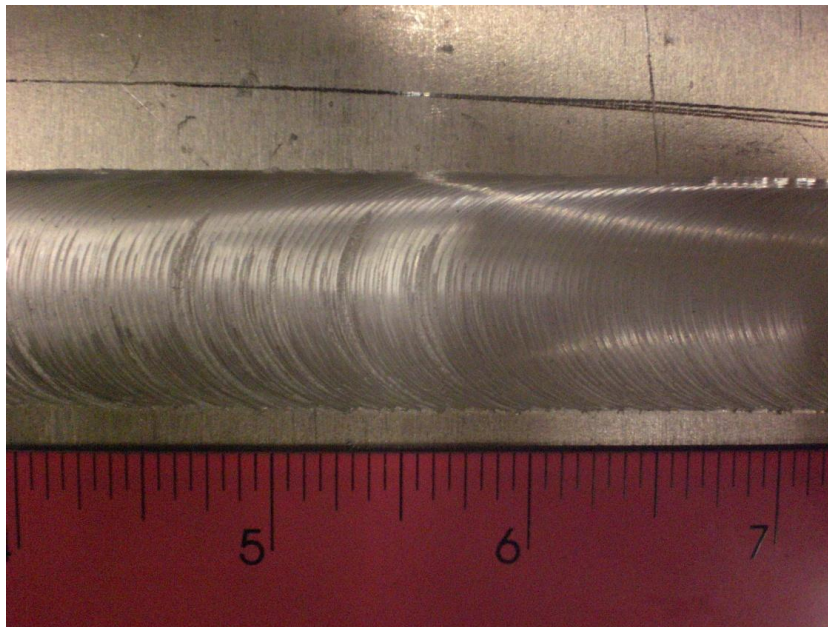


Figure 38: Light galling (rated 2) on the crown of Sample 36.

None of the samples fabricated for this investigation exhibited excessive flash, which is the lip formation next to the weld. However, a small amount of flash was observed on the retreating side. A continuous small amount of flash, as shown in Figure 39, was rated as 2, while a non-continuous, decreasing amount of flash, as shown in Figure 40, was rated as 1.

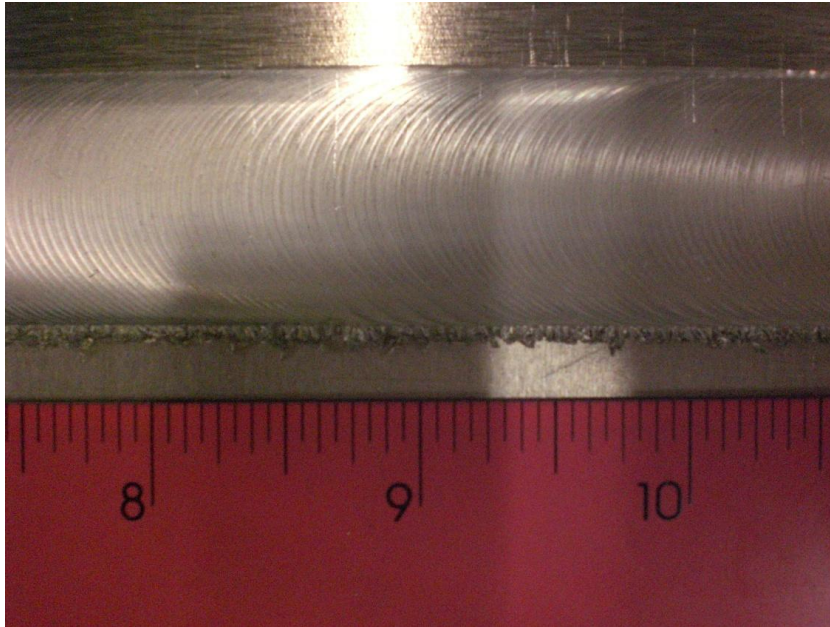


Figure 39: Small amount of continuous flash (rated as 2) observed on Sample 1.



Figure 40: Intermittent, decreasing flash (rated 1) observed on Sample 5.



A normal bead size is one with close correlation to the tool shoulder width (1.0 in. or 25.4 mm). Weld beads measuring less than 0.9 in. (22.86 mm) were considered narrow. An example of a narrow bead is presented in Figure 41.

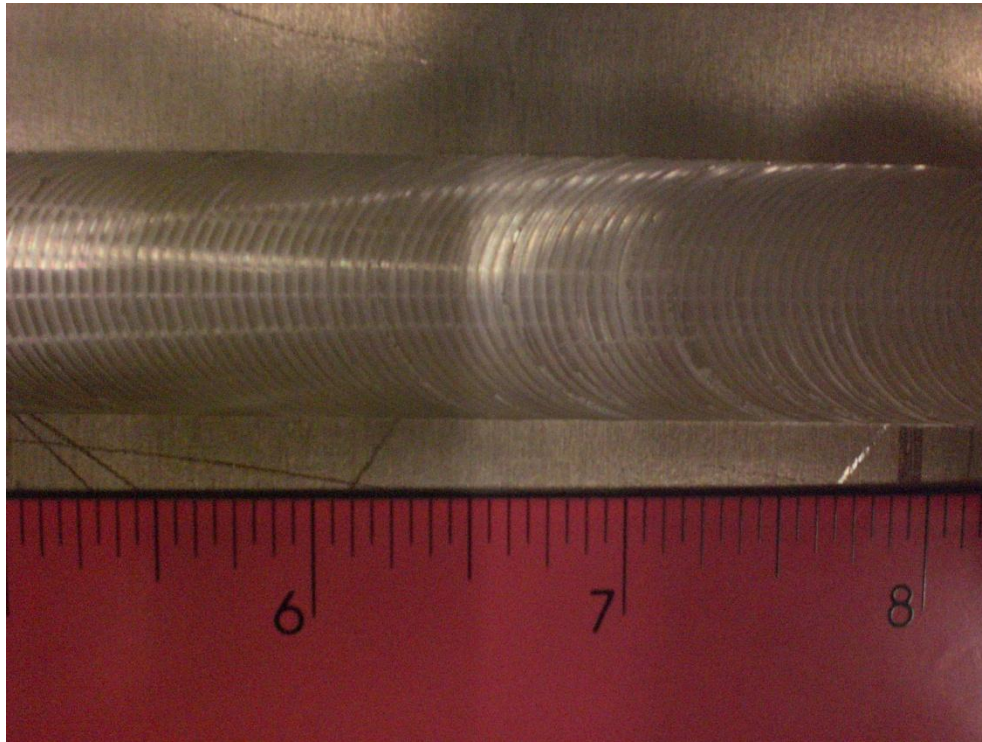


Figure 41: Narrow weld beads (rated 1). Welds measuring less than the tool shoulder width were considered narrow.

Macrographs from the crowns of the welds exhibiting the main defects for all the samples fabricated for this study are presented in Figure 42 to Figure 45. Each figure presents the visual quality macrographs as function of process parameters. All tool plunges forces exhibited an increase in the severity of the surface flaws, as the rotational speed increased.



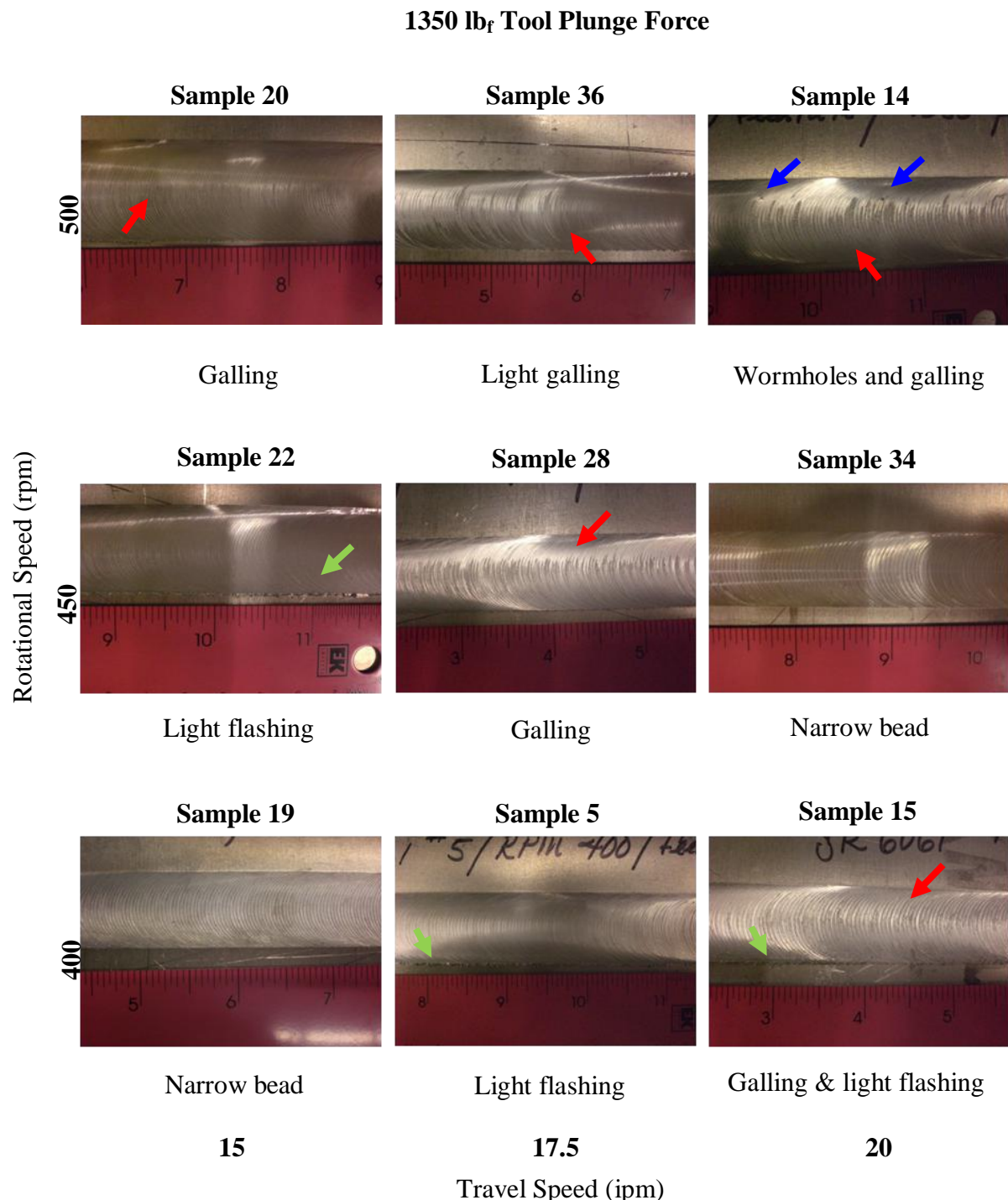


Figure 42: Weld visual appearance as function of process parameters. The description of the visual appearance is shown below the image. The main visual appearance discontinuities observed were visible wormholes (blue arrow), galling (red arrow), and flashing (green arrow).

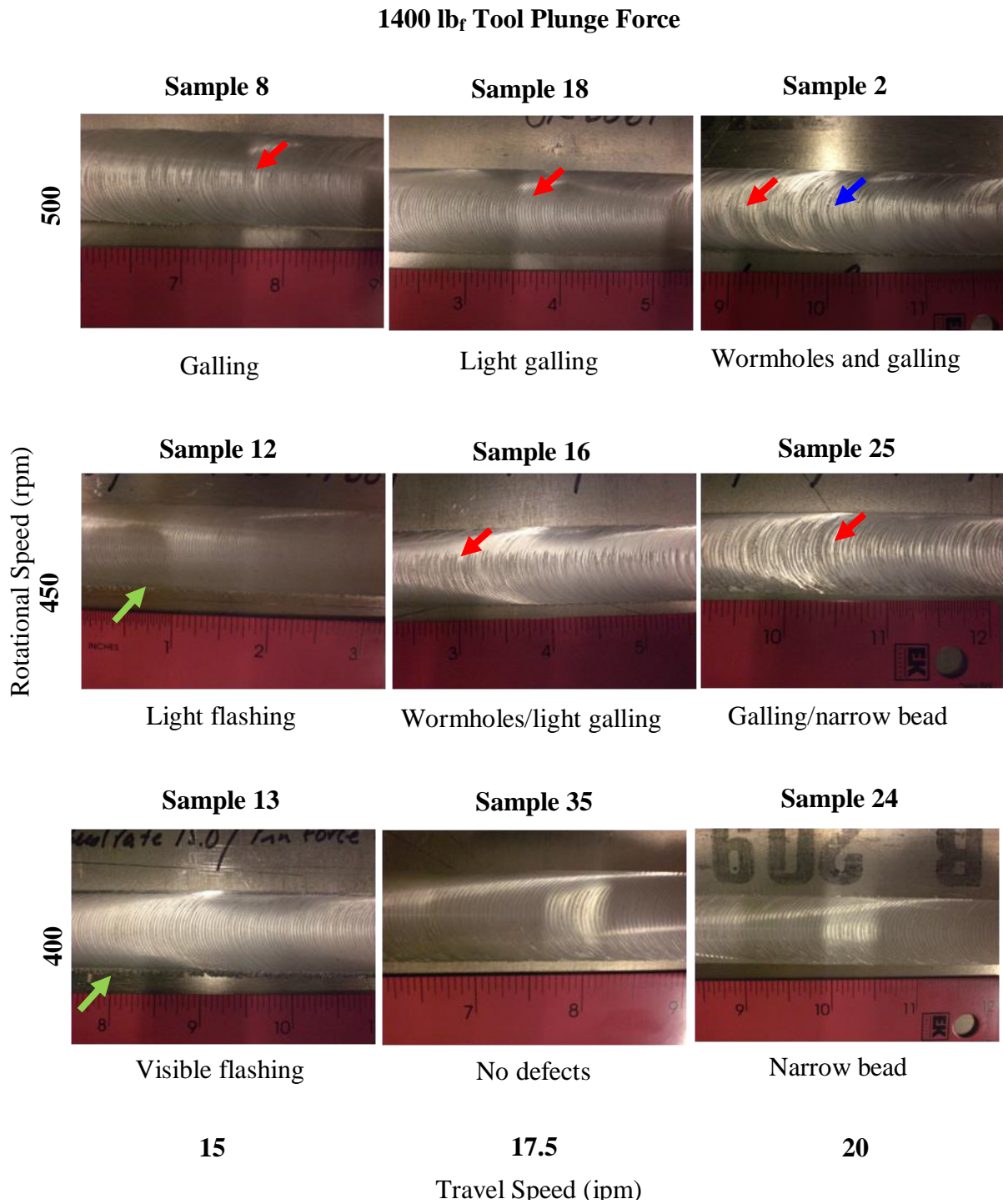


Figure 43: Weld visual appearance as function of process parameters. The description of the visual appearance is shown below the image. The main visual appearance discontinuities observed were visible wormholes (blue arrow), galling (red arrow), and flashing (green arrow).

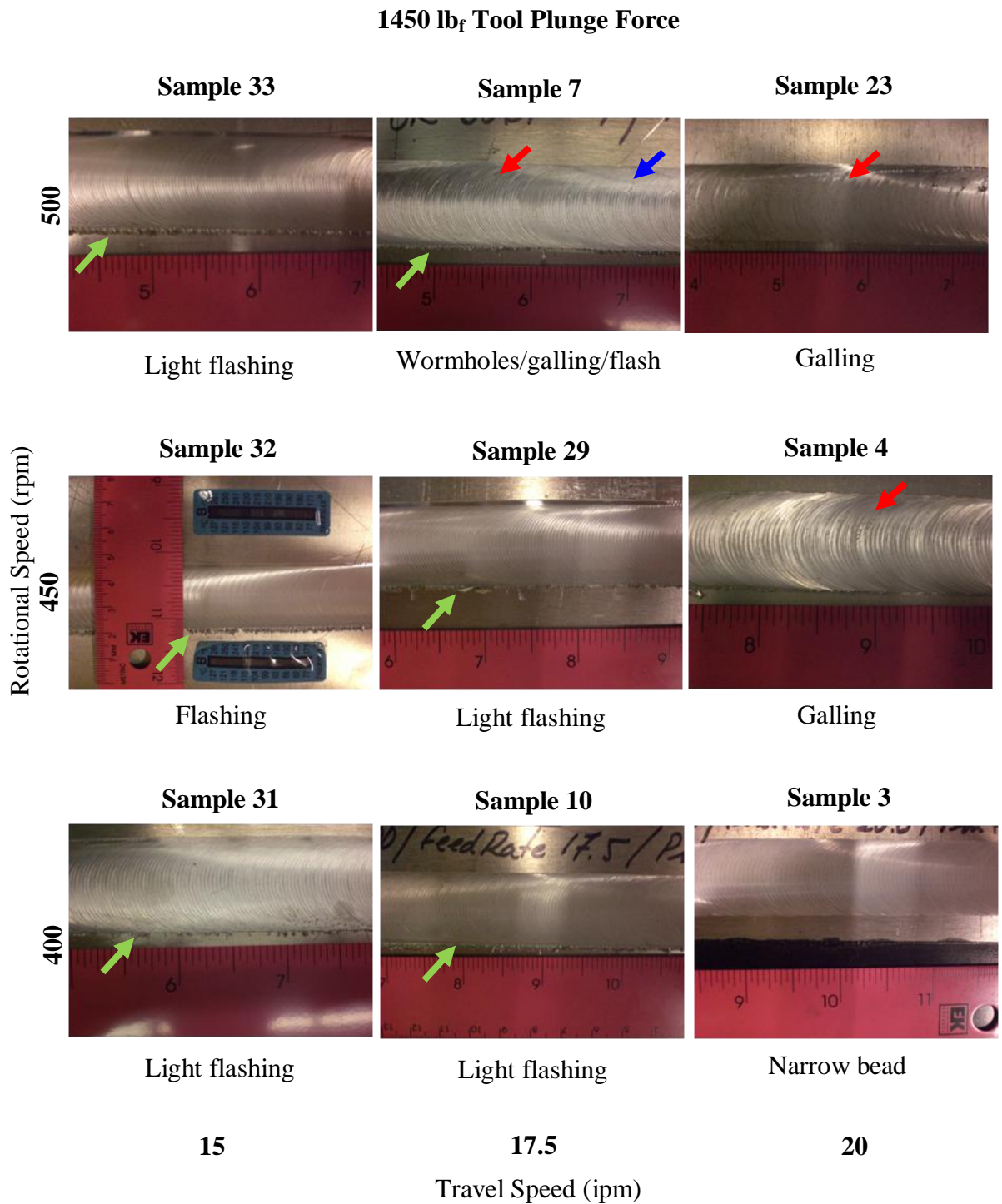


Figure 44: Weld visual appearance as function of process parameters. The description of the visual appearance is shown below the image. The main visual appearance discontinuities observed were visible wormholes (blue arrow), galling (red arrow), and flashing (green arrow).

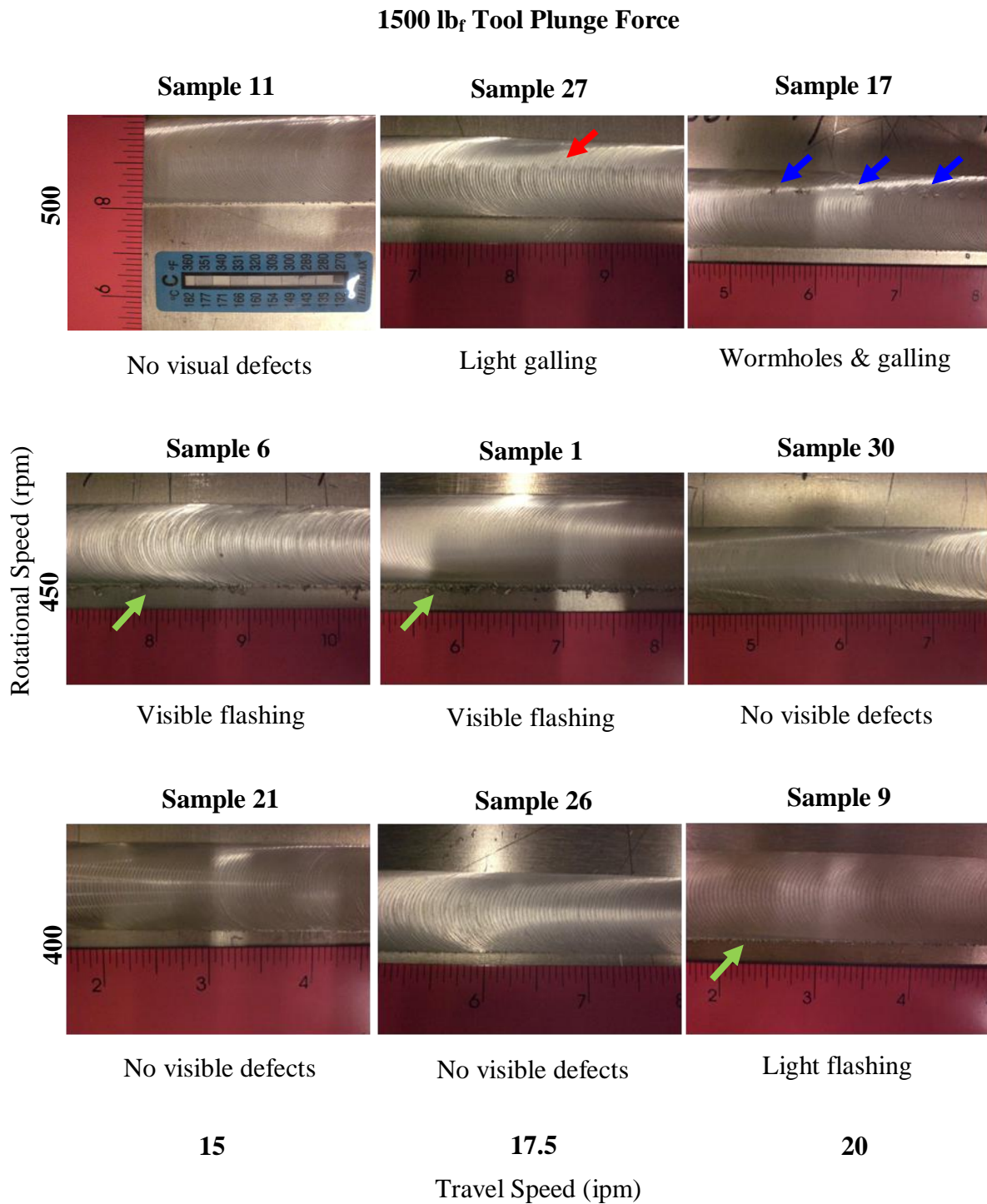


Figure 45: Welds visual appearance as function of process parameters. The description of the visual appearance is shown below the image. The main visual appearance discontinuities observed were visible wormholes (blue arrow), galling (red arrow), and flashing (green arrow).



Table 9 presents the samples that exhibited a narrow bead, which are weld beads that measured less than 0.9 in. (22.86 mm). Welds fabricated at a high tool plunge force (1500 lb<sub>f</sub>) did not exhibit a narrow bead.

Table 9: Welds with a Narrow Bead

Weld Number	Rotational Speed (rpm)	Travel Speed (ipm)	Plunge Force (lb <sub>f</sub> )	Bead size (in)
3	400	20	1450	0.855 (21.71 mm)
19	400	15	1350	0.874 (22.19 mm)
24	400	20	1400	0.842 (21.19 mm)
25	450	20	1400	0.888 (22.55 mm)
34	450	20	1350	0.854 (21.69 mm)

All tool plunge forces used for this study exhibited a better surface appearance at low rotational speed, as the severity of the surfaces flaws increased with increasing rotational speed. Visible wormholes, which are internal voids that extend to the surface of the weld, were developed at high rotational and high traverse speeds for all tool plunge forces, except for a plunge force of 1450 lb<sub>f</sub> where wormholes were observed at high rotational and medium traverse speed. None of the studied samples exhibited excessive flashing. However, a small amount of flash was observed in samples fabricated at a medium rotational and low traverse speeds, for all tool plunge forces.

The weld visual quality as function of the number of and severity of visual defect swas evaluated as previously discussed, results are presented in Table 10. Samples listed under low quality exhibited a greater number of and more severe macroscopic defects such as wormholes, galling, flash, and narrow bead. In contrast, samples with high quality exhibited a smooth, regular, and defect free surface. Samples fabricated at lower rotational speed and high tool plunge force exhibited the best surface appearance, whereas, samples fabricated at high rotational speed resulted in the lowest visual appearance quality.

Table 10: SR-FSW Joints Visual Quality

Sample Number	Rotational Speed (rpm)	Traverse Speed (ipm)	Tool Plunge Force (lbf)	Visual Appearance Rating	Visual Surface Quality
7	500	17.5	1450	9	Low
17	500	20	1500	7	
14	500	20	1350	7	
15	400	20	1350	4	
25	450	20	1400	4	
2	500	20	1400	4	
16	450	17.5	1400	3	
20	500	15	1350	3	
8	500	15	1400	3	
23	500	20	1450	3	
4	450	20	1450	3	
28	450	17.5	1350	3	
27	500	17.5	1500	2	Medium
12	450	15	1400	2	
1	450	17.5	1500	2	
32	450	15	1450	2	
18	500	17.5	1400	2	
6	450	15	1500	2	
22	450	15	1350	2	
13	400	15	1400	2	
36	500	17.5	1350	2	
33	500	15	1450	1	High
10	400	17.5	1450	1	
31	400	15	1450	1	
24	400	20	1400	1	
5	400	17.5	1350	1	
9	400	20	1500	1	
29	450	17.5	1450	1	
19	400	15	1350	1	
3	400	20	1450	1	
34	450	20	1350	1	
11	500	15	1500	0	
35	400	17.5	1400	0	
21	400	15	1500	0	
26	400	17.5	1500	0	
30	450	20	1500	0	

Main effects plot was produced in order to determine the effect of process parameters on the visual appearance of the welds. The overall visual appearance was rated according to the type of defects and their severity (Table 10). From the main effects plot presented in Figure 46, it can be seen that the rotational speed has a bigger effect on the visual quality, followed by the travel speed. The best visual appearance is achieved at a low rotational speed, low travel speed, and high tool plunge force, whereas the worst visual appearance occurs at high rotational speed, high travel speed, and low tool plunge force.

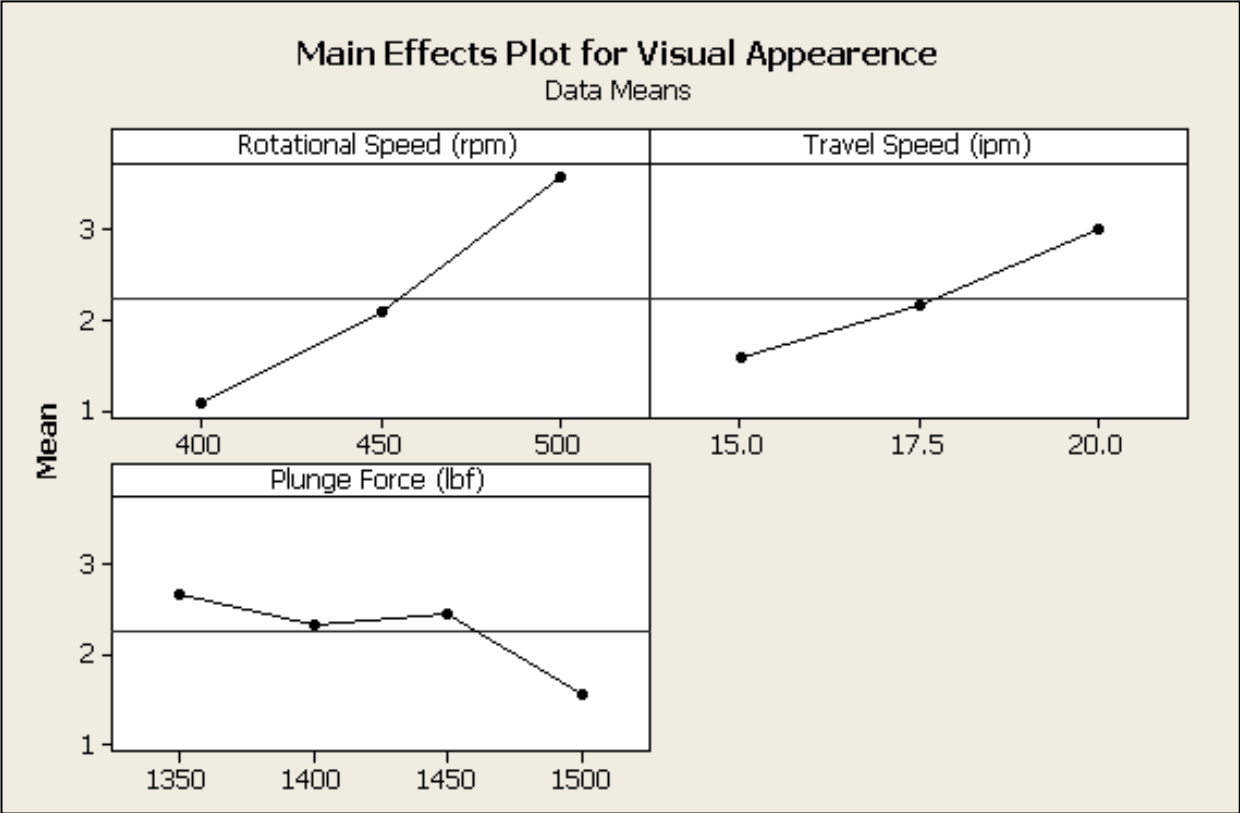


Figure 46: Visual appearance main effects analysis. Rotational speed has a bigger effect in the weld visual appearance. The best visual appearance is achieved at low rotational speed, low travel speed, and high tool plunge force.

### 3.3 MICROSTRUCTURE

All of the samples fabricated for this study exhibited the conventional friction stir weld microstructure consisting of four main zones: weld nugget, thermo-mechanically affected zone (TMAZ), heat-affected zone (HAZ), and parent metal. However, the SR-FS welded joint microstructure exhibits similar characteristics between the crown and root of the weld, as compared to the conventional FSW microstructure. The macrograph in Figure 47 presents the weld nugget, the TMAZ and the HAZ in a SR-FSW butt weld; the advancing side is shown on the right side.

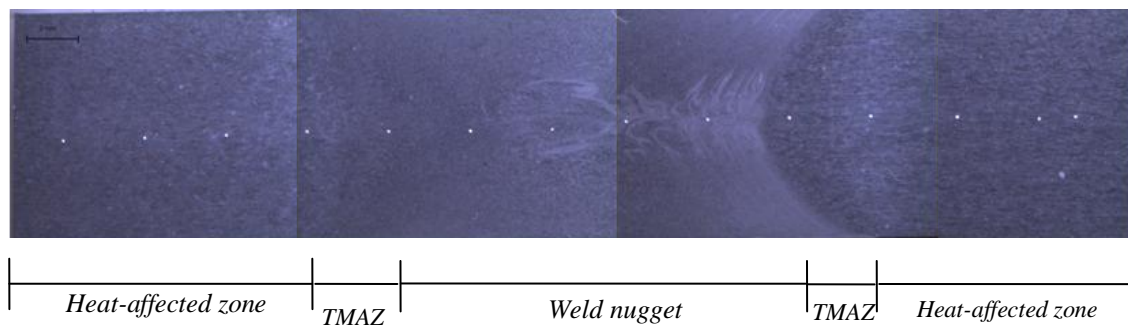


Figure 47: Self-reacting friction stir weld zones. The weld nugget, the thermo-mechanically affected zone (TMAZ), and the heat-affected zone are presented on the macrograph. The advancing side is shown on the right side of the macrograph.



The SR-FSW weld zone exhibits what appear to be bands running from the sides, top, and bottom of the weld towards the center. The red arrows in Figure 48 indicate the location of these bands, which are more distinguishable on the advancing side as compared to the retreating side.

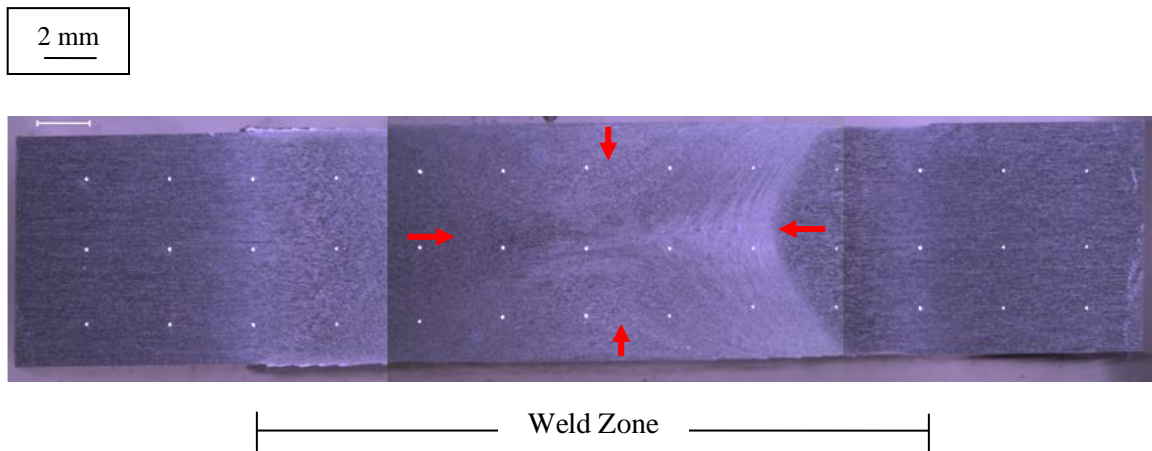
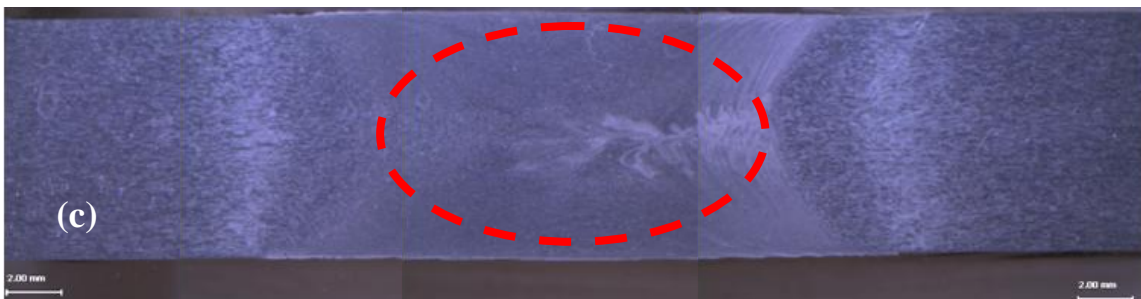
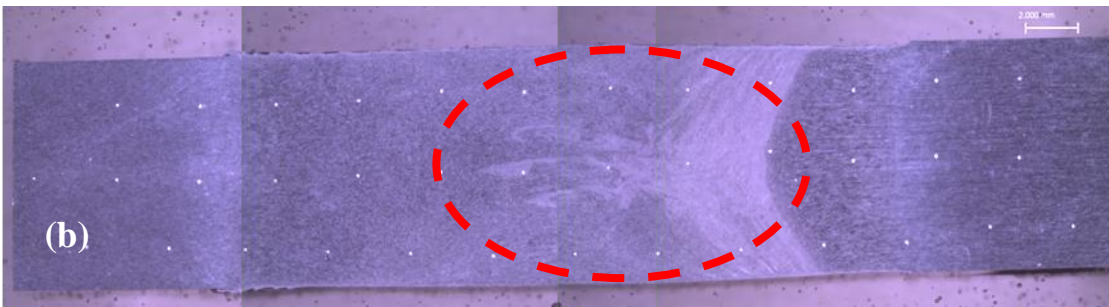
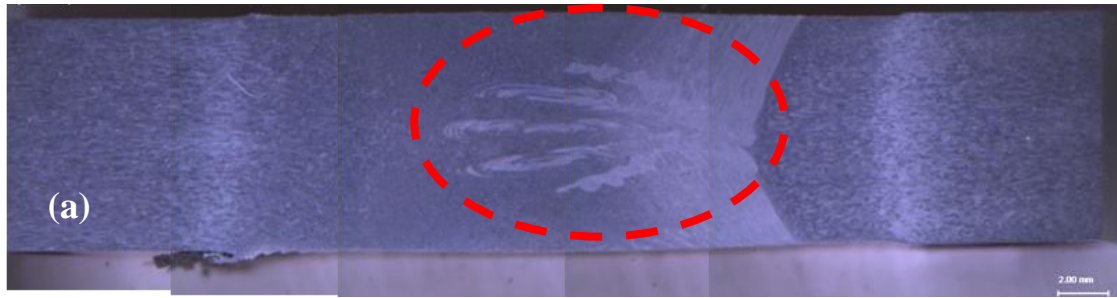


Figure 48: SR-FSW weld zone bands macrograph from Sample 21. Bands (indicated by red arrows) running towards the center of the weld. White dots in the macrographs are microhardness indentations.

All the samples fabricated for this investigation exhibited a discernable pattern in the central region of the weld nugget. This pattern starts on the advancing side towards the center of the nugget region forming what appear to be “fingers”. However, the appearance of this pattern differed for each sample. Some samples exhibited more of this “finger like” pattern, which appear to be formed by concentric rings. Samples that exhibited a clear and visible “finger” pattern are shown in Figure 49. An example of weld nuggets in which the features of this pattern are not as clear are shown in Figure 50. The SR-FSW nugget pattern appears similar to the “onion ring” pattern, which is a typical feature observed in the nugget region of tradition FS welds. The somewhat unique variations seen in this study are most likely due to the differing tool characteristics between conventional and SR-FSW tools.



*Retreating*

*Advancing*

Figure 49: Weld nugget distinguishing “finger” pattern macrographs. A discernable concentric ring pattern is observed in the nugget region on (a) Sample 1, (b) Sample 5, and (c) Sample 9, and (d) Sample 6.



*Retreating*

*Advancing*

Figure 50: Weld nugget pattern macrographs. No distinct “finger like” pattern is observed in the weld nugget of Sample 34.

All the samples fabricated for this study exhibited a weld nugget microstructure characterized by a fine and equiaxed grain structure, as a result of dynamic recrystallization. Dynamic recrystallization occurs due to the high strains and temperatures developed in the nugget region during the welding process. However, slight differences were observed between the microstructures of the weld nugget center and the region near the shoulders as well as between the advancing and retreating side microstructures. The microstructure in the center of the weld nugget exhibits fine grains and a characteristic pattern that appears to have regions with slightly larger grains, as shown in Figure 51 and Figure 52, whereas the area near the tool shoulders exhibits a more uniform, fine microstructure, shown in Figure 54. The average nugget grain size was estimated to be about 16  $\mu\text{m}$ .

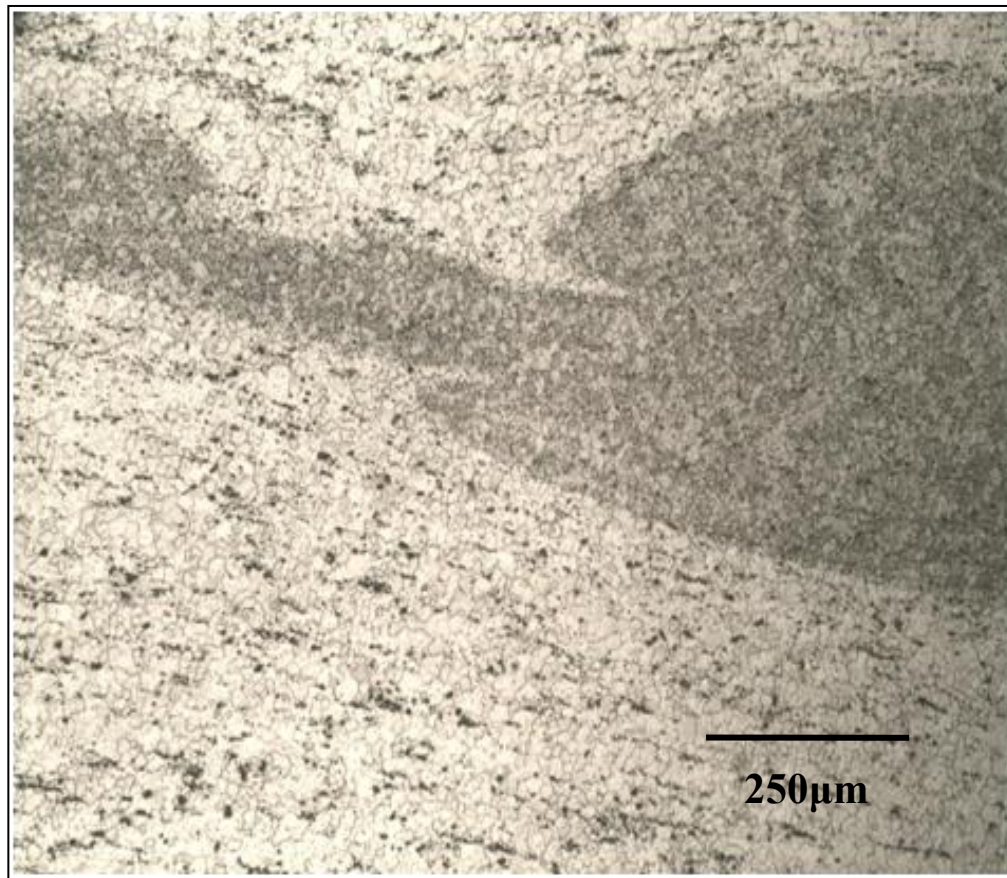


Figure 51: Representative microstructure from the center of the weld nugget, Sample 1. Dix-Keller's reagent.



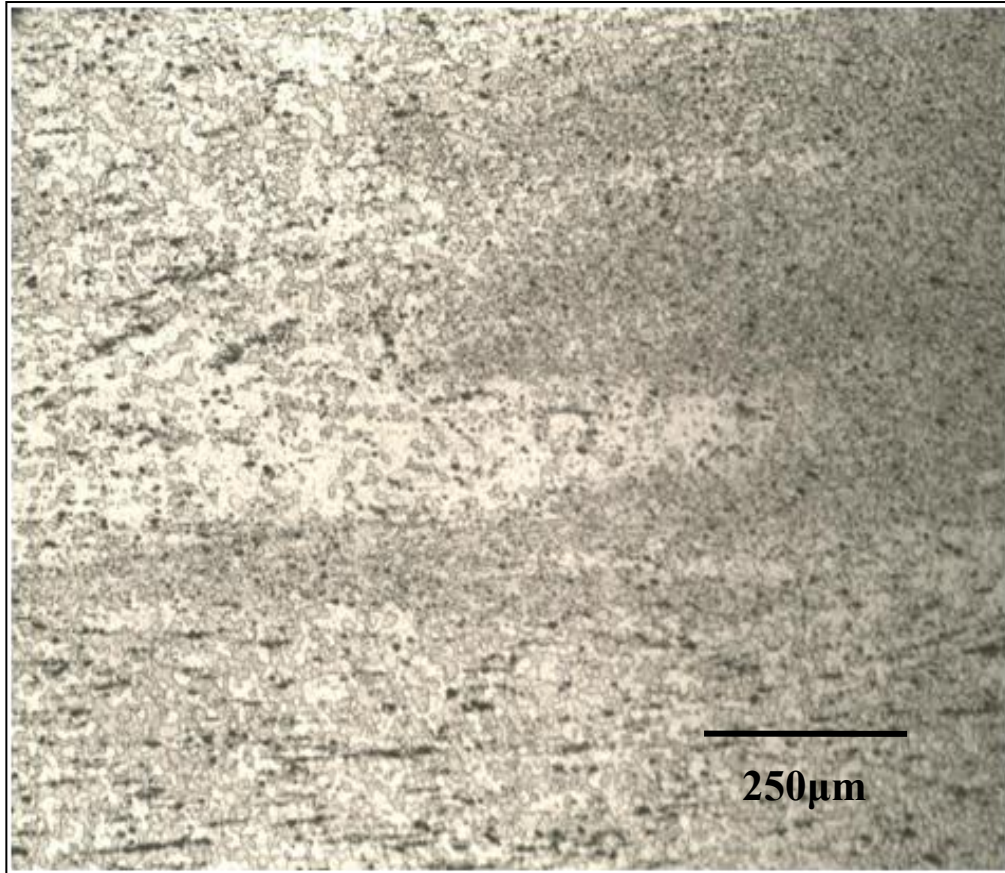


Figure 52: Representative microstructure from the center of the weld nugget, Sample 3. Dix-Keller's reagent.

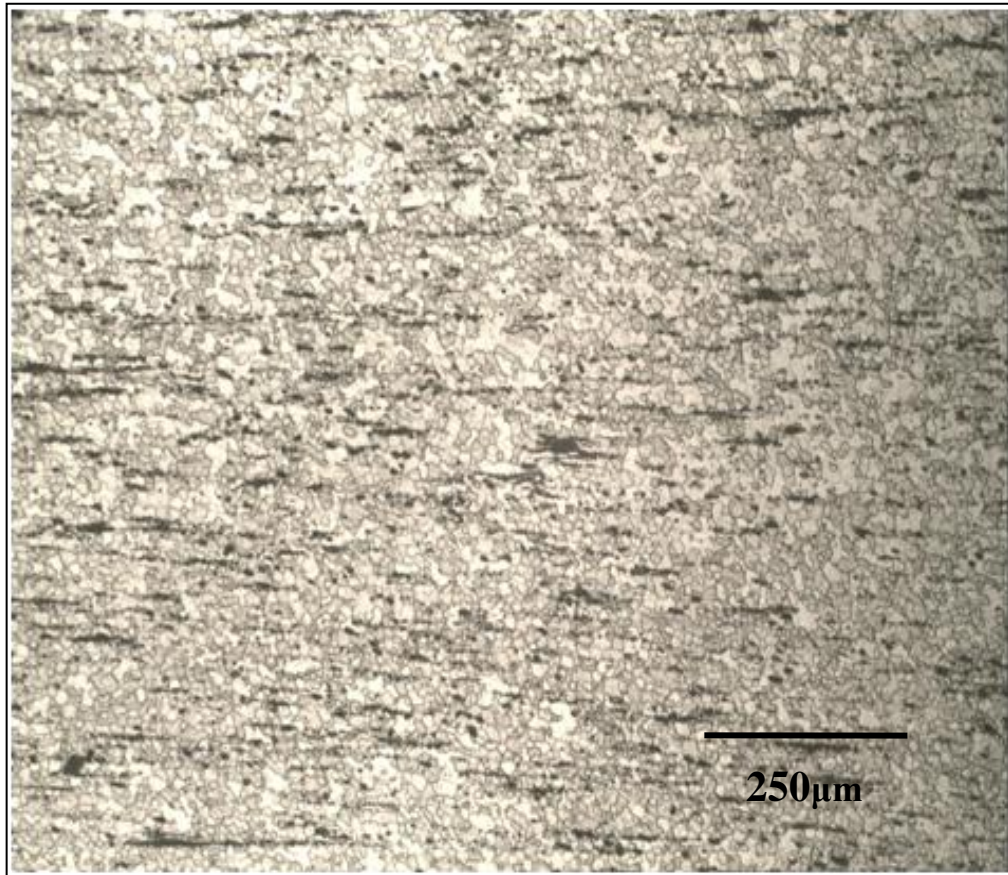


Figure 53: Representative nugget microstructure near the top shoulder. Dix-Keller's reagent.

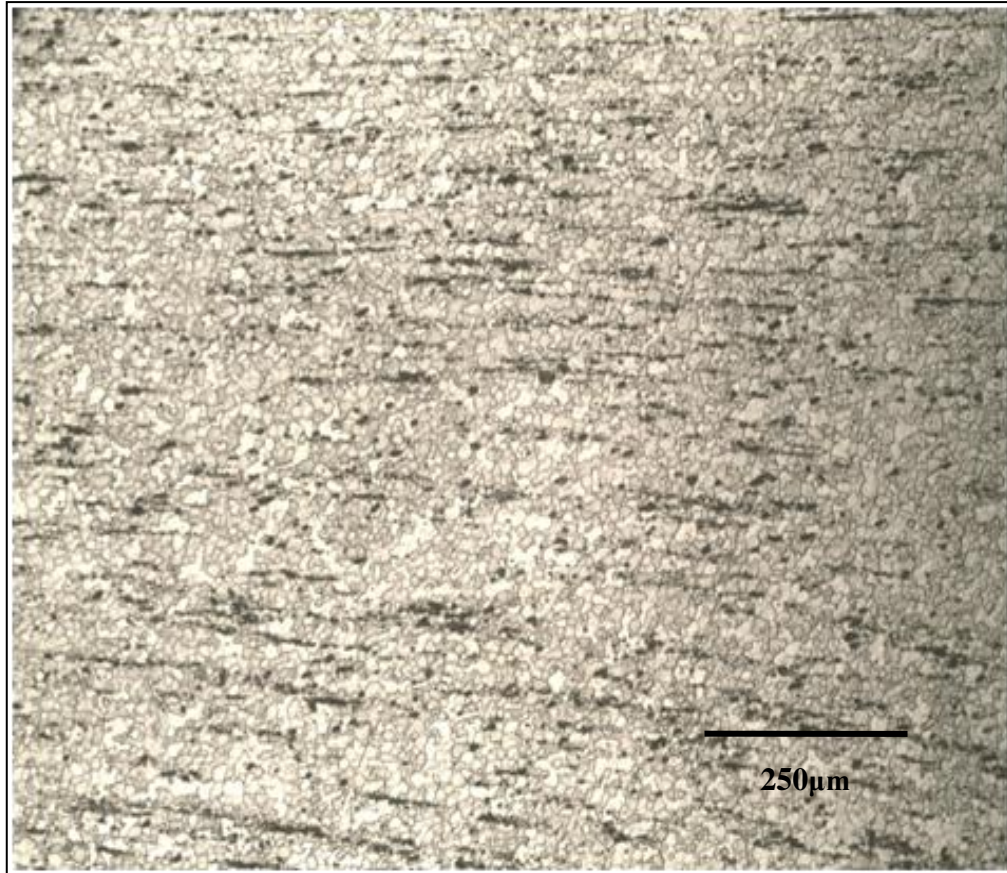


Figure 54: Representative nugget microstructure near the bottom shoulder.  
Dix-Keller's reagent.



The nugget microstructure on the advancing side exhibits fine and equiaxed grains (Figure 55 to Figure 57), and what appear to be bands flowing towards the center of the weld, as shown in Figure 58 and Figure 59. In contrast, the nugget microstructure on the retreating side is characterized by what seems to be a mixture of smaller and larger grains, as shown in Figure 60 and Figure 61. No bands are visible on the retreating side.

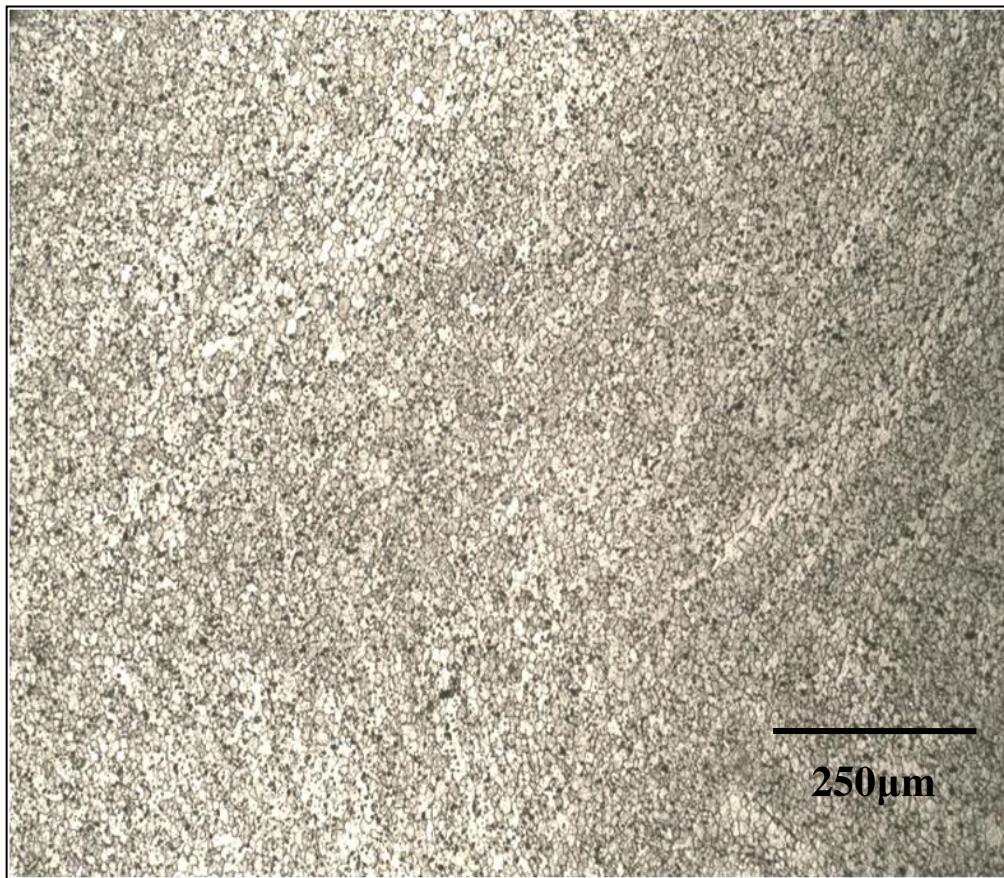


Figure 55: Representative advancing side nugget microstructure, Sample 5.  
Dix-Keller's reagent.



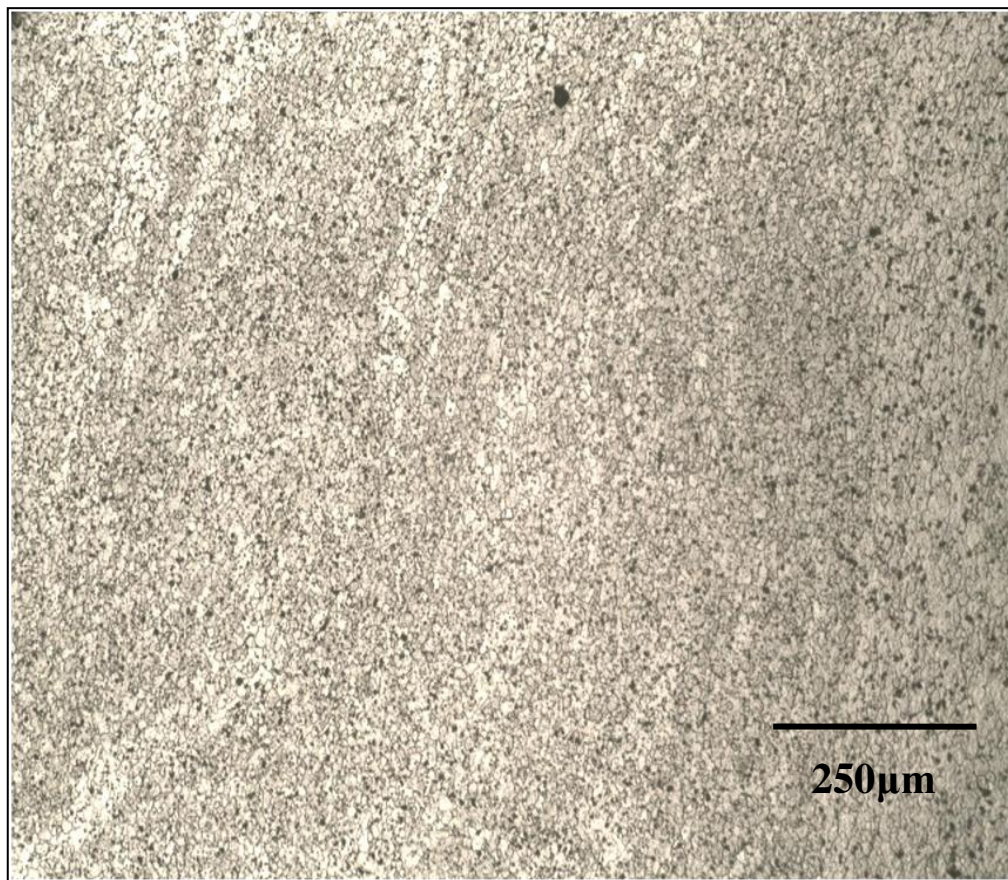


Figure 56: Representative advancing side nugget microstructure, Sample 15.  
The microstructure is characterized by a fine grains. Dix-Keller's reagent.

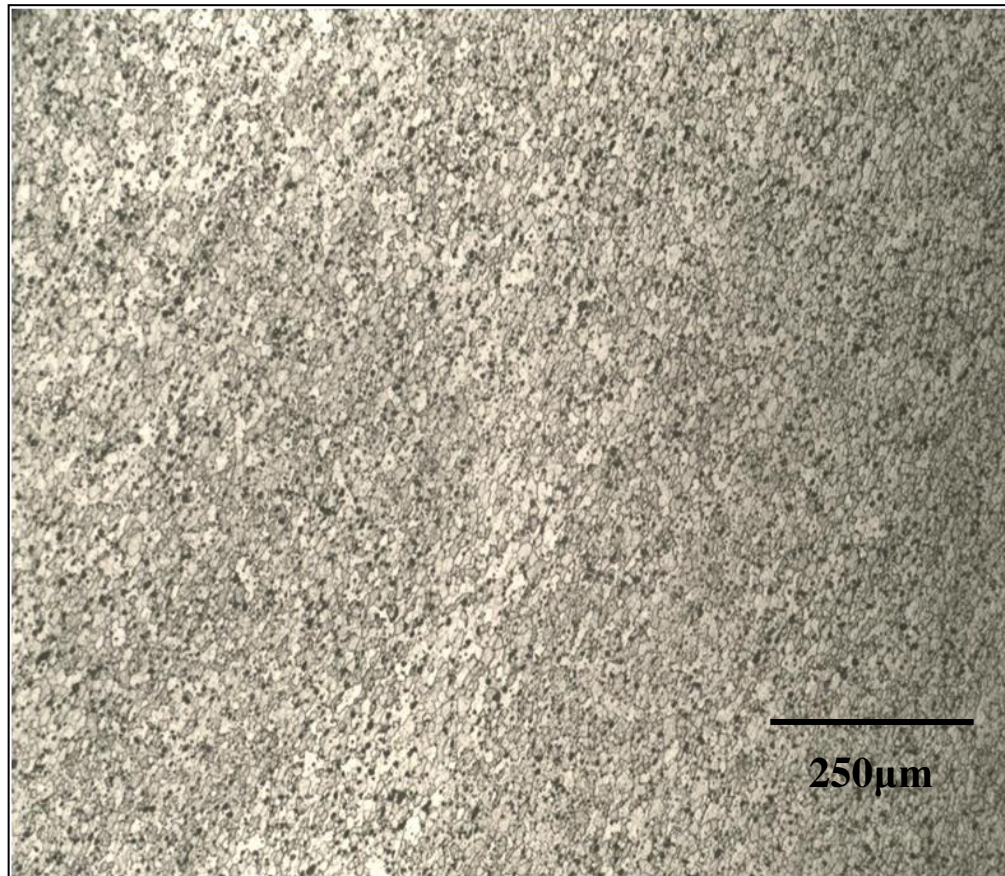


Figure 57: Advancing side nugget microstructure from sample 21. The microstructure is characterized by a fine grains. Dix-Keller's reagent.



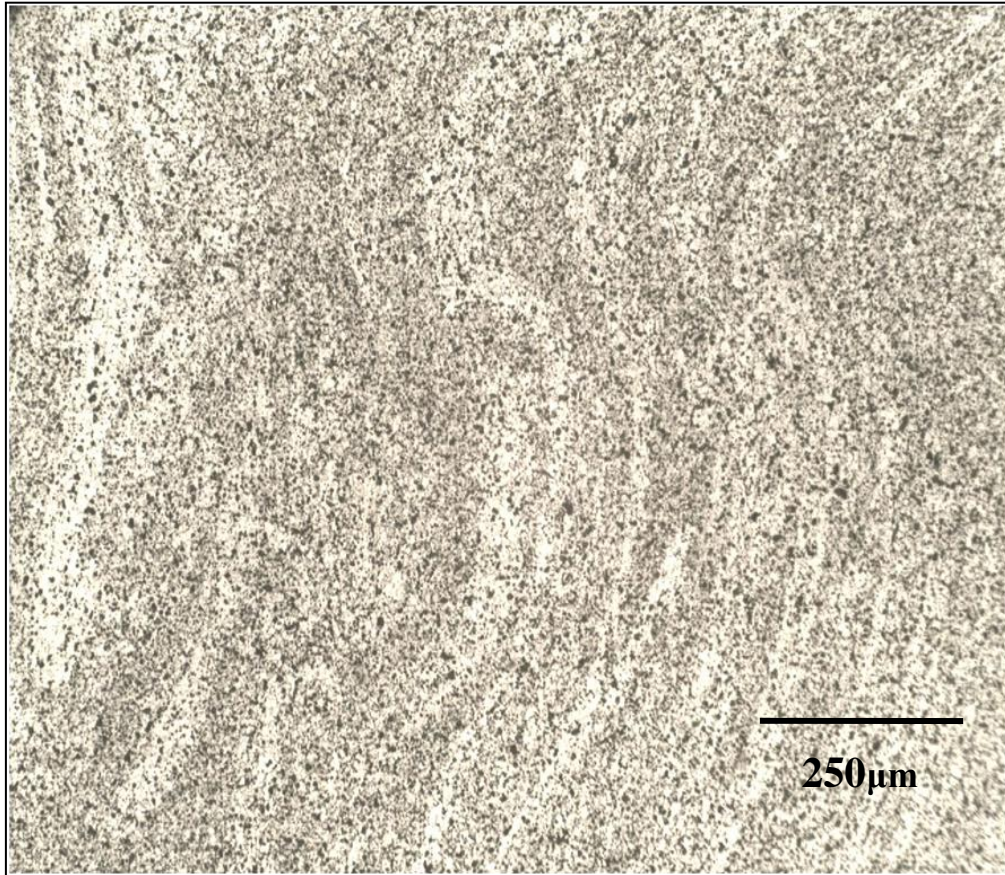


Figure 58: Advancing side nugget microstructure from Sample 13. What appear to be bands were observed in the nugget region in the advancing side. Dix-Keller etchant.

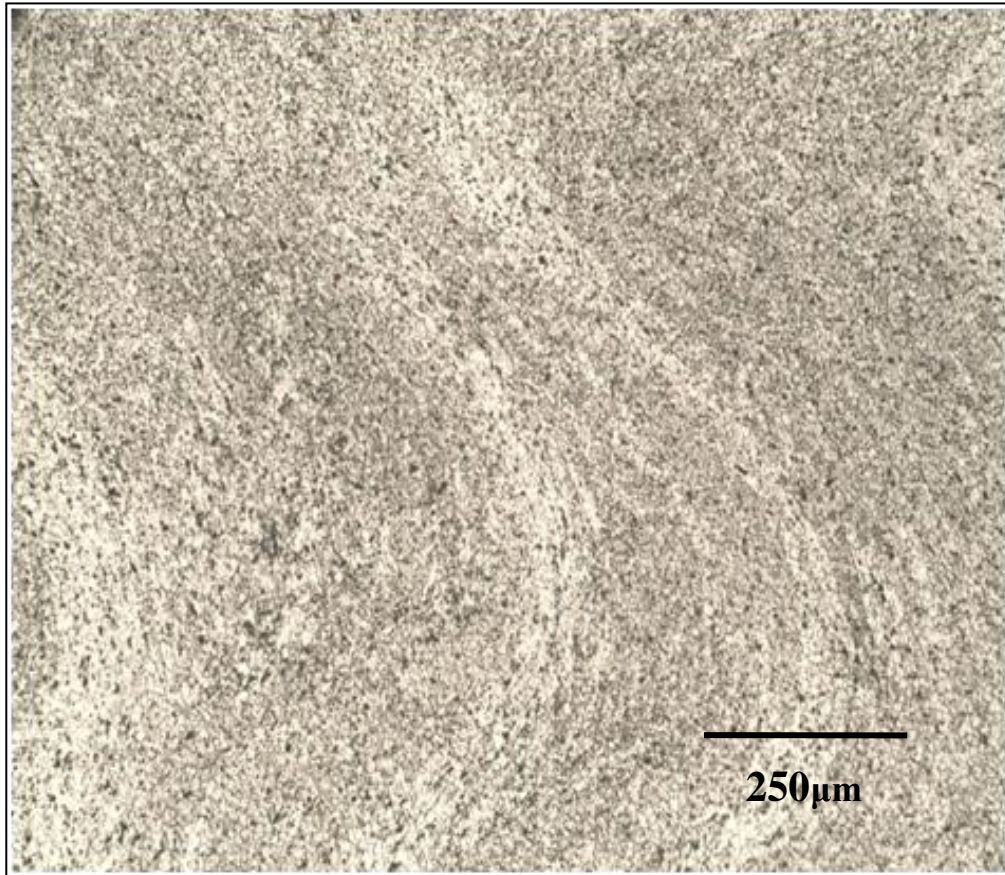


Figure 59: Advancing side nugget microstructure from Sample 2. What appear to be bands were observed in the nugget region in the advancing side. Dix-Keller's reagent.



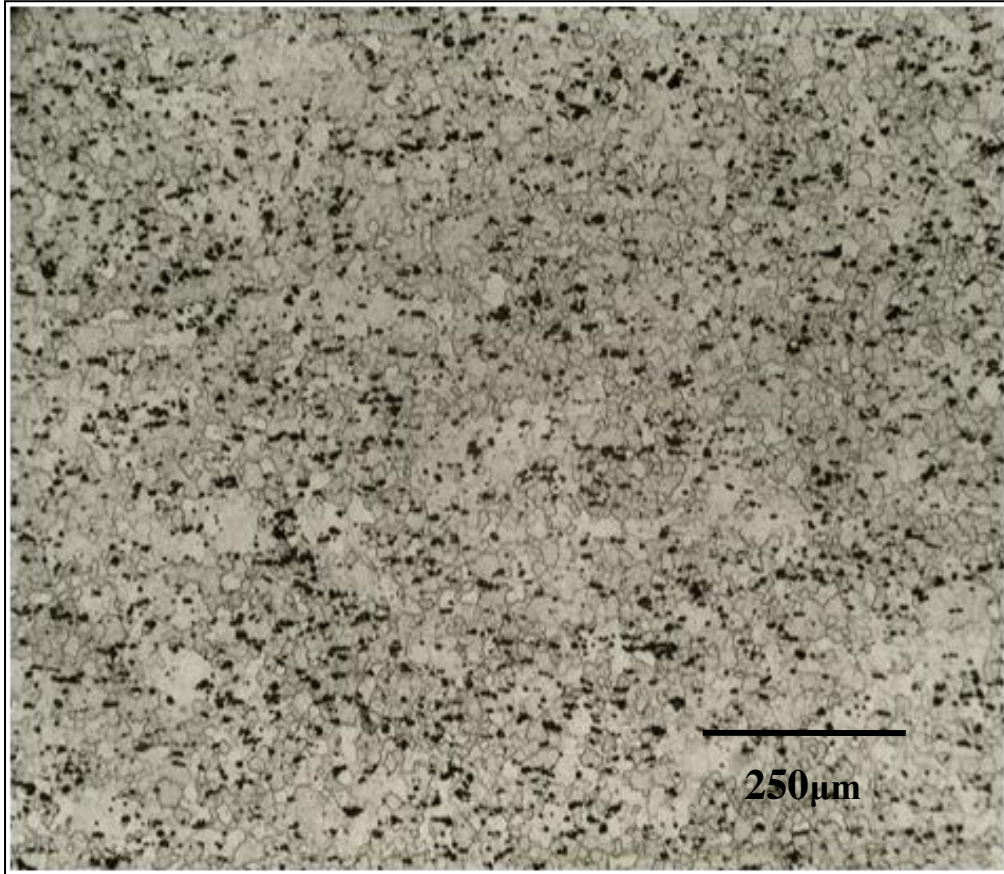


Figure 60: Retreating side nugget microstructure from Sample 9. A mixture of small and large grains is observed. Dix-Keller's reagent.

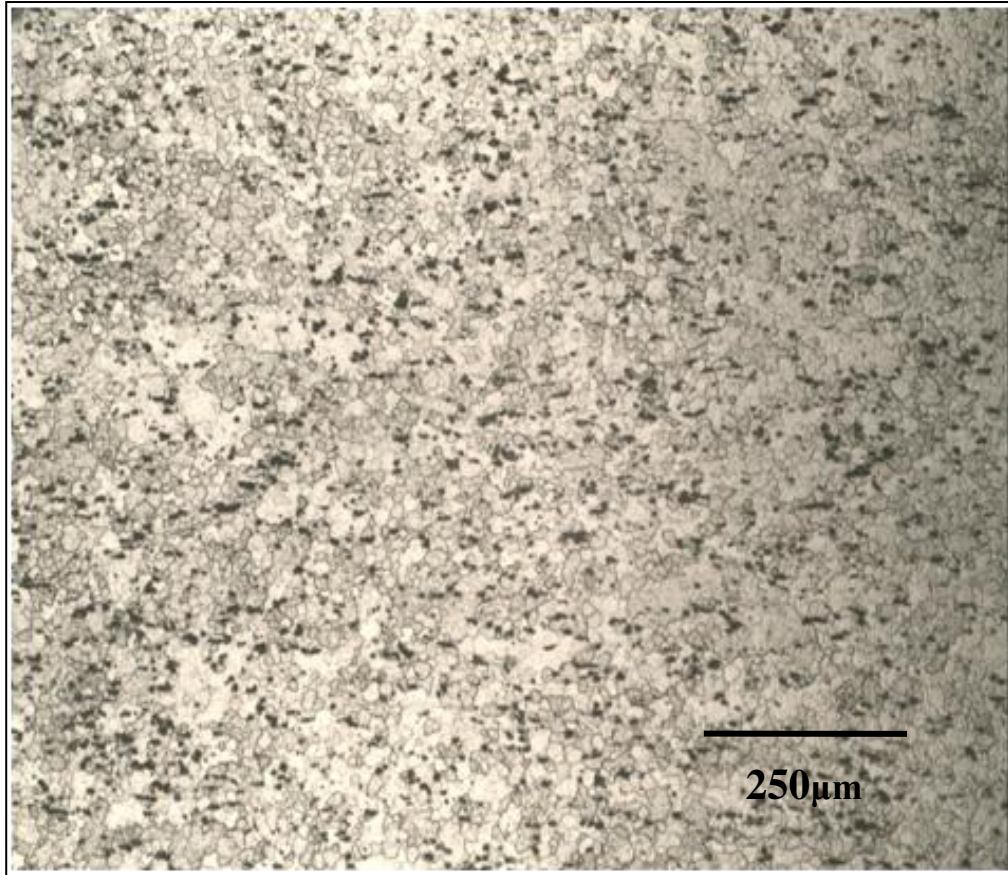


Figure 61: Retreating side nugget microstructure from Sample 10. A mixture of small and large grains is observed. Dix-Keller's reagent.

Adjacent to the weld nugget is the TMAZ. The transition between the weld nugget and the thermo-mechanically affected zone is clear and sharp on the advancing side, whereas, on the retreating side this transition is not that discernible, as shown in Figure 62. This is consistent with what has been observed by other authors during conventional FSW [66] [67].

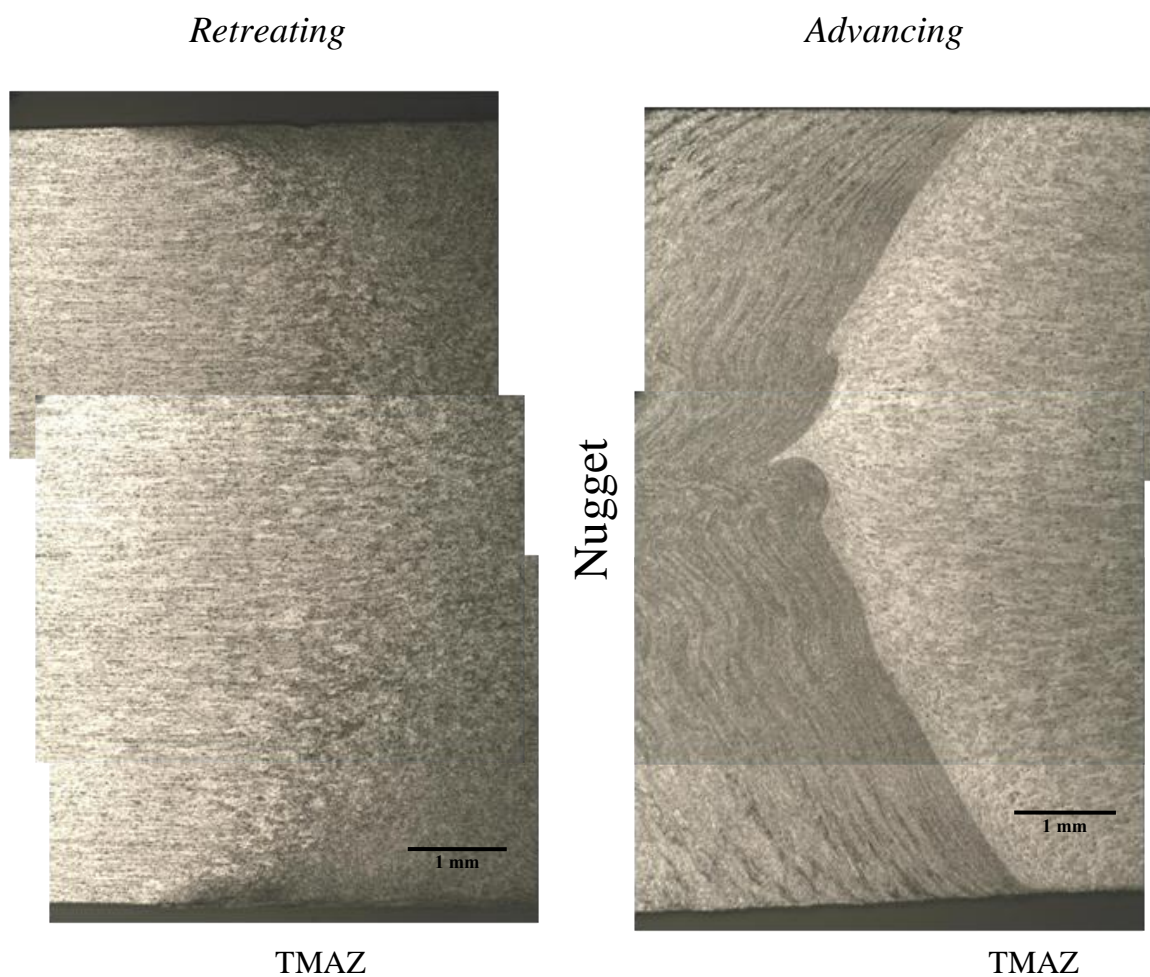


Figure 62: Nugget—TMAZ border. The transition zone between the nugget and the thermo-mechanically affected zone is more distinguishable on the advancing side (right side) compared to the retreating side (left side). Dix-Keller etchant.



The thermo-mechanically affected zone is the transition between the elongated grains from the HAZ and the recrystallized microstructure on the nugget. The TMAZ microstructure on the advancing and retreating sides is characterized by rotated and deformed grains. A representative TMAZ microstructure from the advancing side is shown in Figure 63 to Figure 64. The retreating TMAZ microstructure is shown in Figure 65.

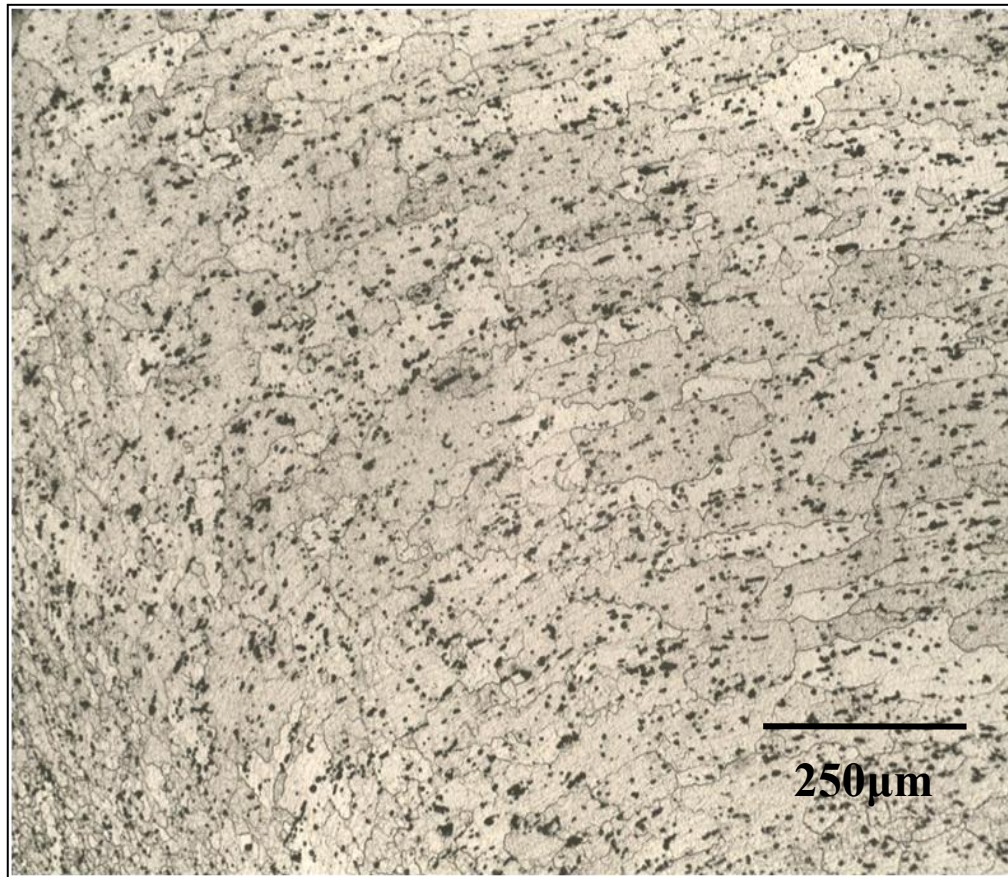


Figure 63: Advancing side TMAZ microstructure from Sample 31. Dix-Keller etchant.



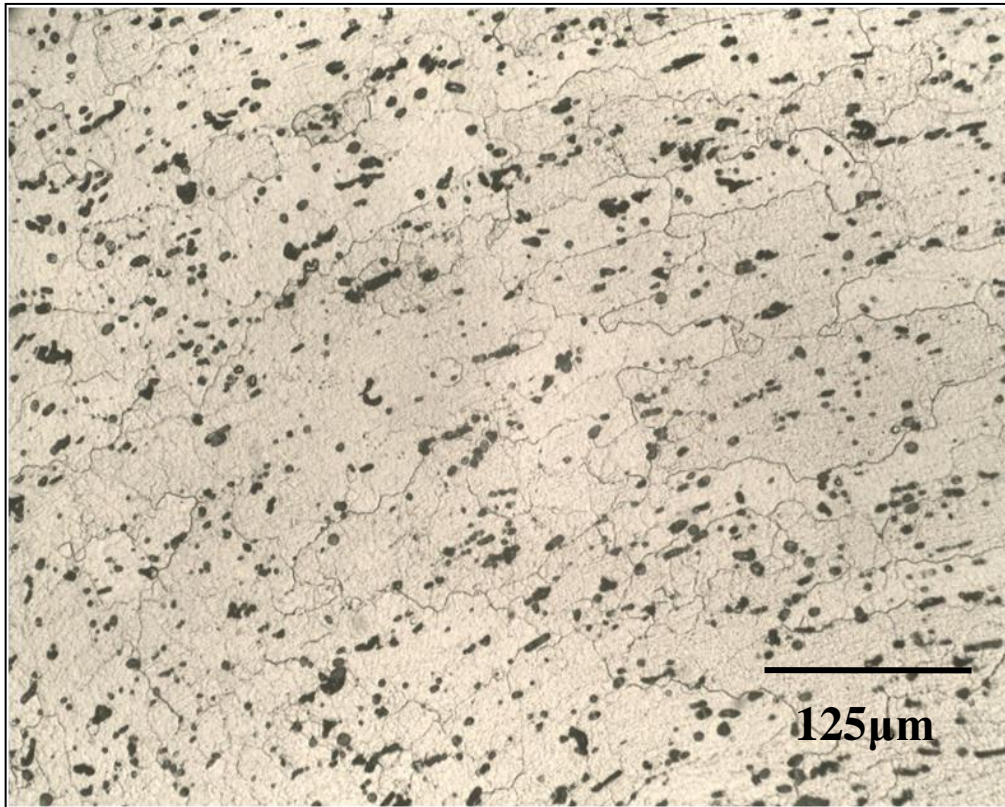


Figure 64: Advancing side TMAZ microstructure from Sample 31. Dix-Keller etchant.

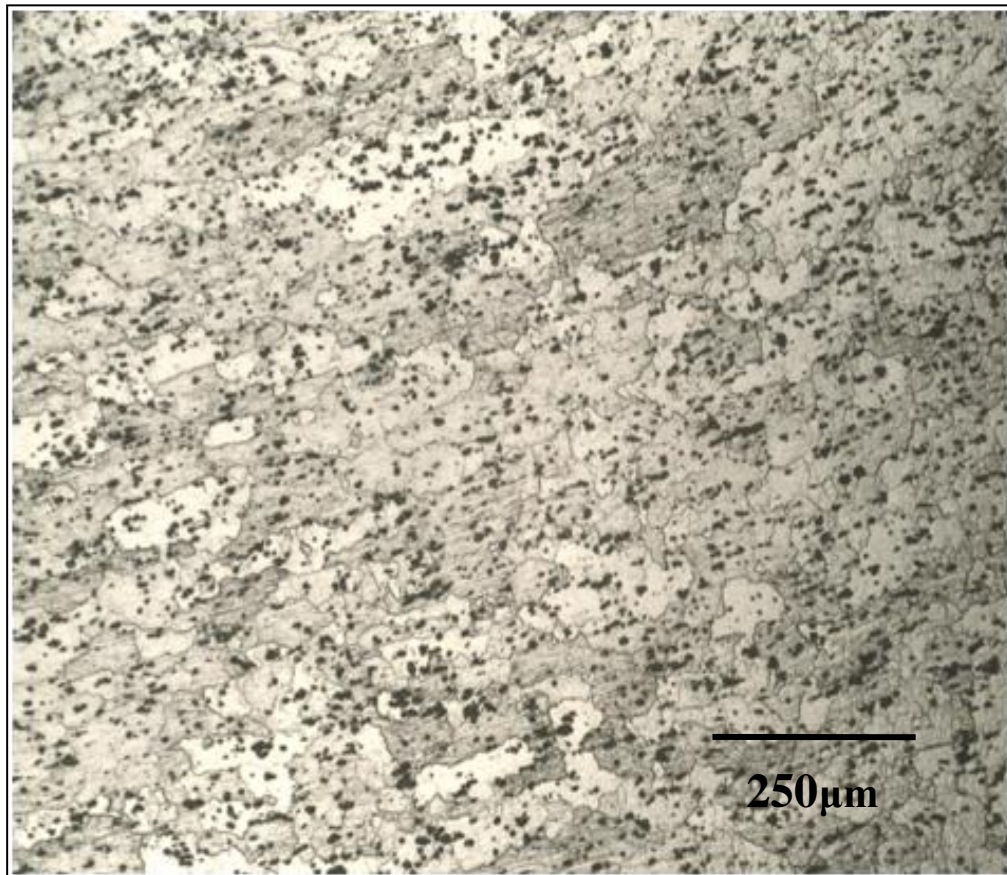


Figure 65: Representative retreating side TMAZ microstructure Sample 10.  
Dix-Keller etchant.

The TMAZ grain structure appears to be bent towards the tool shoulders, due to the effect of the stirring deformation from the process; this rotation of the grains is more evident near the tool shoulder region than in the middle section of the weld. The TMAZ microstructure near the top shoulder, the center of the weld, and the bottom shoulder is shown in Figure 66 and Figure 67, and Figure 68 respectively.

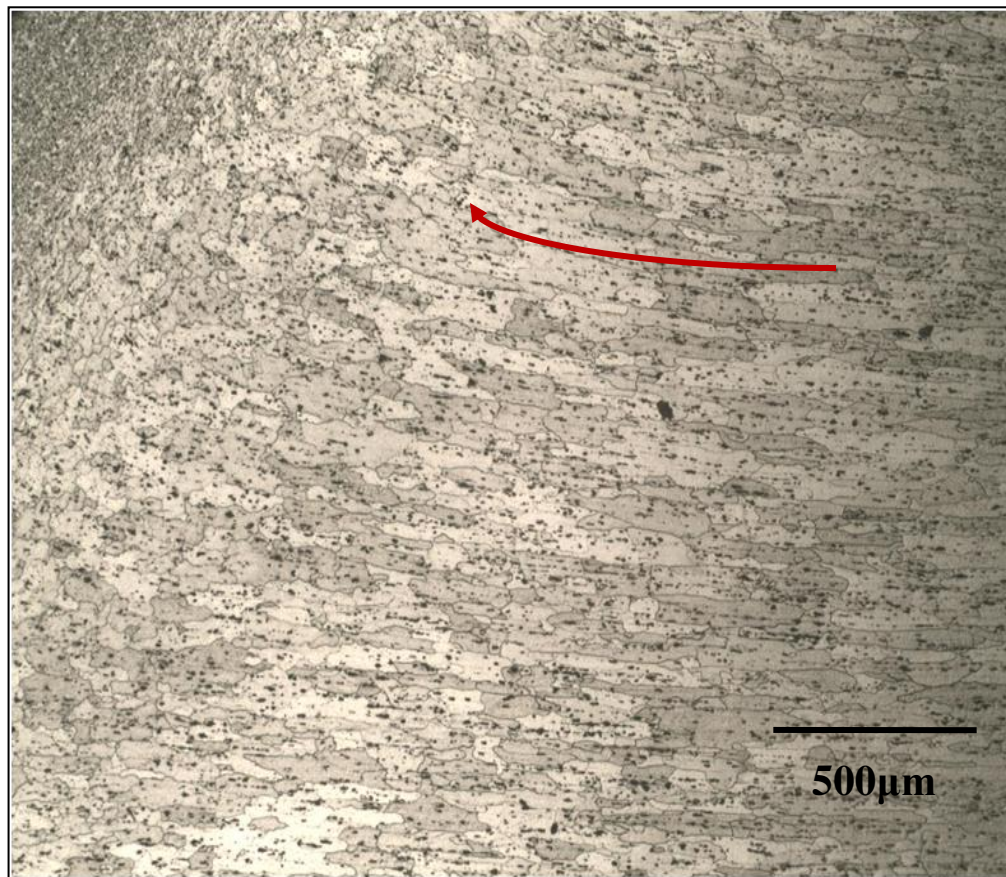


Figure 66: Advancing side top shoulder thermo-mechanically affected zone microstructure, Sample 5. The microstructure in this region exhibits deformed grains bent toward the tool shoulder (red arrow). The advancing side is shown on the right side of the micrograph. Dix-Keller etchant.



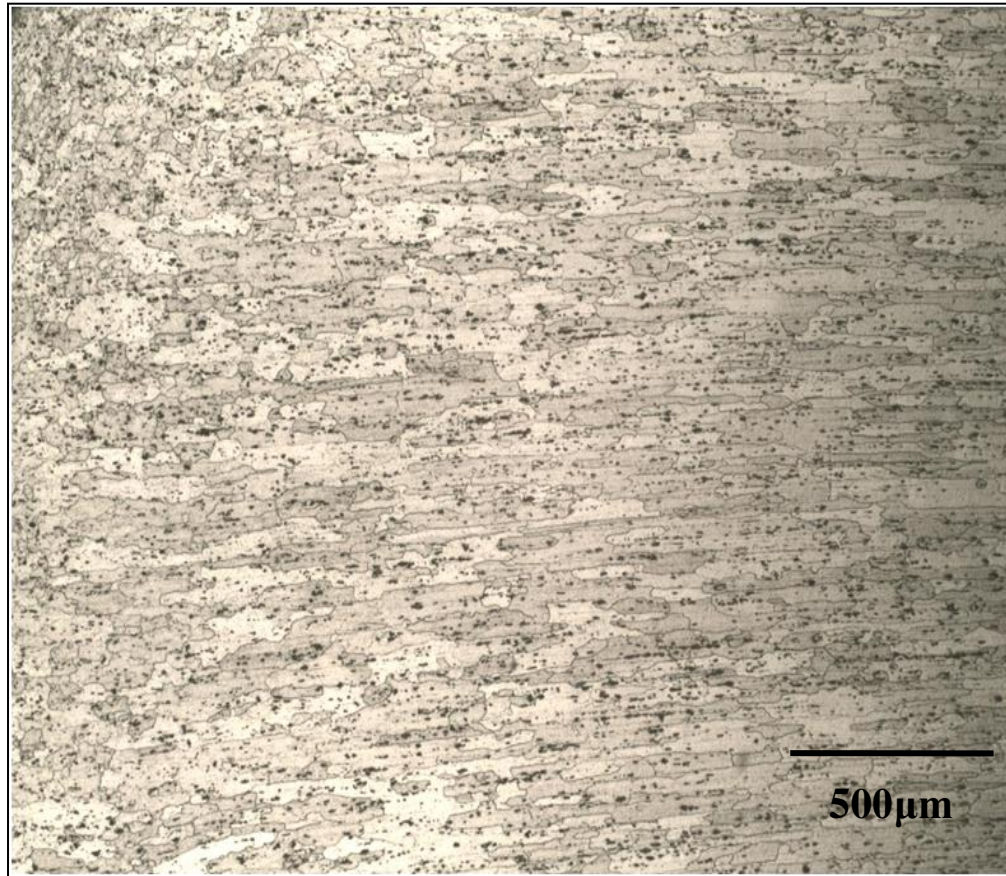


Figure 67: Advancing side weld center thermo-mechanically affected zone microstructure, Sample 5. The microstructure in this region exhibits deformed grains. The advancing side is shown on the right side of the micrograph. Dix-Keller etchant.

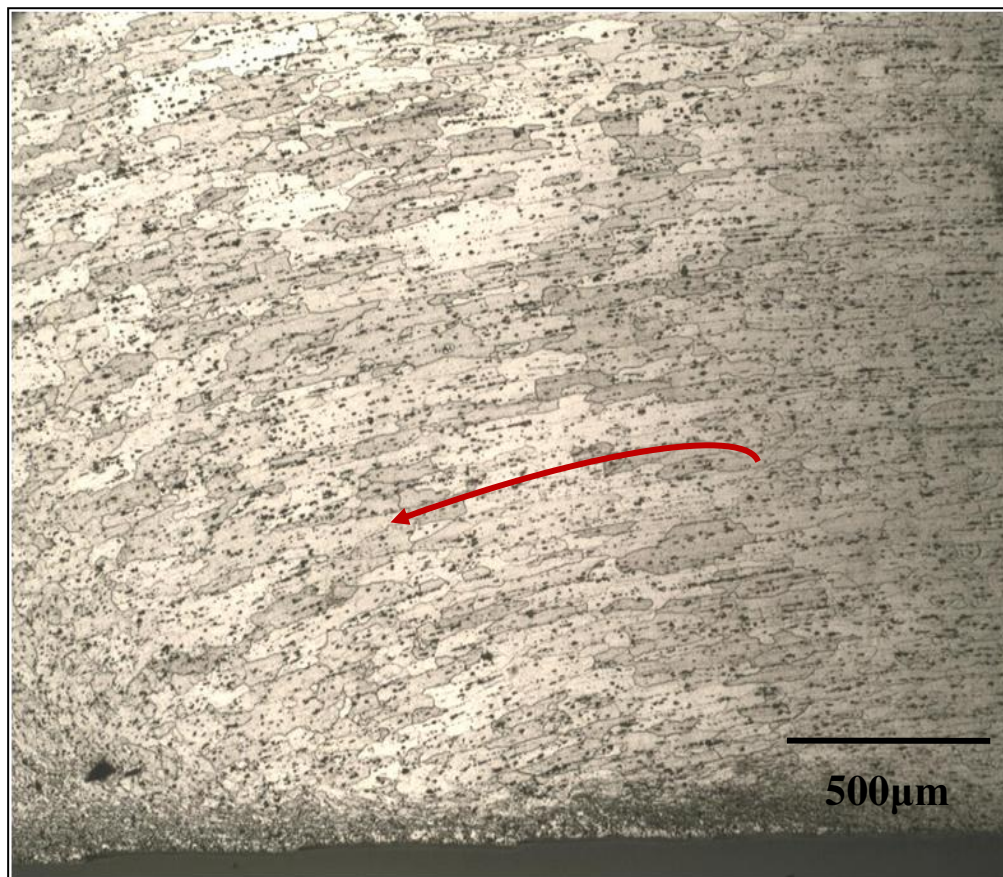


Figure 68: Advancing bottom shoulder thermo-mechanically affected zone microstructure, Sample 5. The microstructure in this region exhibits deformed and bent grains, toward the tool shoulder (red arrow). The advancing side is shown on the right side of the micrograph. Dix-Keller etchant.



A comparison between the fine and recrystallized nugget microstructure and the deformed grains observed in the TMAZ is shown in Figure 69 and Figure 70. The nugget region is shown on the left side of the micrographs

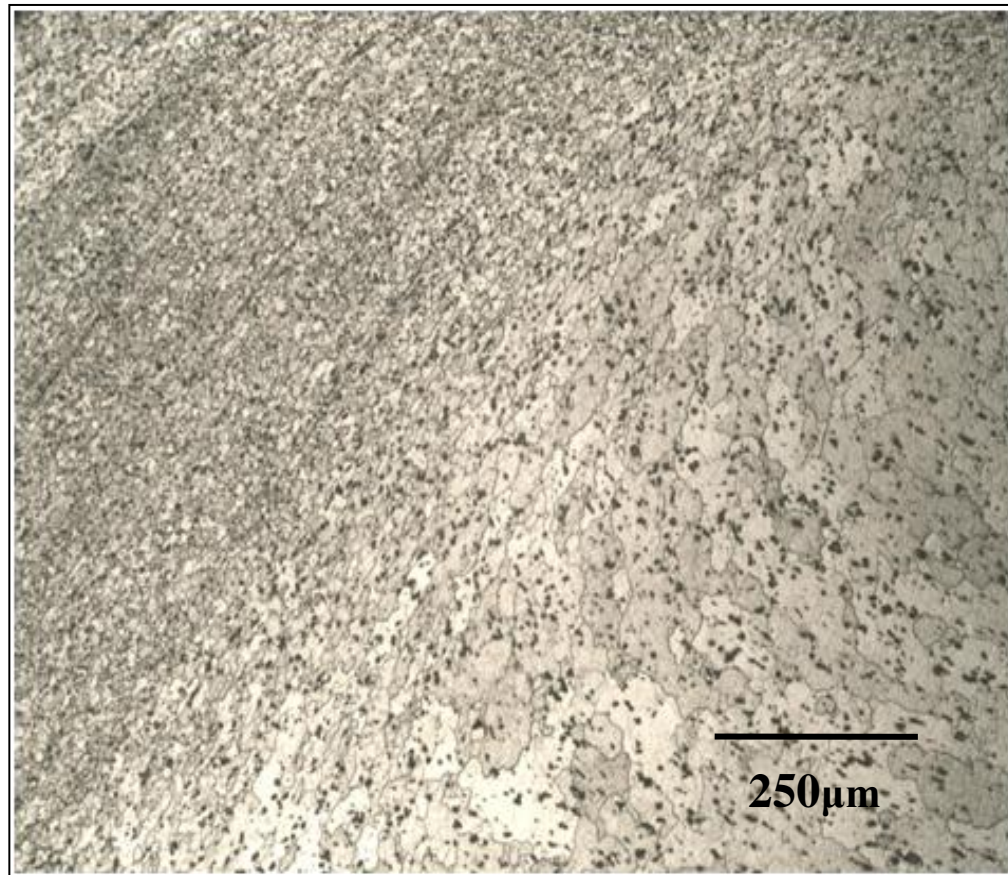


Figure 69: Comparison between the nugget and the thermo-mechanically affected zone microstructures near the top shoulder, Sample 5. The micrograph presents the TMAZ deformed and rotated grains (right) and the fine, recrystallized nugget microstructure (left). Dix-Keller etchant.

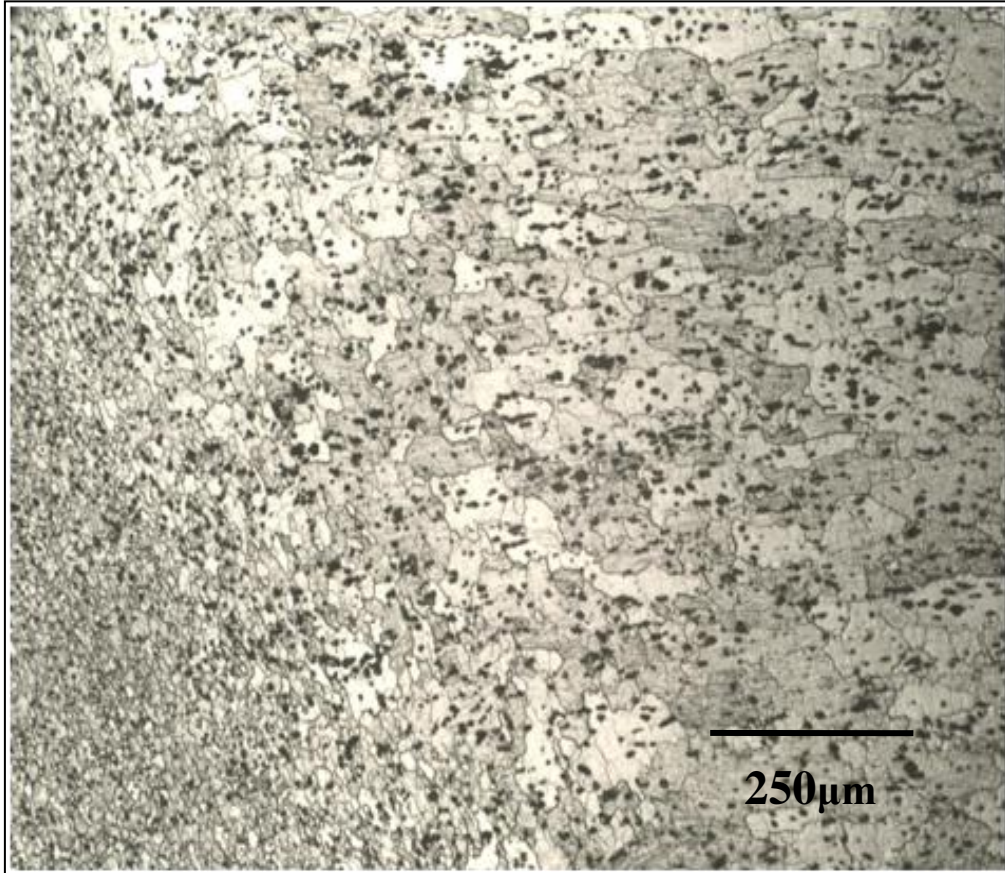


Figure 70: Nugget-TMAZ microstructure, near the bottom shoulder from Sample 10. The nugget microstructure (left bottom corner) exhibits fine, equiaxed grains, whereas, the TMAZ microstructure (right) is characterized by deformed grains. Dix-Keller etchant.

The heat-affected zone is located between the TMAZ and the base metal. All samples fabricated for this study exhibited a HAZ microstructure (advancing and retreating sides) similar to the base metal microstructure, consisting of elongated grains. However, an increase in grain diameter was observed, the average HAZ grain size was estimated to be 97  $\mu\text{m}$ ., compared to 64  $\mu\text{m}$  for the base metal. Representative micrographs from the HAZ microstructure are presented in Figure 71 to Figure 74 for the advancing side and on Figure 75 to Figure 78 for the retreating side.

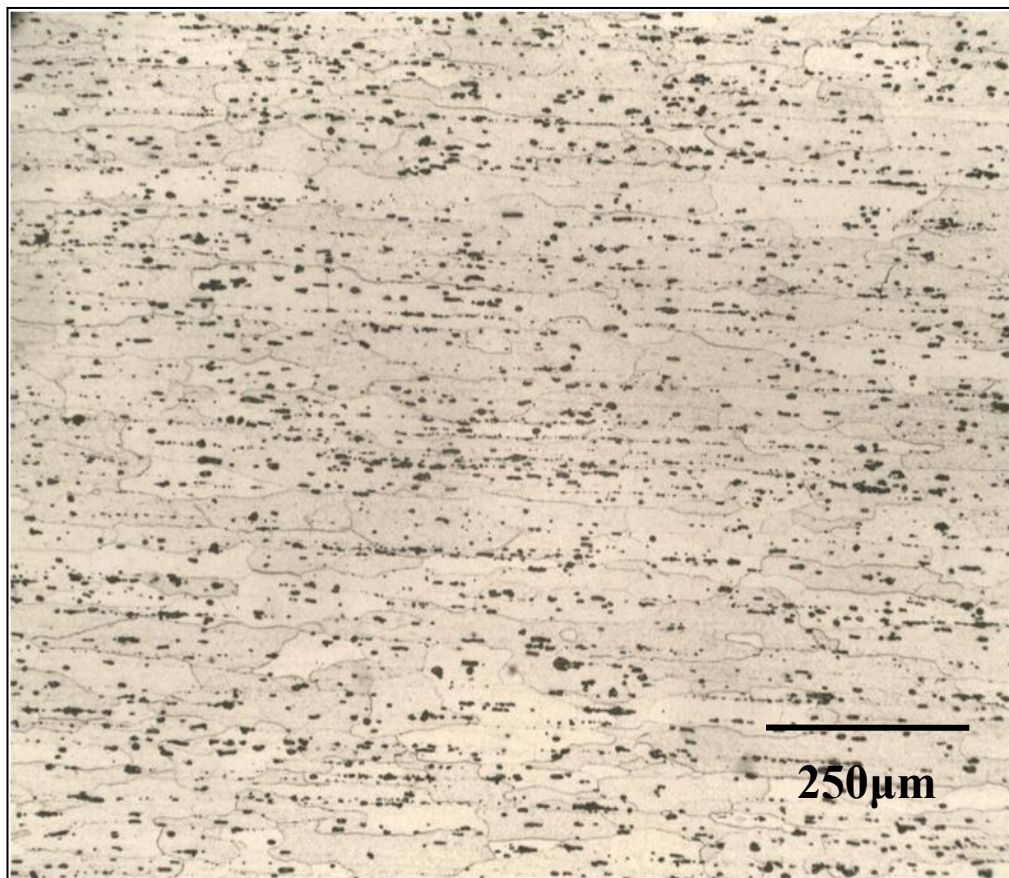


Figure 71: Representative advancing side heat-affected zone microstructure, Sample14. Dix-Keller etchant.



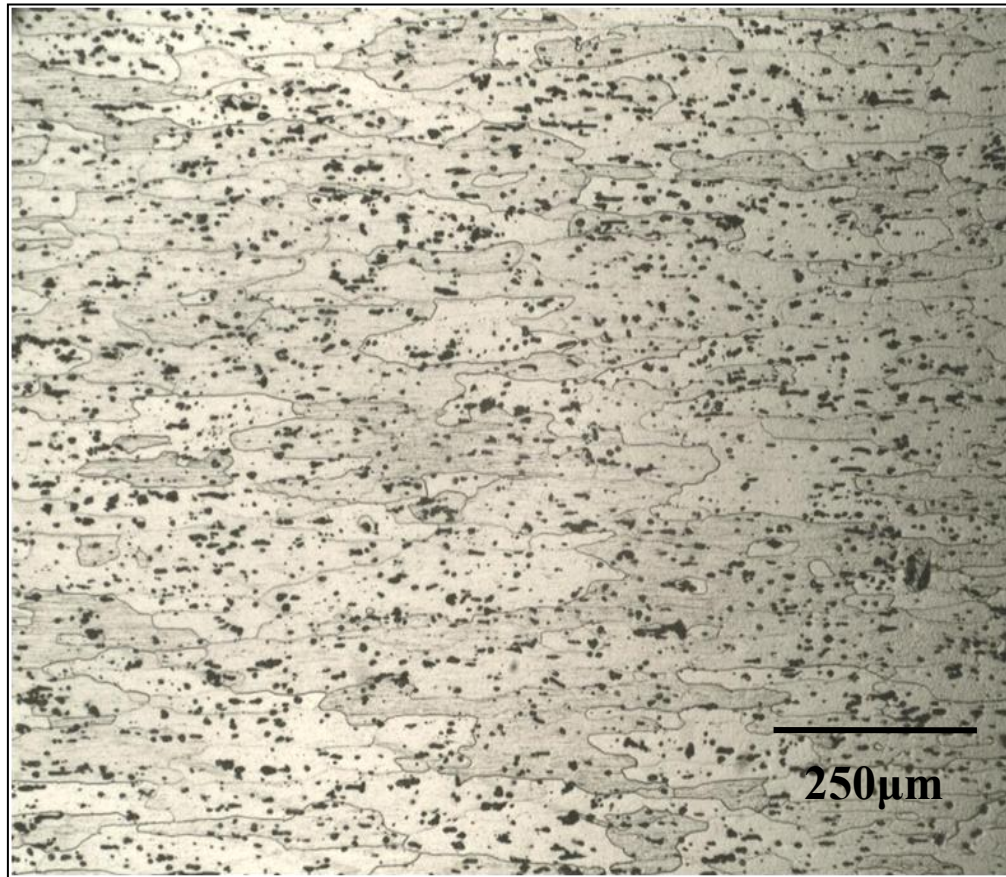


Figure 72: Representative advancing side heat-affected zone microstructure, Sample 10. Dix-Keller etchant.

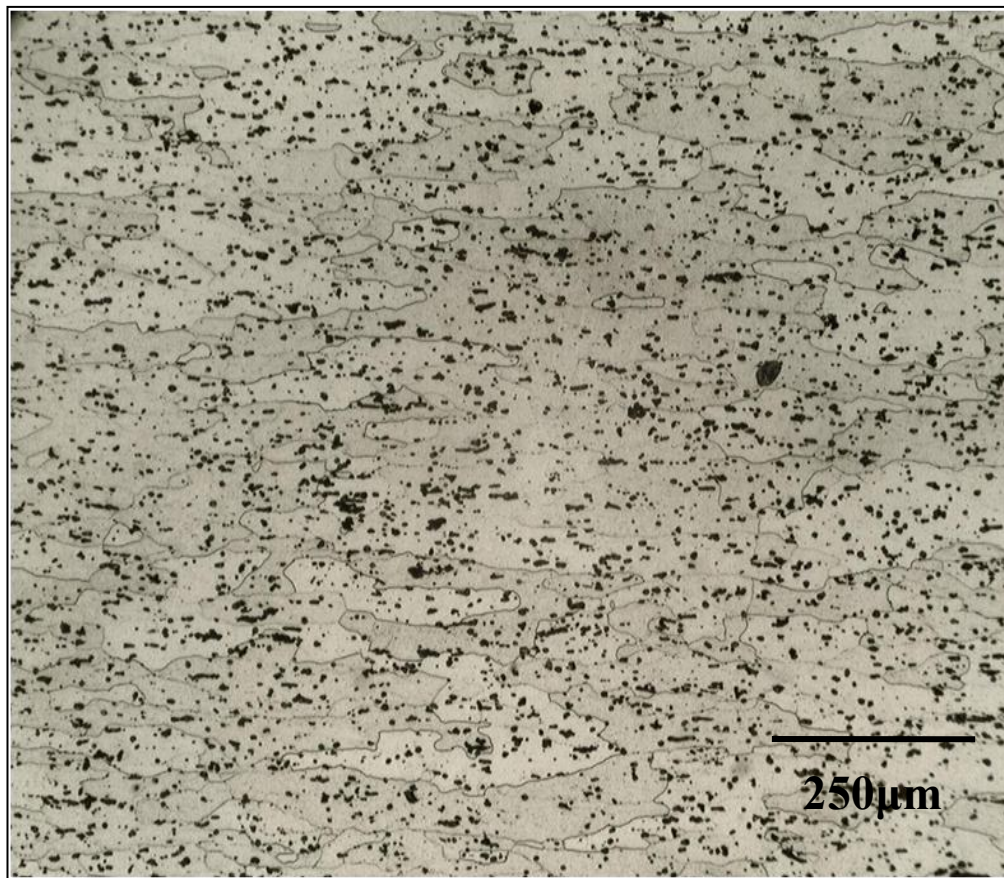


Figure 73: Representative advancing side heat-affected zone microstructure, Sample 9. Dix-Keller etchant.

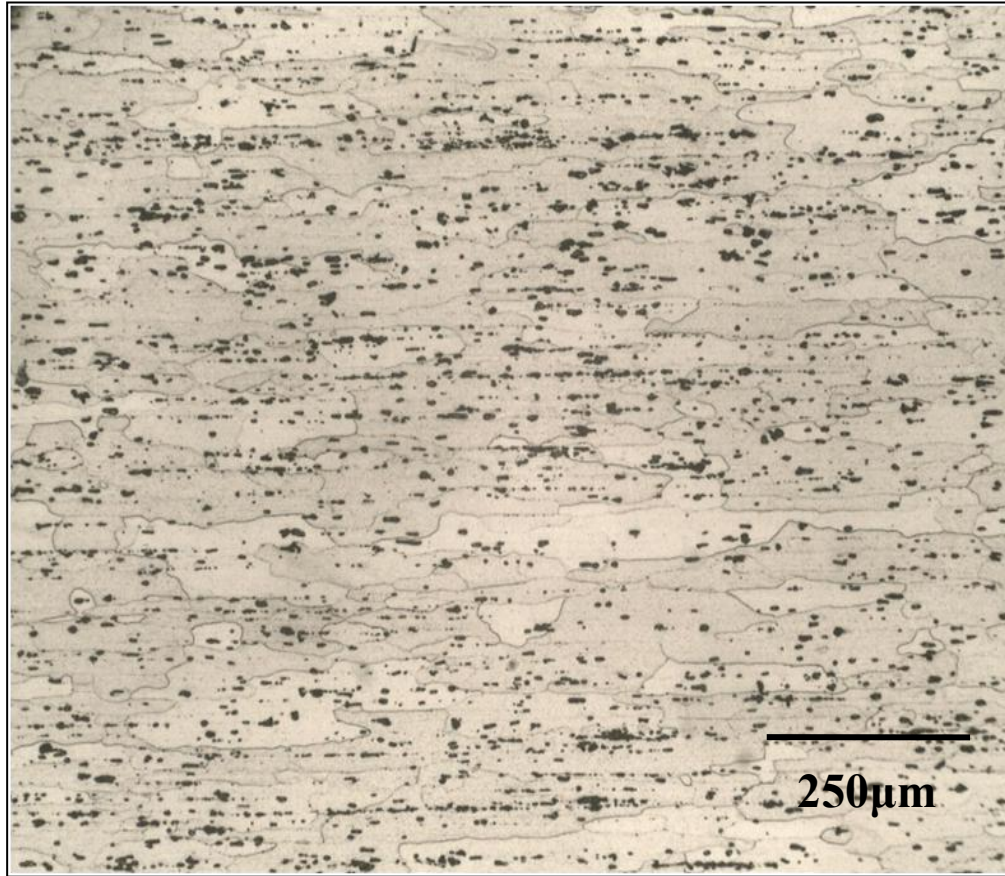


Figure 74: Representative advancing side heat-affected zone microstructure, Sample 8. Dix-Keller etchant.



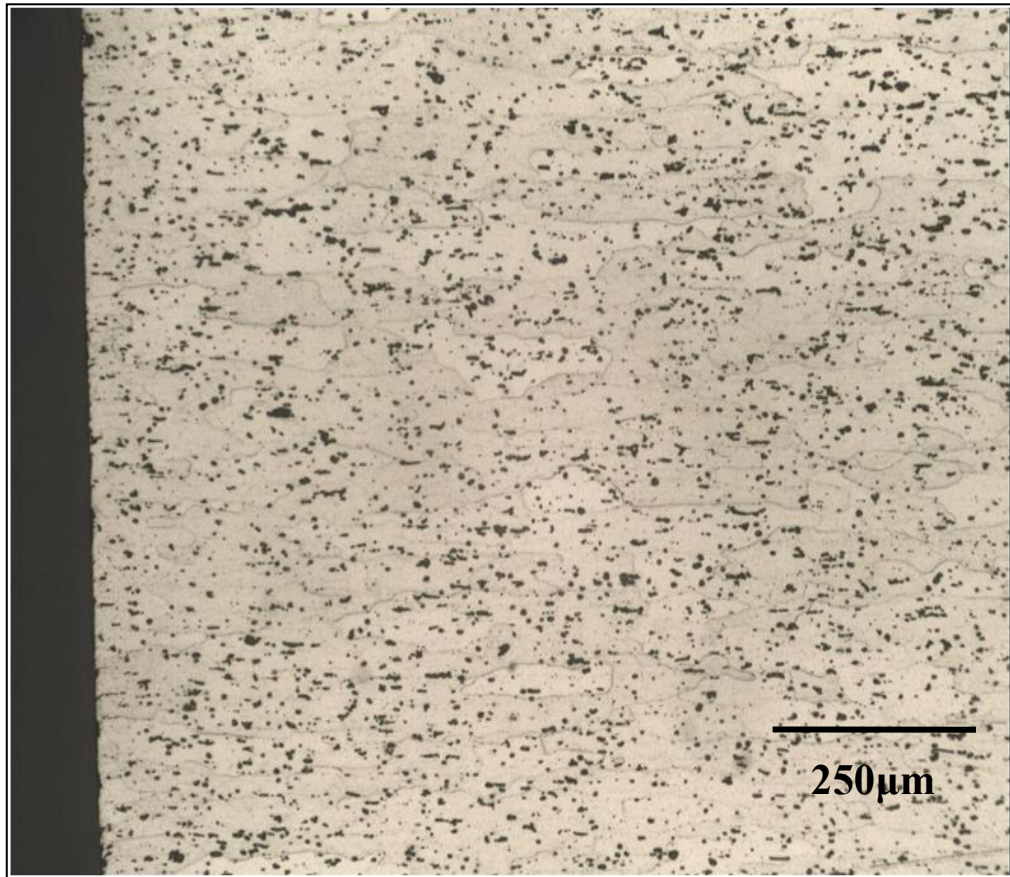


Figure 75: Representative retreating side heat-affected zone microstructure, Sample 14. Dix-Keller etchant.

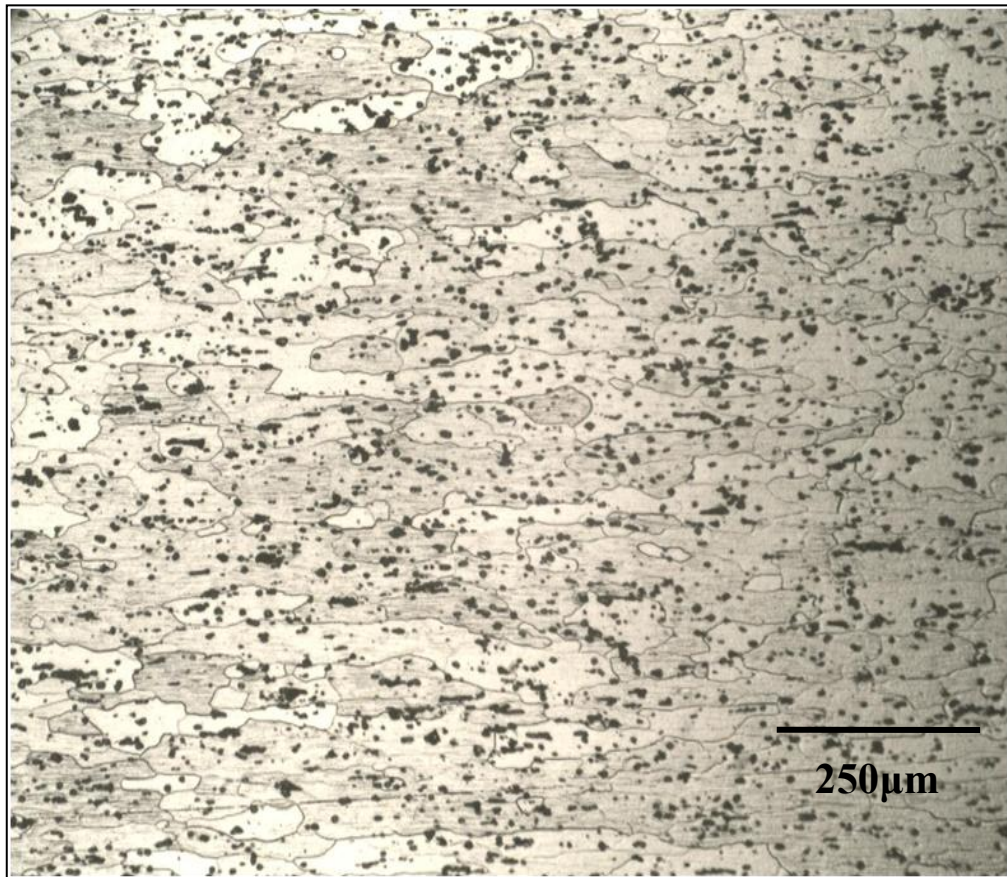


Figure 76: Representative retreating side heat-affected zone microstructure, Sample 10. Dix-Keller etchant.

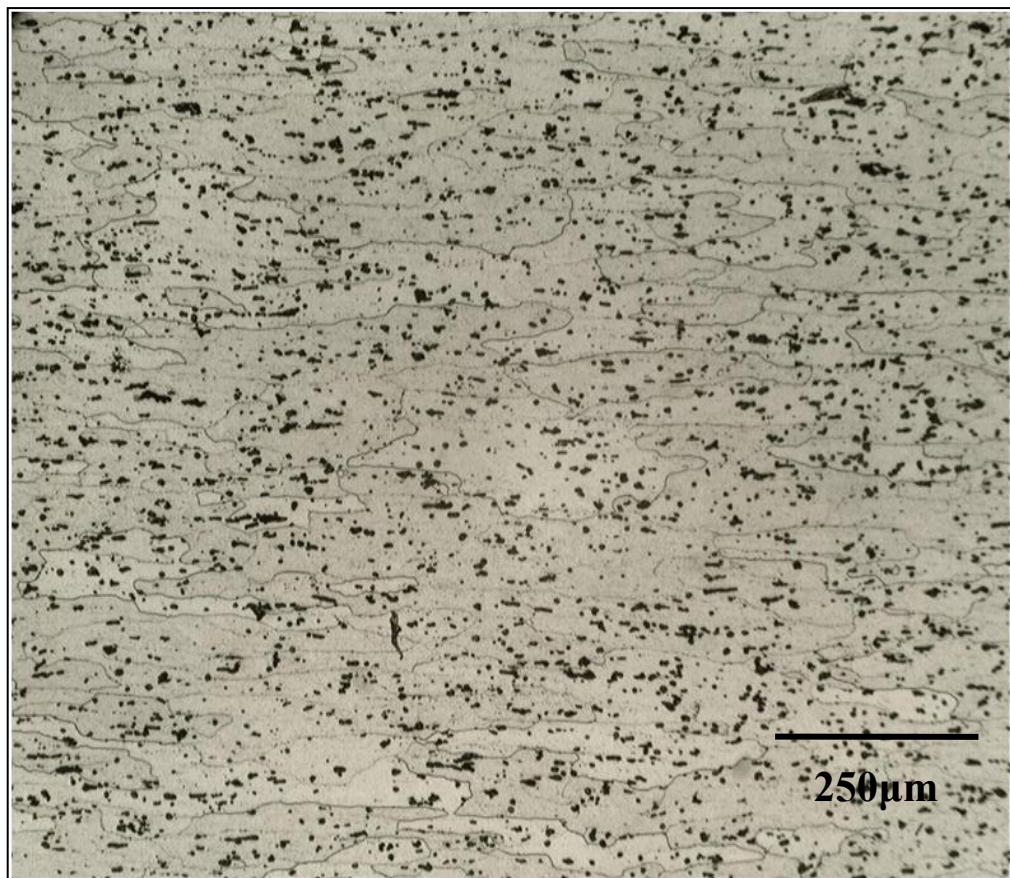


Figure 77: Representative retreating side heat-affected zone microstructure, Sample 9. Dix-Keller etchant.



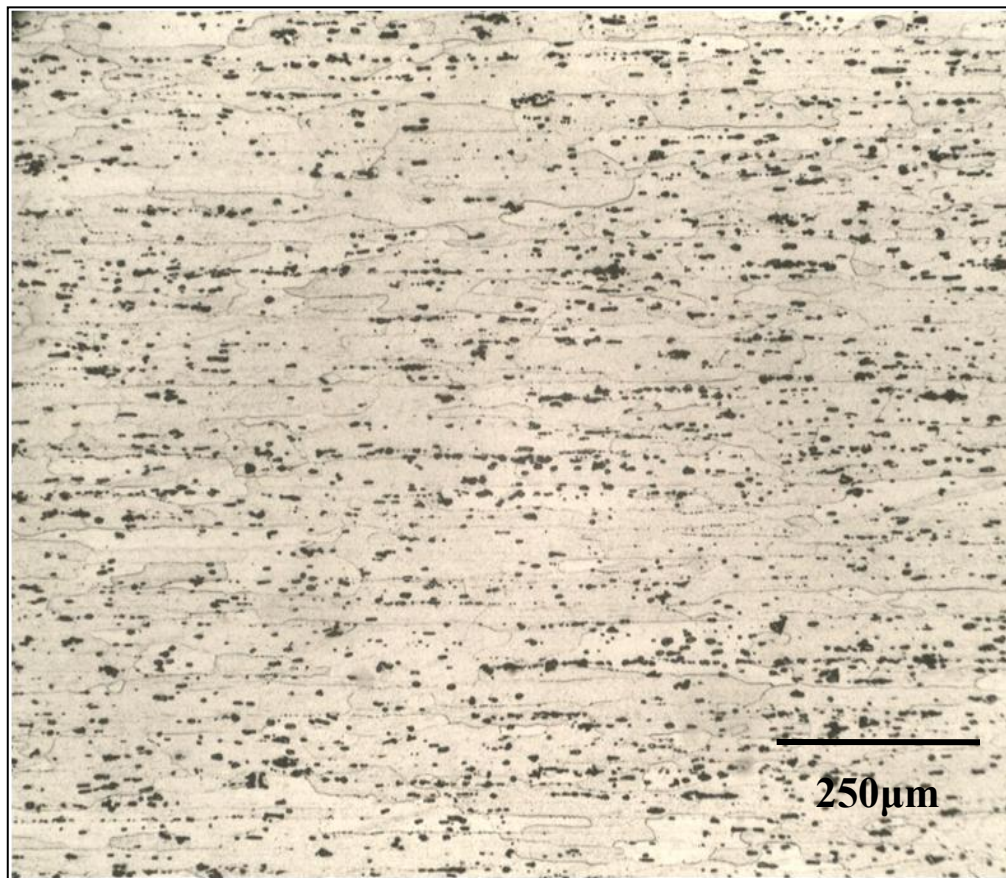


Figure 78: Representative retreating side heat-affected zone microstructure, Sample 8. Dix-Keller etchant.

The base metal microstructure consists of elongated grains as a result of the rolling process. The average grain diameter on the base metal is about 64  $\mu\text{m}$ . The base metal microstructure is presented in Figure 79 and Figure 80.

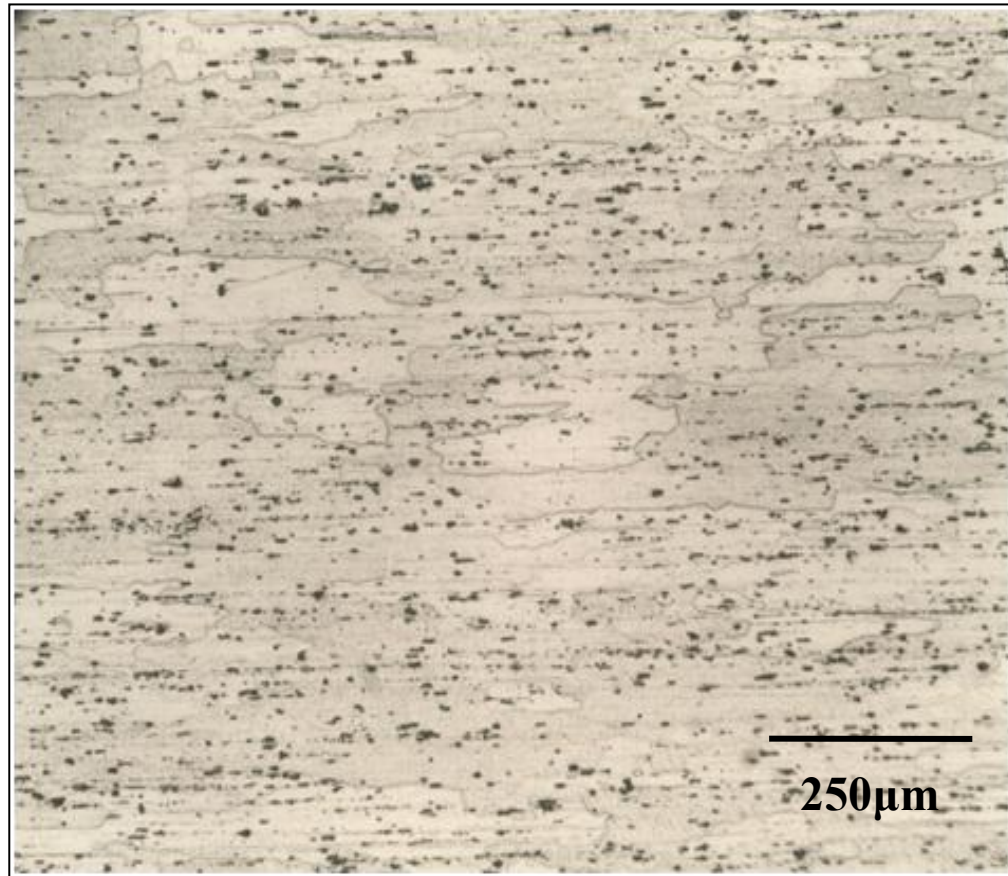


Figure 79: Parent metal microstructure. The base metal microstructure consists of elongated grains due to the rolling process. Dix-Keller etchant.



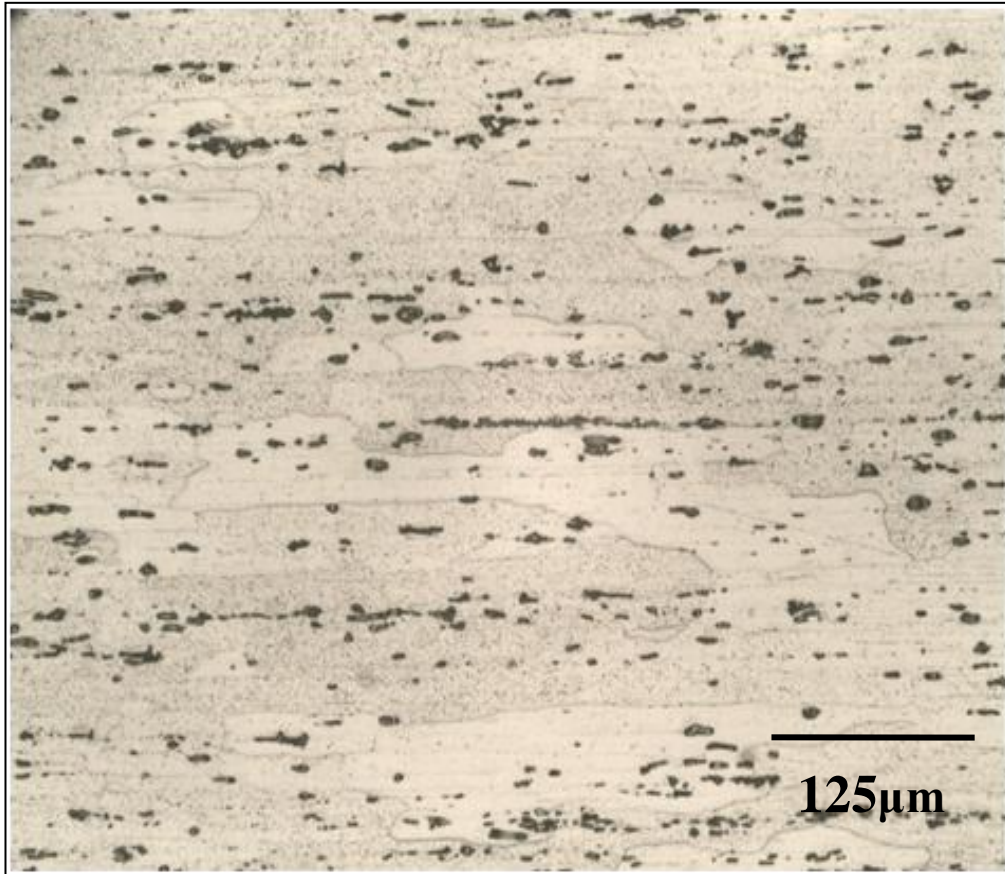


Figure 80: Parent metal microstructure. The base metal microstructure consists of elongated grains due to the rolling process. Dix-Keller etchant.

### 3.4 SELF-REACTING FRICTION STIR WELDING DEFECTS

The main metallurgical discontinuities found in this study were the lazy S defect and voids. The lazy S defect is an artifact left over from the oxides and other impurities present on the faying surfaces to be welded. Figure 81 shows a micrograph from Sample 7, which exhibits a lazy-s defect in the nugget region extending from the bottom shoulder to the top shoulder; voids were observed in nugget zone on the advancing side. The advancing side is shown on the right side of the micrograph.

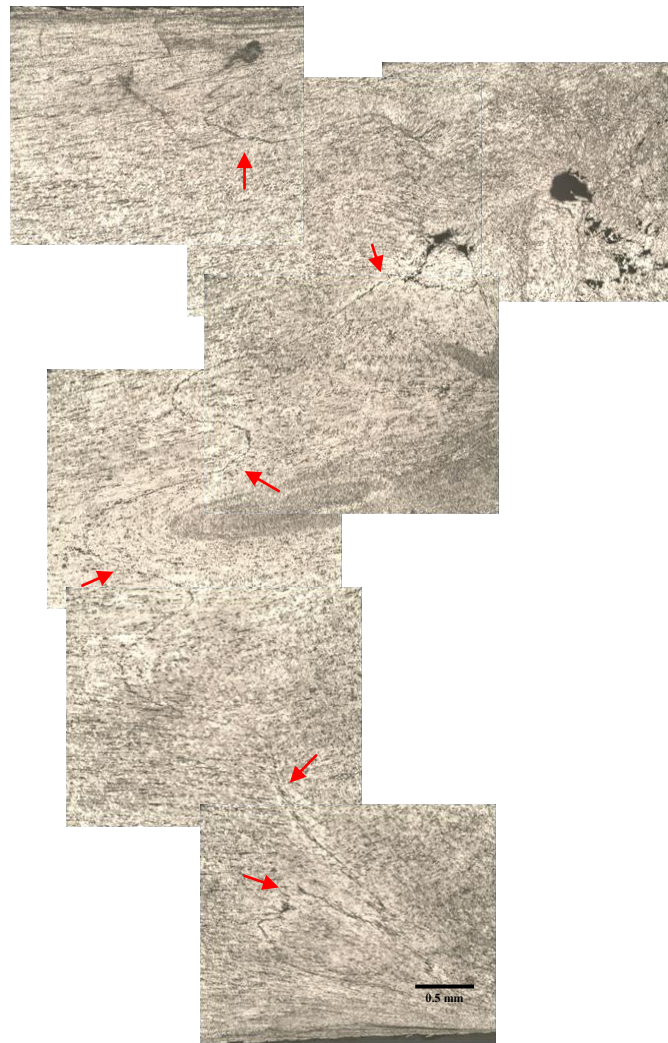


Figure 81: Lazy S defect and voids. The lazy S defect (indicated by arrows) and voids are observed in the nugget region of a self-reacting friction stir weld. The advancing side is shown on the right side of the micrograph.

### 3.4.1 Lazy S Defect

The lazy S defect was detected on the weld nugget region, extending from the bottom shoulder to the top shoulder. Micrographs from the samples that exhibited the lazy S defect are presented in Figure 82 to Figure 85. Each figure presents the lazy S micrographs as function of process parameters. The gray boxes indicates no lazy S defect was produced.

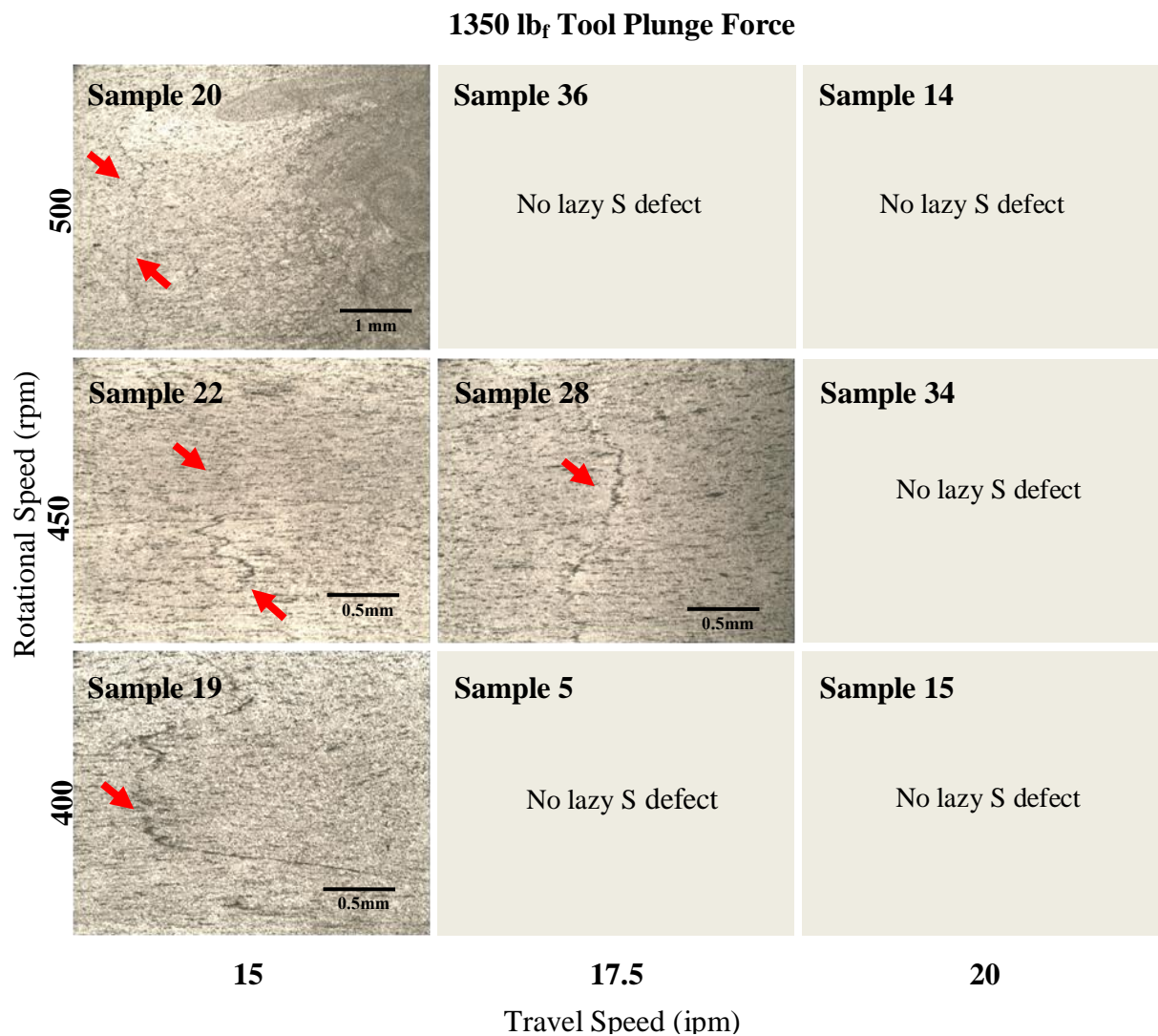


Figure 82: Lazy S defect s for the 1350 lb<sub>f</sub> plunge force. Welds that exhibited the lazy S defect are listed as function of process parameters.



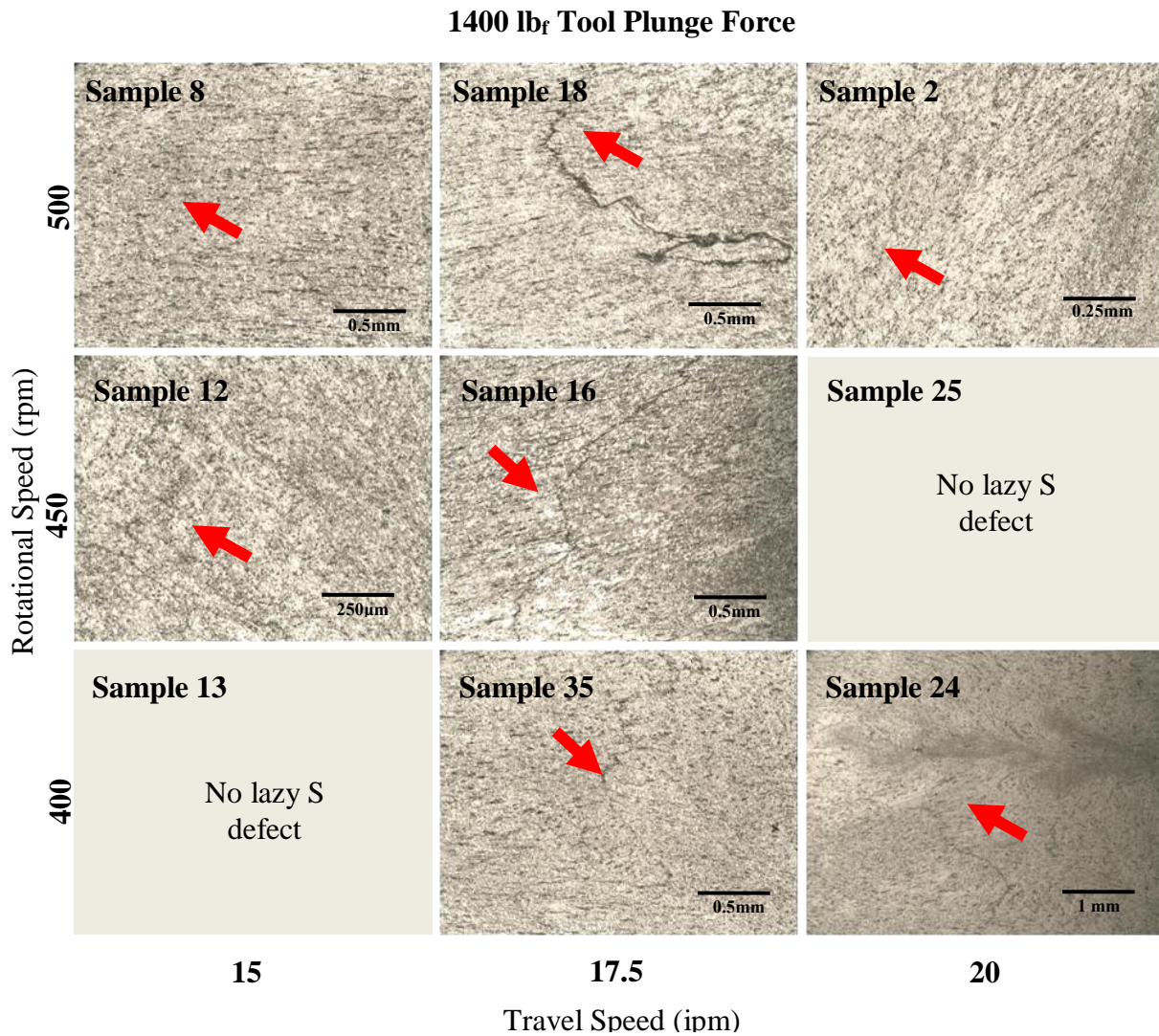


Figure 83: Lazy S defects for the 1400 lb<sub>f</sub> plunge force. Welds that exhibited the lazy S defect are listed as function of process parameters.

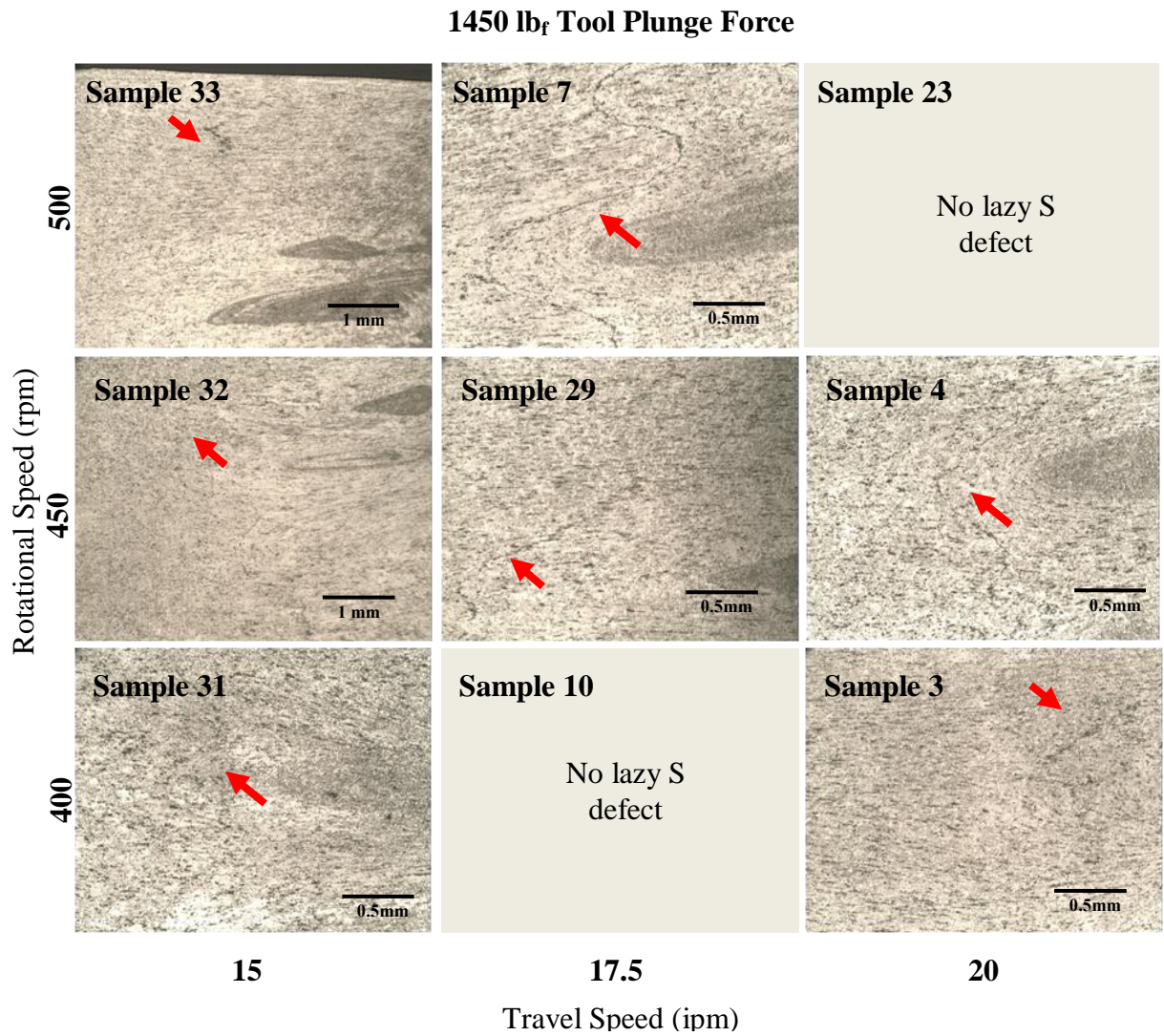


Figure 84: Lazy S defects for the 1450 lb<sub>f</sub> plunge force. Welds that exhibited the lazy S defect are listed as function of process parameters.

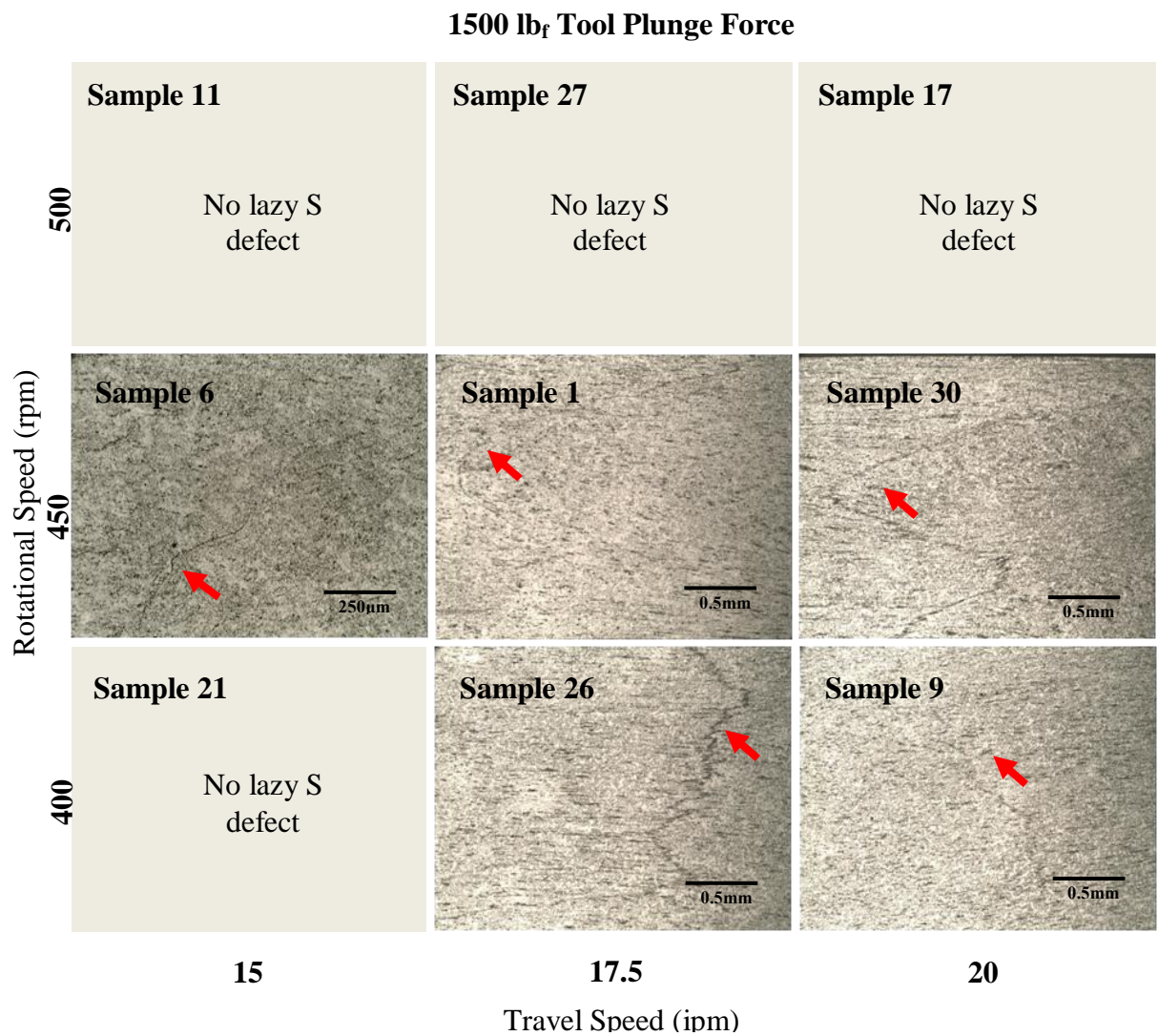


Figure 85: Lazy S defects for the 1500 lb<sub>f</sub> plunge force. Welds that exhibited the lazy S defect are listed as function of process parameters.



The lazy S defect predominated the samples fabricated for this study. Table 11 presents the welds that did not exhibit the lazy S defect. Lazy S defect-free welds were observed at a high tool plunge force (1500 lb<sub>f</sub>) and high rotational speed (500 rpm) and at a low tool plunge force (1350 lb<sub>f</sub>) and high travel speed (20 ipm). Overall, a tool plunge force of 1350 lb<sub>f</sub> produced least number of samples with the lazy S defect; however, no clear relationship between process parameters and the lazy S defect formation was found.

Table 11: Lazy S Defect Free Welds

<b>Weld Number</b>	<b>Rotational Speed (rpm)</b>	<b>Travel Speed (ipm)</b>	<b>Plunge Force (lb<sub>f</sub>)</b>
<b>5</b>	400	17.5	1350
<b>15</b>	400	20	1350
<b>34</b>	450	20	1350
<b>36</b>	500	17.5	1350
<b>24</b>	500	20	1350
<b>13</b>	400	15	1400
<b>25</b>	450	20	1400
<b>10</b>	400	17.5	1450
<b>4</b>	450	20	1450
<b>21</b>	400	15	1500
<b>36</b>	500	15	1500
<b>27</b>	500	17.5	1500
<b>17</b>	500	20	1500

### 3.4.2 Voids

About 60% from all the samples fabricated for this study exhibited voids in the nugget region on the advancing side of the weld. An exemplar macrograph exhibiting the region where voids were found is presented in Figure 86. None of the analyzed samples exhibited significant void formation on the retreating side.

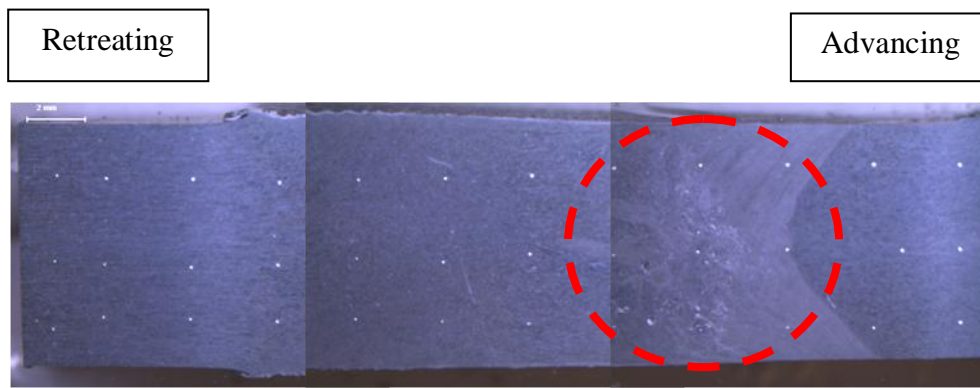


Figure 86: Representative macrograph (Sample 7) from the typical location of voids, which are usually observed on the nugget region on the advancing side (circle)

Void concentration was visually rated on a semi-quantitative scale from 0 to 3. A rating of three indicates the largest voids with the widest distribution; whereas, a rating of zero indicates that no voids were observed. Figure 87 to Figure 90 present exemplar micrographs and descriptions for this void rating scale. Micrographs only exhibit the nugget region on the advancing side, where voids were observed.



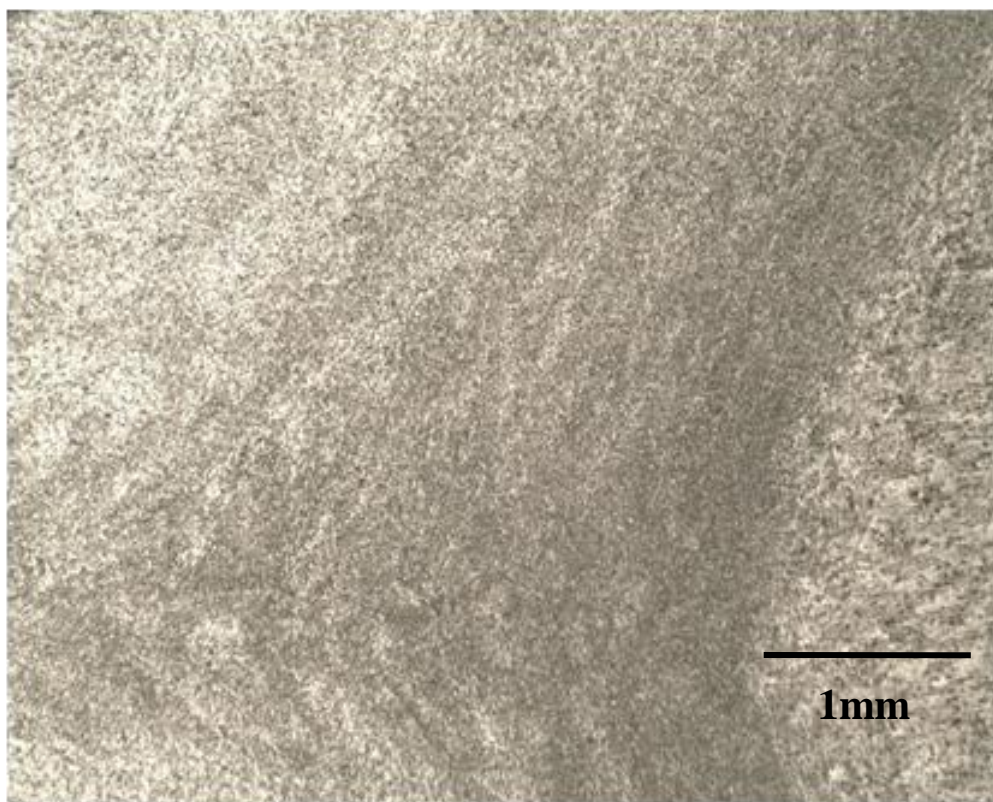


Figure 87: Void concentration 0. No voids are observed (Sample 21).

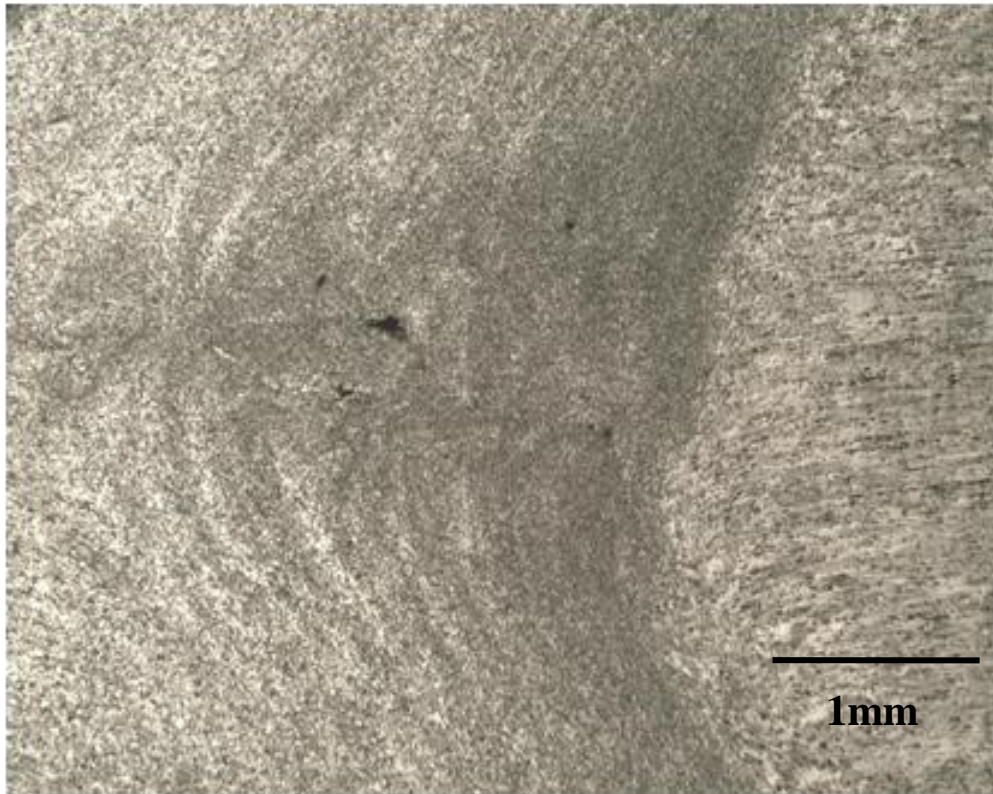


Figure 88: Void concentration 1. Sample 34 represents a void concentration of 1, which is characterized by small voids in the same region.

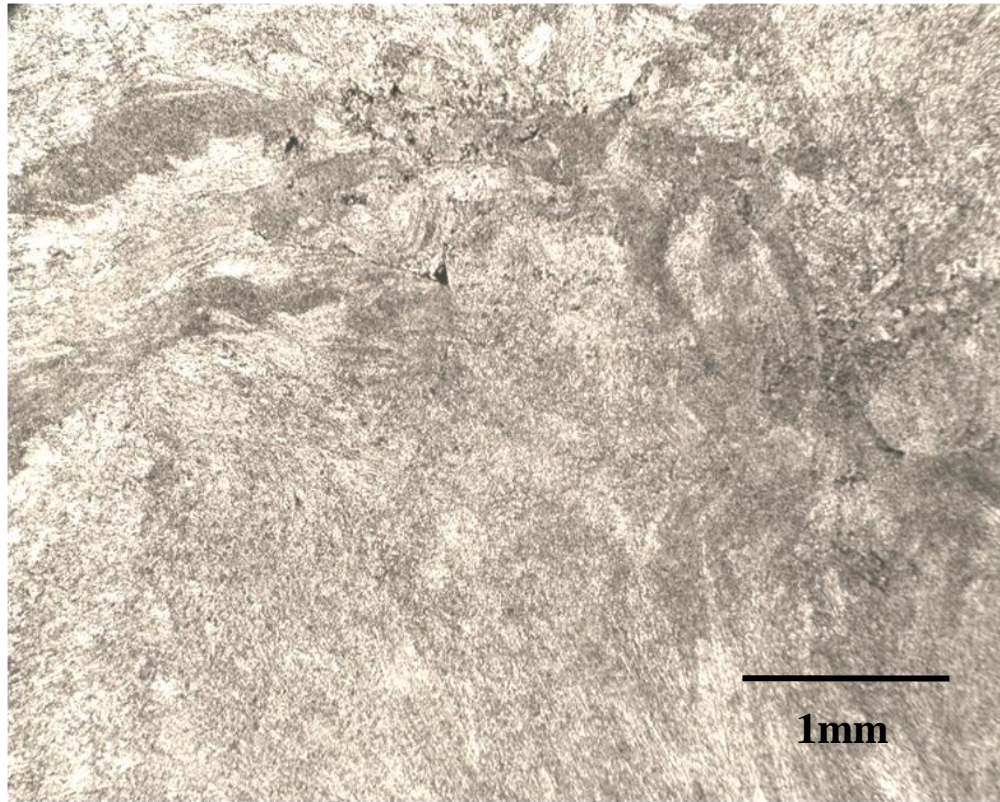


Figure 89: Void concentration 2. Sample 11 represents a void concentration of 2, which is characterized by small voids distributed over larger areas.

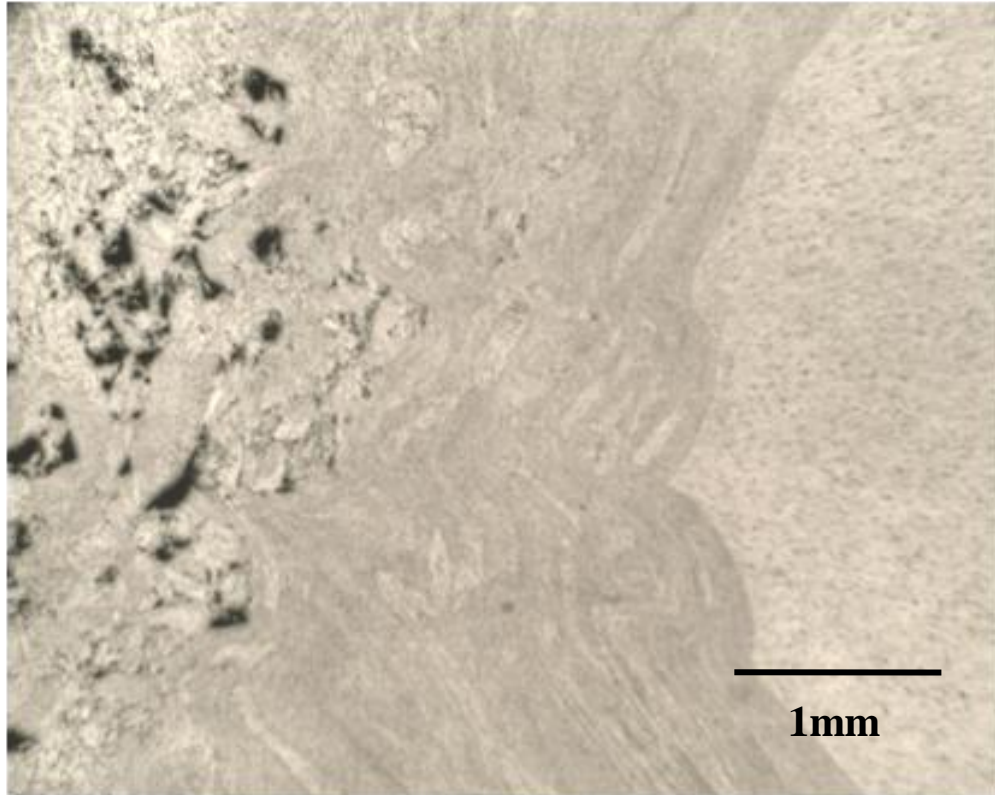


Figure 90: Void concentration 3. Sample 7 represents a void concentration of 3, which is characterized by large voids distributed over larger areas.



Figure 91 to Figure 94 exhibit the void concentration (VC) as function of process parameters for all the samples fabricated in this study. Void concentration was rated as previously discussed.

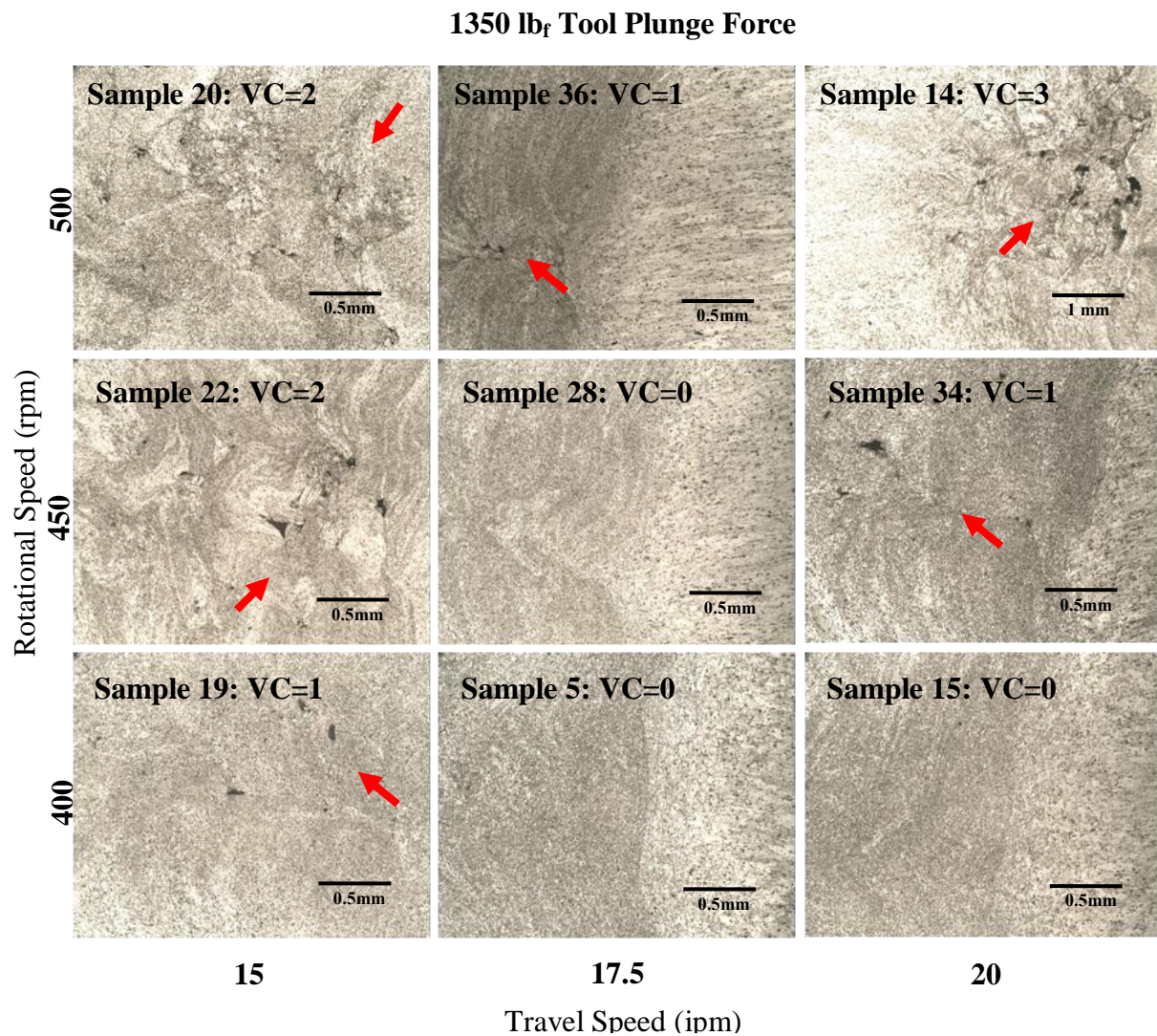


Figure 91: Void concentration for a 1350 lb<sub>f</sub> plunge force. Micrographs exhibit the void concentration on the nugget region, as function of process parameters. Advancing side is on the right side for all micrographs.



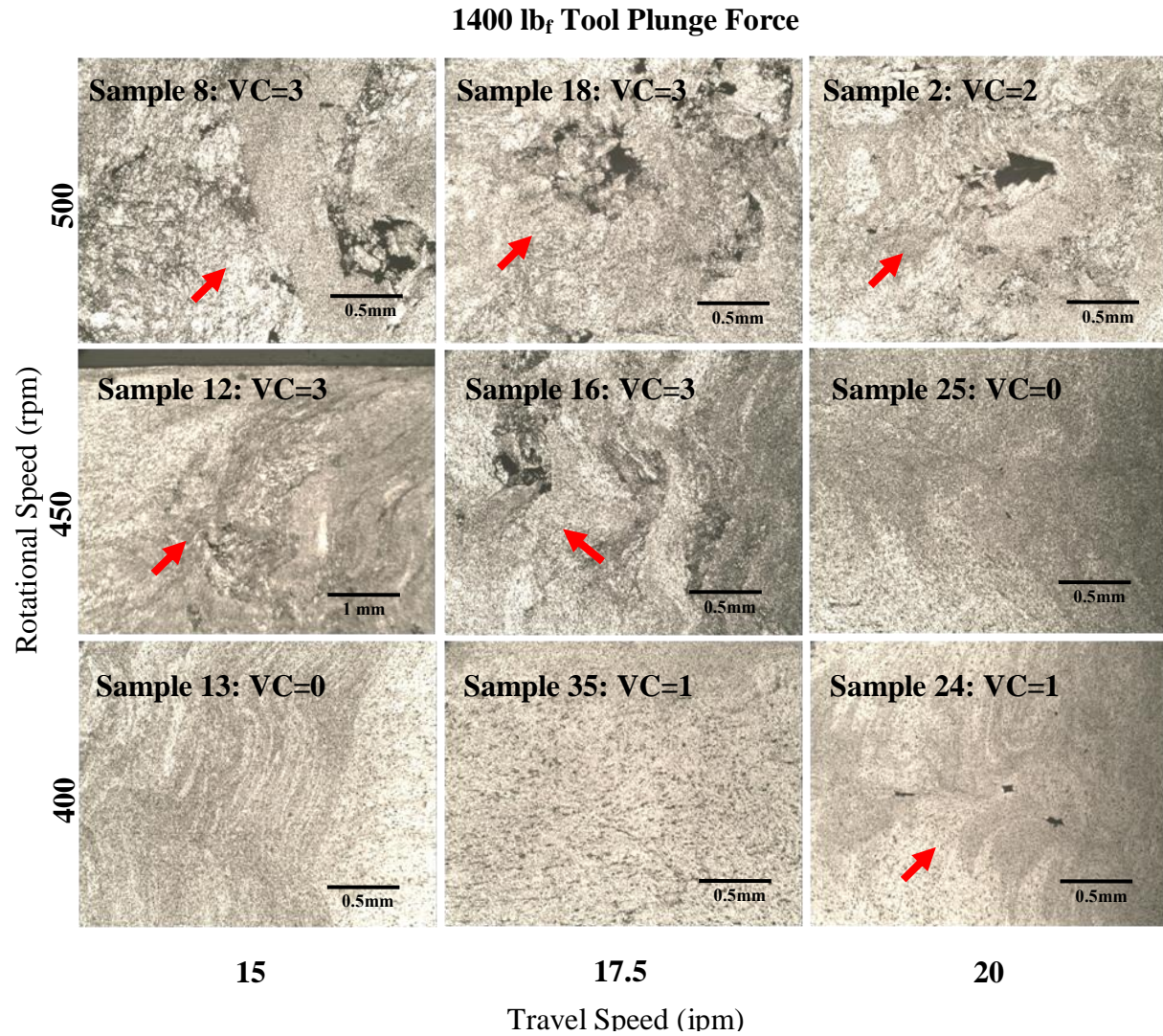


Figure 92: Void concentration for a 1400 lb<sub>f</sub> plunge force. Micrographs exhibit the void concentration on the nugget region, as function of process parameters. Advancing side is on the right side for all micrographs.

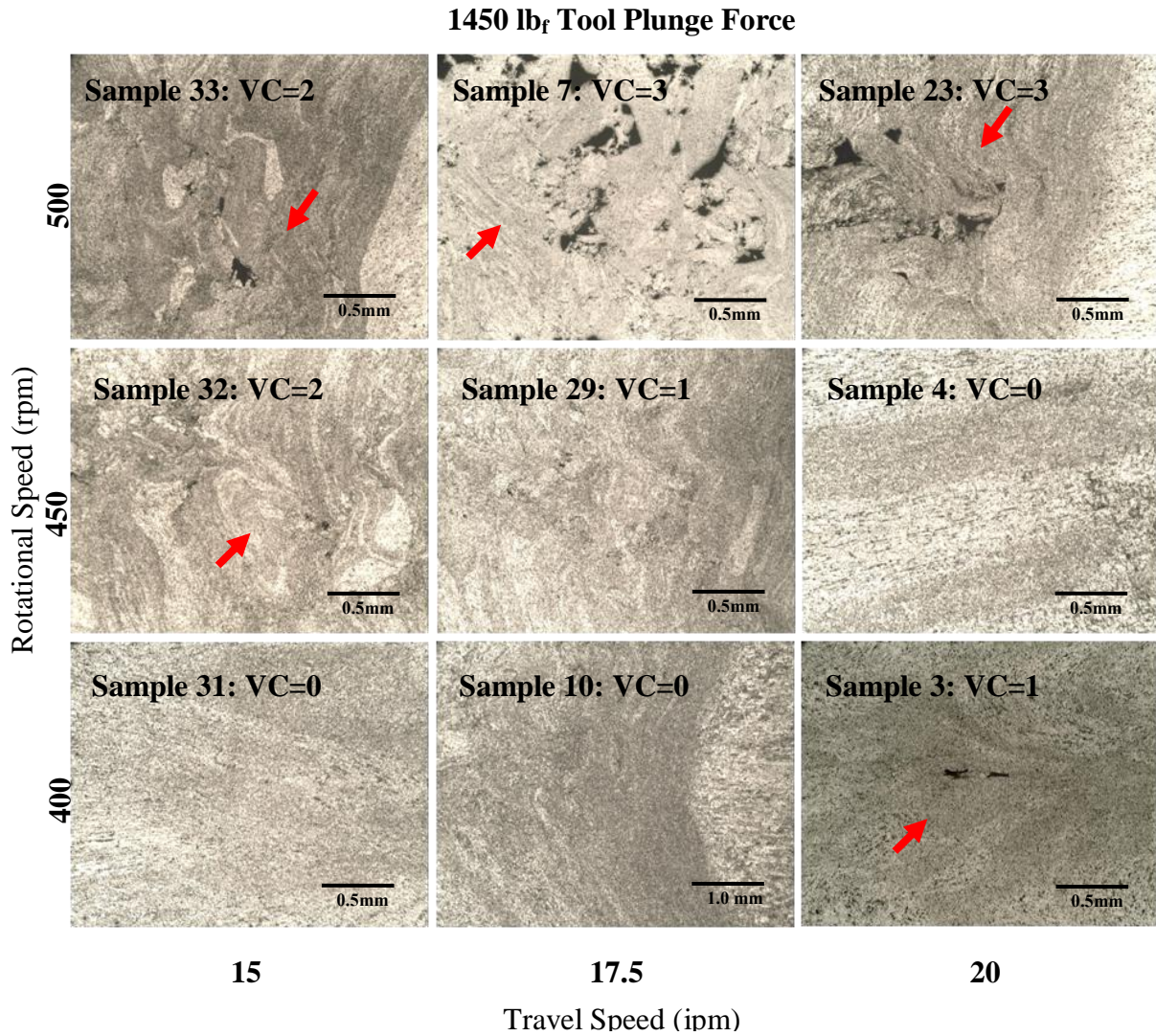


Figure 93: Void concentration for a 1450 lb<sub>f</sub>plunge force. Micrographs exhibit the void concentration on the nugget region, as function of process parameters. Advancing side is on the right side for all micrographs.



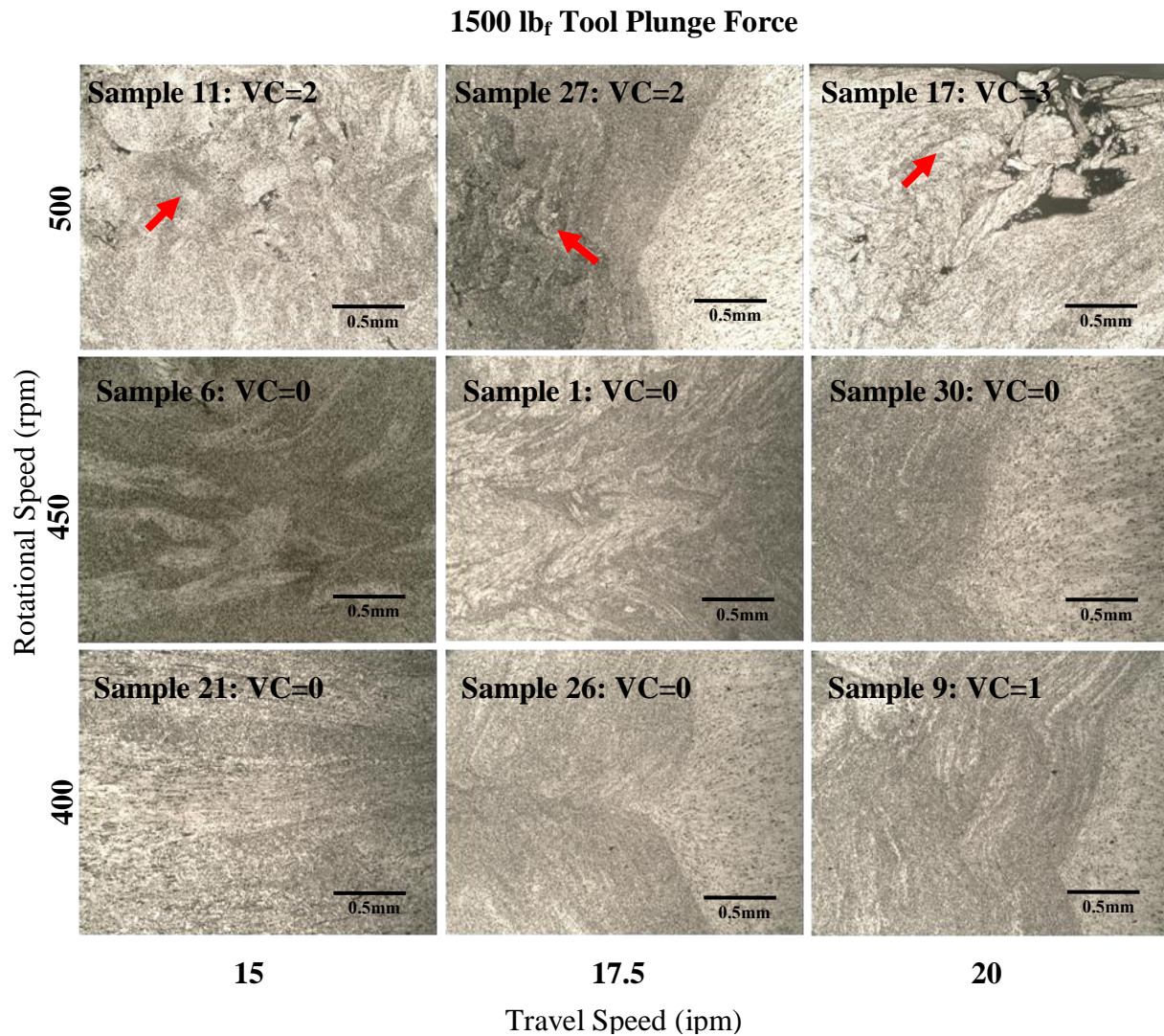


Figure 94: Void concentration for a 1500 lb<sub>f</sub>plunge force. Micrographs exhibit the void concentration on the nugget region, as function of process parameters. Advancing side is on the right side for all micrographs.

For all tool plunge forces, as the rotational speed decreased, the void concentration decreased significantly. A tool plunge force of 1400 lb<sub>f</sub> produced the greatest number of samples with high void concentration, whereas, a tool plunge force of 1500 lb<sub>f</sub> produced the fewest number of samples with high void concentration. Figure 95 presents the main effects plot for void concentration. Rotational speed has the biggest effect on void concentration, as compared to the travel speed and the tool plunge force; the travel speed effect is the least significant. According to the main effects analysis, less void concentration is achieved at a low rotational speed, medium travel speed, and high plunge force (400 rpm/ 17.5 ipm/ 1500 lb<sub>f</sub>). On the other hand, a combination of high rotational speed, low travel speed, and medium-high tool plunge force (500 rpm/ 15 ipm/ 1400 lb<sub>f</sub>) produces severe void concentrations.

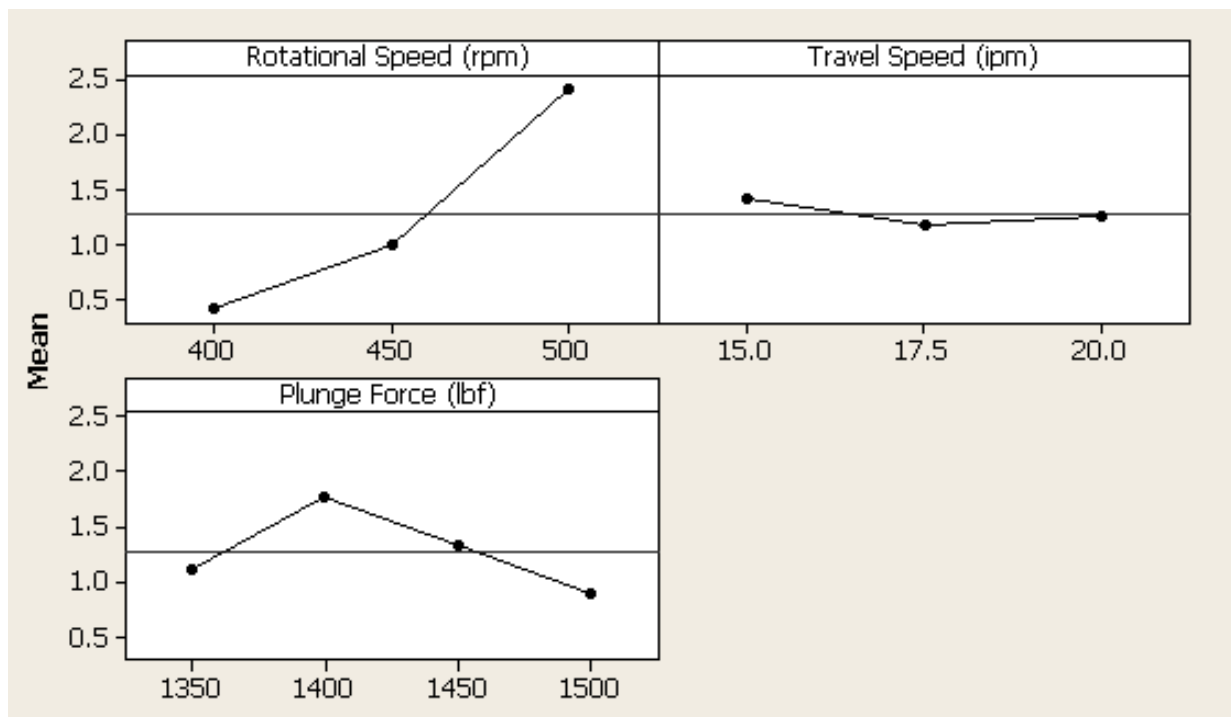


Figure 95: Void concentration main effects plot. The steep line for rotational speed in the main effect plot is indicative of its higher effect on the void concentration, as compared to plunge force and travel speed.

### 3.4.3 Other Metallurgical Observations

A distinctive feature was observed on the weld nugget on the advancing side, in the region near the top and bottom shoulders. The samples that exhibited these metallurgical features (Table 12) were fabricated at low and medium rotational speeds and at medium and high travel speeds. Figure 96 to Figure 102 presents micrographs from the samples that exhibited this defect.

Table 12: Subsurface Discontinuity

<b>Sample Number</b>	<b>Rotational Speed (rpm)</b>	<b>Traverse Speed (ipm)</b>	<b>Plunge Force (lbf)</b>
<b>1</b>	450	17.5	1500
<b>5</b>	400	17.5	1350
<b>10</b>	400	17.5	1450
<b>15</b>	400	20	1350
<b>26</b>	400	17.5	1500
<b>30</b>	450	20	1500



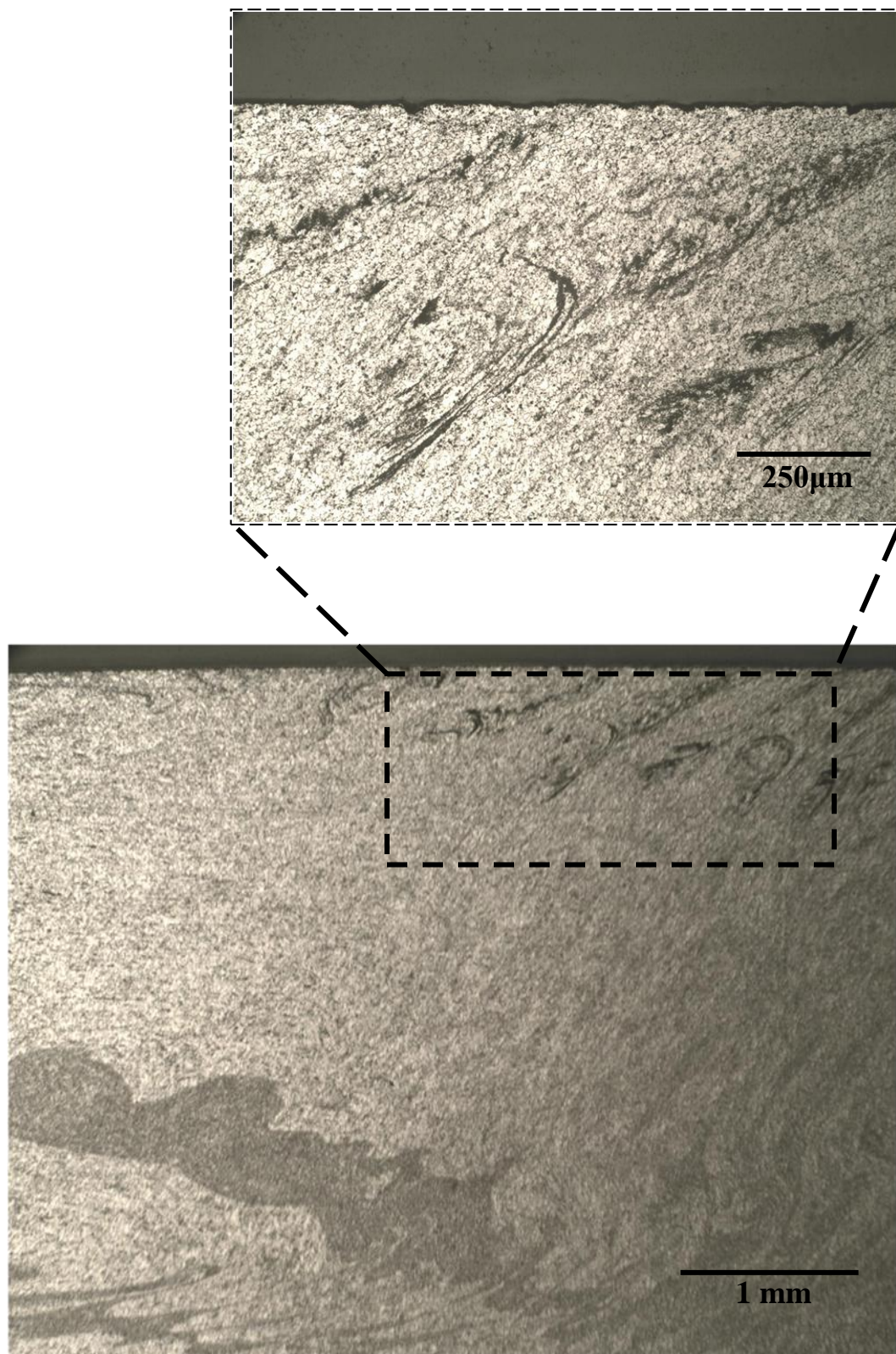


Figure 96: Metallurgical discontinuity observed below the crown of the weld, in Sample 1

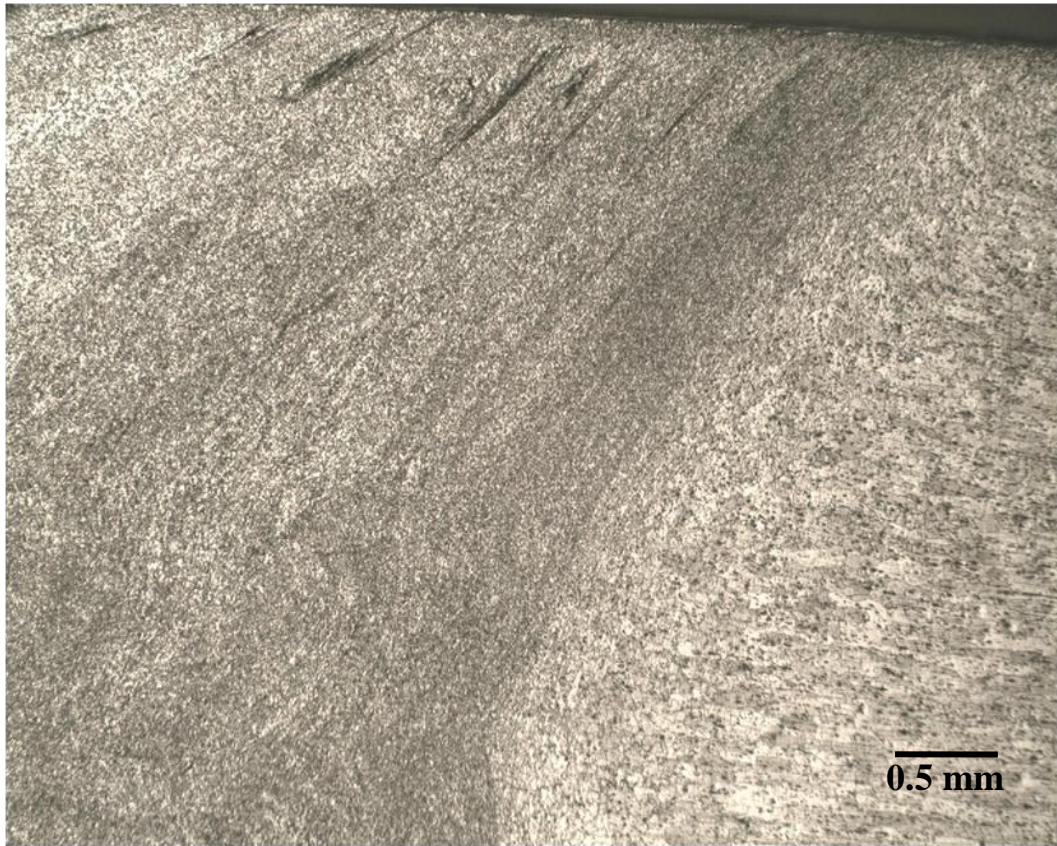


Figure 97: Metallurgical discontinuity observed below the crown of the weld, in Sample 5.



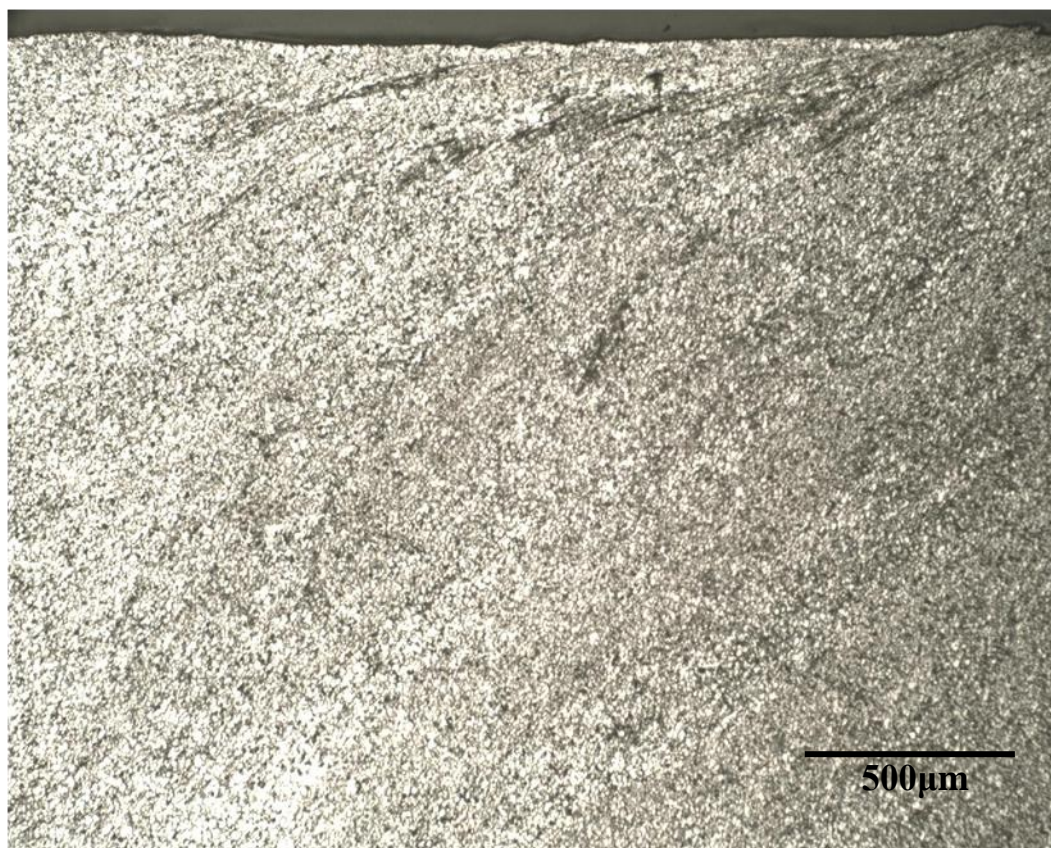


Figure 98: Metallurgical discontinuity observed below the crown of the weld, in Sample 10.

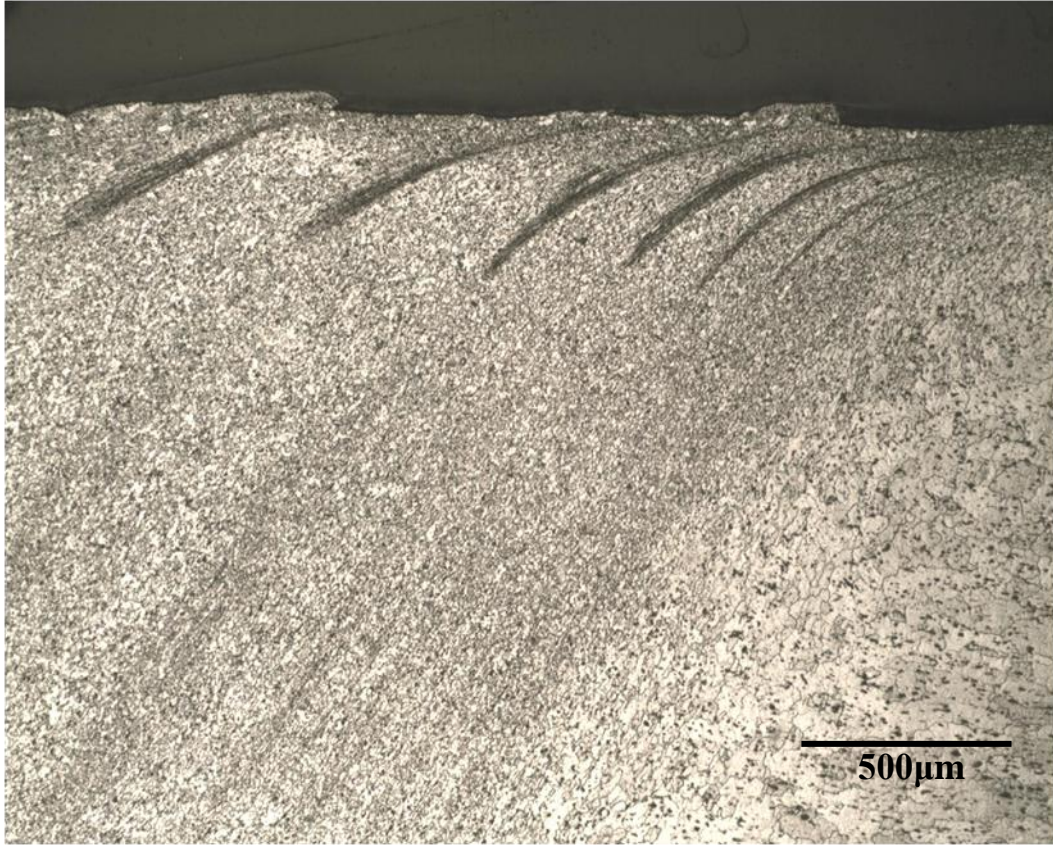


Figure 99: Metallurgical discontinuity observed below the crown of the weld, in Sample 15



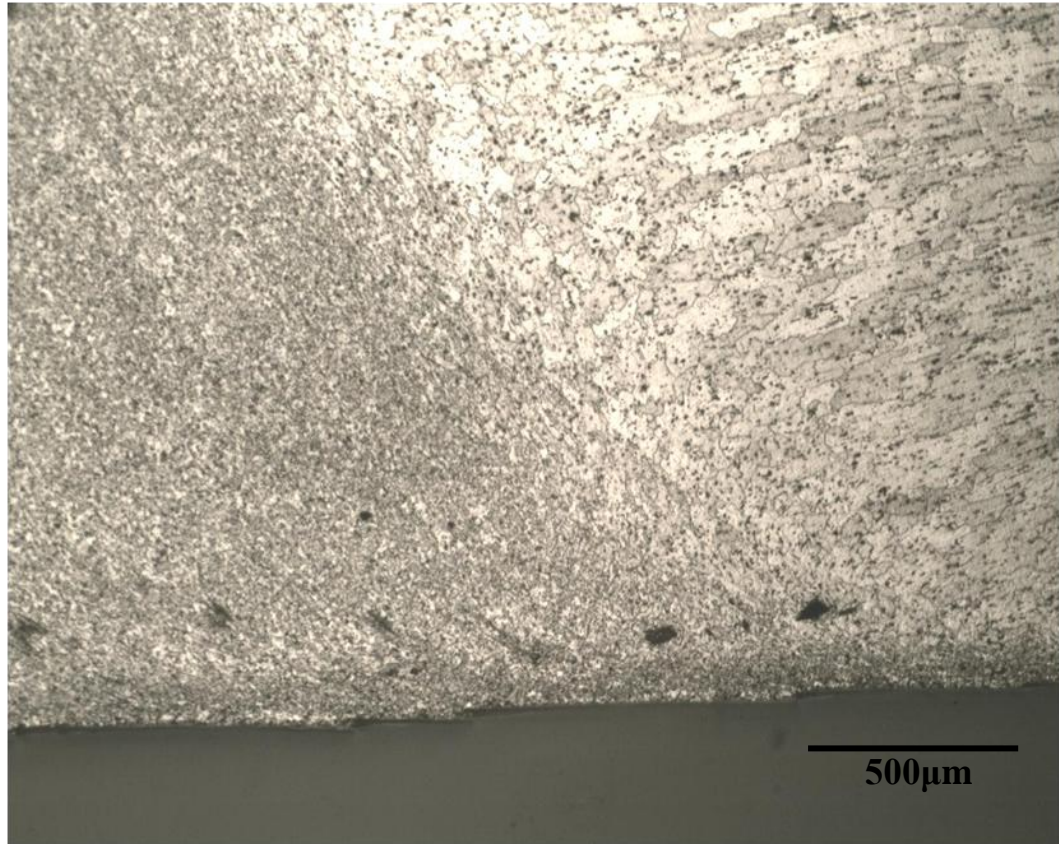


Figure 100: Metallurgical discontinuity observed below the root of the weld (Sample 15).



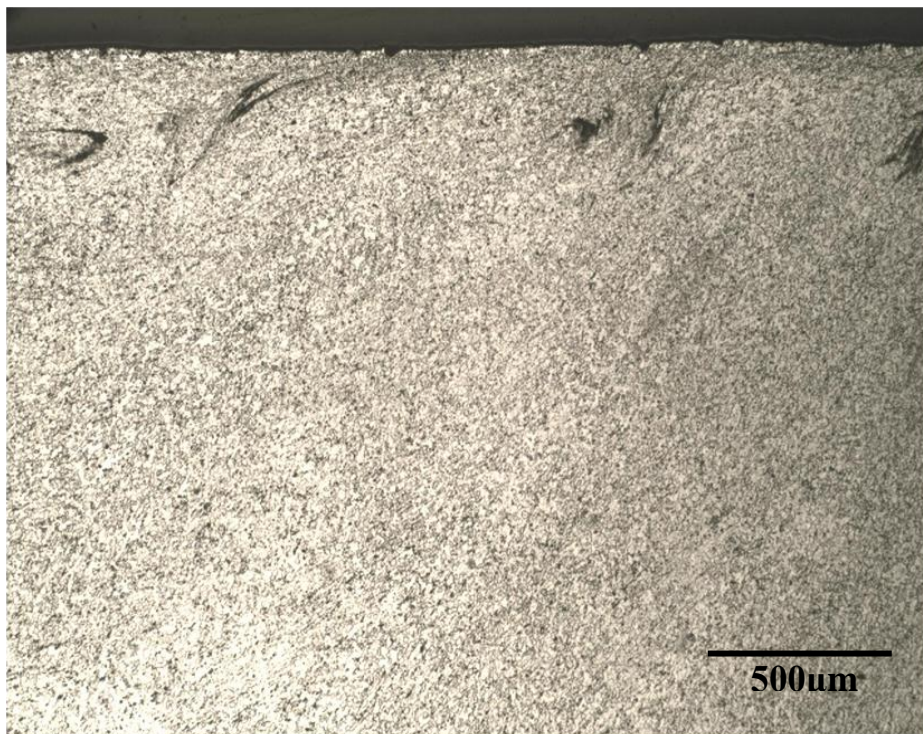
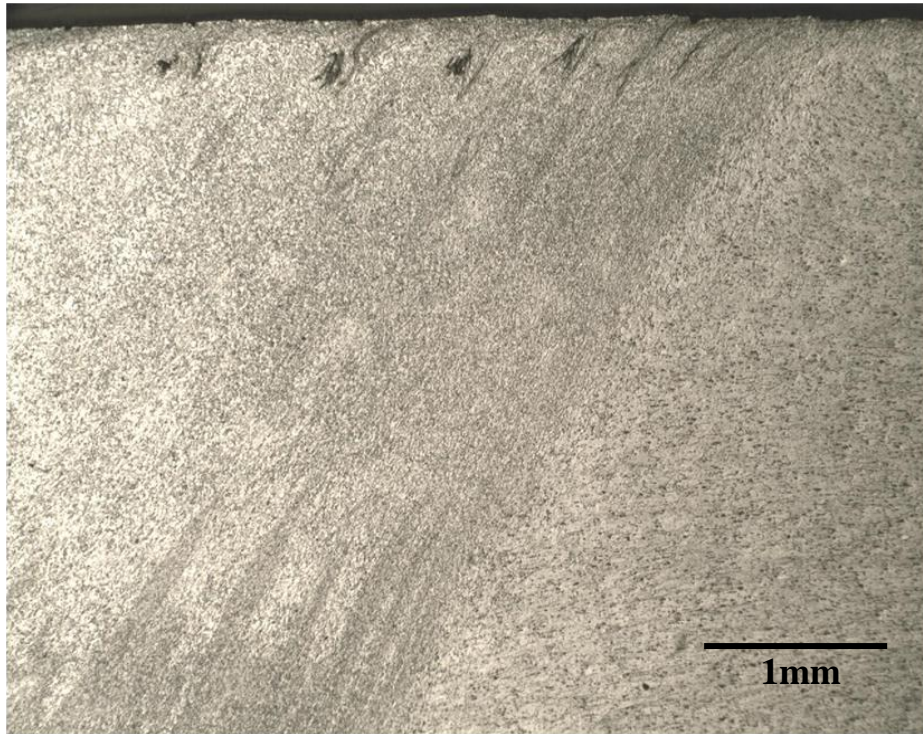


Figure 101: Metallurgical discontinuity observed below the crown of the weld (Sample 26).



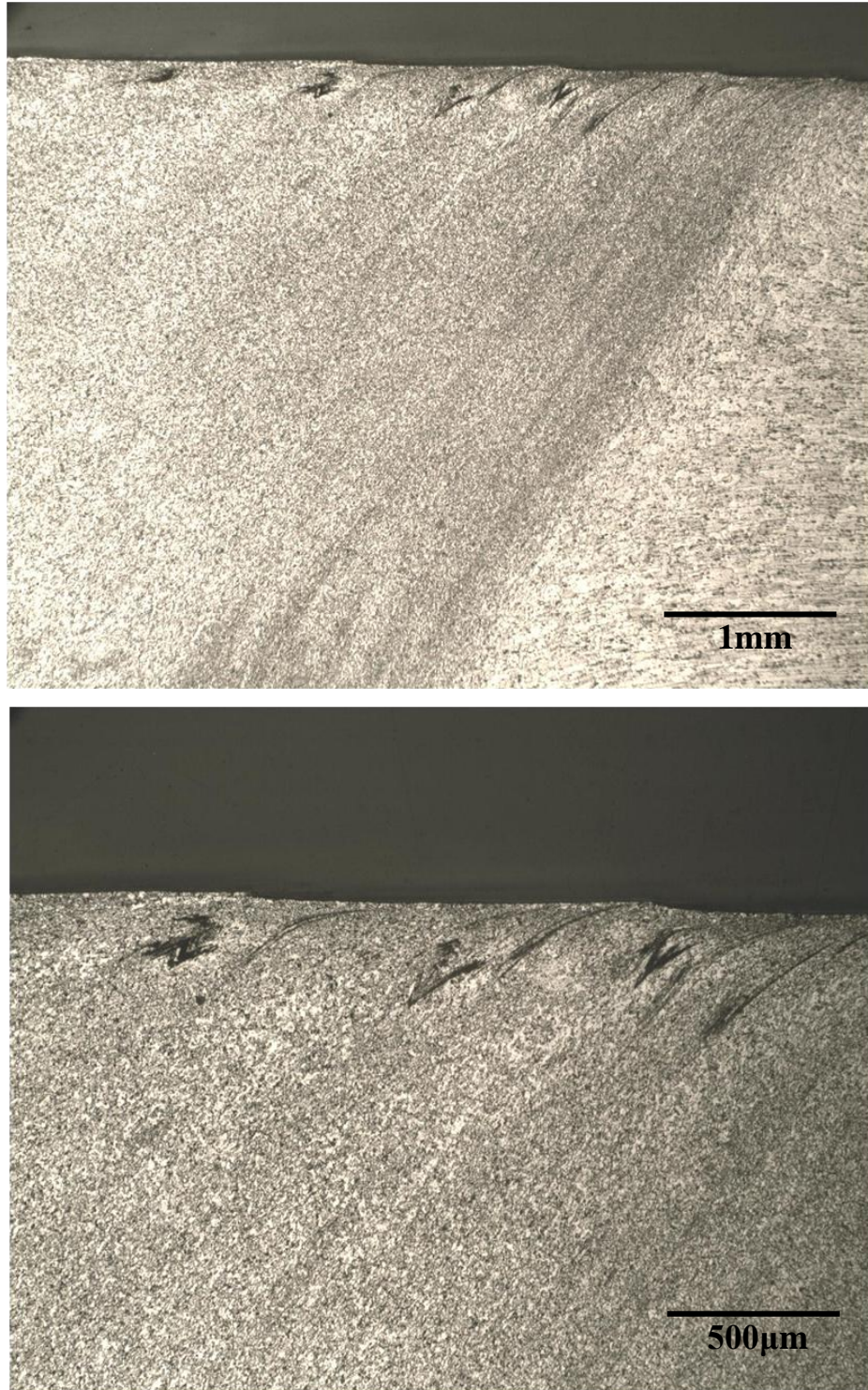


Figure 102: Metallurgical discontinuity observed below the crown of the weld (Sample 30).

Chemical analysis (Figure 103) was performed in one of the “lines” from Sample 15. Analysis revealed the presence of aluminum and magnesium. Figure 104 exhibits the region where the chemical analysis was carried out, the crown of the weld is shown in the bottom of the micrograph.

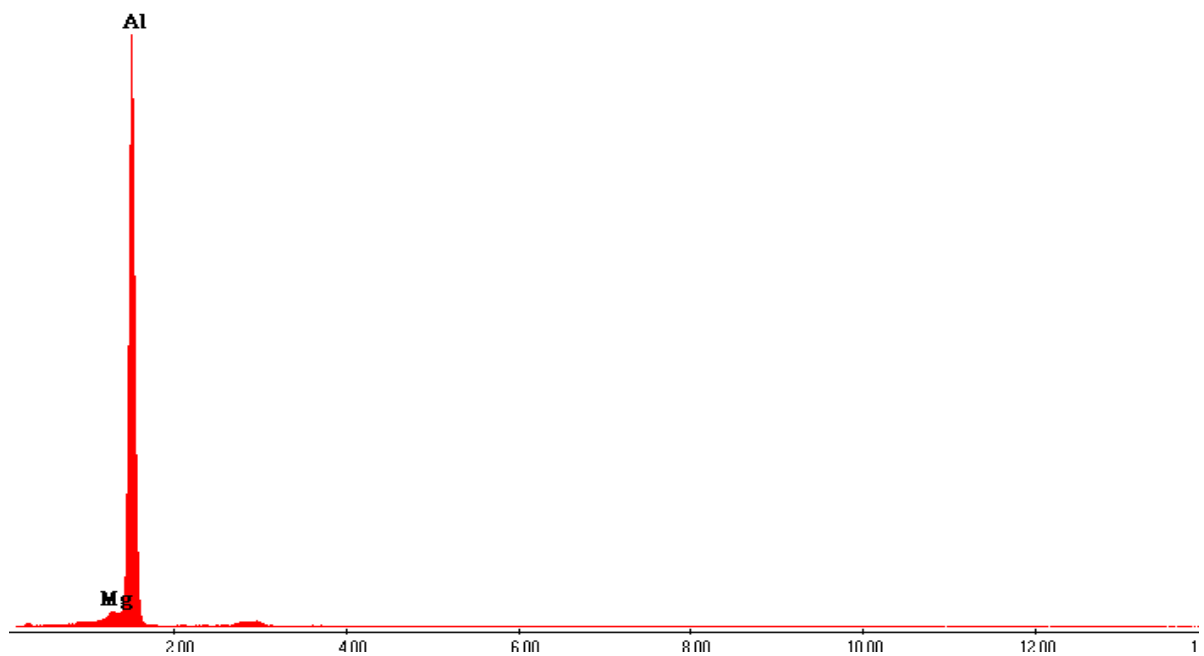


Figure 103: Chemical analysis from the metallographic features observed on Sample 15

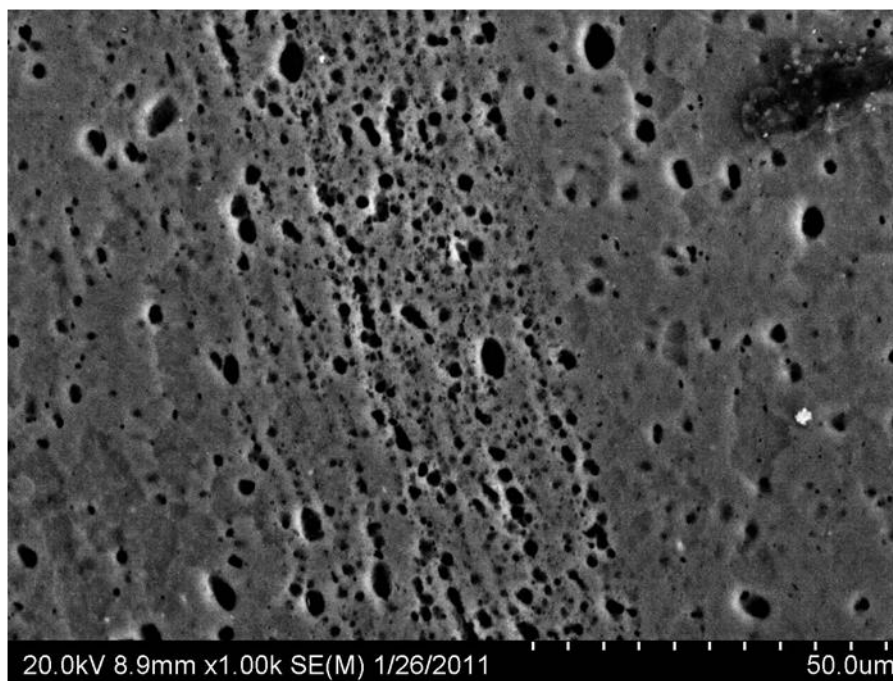
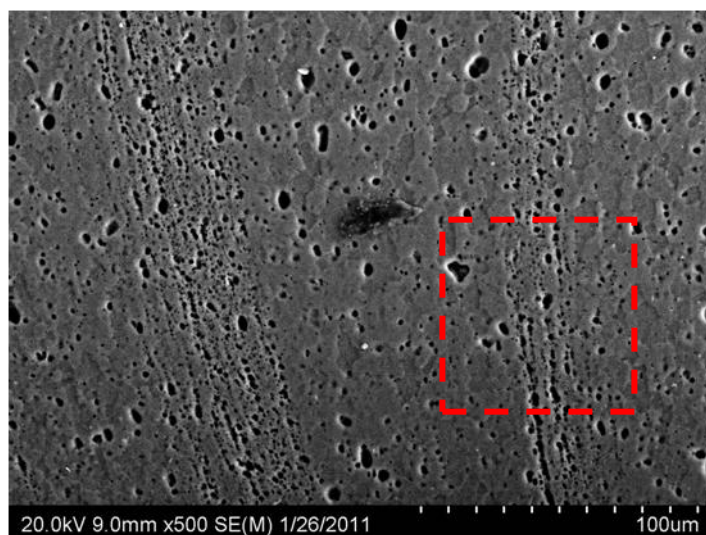


Figure 104: SEM image from metallographic feature on Sample 15.

### 3.5 MICROHARDNESS WELD PROFILE

Vicker microhardness testing was conducted using a 500 g load. The hardness profile as a function of distance from the weld centerline was performed in the middle section of all the samples fabricated for this study. All samples exhibited the typical “W” shape hardness profile with four distinct hardness zones: base metal (BM), heat-affected zone (HAZ), thermo-mechanically affected zone (TMAZ), and weld nugget. A typical weld hardness profile is presented in Figure 105, which was obtained from Sample 6 from in this study. Figure 106 to Figure 117 presents the hardness profile as function of travel speed (rotational speed and plunge force remain constant) for all the samples fabricated for this study; in each figure blue indicates low travel speed (15 ipm), red medium travel speed (17.5 ipm), and green high travel speed (20 ipm). The advancing side is presented on the right side for all hardness profile graphs.

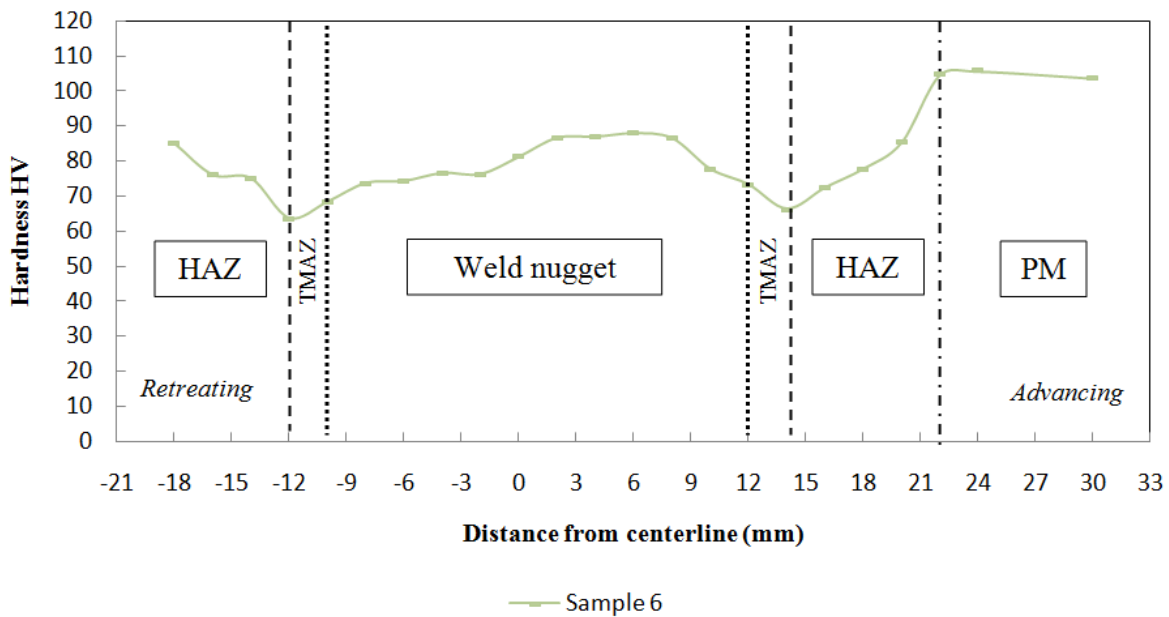


Figure 105: Self-reacting friction stir weld “w” shaped micro-hardness profile. Four main hardness zones have been identified: weld nugget, thermo-mechanically affected zone (TMAZ), heat affected zone (HAZ) and base metal (BM).



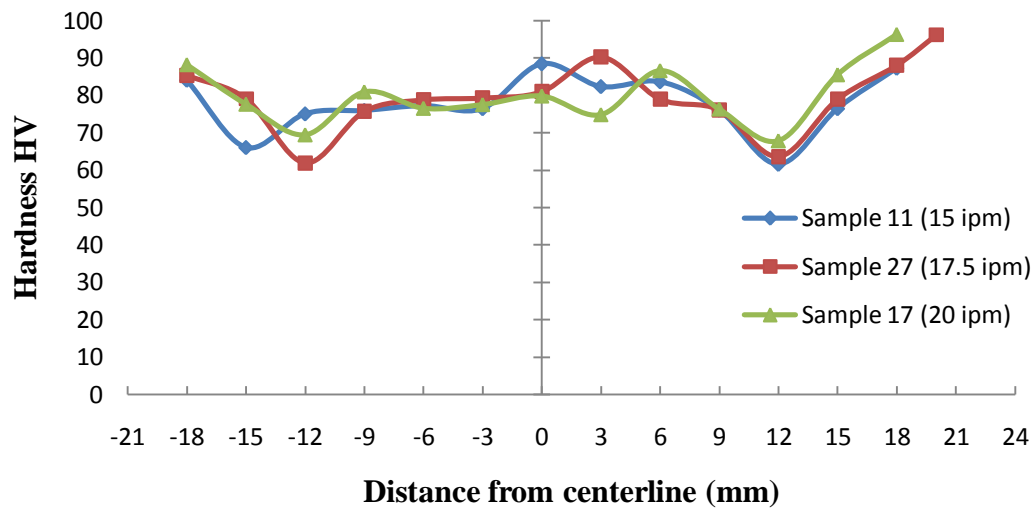


Figure 106: Hardness profile for samples fabricated at 500 rpm and 1500 lb<sub>f</sub>.

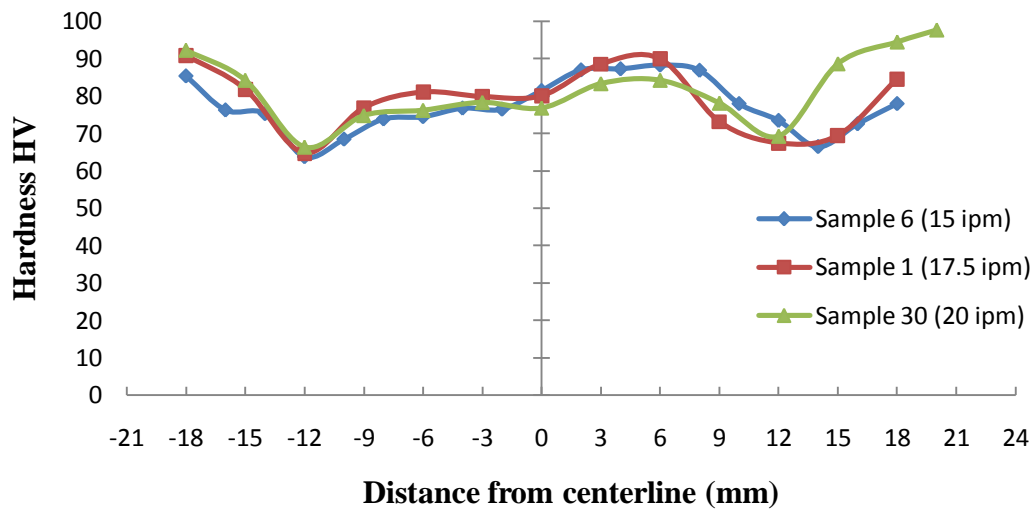


Figure 107: Hardness profile for samples fabricated at 450 rpm and 1500 lb<sub>f</sub>.

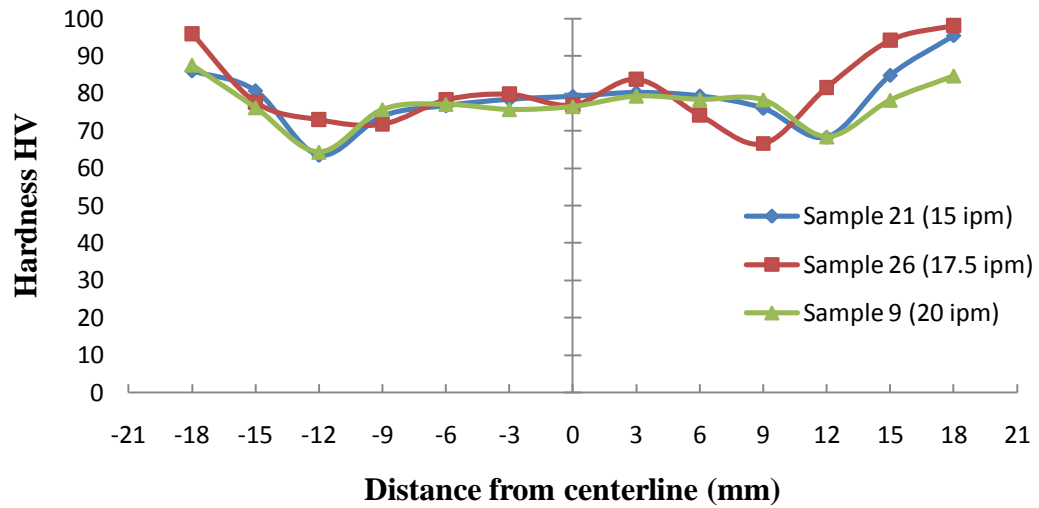


Figure 108: Hardness profile for samples fabricated at 400 rpm and 1500 lb<sub>f</sub>.

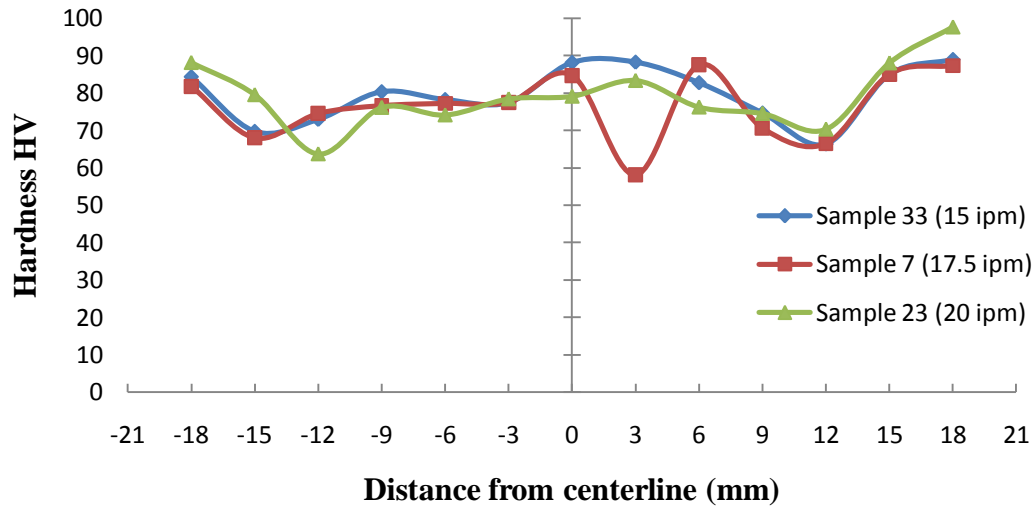


Figure 109: Hardness profile for samples fabricated at 500 rpm, and 1450 lb<sub>f</sub>. The sharp drop in hardness observed at a medium travel speed corresponds to a region in which voids exists.

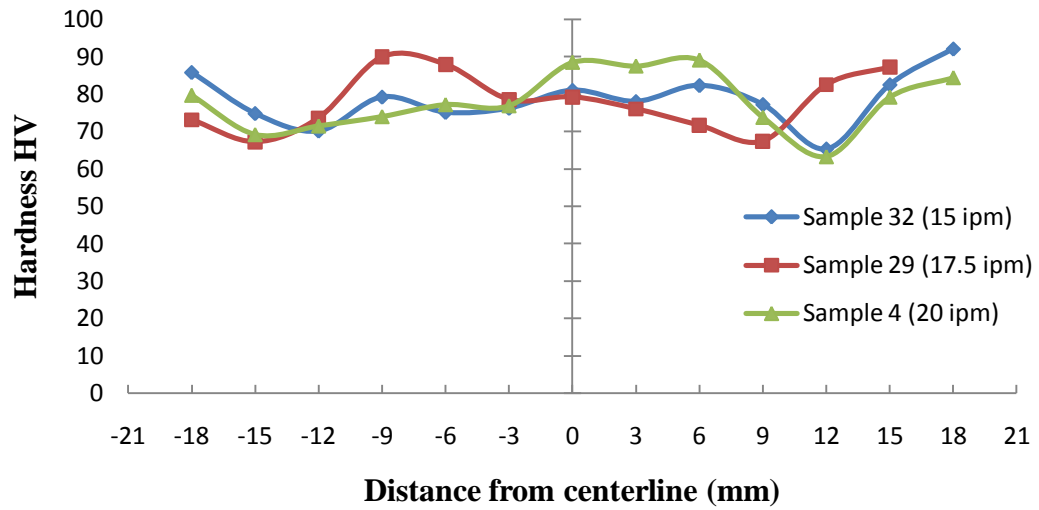


Figure 110: Hardness profile for samples fabricated at 450 rpm and 1450 lb<sub>f</sub>.

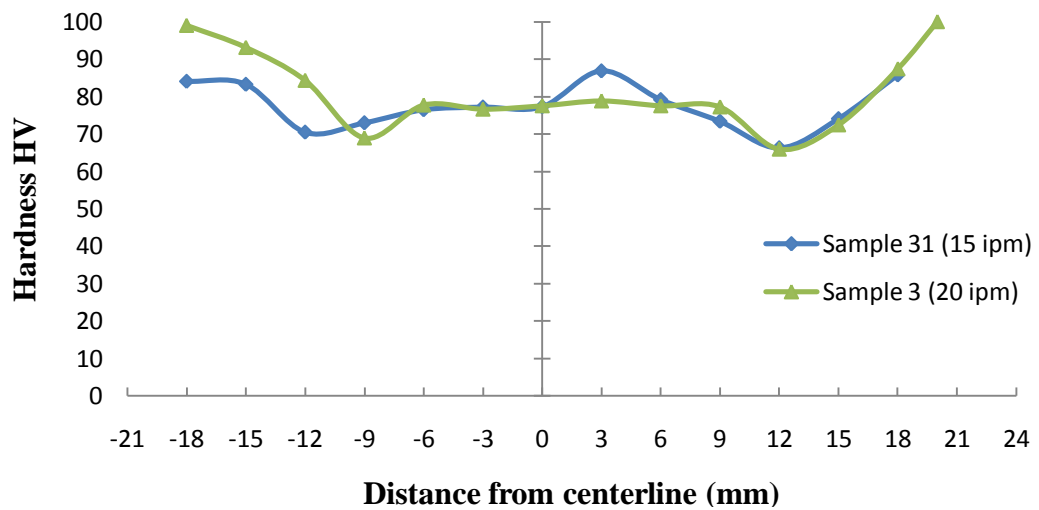


Figure 111: Hardness profile for samples fabricated at 400 rpm, 1450 lb<sub>f</sub>. Sample 10 fabricated at a medium travel speed hardness data is not shown due to human error.

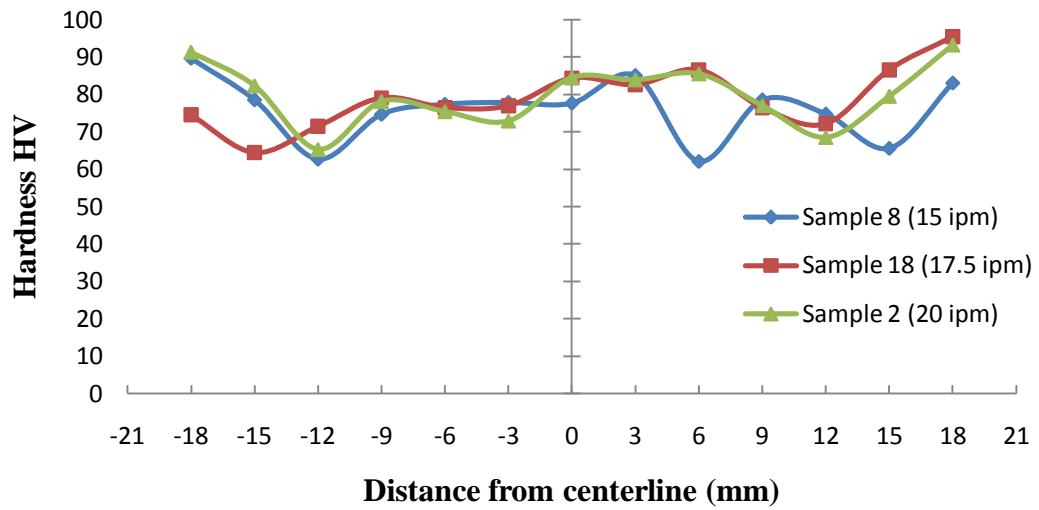


Figure 112: Hardness profile for samples fabricated at 500 rpm and 1400 lb<sub>f</sub>. The sharp drop in hardness observed at a medium travel speed corresponds to a region with voids.

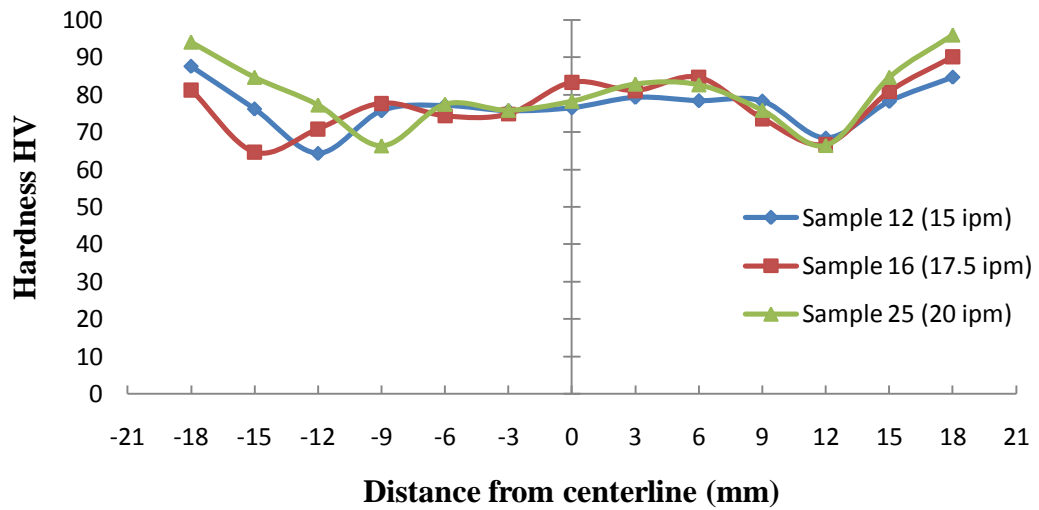


Figure 113: Hardness profile for samples fabricated at 450 rpm and 1400 lb<sub>f</sub>.

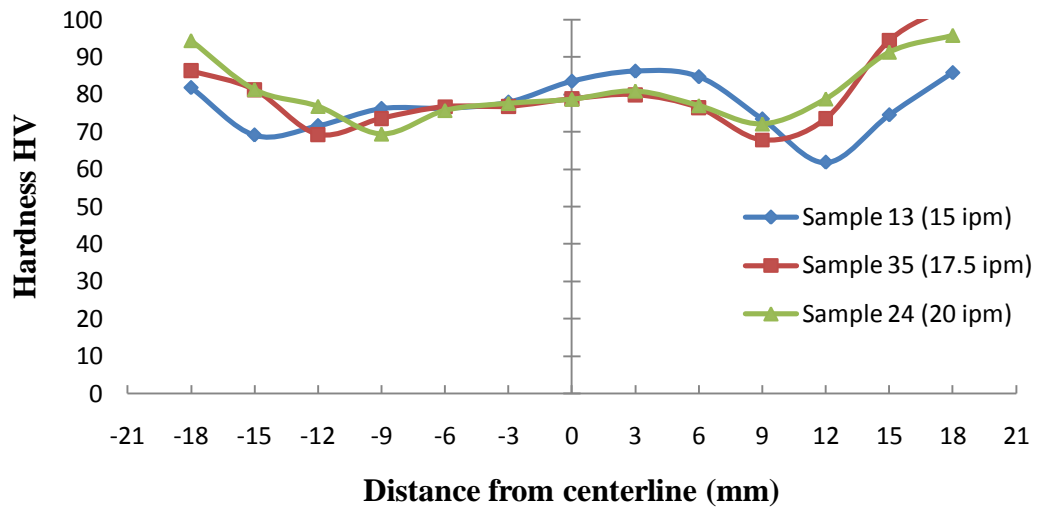


Figure 114: Hardness profile for samples fabricated at 400 rpm and 1400 lb<sub>f</sub>.

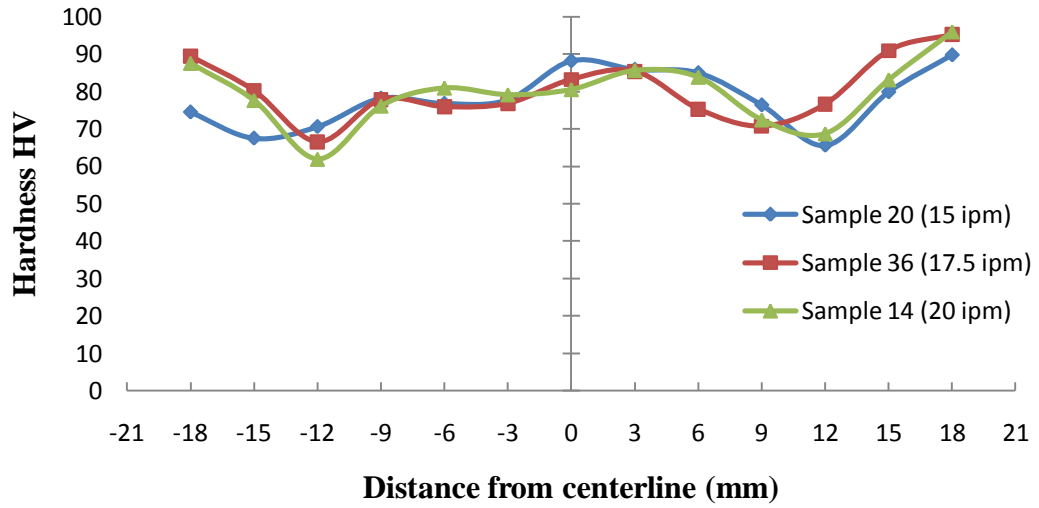


Figure 115: Hardness profile for samples fabricated at 500 rpm and 1350 lb<sub>f</sub>.



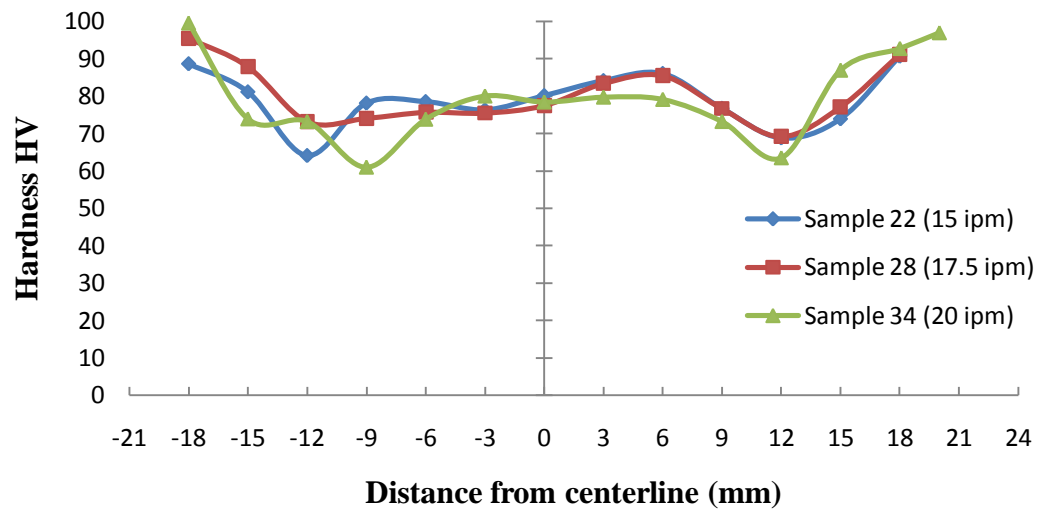


Figure 116: Hardness profile for samples fabricated at 450 rpm and 1350 lb<sub>f</sub>.

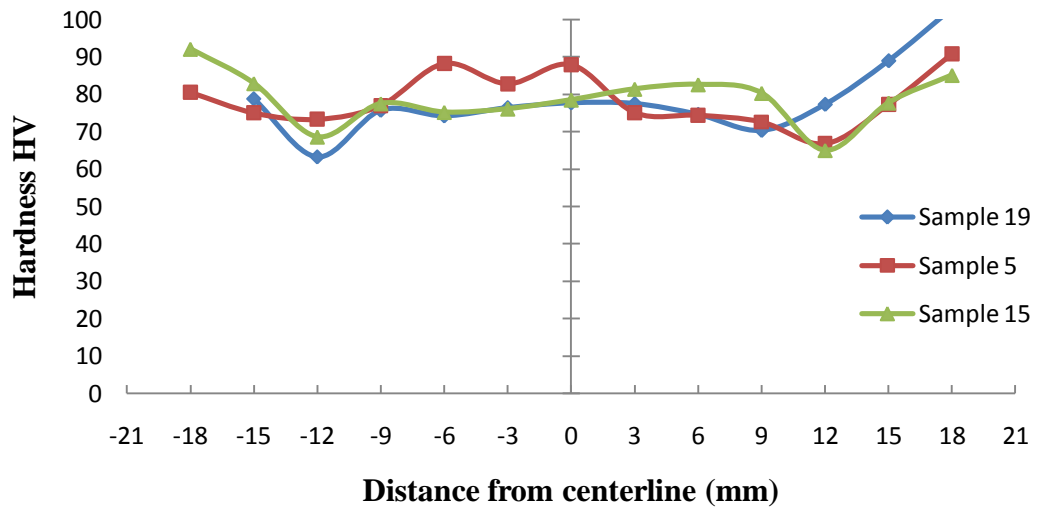


Figure 117: Hardness profile for samples fabricated at 400 rpm and 1350 lb<sub>f</sub>.

### 3.5.1 Summary of Microhardness Testing

As previously discussed, all the samples fabricated for this investigation exhibited a “W” shaped hardness profile with four main hardness zones. The central region of the weld corresponds to the weld nugget, which exhibited a nearly constant hardness with slightly higher values in the advancing side; only two samples (29 and 5) showed a slightly higher hardness on the retreating side. More uniform weld nuggets (Figure 118) were observed at a low rotational speed and high travel speed for all tool plunge forces. More uniform weld nuggets also exhibited slightly lower hardness values, as shown in Figure 119. The average hardness reduction experienced on the weld nugget is about 25-26% as compared to the parent metal.

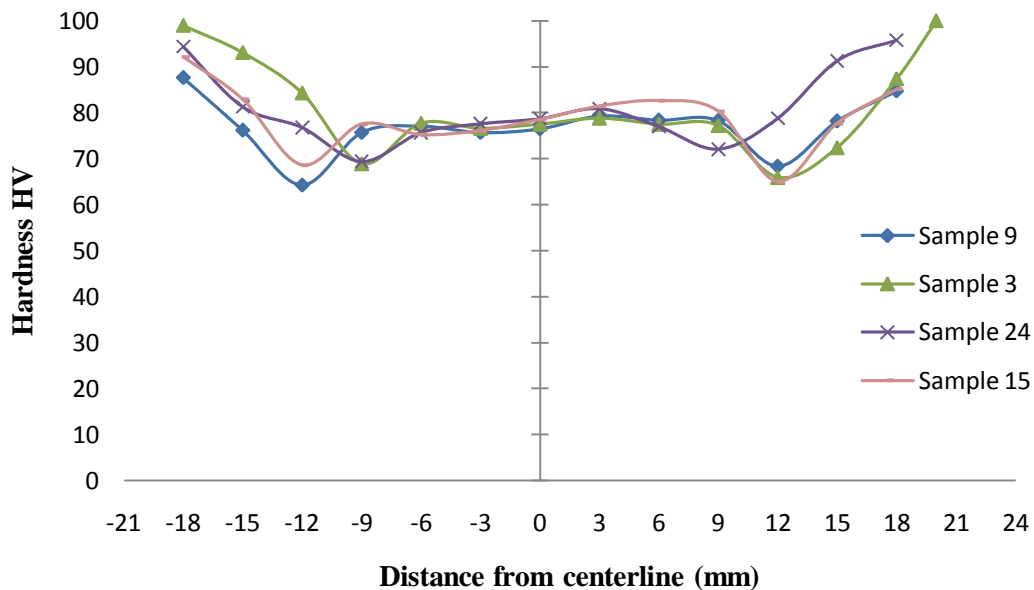


Figure 118: More uniform weld nuggets. All tool plunge forces developed more uniform weld nugget at low rotational speed and high travel speed.

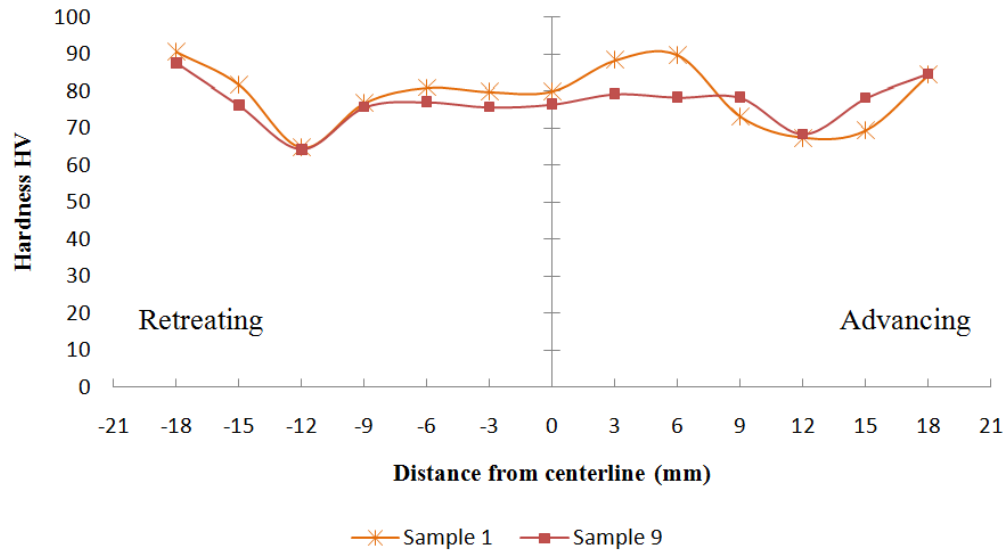


Figure 119: Microhardness comparison between a uniform nugget and a weld nugget with slightly higher values in the advancing side.

During this investigation, the average nugget size was about 18 mm (0.708 in.); with a minimum size of 12 mm (0.472 in.) and a maximum size of 21 mm (0.826 in.). Figure 120 presents a comparison between a small and a larger weld nugget, while Table 13 presents the approximate nugget size for all the fabricated samples.

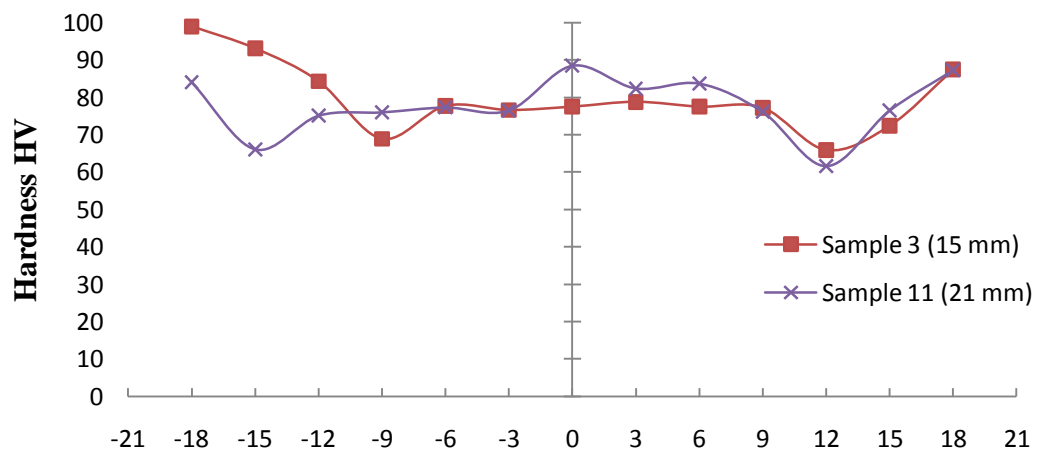


Figure 120: Comparison between a small (Sample 3) and a larger (Sample 11) weld nugget.

Table 13: Weld Nugget Size

Sample	Rotational Speed (rpm)	Travel Speed (ipm)	Plunge Force (lb <sub>f</sub> )	Weld Nugget Size (mm)
26	400	17.5	1500	12
24	400	20	1400	12
3	400	20	1450	15
35	400	17.5	1400	15
25	450	20	1400	15
36	500	17.5	1350	15
34	450	20	1350	15
19	400	15	1350	15
21	400	15	1500	15
1	450	17.5	1500	18
27	500	17.5	1500	18
30	450	20	1500	18
9	400	20	1500	18
33	500	15	1450	18
23	500	17.5	1450	18
32	450	15	1450	18
29	450	17.5	1450	18
31	400	15	1450	18
10	400	17.5	1450	18
2	500	20	1400	18
14	500	17.5	1350	18
22	450	15	1350	18
28	450	17.5	1350	18
5	400	17.5	1350	18
15	400	20	1350	18
11	500	15	1500	21
17	500	20	1500	21
7	500	17.5	1450	21
4	450	20	1450	21
8	500	15	1400	21
18	500	17.5	1400	21
12	450	15	1400	21
16	450	17.5	1400	21
13	400	15	1400	21
20	500	15	1350	21
6	450	15	1500	21

Next to the weld nugget lies the thermo-mechanically affected zone, which extends approximately 3 mm (0.118 in.) to each side of the weld. A sharp drop in hardness is observed in the TMAZ, reaching its minimum at an average distance of 12 mm (0.472 in.) from the centerline, with a minimum distance of 9 mm (0.354 in.) and a maximum distance of 15 mm (0.59 in.); this region corresponds to the HAZ. The minimum drop in hardness between the thermo-mechanically affected zone and the heat-affected zone was observed in the retreating side of sample 28 as shown in Figure 121.

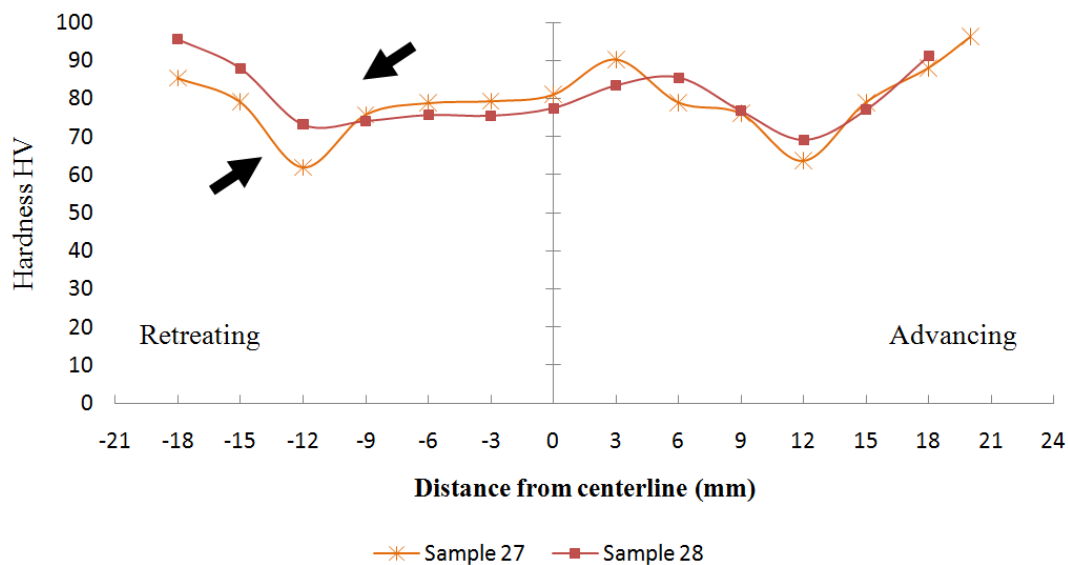


Figure 121: TMAZ-HAZ drop in hardness. Sample 28 exhibits a sharp drop in hardness in the retreating side, between TMAZ and HAZ, whereas, Sample 27 shows a minimum hardness difference.

The lowest hardness averaged about 35-38% less than the parent metal. The hardness profile increases into the base metal, which exhibits an average hardness of 106 HV.



Hardness measurements were taken at three depths for samples that exhibited a low, medium, and high number of defects, as shown in Figure 122, Figure 123, and Figure 124, respectively. The white dots in the macrographs indicate the locations of hardness indentations. The advancing side is shown on the right side and the crown of the weld on the bottom of the macrographs. No significant differences were found between the hardness at different depths.

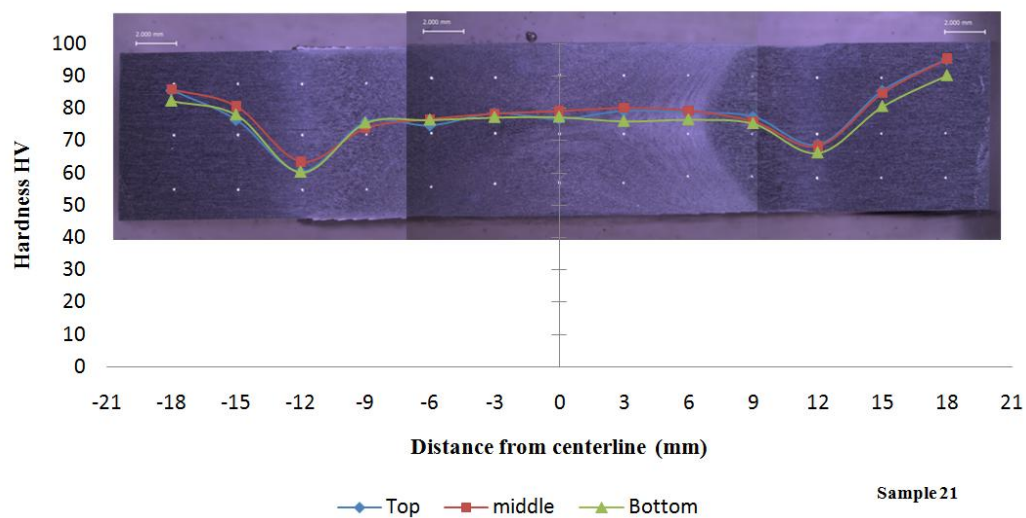


Figure 122: Hardness depth profile for samples with low number of defects. The hardness at different depths did not exhibit significant differences. The advancing side is presented on the right side, and the crown of the weld on the bottom of the macrograph.

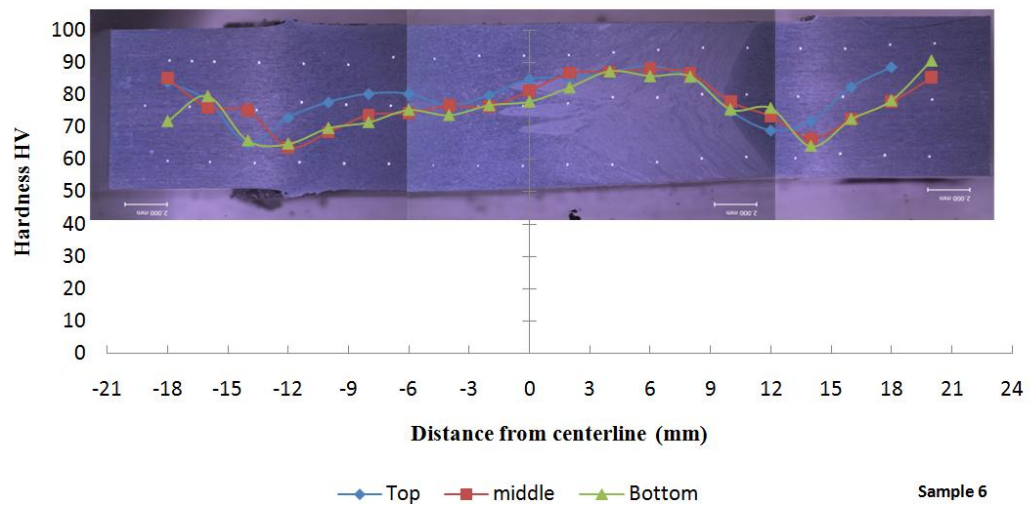
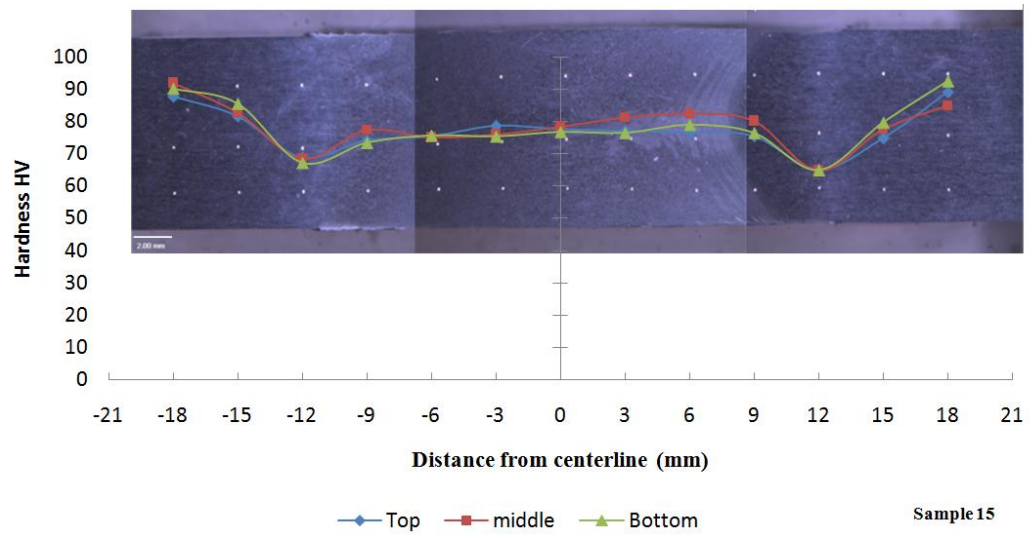


Figure 123: Hardness depth profile for samples with medium number of defects. The hardness at different depths did not exhibit significant differences. The advancing side is presented on the right side, and the crown of the weld on the bottom of the macrograph.

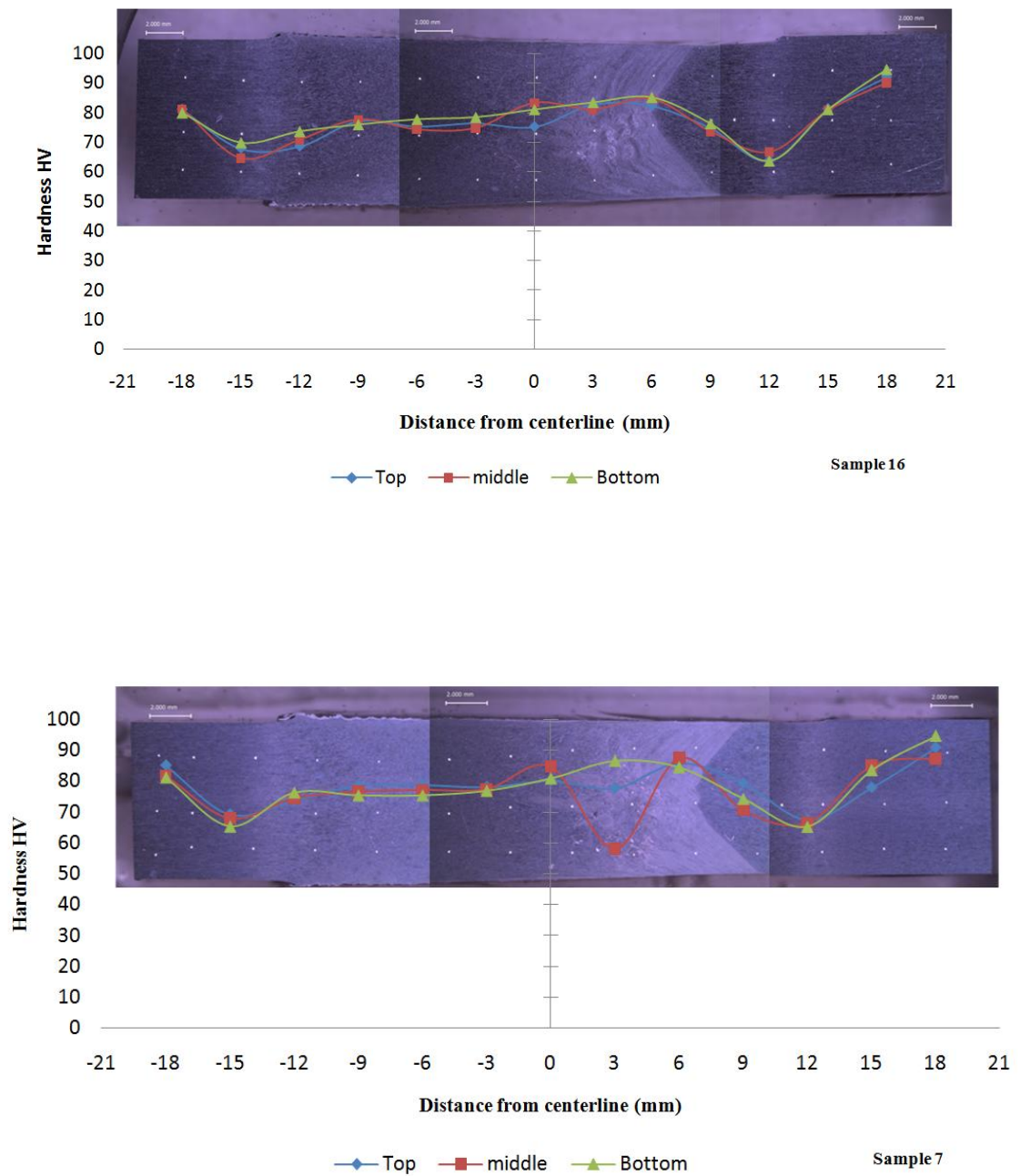


Figure 124: Hardness depth profile for samples with large number of defects. The hardness at different depths did not exhibit significant differences. The sharp drop in hardness on Sample 7 corresponds to the presence of voids. The advancing side is presented on the right side, and the crown of the weld on the bottom of the macrograph.

### 3.6 TENSILE TEST

Tensile test results are listed in order of increasing percent elongation in Table 14. It can be seen that the tensile properties of each of the joints fabricated for this study are lower than the base material properties. The percent elongation for all the samples fabricated for this investigation ranged from 2 to 9%. The samples with the lowest percent elongation, 2 to 5%, were mainly fabricated at high rotational speed and high or medium travel speeds. Tensile fracture for these samples occurred in the nugget region on the advancing side, as shown in Figure 125. The advancing side is shown on the right side for all of the tensile fracture macrographs.

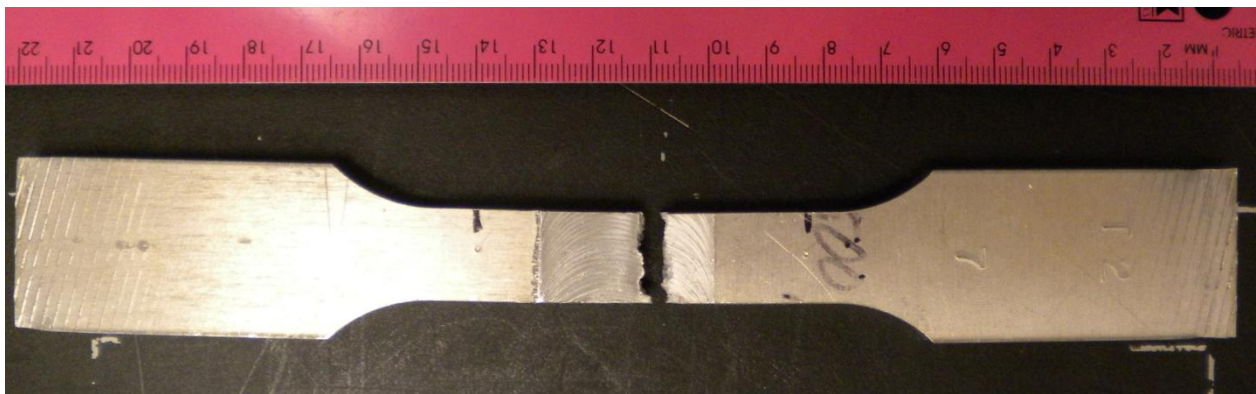


Figure 125: Tensile fracture in the nugget region. Samples that exhibited a low percent elongation exhibited tensile fracture in the nugget region (Sample 7).

The samples with a 6 to 7 percent elongation failed either, on the advancing or retreating side, at the radius of the tool shoulder (see Figure 126).

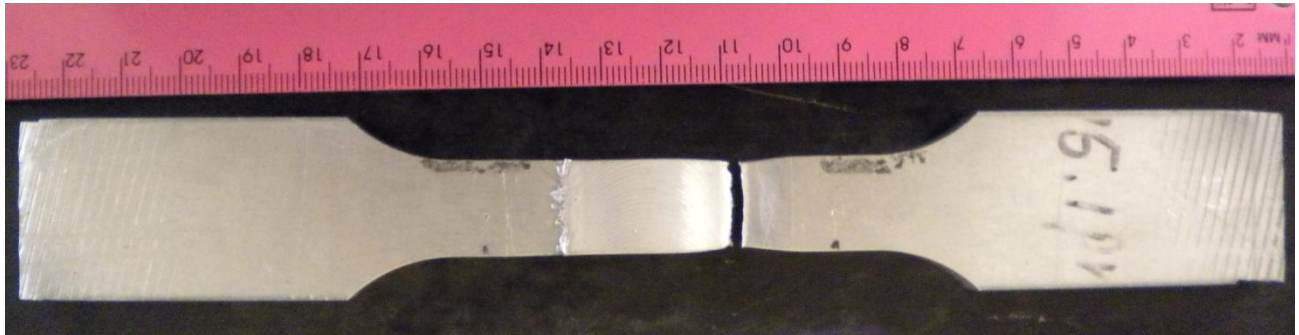


Figure 126: Tensile fracture at the radius of the tool shoulder on the advancing side (Sample 32.)

The samples fabricated at medium and low rotational speeds, exhibited the highest percent elongation, which ranged from 8 to 9%. Tensile failure was generally observed on the retreating side at a distance that corresponds to the edge of the tool shoulder, as shown in Figure 127.

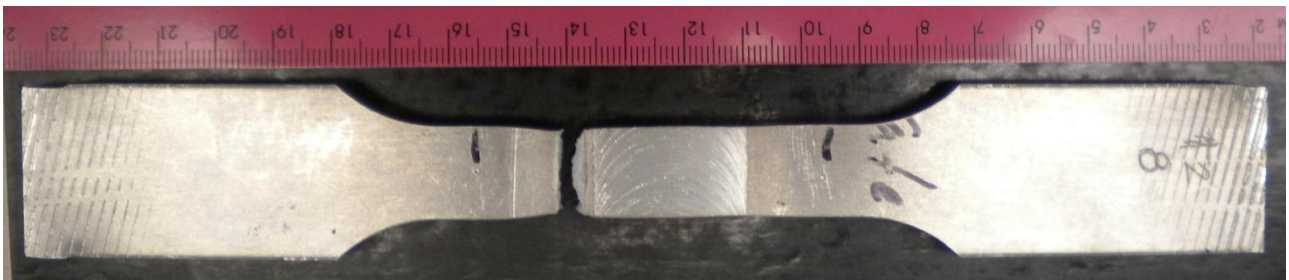


Figure 127: Tensile fracture observed at the radius of the tool shoulder. Fracture generally occurred on the retreating side of samples that exhibited a high percent elongation (Sample 8).



Table 14: Self-Reacting Friction Stir Welding Tensile Test Results

Sample Number	Percent Elongation	Yield Strength at 0.2% Offset (MPa)	Tensile Strength (MPa)	Failure zone
7	2 %	159.6	185	Nugget advancing side
17	2 %	161.5	197.8	Nugget advancing side
14	4 %	160.3	223.5	Nugget advancing side
23	4 %	160.6	237.3	Nugget advancing side
18	4 %	160.4	232.9	Nugget advancing side
16	5 %	156.8	225.8	Nugget advancing side
1	5 %	161.1	228.9	Nugget advancing side
33	5 %	158.4	229.7	Nugget advancing side
27	5 %	154.1	222.0	Nugget advancing side
3	5 %	161.1	240.8	Shoulder edge- RE side
35	5 %	158.9	235.8	Nugget advancing side
5	6 %	159.3	237.2	Nugget advancing side
24	6 %	158.6	237.2	Shoulder edge- RE side
9	7 %	159.1	237.8	Shoulder edge-ADV
29	7 %	161.9	238.0	Shoulder edge-ADV
12	7 %	157	225.5	Shoulder edge-ADV
13	7 %	158.1	236.5	Shoulder edge-ADV
6	7 %	158.3	235.4	Shoulder edge-ADV
15	7 %	158.2	237.7	Shoulder edge- RE side
10	7 %	157.7	234.6	Shoulder edge- RE side
31	7 %	156.4	235.5	Shoulder edge- RE side
20	7 %	161	236.3	Shoulder edge-ADV
25	7 %	160.2	239.8	Shoulder edge- RE side
22	7 %	158.9	235.6	Shoulder edge-ADV
11	7 %	158.5	228.6	Outside shoulder edge
36	7 %	161.6	239.1	Shoulder edge- RE side
32	7 %	156.5	230.9	Shoulder edge-ADV
4	8 %	161.3	238.5	Shoulder edge-ADV
8	8 %	159.6	237.0	Shoulder edge- RE side
26	8 %	157.6	238.5	Shoulder edge- RE side
2	8 %	161.9	243.1	Shoulder edge- RE side
19	8 %	157.7	239	Shoulder edge- RE side
30	8 %	160.9	242.1	Shoulder edge- RE side
21	8 %	156.1	237	Shoulder edge- RE side
28	8 %	160.4	240	Shoulder edge-ADV
34	9 %	161.4	243.4	Shoulder edge- RE side
Base metal	10% (min)	35 ksi (241 MPa) (min)	42 ksi (290 MPa) (min)	Per ASTM B209-07

From the main effects plot shown in Figure 128, it can be seen that all of the experimental factors have an influence on the percent elongation. However, rotational speed appears to have a slightly higher influence on ductility than the other factors.

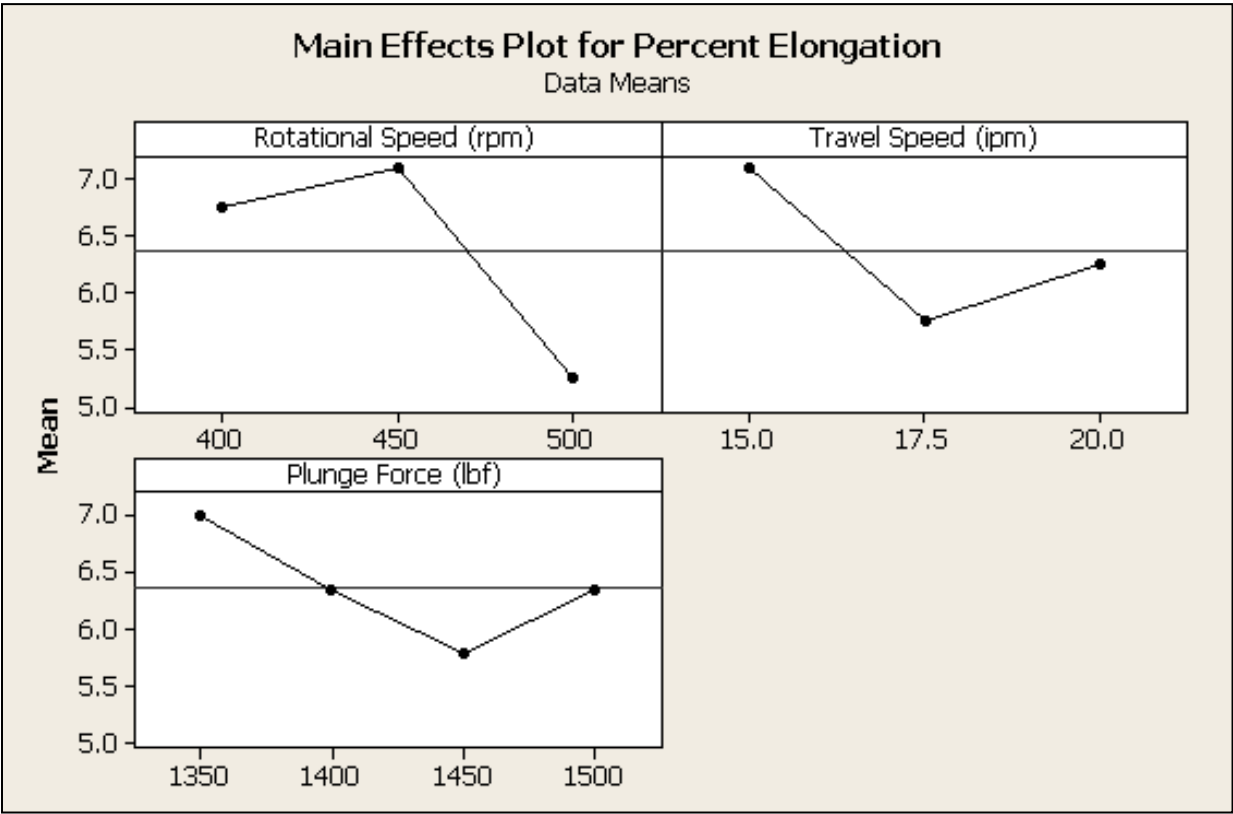


Figure 128: Percent elongation main effects plot. All factors appear to have an influence on the percent elongation.

The mean 0.2% offset yield strength was 159 MPa with a minimum of 154 MPa and a maximum of 162 MPa. The variation in the 0.2% offset yield strength for all the samples fabricated for this investigation does not appear to be significant. The standard deviation for 0.2% offset yield strength is about 2. The tensile strength reached as high as 243 MPa, obtained at a medium rotational speed, high travel speed, and low tool plunge force (450 rpm, 20 ipm, 1350 lb<sub>f</sub>) and at a high rotational speed, high travel speed, and medium plunge force (500 rpm, 20 ipm, 1400 lb<sub>f</sub>. Table 15 to Table 18 presents the ultimate tensile strength for all the samples fabricated for this study as function of process parameters. The lowest tensile strength values are shown in red.

Table 15: Tensile Strength for 1350 lb<sub>f</sub> Tool Plunge Force

<b>Rotational Speed (rpm)</b>	<b>Tensile Strength MPa</b>		
<b>500</b>	236	239	224
<b>450</b>	236	240	243
<b>400</b>	239	237	238
<b>Traverse Speed (ipm)</b>	<b>15</b>	<b>17.5</b>	<b>20</b>

Table 16: Tensile Strength for 1400 lb<sub>f</sub> Tool Plunge Force

<b>Rotational Speed (rpm)</b>	<b>Tensile Strength MPa</b>		
<b>500</b>	237	233	243
<b>450</b>	226	226	240
<b>400</b>	237	236	237
<b>Traverse Speed (ipm)</b>	<b>15</b>	<b>17.5</b>	<b>20</b>

Table 17: Tensile Strength for 1450 lb<sub>f</sub> Tool Plunge Force

Rotational Speed (rpm)	Tensile Strength MPa		
<b>500</b>	230	185	237
<b>450</b>	231	238	238
<b>400</b>	236	235	241
<b>Traverse Speed (ipm)</b>	<b>15</b>	<b>17.5</b>	<b>20</b>

Table 18: Tensile Strength for 1500 lb<sub>f</sub> Tool Plunge Force

Rotational Speed (rpm)	Tensile Strength MPa		
<b>500</b>	229	222	198
<b>450</b>	235	229	238
<b>400</b>	237	239	242
<b>Traverse Speed (ipm)</b>	<b>15</b>	<b>17.5</b>	<b>20</b>

Overall, a low tool plunge force (1350 lbf) exhibited a higher number of samples with a higher tensile strength. In contrast, a high tool plunge force produced a higher number of samples with lower tensile strengths. The maximum tensile strength is equivalent to a joint efficiency of 84%. Joint efficiency is the ratio of the tensile strength of the weld to the tensile strength of the parent metal. The minimum joint efficiency observed was 64%, which corresponds to Sample 7, fabricated at a high rotational speed, medium travel speed, and high plunge force (500 rpm, 17.5 ipm, 1450 lb<sub>f</sub>). The joint efficiency for the 36 samples fabricated for this study is shown in Table 19.

Table 19: Self-Reacting Friction Stir Weld Joint Efficiency

Sample Number	Rotational Speed (rpm)	Traverse Speed (ipm)	Tool Plunge Force (lbf)	Joint Efficiency %
7	500	17.5	1450	64
17	500	20	1500	68
27	500	17.5	1500	77
14	500	20	1350	77
12	450	15	1400	78
16	450	17.5	1400	79
11	500	15	1500	79
1	450	17.5	1500	79
33	500	15	1450	79
32	450	15	1450	80
18	500	17.5	1400	80
10	400	17.5	1450	81
6	450	15	1500	81
31	400	15	1450	81
22	450	15	1350	81
35	400	17.5	1400	81
20	500	15	1350	82
13	400	15	1400	82
21	400	15	1500	82
8	500	15	1400	82
24	400	20	1400	82
5	400	17.5	1350	82
23	500	20	1450	82
15	400	20	1350	82
9	400	20	1500	82
29	450	17.5	1450	82
4	450	20	1450	82
26	400	17.5	1500	82
19	400	15	1350	82
36	500	17.5	1350	82
25	450	20	1400	83
28	450	17.5	1350	83
3	400	20	1450	83
30	450	20	1500	84
2	500	20	1400	84
34	450	20	1350	84



A main effects analysis was carried-out to determine which process parameter has a bigger influence on the tensile strength; from the main effects plot shown in Figure 129 it can be seen that all the analyzed factors appear to have an influence on the tensile strength. However, the rotational speed has a slightly higher influence on the tensile strength (MPa).

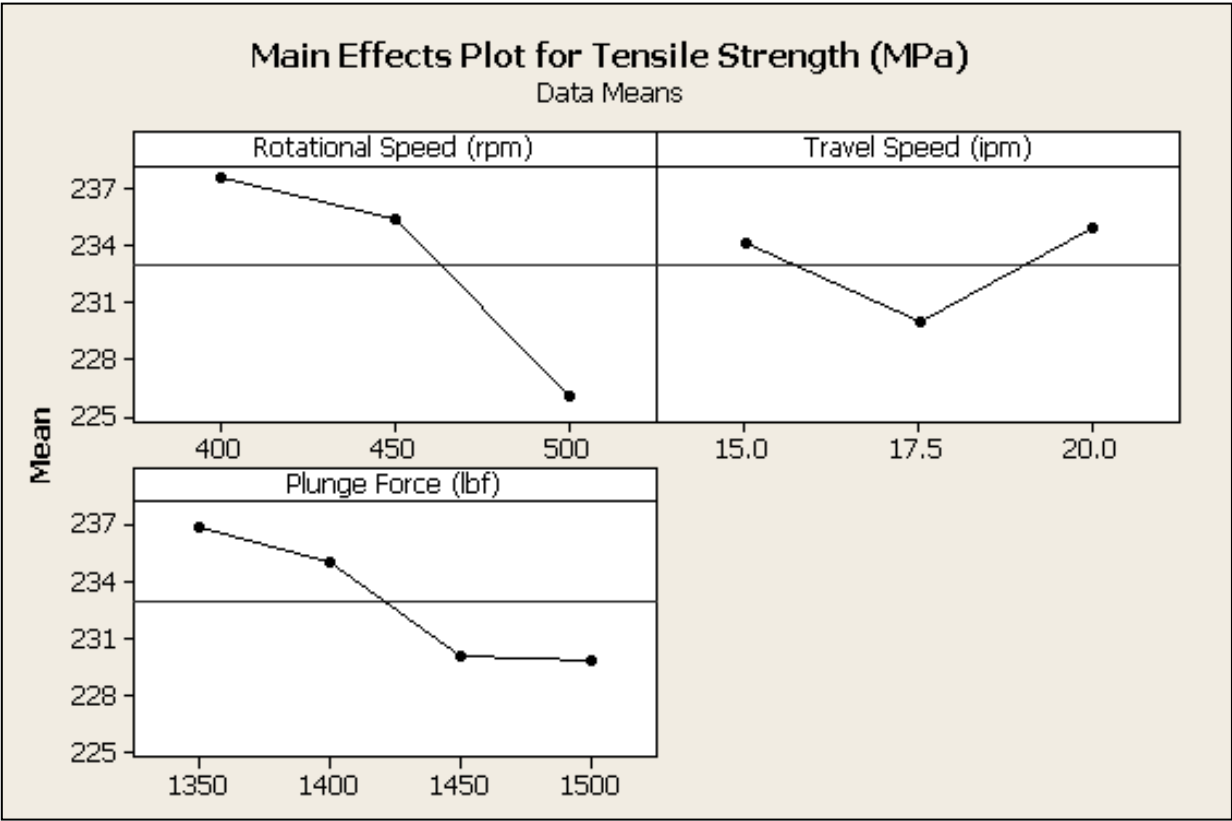


Figure 129: Tensile strength main effects plot. The rotational speed has a bigger effect on the tensile strength.

## **Discussion**

### **4.1 TEMPERATURE**

Temperature measurements of the weld crown during the welding process were obtained with an infrared camera. The overall trend observed was for the retreating side to exhibit higher temperatures as compared to the advancing side. This temperature asymmetry between the retreating and advancing sides appears to be the result of the metal transport to the retreating side and the relative rotational speed of the tool in relation travel during the weld. During FSW, the hot softened metal is transported from the advancing to the retreating side where the opposite rotational and traverse motions result in the buildup of hot material from the advancing to the retreating side, leading to higher temperatures. Generally, lower traverse speeds also resulted in slightly higher temperatures. The highest temperature observed at 0.75" from the tool edge occurred on the retreating side. This temperature was measured to be 1027°F, which is slightly lower than the alloy's solidus temperature (1080°F).

### **4.2 VISUAL APPEARANCE**

The crown and the root of SR-FS welded joints exhibit the typical FSW semi-circular pattern, as a result of the contact of the workpiece with the tool. This pattern has been associated with the tool advance for each revolution [4]. A visual inspection from the crown of the weld revealed different external defects, such as visible wormholes, galling, and a small amount flash. During this investigation, it was found that the weld's visual quality is significantly influenced by rotational speed. The number of and severity of macroscopic defects increased as the rotational speed increased. In the case of samples fabricated at high rotational and traverse speeds (samples 2, 14, and 17), visible wormholes and galling were encountered. Wormholes were mainly observed on the advancing side. It is believed that a combination of high rotational and traverse speeds lead to insufficient forging and thus a lack of material consolidation, resulting in visible wormholes. The presence of visible wormholes was found to be detrimental not only to the visual quality but to the final mechanical properties. Welded joints with visible wormholes exhibited a decrease in ductility and ultimate tensile strength. The samples that exhibited the best visual quality, consisting of a smooth, regular, and defect free surface, were fabricated at the low and medium levels of rotational speed. These samples exhibited a more uniform temperature

profile between the advancing and retreating sides as well as lower overall temperatures. The temperature in the vicinity of the tool on the advancing side ranged from 330 to 400°F and on the retreating side between 400 and 421°F. In contrast, on the samples that exhibited visible wormholes and thus a low visual quality, the temperature difference between the advancing and the retreating side appears to be higher. In the vicinity of the tool, the samples that exhibited wormholes and galling (Samples 16, 14, 17, 2, and 7) reached temperatures ranging from 415 to 550°F on the advancing side and from 550 to 880°F on the retreating side.

#### **4.3 MICROSTRUCTURAL EVOLUTION**

Friction stir welding involves severe plastic deformation under rapid, transient strain, strain rate, and temperature gradients [68]. During the friction stir welding the material flows in a complex pattern around the pin, from the advancing side to the retreating side [68]. Therefore, the material around the tool undergoes extreme levels of plastic deformation [69]. The temperature gradient and plastic deformation occurring during self-reacting friction stir welding results in four main microstructural zones—parent metal, heat-affected zone, thermo-mechanically affected zone, and weld nugget—as in conventional FSW. However, during conventional friction stir welding, the weld nugget resembles an inverted bell [70], leading to an asymmetry between the crown and root of the weld, whereas the SR-FSW nugget exhibits an hourglass shape, with similar characteristics between the crown and root of the weld. In both cases, the weld nugget microstructure is characterized by small, equiaxed, and recrystallized grains. Recrystallization is the result of the severe plastic deformation at high temperatures [71] occurring during the welding process. Figure 130, presents a comparison between conventional FSW [16] and SR-FSW microstructures.

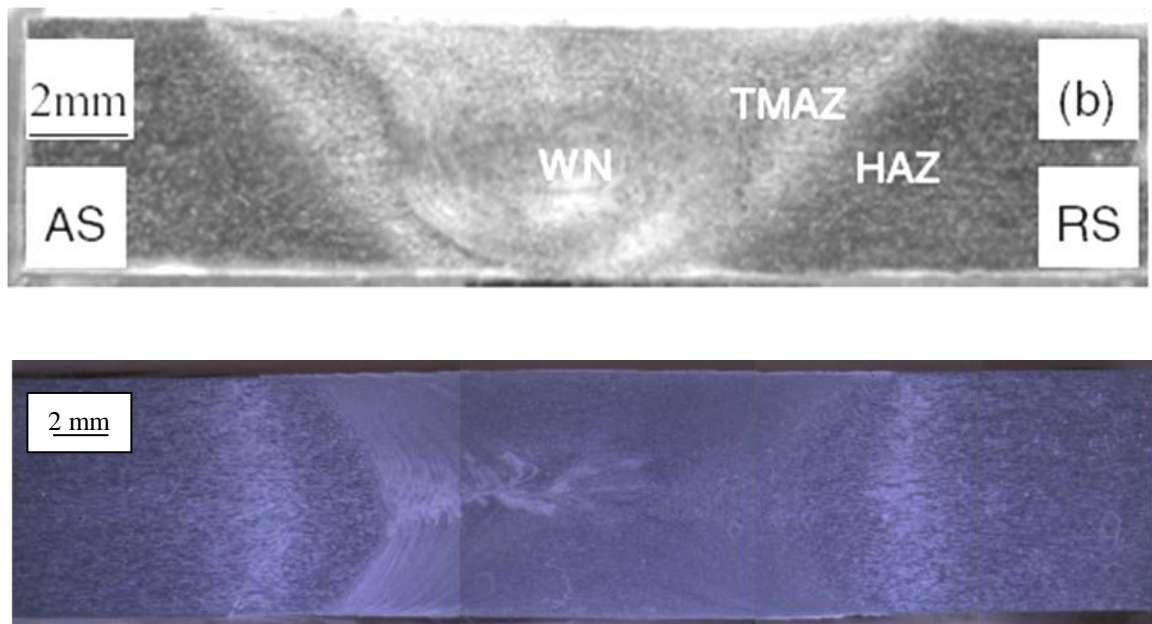


Figure 130: Friction stir welded joints microstructures. Conventional FSW [16] (top) and SR-FSW (bottom) microstructures. The advancing side is shown on the left side of the micrographs.

#### 4.3.1 Weld Nugget Pattern

In this investigation, the central region of the weld nugget exhibited a unique, discernable pattern, which starts on the advancing side towards the center of the nugget region, forming what appear to be “fingers”. This “finger like” pattern appears to be formed by concentric rings of slightly varying orientation. However, the appearance of this feature varied for each sample. The SR-FS weld nugget pattern appears similar to the “onion ring” pattern, which is a typical feature observed in the nugget region of conventional FS welded joints with differences that can be explained by the presence of a rotation shoulder at the root of the weld. The onion ring pattern is the result of the complex material

movement due to the tool mixing and forging action taking place during the FSW process [7]. The frictional heating and extrusion of metal to the retreating side, caused by the rotational and traverse movements of the tool, result in the formation of the onion ring pattern [9], which is characterized by circles that progressively decrease in radii and take on the configuration of a tube [10]. The onion ring pattern corresponds to bands of shear-induced fiber texture [2]. These bands have been attributed to the different levels of plastic deformation experienced by the material [72]. During conventional FSW, some studies documented visible onion ring pattern in colder welds, as compared to hotter welds [2]. Figure 131 presents a dark field image from a conventional FSW weld nugget, which exhibits the onion ring structure [70].

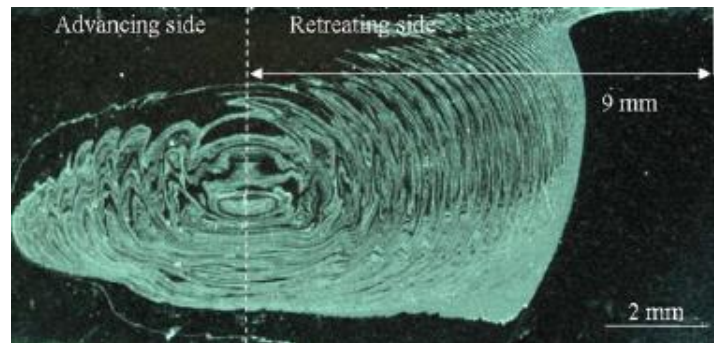


Figure 131: Dark field micrographs from a conventional friction stir weld nugget exhibiting the onion ring pattern [70].

The SR-FSW “fingers” pattern appears to be the stacking of multiple, compressed conventional FSW “onion rings”. The unique variations on the nugget pattern seen in this study and the onion ring pattern observed in conventional FS welded joints are most likely due to the differing tool characteristics between SR-FSW and conventional FSW tools. However, both patterns can be attributed to the complex material flow taking place during the welding process [10]. Figure 132 exhibits the “finger” pattern observed on a SR-FSW nugget.



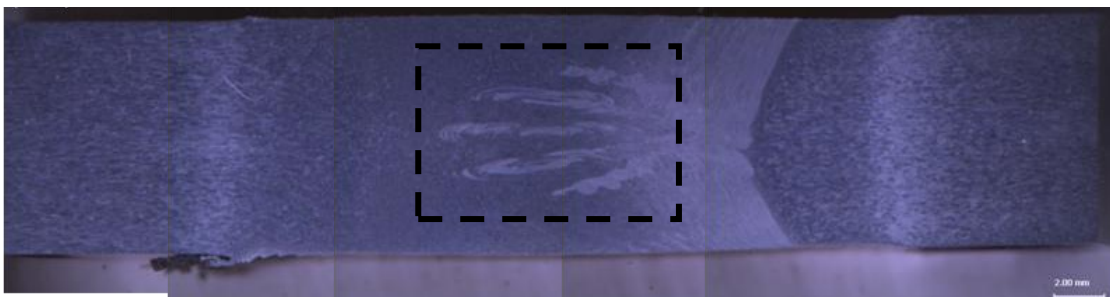
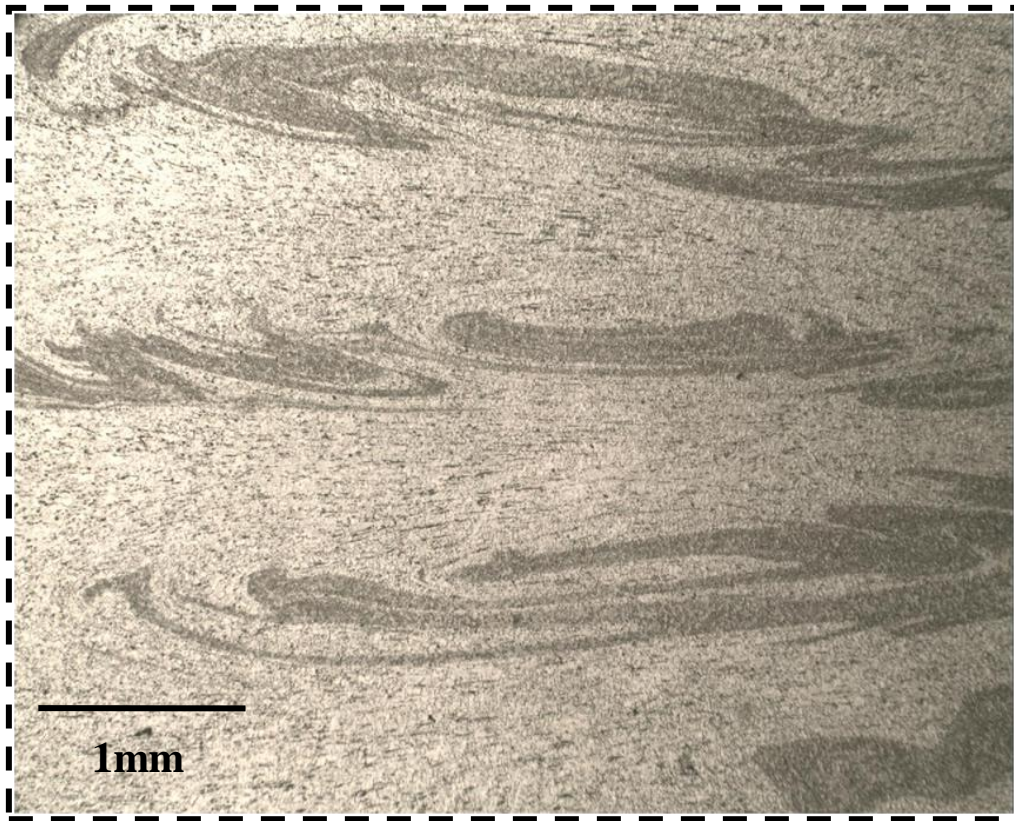


Figure 132: Exemplar of a SR-FSW nugget pattern (Sample 1).

## **4.4 MICROSTRUCTURAL DEFECTS**

### **4.4.1 Lazy S**

The Lazy S defect usually observed in the nugget region has been attributed to the presence of an oxide layer on the surfaces to be welded [2]. The removal of the oxide layer is necessary to allow a complete joining of the materials [2] and thus to produce quality weldments. During this investigation, the faying surfaces of the aluminum plates were wiped with methanol prior to welding. However, a clear relationship between the lazy S defect formation and process parameters was not found as the lazy S defect was observed in the majority of the fabricated samples. This appears to indicate that cleaning with methanol is not sufficient to prevent lazy S defect formation. Appropriate cleaning of the plates previous to welding can help remove or decrease the oxide layer thickness that can be subsequently dispersed during the welding process [51]. Machining, grit blasting, and chemical etching are some of the recommended methods for the oxide layer removal [4]. Tensile test results revealed that there was no correlation between the presence of the lazy S defect and mechanical properties. We can conclude that the lazy S defect has no influence on the mechanical properties. However, as the presence of a thick oxide layer may have contributed to not seeing an effect of process parameters on the lazy S defect formation, further research on joint preparation and process parameters to lazy S defect formation are required.

### **4.4.2 Voids**

About 60% of the samples fabricated for this study exhibited voids. Voids were encountered in the nugget region on the advancing side. During this investigation it was determined that rotational speed has a significant effect on void formation – samples fabricated at high rotational speed exhibited more severe voids as compared to samples fabricated at lower rotational speeds. In addition, the mechanical properties of friction stir welded joints are strongly influenced by voids—samples with high void concentration exhibited the lowest percent elongation, yield strength, and tensile strength. The tensile fracture for samples with severe voids occurred in the nugget zone, in the area that corresponds to the void location. In contrast, defect free samples exhibited tensile failure in the region that corresponds to the heat-affected zone.

## **4.5 HARDNESS**

Four hardness zones were identified on SR-FS welded joints, the nugget region, TMAZ, HAZ and base metal. The nugget region exhibits a nearly constant hardness with a slightly higher hardness on the advancing side. The weld nugget experienced a decrease in hardness of 25-26% as compared to the parent metal. The nugget size ranged from 12 mm to 21 mm (0.472 to 0.826 in.); narrower weld nuggets are consistent with the welds that exhibited lower temperature profiles as a function of distance from the tool edge. The samples that exhibited larger nuggets exhibited higher temperatures over larger distances, away from the tool edge. This is consistent with the literature; during conventional FSW, the heat generated controls the size of the weld nugget; hotter welds exhibit larger weld nuggets compared to colder welds [2]. A process parameter combination of low rotational speed and high travel speed resulted in more uniform weld nuggets, resulting in median mechanical properties with a 6-7% elongation and 237 MPa tensile strength. Adjacent to the weld nugget is the TMAZ, where the hardness drops until it reaches a minimum in the heat-affected zone. The minimum hardness value is approximately 35-38% less than the parent metal; tensile fracture occurred in the minimum hardness region for defect free samples. The difference in hardness between the different weld zones is the result of the different grain sizes and overaging due to heat input from the welding process. The hardness of the weld was uniform through the thickness of the plate; this can be attributed to the top and bottom microstructure symmetry. In contrast, during conventional FSW the crown of the weld exhibits a lower hardness compared to the weld root due to the higher heat input created by the contact of the crown with the tool shoulder [54].

## **4.5 TENSILE PROPERTIES**

All the samples fabricated for this study exhibited lower mechanical properties, as compared to the parent metal. The ductility reached a maximum percent elongation of 9%. The yield strength exhibited little variation between all the samples fabricated for this investigation. Tensile failure occurred either on the advancing or retreating side except for samples that exhibited voids, in which tensile fracture was observed in the nugget region. During this investigation, it was found that the mechanical properties of the welded joints are significantly influenced by rotational speed. The samples

that exhibited the best mechanical properties were fabricated at a medium rotational speed, whereas, the samples that exhibited the worst mechanical properties were manufactured at a high rotational speed. Table 20 and Table 21 present the samples with the best and worst mechanical properties. The maximum tensile strength obtained (Sample 34) was 243 MPa, which corresponds to a joint efficiency of 84%.

Table 20: Samples with the Best Mechanical Properties

<b>Sample Number</b>	<b>Rotational Speed (rpm)</b>	<b>Travel Speed (ipm)</b>	<b>Plunge Force (lbf)</b>	<b>Percent Elongation %</b>	<b>Tensile Strength (Mpa)</b>
34	450	20	1350	9.24	243
28	450	17.5	1350	8.40	240
30	450	20	1500	7.97	242

Table 21: Samples with the Lowest Mechanical Properties

<b>Sample Number</b>	<b>Rotational Speed (rpm)</b>	<b>Travel Speed (ipm)</b>	<b>Plunge Force (lbf)</b>	<b>Percent Elongation %</b>	<b>Tensile Strength (Mpa)</b>
7	500	17.5	1450	1.74	185
17	500	20	1500	2.10	198
14	500	20	1350	3.71	224

## Conclusions

6061-T651 aluminum plates with a thickness of .3125” were self-reacting friction stir welded in a butt weld configuration. The SR-FS welded joints revealed the same microstructural zones as conventional FSW; however, during SR-FSW the nugget exhibited an hourglass shape with a unique “finger like” pattern in the central region, in contrast to the bell-shaped nugget observed during conventional FSW. The SR-FSW “finger” pattern appears to be the stacking of multiple onion ring structures, which are the result of the complex material flow taking place during the welding process. The SR-FSW hardness depth profile exhibited no significant differences; this can be attributed to the microstructure symmetry.

This investigation revealed that rotational speed significantly influences the visual quality, void formation, and mechanical properties of the welded joints. As the rotational speed increased, the weld’s visual quality decreased, exhibiting more severe macroscopic defects such as visible wormholes. The severity of the internal voids also increased with increased rotational speed. The SR-FS welded joints exhibited lower mechanical properties compared to the parent metal. During tensile tests, failures occurred in the region that corresponds to the minimum hardness, for defect-free samples. The samples that exhibited severe internal voids resulted in the lowest mechanical properties and tensile fracture occurred in the nugget region. The lazy S defect, which predominated the samples fabricated for this investigation, appears to have no influence on the final mechanical properties.

The optimal rotational speed, traverse speed, and tool plunge force during SR-FSW of 6061-T651 aluminum plates with a thickness of .3125” were found to be 450 rpm, 20 ipm, and 1350 lb<sub>f</sub>, respectively. This process parameter combination resulted in the highest ductility and joint efficiency.



## References

- [1] American Welding Society, "AWS Welding Handbook 9.3," American Welding Society, United States of America, pp. 248-255, Chap. Chapter 7.
- [2] Mishra, R.S., and Mahoney, M.W., 2007, "Friction Stir Welding and Processing," ASM International, Ohio, pp. 352.
- [3] Colegrove, P., Dr., 2007, "Airbus Evaluates Friction Stir Welding," COSMOL News, pp. 4-7.
- [4] Totten, G.E., and Mackenzie D. Scott, 2003, "Handbook of Aluminum," Marcel Dekker Inc., New York, pp. 579.
- [5] Covington, J. L., 2005, "Experimental and Numerical Investigation of Tool Heating during Friction Stir Welding," pp. 1-89.
- [6] Nandan, R., DebRoy, T., and Bhadeshia, K. D. H., 2008, "Recent Advances in Friction Stir Welding - Process, Weldment Structure and Properties," Progress in Materials Science, (53) pp. 980-1023.
- [7] Adamowski, J., Gambaro, C., Lertora, E., 2007, "Analysis of FSW Welds made of Aluminium Alloy AW6082-T6," International OCSCO World Press, pp. 453.
- [8] Guerra, M., Schmidt, C., McClure, J. C., 2002, "Flow Patterns during Friction Stir Welding," Materials Characterization, **49**(2) pp. 95-101.
- [9] Krishnan, K. N., 2002, "On the Formation of Onion Rings in Friction Stir Welds," Materials Science and Engineering A, **327**(2) pp. 246-251.

- [10] Srivatsan, T. S., Vasudevan, S., and Park, L., 2007, "The Tensile Deformation and Fracture Behavior of Friction Stir Welded Aluminum Alloy 2024," *Materials Science and Engineering: A*, **466**(1-2) pp. 235-245.
- [11] Elangovan, K., and Balasubramanian, V., 2008, "Influences of Post-Weld Heat Treatment on Tensile Properties of Friction Stir-Welded AA6061 Aluminum Alloy Joints," *Materials Characterization*, **59**(9) pp. 1168-1177.
- [12] Scialpi, A., De Filippis, L. A. C., and Cavaliere, P., 2007, "Influence of Shoulder Geometry on Microstructure and Mechanical Properties of Friction Stir Welded 6082 Aluminium Alloy," *Materials & Design*, **28**(4) pp. 1124-1129.
- [13] Kumar, K., and Kailas, S. V., 2008, "The Role of Friction Stir Welding Tool on Material Flow and Weld Formation," *Materials Science and Engineering: A*, **485**(1-2) pp. 367-374.
- [14] Moreira, P. M. G. P., Santos, T., Tavares, S. M. O., 2009, "Mechanical and Metallurgical Characterization of Friction Stir Welding Joints of AA6061-T6 with AA6082-T6," *Materials & Design*, **30**(1) pp. 180-187.
- [15] Sato, Y. S., Urata, M., and Kokawa, H., "Parameters Controlling Microstructure and Hardness during Friction-Stir Welding of Precipitation-Hardenable Aluminum Alloy 6063," *Metallurgical and Materials Transactions A*, (Volume 33, Number 3 / March, 2002) pp. 625-635.
- [16] Huijie Liu, H. Fujii, M. Maeda and K. Nogi, 2003, "Tensile Properties and Fracture Locations of Friction-Stir Welded Joints of 6061-T6 Aluminum Alloy," *Journal of Materials Science Letters*, **22**(15) pp. 1061-1063.

- [17] Vijayan, S., Raju, R., Subbasah, K., 2009, "Friction Stir Welding of Al-mg Alloy Optimization of Process Parameters using Taguchi Method," Society for Experimental Mechanics, pp. 1747-1567.
- [18] Rodrigues, D. M., Loureiro, A., Leitao, C., 2009, "Influence of Friction Stir Welding Parameters on the Microstructural and Mechanical Properties of AA 6016-T4 Thin Welds," Materials & Design, **30**(6) pp. 1913-1921.
- [19] Chen, Z. W., and Cui, S., 2008, "On the Forming Mechanism of Banded Structures in Aluminum Alloy Friction Stir Welds," Scripta Materialia, **58**pp. 417-420.
- [20] Burford, D., Widener, C., and Tweedy, B., 2006, "Advances in Friction Stir Welding for Aerospace Applications," Airframer, (14) pp. 3.
- [21] Zhang, H. W., Zhang, Z., and Chen, J. T., 2007, "3D Modeling of Material Flow in Friction Stir Welding Under Different Process Parameters," Journal of Materials Processing Technology, **183**(1) pp. 62-70.
- [22] Fujii, H., Cui, L., Maeda, M., 2006, "Effect of Tool Shape on Mechanical Properties and Microstructure of Friction Stir Welded Aluminum Alloys," Material Science and Engineering, (419) pp. 25-31.
- [23] Zhang, Z., Liu, Y. L., and Chen, J. T., 2009, "Effect of Shoulder Size on the Temperature Rise and the Material Deformation in Friction Stir Welding," Int J Adv Manuf Technol, (45) pp. 889.
- [24] Elangovan, K., and Balasubramanian, V., 2008, "Influences of Tool Pin Profile and Tool Shoulder Diameter on the Formation of Friction Stir Processing Zone in AA6061 Aluminium Alloy," Materials & Design, **29**(2) pp. 362-373.

- [25] Lockheed Martin Corporation, 2010, "Friction Stir Welding,"  
<http://www.lockheedmartin.com/products/FrictionStirWelding/index.html> **2010**(May/27) pp. 1.
- [26] NASA, , 2010, "Space Shuttle Technology Summary,"  
[http://www.nasa.gov/centers/marshall/pdf/104835main\\_friction.pdf](http://www.nasa.gov/centers/marshall/pdf/104835main_friction.pdf) **2010**(May/27) pp. 1.
- [27] Ding, R. J., and Oelgoetz, P. A., 1999, "Auto-Adjustable Pin Tool for Friction Stir Welding," U.S. Patent **5893507**pp. 1-7.
- [28] Carter, R., 2006, "Tool for Two Types of Friction Stir Welding,"  
<http://www.techbriefs.com/component/content/article/1055> **2010**pp. 1.
- [29] Matlack, M. P., and Burton, K. A., 2010, "Friction Stir Welding Tool Cleaning Method," U.S. Patent **11/451729**(7641739).
- [30] Hwang, Y., Kang, Z., Chiou, Y., 2008, "Experimental Study on Temperature Distributions within the Workpiece during Friction Stir Welding of Aluminum Alloys," International Journal of Machine Tools and Manufacture, **48**(7-8) pp. 778-787.
- [31] Litynska, L., Baun, R., Staniek, G., 2003, "TEM Study of the Microstructure Evolution in a Friction Stir Welded AlCuMgAg Alloys," Materials Chemistry and Physics, **81**pp. 293-295.
- [32] Cam, G., Gucluer, S., Caka, A., 2009, "Mechanical Properties of Friction Stir Butt-Welded Al-5086 H32 Plate," Mat.-Wiss. u. Werkstofftech, (8) .
- [33] Uematsu, Y., Tokaji, K., Shibata, H., 2009, "Fatigue Behaviour of Friction Stir Welds without neither Welding Flash nor Flaw in several Aluminium Alloys," International Journal of Fatigue, **31**(10) pp. 1443-1453.

- [34] Hirata, T., Oguri, T., Hagino, H., 2007, "Influence of Friction Stir Welding Parameters on Grain Size and Formability in 5083 Aluminum Alloy," *Materials Science and Engineering A*, (456) pp. 344-349.
- [35] Meran, C., Kovan, V., and Alptelan, A., 2007, "Friction Stir Welding of AISI 304 Austenitic Stainless Steel," *Mat.-Wiss. u. Wrkstofftech*, (10) pp. 38.
- [36] Ghosh, M., Kumar, K., Kailas, S. V., 2010, "Optimization of Friction Stir Welding Parameters for Dissimilar Aluminum Alloys," *Materials and Design*, **31**pp. 3033-3037.
- [37] Uematsu, Y., Tokaji, K., Tozaki, Y., 2006, "Fatigue Behaviour of Friction Stir Welded 6061-T6 Aluminum Alloy," *Proceeding of the 16th European Conference of Fracture*, E. E. Gdoutos, ed. Springer, Netherlands, pp. 287.
- [38] Chen, H., Yan, K., Lin, T., 2006, "The Investigation of Typical Welding Defects for 5456 Aluminum Alloy Friction Stir Welds," *Materials Science and Engineering: A*, **433**(1-2) pp. 64-69.
- [39] Hilgert, J., Schmidt, H., and dos Santos, J. F., 2009, "Bobbin Tool FSW- A Moving Geometry Model," *Proceedings of the COMSOL*, .
- [40] Chao, Y. J., Qi, X., and Tang, W., 2003, "Heat Transer in Friction Stir Welding-- Experimental and Numerical Studies," *Journal of Manufacturing Science and Engineering*, **125**pp. 138-145.
- [41] McGee, T., D., 1988, "Principes and Methods of Temperature Measurment," John Wiley & Sons Inc, Canada, pp. 237.
- [42] DATAQ Instruments, I., 2010, "Thermocouple Applications," **2010**pp. 1.



- [43] Vollmer, M., and Mollmanhn, K.-., 2010, "Infrared Thermal Imaging," Willey-VCH Verlag GmbH & Co., Germany, pp. 589.
- [44] Song, M., and Kovacevic, R., 2003, "Thermal Modeling of Friction Stir Welding in a Moving Coordinate System and its Validation," International Journal of Machine Tools and Manufacture, **43**(6) pp. 605-615.
- [45] Ouyang, J., Yarrapareddy, E., and Kovacevic, R., 2006, "Microstructural Evolution in the Friction Stir Welded 6061 Aluminum Alloy (T6-Temper Condition) to Copper," Journal of Materials Processing Technology, **172**(1) pp. 110-122.
- [46] Vilaça, P., Quintino, L., and dos Santos, J. F., 2005, "ISTIR—Analytical Thermal Model for Friction Stir Welding," Journal of Materials Processing Technology, **169**(3) pp. 452-465.
- [47] Woo, W., Choo, H., Withers, J. P., 2009, "Prediction of Hardness Minimum Locations during Natural Aging in an Aluminum Alloy 6061-T6 Friction Stir Weld," Journal of Materials Science, **44**(23)
- [48] Russell, S.S., and Ezell, D., "Development of Weld Inspection of the Ares I Crew Launch Vehicle Upper Stage", [http://ntrs.nasa.gov/archive/nasa/casi.ntrs.nasa.gov/20100017377\\_2010017702.pdf](http://ntrs.nasa.gov/archive/nasa/casi.ntrs.nasa.gov/20100017377_2010017702.pdf), 2010.
- [49] Zhi-hong, F., and Di-qiu, H. H., W., 2004, "Friction Stir Welding of Aluminum Alloys," Journal of Wuhan University of Technology, **19**(1) .
- [50] Azimzadegan, T., and Sevajzadeh, S., 2010, "An Investigation into Microstructure and Mechanical Properties of AA7075-T6 during Friction Stir Welding at Relatively High Rotational Speed," Journal of Materials Engineering and Performance, .

- [51] Sato, Y. S., Takauchi, H., Park, S. H. C., 2005, "Characteristics of the Kissing-Bond in Friction Stir Welded Al Alloy 1050," *Materials Science and Engineering: A*, **405**(1-2) pp. 333-338.
- [52] Sato, Y. S., Yamashita, F., Sugiura, Y., 2004, "FIB-Assisted TEM Study of an Oxide Array in the Root of a Friction Stir Welded Aluminium Alloy," *Scripta Materialia*, **50**(3) pp. 365-369.
- [53] Zhou, C., and Yang, X., 2006, "Effect of Kissing Bond on Fatigue Behaviour of Friction Stir Welds on Al 5083 Alloys," *J Mater Sci*, **41**pp. 2771.
- [54] Liu, G., Murr, L. E., Niou, C., 1997, "Microstructural Aspects of the Friction-Stir Welding of 6061-T6 Aluminum," *Scripta Materialia*, **37**(3) pp. 355-361.
- [55] Heinz, B., and Skrotzki, B., 2002, "Characterization of a Friction-Stir-Welded Aluminum Alloy 6013," *Metallurgical and Materials Transactions B*, (Volume 33, Number 3 / June, 2002) pp. 489-498.
- [56] Jata, V. K., Sankaran, K. K., and Ruschau, J. J., 2007, "Friction-Stir Welding Effects on Microstructure and Fatigue of Aluminum Alloy 7050-T7451," *Metallurgical and Materials Transactions A*, (Volume 31, Number 9 / September, 2000) pp. 2181-2192.
- [57] Cavaliere, P., Campanile, G., Panella, F., 2006, "Effect of Welding Parameters on Mechanical and Microstructural Properties of AA6056 Joints Produced by Friction Stir Welding," *Journal of Materials Processing Technology*, **180**(1-3) pp. 263-270.
- [58] Lafly, L. A., Allehaux, D., Marie, F., 2005, "Impact of Friction Stir Welding Techniques on Microstructure Changes and Mechanical Properties," 58th Annual Assembly and International Conference of International Insittute of Welding (IIW), Prague, 10-16 July 2005.

- [59] Sakthivel, T., Sengar, S. G., and Mukhopadhyay, J., 2008, "Effect of Welding Speed on Microstructure and Mechanical Properties of Friction-Stir-Welded Aluminum," *Int J Adv Manug Technol*, **43**pp. 468-473.
- [60] Peel, M., Steuwer, A., Preuss, M., 2003, "Microstructure, Mechanical Properties and Residual Stresses as a Function of Welding Speed in Aluminium AA5083 Friction Stir Welds," *Acta Materialia*, **51**(16) pp. 4791-4801.
- [61] Mahoney, W. M., Rhodes, G. J., Bingel, H. W., "Properties of Friction-Stir-Welded 7075 T651 Aluminum," *Metallurgical and Materials Transactions A*, (Volume 29, Number 7 / July, 1998) pp. 1955-1964.
- [62] Ericsson, M., and Sandström, R., 2003, "Influence of Welding Speed on the Fatigue of Friction Stir Welds, and Comparison with MIG and TIG," *International Journal of Fatigue*, **25**(12) pp. 1379-1387.
- [63] Liu, H., Fijuu, H., and Nogi, M., K., 2003, "Tensile Properties and Fracture Locations of Friction-Stir Welded Joints of 6061-T6 Aluminum Alloy," *Journal of Materials Science Letters*, **22**pp. 1061-1063.
- [64] Liu, H. J., Fujii, H., Maeda, M., 2003, "Tensile Properties and Fracture Locations of Friction-Stir-Welded Joints of 2017-T351 Aluminum Alloy," *Journal of Materials Processing Technology*, **142**(3) pp. 692-696.
- [65] Singh, R. K. R., Sharma, C., Dwivedi, D. K., 2010, "The Microstructure and Mechanical Properties of Friction Stir Welded Al-Zn-mg Alloy in as Welded and Heat Treated Conditions," *Materials and Design*, **32**pp. 682-687.

- [66] Aydin, H., Bayrma, A., Uguz, A., 2009, "Tensile Properties of Friction Stir Welded Joints of 2024 Aluminum Alloys in Different Heat-Treated-State," *Materials and Design*, (30) pp. 2211.
- [67] Heurtier, P., "Characterising Texture Variation in a Friction Stir Welded Aluminum Alloy," <http://www.oxford-instruments.com/products/microanalysis/ebsd/ebsd-applications/Pages/Friction%20stir%20welded%20aluminium.pdf> 2010.
- [68] McNelley, T. R., Swaminathan, S., and Su, J. Q., 2008, "Recrystallization Mechanisms during Friction Stir Welding/Processing of Aluminum Alloys," *Scripta Materialia*, **58**(5) pp. 349-354.
- [69] Prangnell, P. B., and Heason, C. P., 2005, "Grain Structure Formation during Friction Stir Welding Observed by the 'Stop Action Technique'," *Acta Materialia*, **53**(11) pp. 3179-3192.
- [70] Hamilton, C., Dymek, S., and Sommers, A., 2008, "A Thermal Model of Friction Stir Welding in Aluminum Alloys," *International Journal of Machine Tools and Manufacture*, **48**(10) pp. 1120-1130.
- [71] Murr, L. E., Trillo, E. A., Pappu, S., 2002, "Adiabatic Shear Bands and Examples of their Role in Severe Plastic Deformation," *Journal of Materials Science*, **37**pp. 3337-3360.
- [72] Xu, S., and Deng, X., 2008, "A Study of Texture Patterns in Friction Stir Welds," *Acta Materialia*, **56**(6) pp. 1326-1341.

## **Curriculum Vita**

Monica Torres, the middle child of Jesus Torres and Alejandrina Obregon, was born in January 13, 1983 in Ciudad Juarez, Chihuahua Mexico. Monica Torres received her Bachelor of Science Degree in Industrial Engineering from Tecnologico de Monterrey, Campus Juarez, while working for Delphi Automotive Systems. During this time, she had the opportunity to work with many talented individuals from the materials laboratory, which awoke her interest in material science. In 2007, she enrolled in The Graduate School at The University of Texas at El Paso to pursue a Master of Science in Metallurgical and Material Engineering. After a year into the program, she started working with Dr. Luis Trueba on friction stir welding. This lead to new opportunities and challenges; in 2009, she worked with Jacobs Engineering and NASA as part of her research project. In her spare time, Monica enjoys training for and participating in triathlons.

After graduation, Monica Torres plans to continue her studies by pursuing a PhD in materials science at The University of Texas at El Paso.

Permanent address: 200 N. Mesa Hills Dr. Apt 304  
El Paso, Texas, 79912

This thesis/dissertation was typed by Monica Torres